Structural, Morphological and Photoluminescence studies of certain doped Titanate Phosphors for Photonic Applications

Thesis

Submitted to

Delhi Technological University

in partial fulfilment for the requirements for the Degree of

DOCTOR OF PHILOSOPHY

in

APPLIED PHYSICS

By

Pooja Rohilla

(Reg. No. 2K18/Ph.D./AP/502)

Under the Supervision

of

Prof. A. S. Rao

Head & DRC Chairperson

Department of Applied Physics

Delhi Technological University

Bawana Road, Delhi-110042

DEPARTMENT OF APPLIED PHYSICS

DELHI TECHNOLOGICAL UNIVERSITY

DELHI-110 042, INDIA

FEBRUARY-2024

Dedicated to my beloved family

DECLARATION

This is to certify that the Ph.D. thesis entitled **"*Structural, Morphological and Photoluminescence studies of certain doped Titanate Phosphors for Photonic Applications*"** submitted to Delhi Technological University (DTU) for the award of the degree of **"Doctor of Philosophy"** in Applied Physics is a record of bonafide work carried out by me under the guidance and supervision of **Prof. A. S. Rao** at Materials and Atmospheric Science Research Laboratory, Department of Applied Physics, DTU and has fulfilled the requirements for the submission of this thesis. The results contained in this thesis are original and have not been submitted to any other University/Institutions for the award of any degree or diploma.

Pooja Rohilla
Research Scholar
(Reg. No. 2K18/Ph.D./AP/502)

Delhi Technological University

Formerly Delhi College of Engineering

(Under Delhi Act 6 of 2009, Govt. of NCT of Delhi)

Shahbad Daulatpur, Bawana Road, Delhi-110042

CERTIFICATE

This is to certify that the Ph.D. thesis entitled **"*Structural, Morphological and Photoluminescence studies of certain doped Titanate Phosphors for Photonic Applications*"** submitted to Delhi Technological University (DTU) for the award of the degree of **"Doctor of Philosophy"** in Applied Physics is a record of bonafide work carried out by me under the guidance and supervision of Prof. A. S. Rao at Materials and Atmospheric Science Research Laboratory, Department of Applied Physics, DTU and has fulfilled the requirements for the submission of this thesis. The results contained in this thesis are original and have not been submitted to any other University/Institutions for the award of any degree or diploma.

Pooja Rohilla

Research Scholar
(Reg. No. 2K18/Ph.D/AP/502)

This is to certify that the above statement made by the candidate is correct to the best of our knowledge.

Prof. A. S. Rao
(Supervisor)

Prof. A.S. Rao
Head & DRC Chairperson
Department of Applied Physics
Delhi Technological University, Delhi, India

ACKNOWLEDGEMENTS

My study journey has been made possible by the invaluable assistance of many individuals. The fact that I can now thank each and every one of them is a pleasant aspect.

First and foremost, I am thankful to ***Almighty God*** *for his grace throughout my life.*

I would like to express my sincere thanks, debt of gratitude, and respect to my ***Supervisor***, ***Prof. A.S. Rao***, ***Head & DRC Chairperson, Department of Applied Physics*** *at Delhi Technological University in Delhi. He helped me develop the research skills I needed to pursue a fruitful scientific career. It has been an honor to work for such a wonderful, dynamic, and accomplished supervisor. His unwavering support, assistance, careful oversight during my studies have all contributed to me reaching yet another academic milestone. Throughout the duration of this thesis study, his vast topic knowledge, intellectual gaze, vision, and endurance served as a continual source of inspiration.*

It is my pleasure to express my sincere thanks to all the ***DRC and SRC members***, ***other faculty members*** *of Department of Applied Physics, DTU for their continuous encouragement and help during my research work. I am also appreciative of the technical and non-technical staff for their prompt assistance and collaboration as needed.*

I sincerely thank my dear former and present lab-mates whose support helped in accomplishing my work. It is my pleasure to thank my seniors ***Dr. Nisha Deopa, Dr. Sumandeep Kaur, Dr. Aman Prasad, Dr. Arti Yadav, Dr. Kanika Bhatiya, Dr. Harpreet Kaur, Dr. Mukesh Sahu, Dr. Yasha Tayal, Dr. Mohit Tyagi, Dr. Kartika Maheshawri,*** *and other labmates* ***Mrs. Shristy Malik, Mr. Rajat Bajaj, Dr. Ravita, Dr. Deepali, Ms. Sheetal kumari, Ms. Anu, , Mrs. Shweta Yadav, Mr. Vikas Sangwan, Mr. Videsh, Ms. Kanika, Mr. Inderjeet Maurya and Ms. Vertika*** *for their support. I would also like to thank my friends in DTU* ***Mrs. Ritika Ranga*** *and*

Dr. Prateek Sharma *for their continuous help and support whenever needed. Achieving a work-life balance is crucial, and it wouldn't have been possible without my friends* ***Mrs. Vandana Rohilla, Mr. Parveen Rohilla, Mrs. Jyoti Jangra, Mrs. Seema*** *and* ***Mrs. Jyoti Sharma.*** *These are my stress busters during this time.*

I extend my heartfelt gratitude to my family whose unwavering support, love, and encouragement have been invaluable throughout my academic journey. I am deeply indebted to my father, ***Mr. Krishan Rohilla****, and my mother,* ***Mrs. Sushila Rohilla****, for their constant guidance and affection. My sincere appreciation goes to my* ***Chacha ji, Mr. Darshan Rohilla****, and* ***Chachi ji, Mrs. Sushma Rohilla****, for their encouragement and support. I am also thankful to my siblings,* ***Vikas Rohilla****,* ***Kapil Rohilla****,* ***Kavita Rohilla****,* ***Ankita Rohilla****, and* ***Kajal Rohilla****, for their belief in me and their invaluable advice. Special gratitude is reserved for my husband,* ***Mr. Shubham Rohilla****, for his guidance and support during the challenging phases of my thesis submission. I would also like to express my gratitude to my in-laws,* ***Mr. Mahesh Rohilla****,* ***Mrs. Pavitra Rohilla****,* ***Mr. Shivam Rohilla****, and* ***Mrs. Aayushi Rohilla****, for their unwavering support and understanding. I am appreciative of my paternal and extended families for supporting me in keeping a good outlook during my academic career. I am eternally grateful to all of my dear friends throughout the world for being there to share both my joy and my grief.*

I would like to express my gratitude to Delhi Technological University for the financial support which I received in the form of Junior and Senior Research Fellowships during the course of my Ph.D. work. I would also like to express my sincere thanks to the employees of Delhi Technological University's Administration, Accounts, Store and Purchase, Library, and Computer Center for their assistance and support.

I thank one and all for helping me accomplish the successful realization of the thesis.

Thank you all!!!

Pooja Rohilla

List of Publications

Included in the thesis

1. Synthesis optimization and efficiency enhancement in Eu^{3+} doped barium molybdenum titanate phosphor for w-LED applications.

   Pooja Rohilla, A. S. Rao

   Materials Research Bulletin, 150 (2022) 111753. (**I.F.= 5.4)**

2. Linear and non-linear photoluminescence studies of Ho^{3+}/Yb^{3+} co-doped titanate phosphor for photonic applications.

   Pooja Rohilla, A. S. Rao

   Journal of Alloys and Compounds, 928 (2022) 167156. (**I.F.= 6.2)**

3. Energy transfer induced colour tunable photoluminescence performance of thermally stable Sm^{3+}/Eu^{3+} co-doped Ba_3MoTiO_8 phosphors for white LED applications.

   Pooja Rohilla, A. S. Rao,

   Journal of Materials Science: Materials in Electronics, 34 (2023) 1662. (**I.F.= 2.8)**

4. Structural and luminescence studies on Bi^{3+} activated Ba_3MoTiO_8 phosphors for near UV pumped w-LED applications.

   Pooja Rohilla, Aman Prasad, A. S. Rao,

   International Journal of Applied Ceramic Technology, 21 (2024) 1208-1219.

   (**I.F.= 2.1)**

Other than the thesis

1. Visible emission characteristics in Tb^{3+}-doped $KNa_3Al_4Si_4O_{16}$ phosphor.
   Vijay Singh, R. Kokate, **Pooja Rohilla**, Sumandeep Kaur, A.S. Rao,
   Optik, 243 (2021) 167391 (**IF: 3.1**)
2. Tb^{3+} activated $Na_3YSi_2O_7$ phosphors for display panels.
   Vijay Singh, **Pooja Rohilla**, Sumandeep Kaur, A.S. Rao,
   Optik, 271 (2022) 170221 **(IF: 3.1)**
3. Thermally stable Sm^{3+}-doped alkali zinc alumino borosilicate (AZABS) glass for warm white light generation and w-LED applications**.**
   Rajat Bajaj, **Pooja Rohilla**, Aman Prasad, Ravita, Ankur Shandilya, Allam Srinivasa Rao,
   Luminescence, 38 (2023) 428-436 (**IF: 2.9**)
4. Photoluminescence and energy transfer studies on Tm^{3+}/Dy^{3+} /Eu^{3+}doped borosilicate glasses for color tunability and warm white light generation**.**
   Ravita, Aman Prasad, **Pooja Rohilla,** Ankur Shandilya, A.S. Rao,
   Journal of Non-Crystalline Solids, 606 (2023) 122192 (**IF: 3.5**)
5. Down-shifting photoluminescence studies of thermally stable Dy^{3+} ions doped borosilicate glasses for optoelectronic device applications**.**
   Rajat Bajaj, Aman Prasad, A. V. S. Yeswanth, **Pooja Rohilla**, Sumandeep Kaur, and A. S. Rao,
   Journal of Materials Science: Materials in Electronics, 33 (2022) 4782-4793 (**IF: 2.8**)
6. Prospective applications of thermally stable Dy^{3+} doped potassium zinc strontium borate (KZSB) glasses in w-LEDs.
   Sheetal Kumari, Anu, Aman Prasad, **Pooja Rohilla**, and A. S. Rao
   Journal of Materials Science: Materials in Electronics, 34 (2023) 907 **(IF: 2.8)**

7. Luminescence Studies on Dy^{3+} Doped Calcium Aluminum Borosilicate (CABS) Glasses for White Light Emission and Applications in w-LEDs.

Ravita, Aman Prasad, **Pooja Rohilla**, Rajat Bajaj, Anu, Rajesh Punia, Allam Srinivasa Rao,

Journal of Fluorescence, (2023) **(IF: 2.7)**

8. Photoluminescence Studies on Dy^{3+} ions doped $CaBi_2Nb_2O_9$ Phosphors for Optoelectronic Device Applications.

Sheetal Kumari, **Pooja Rohilla**, Samarthya Diwakar, Rupesh A. Talewar, Ankur Shandilya, Yasha Tayal, K. Swapna, Aman Prasad, A.S. Rao

Journal of Materials Science: Materials in Electronics, (2024) ***(Under Revision)*** **(IF: 2.8)**

9. Colour tuning in thermally stable Sm^{3+} activated and Sm^{3+}/Eu3+ co-activated $SrBi_4Ti_4O_{15}$ phosphors for w-LED applications.

Pooja Rohilla, Sheetal Kumari, Ravita, Samarthya Diwakar, Rupesh Talewar, Ankur Shandilya, Kartika Maheshwari, M. Venkateswarlu, Aman Prasad, A.S. Rao

Journal of Molecular Structure, (2024) ***(Under Revision)*** **(IF: 3.8)**

10. Dy^{3+} doped $KCa(PO_3)_3$ phosphor for white light generation: Structural and Luminescent Studies.

Deepti, Sandip Maurya, Sheetal Kumari, **Pooja Rohilla**, Aman Prasad, A.S. Rao

Physica Scripta, (2024) ***(Communicated)*** **(IF: 2.9)**

11. On the optical features of blue emitting $La_2Zr_2O_7:Tm^{3+}$ phosphor

Vijay Singh, Aman Prasad, **Pooja Rohilla**, A.S. Rao

Journal of Electronic Materials, (2024) ***(Under Revision)*** **(IF: 2.1)**

ABSTRACT

Recent advances in solid-state lighting (SSL) devices have made a substantial and practical contribution to the lighting industries. SSL devices are small, robust, and energy-efficient and also environmentally friendly. The SSL based white light emitting diodes (w-LEDs) are more superior when compared to traditional conventional light sources like incandescent lamps, electric bulbs, and fluorescent tubes because they last longer, require less energy, have excellent colour rendering index, compact, and are ecologically friendly. The phosphor converted w-LEDs (pc-wLEDs) are appealing because of their low power consumption, excellent luminous efficacy, and environmentally beneficial features. The most widely used and readily accessible pc-wLEDs are built using a mix of blue-chip, green, and red phosphors or blue-chip and yellow phosphor. However, pc-wLEDs made by means of blue-LED and YAG: Ce^{3+} yellow phosphors suffer with some weaknesses, such as poor color rendering index (CRI) and low stability of color temperature. In tricolor (RGB) phosphors, the excitation is achieved by n-UV/UV LEDs. Moreover, in tricolor pc-wLED the efficiency of red phosphors is low in comparison with green and blue phosphors and the rate of degradation of tricolor phosphors is different. Therefore, it is necessary to develop single phase phosphor with tunable emission containing white emission such that luminous efficiency, CRI and correlated color temperature (CCT) can be improved.

Both the up-conversion and down-conversion are the fields in which phosphors are used. The most well-known method of obtaining the good luminous characteristics has traditionally been the doping of lanthanide ions/transition metal ions in an appropriate host matrix. Lanthanides are part of the f-block series of elements and are more commonly known as rare earths (RE). The typical behavior of lanthanide ions is to become excited by absorbing UV or near-UV light and then release the energy in the form of visible light. To trigger the luminescence phenomena in such

hosts, they need a luminescent ion (or activator). Even in some cases, the activator may occasionally fall short of effectively absorbing the energy and transforming it into visible light emission. In such cases, a sensitizer ion plays a supporting role by effectively absorbing energy and transferring part or all of it to the activator, significantly improving the light emission capacity of activator. Some hosts such as vanadates and tungstates have the ability to excite themselves by UV light and emit radiation in the near-UV or visible range. Such hosts are called as host luminophores. The primary need for a phosphor to be used in a pc-LED is that they must have a substantial absorption in the UV or near-UV area and must have an effective emission in the visible light zone. Titanate-based phosphors have gathered the most attention among all of these substances because of the broad bandgap and high refractive index of the titanate group, which improve emission intensity. By changing some synthesis parameters and doping them with a 3d or 4f ions, titanate-based systems' chromaticity can be managed. This thesis comprises the work done on Barium Molybdenum Titanate (Ba_3MoTiO_8) (now onwards abbreviated as BMT) phosphor lattice as the structural and luminescent properties of this ternary compound doped with RE ions has not been extensively studied till now. Seven chapters make up this thesis' structure in order to meet the objectives of my research. Each chapter is structured such that it may be read alone.

Chapter 1 includes an explanation of the introduction, the origin of the problem, the motivation for the study, and an overview of recent literature. This chapter focuses on the white light generation's brief technological history, benefits, and related difficulties. Theoretical models for analyzing observed spectrum data, ionic interaction, and energy transfer between RE ions are used in conjunction with the spectroscopy of RE ions. Dexter theory was used to know the type of interaction between the acceptor/donor ions. Evaluation of the CIE coordinates, color purity, and corresponding color temperature are made possible by the emission spectral data. In addition to

this, analysis of PL decay curves was also discussed to know the lifetime of these activator/ sensitizer ions.

Chapter 2 describes the synthesis of BMT phosphors doped with certain RE ions/post transition metal ions (Eu^{3+}, Sm^{3+}, Ho^{3+}, and Yb^{3+}, Bi^{3+}) at variable concentrations using different techniques. Additionally, it describes the experimental apparatus used to examine the structural, morphological, optical and photoluminescence (PL) characteristics of BMT phosphors. Discussion has also been extended to the structural, vibrational and PL characteristics discovered by X-ray diffractometer (XRD), Fourier transform infrared (FT-IR) spectroscopy, Raman spectroscopy, Diffuse reflectance spectroscopy (DRS) and PL Spectroscopy.

Chapter 3 explains synthesis optimization and efficiency enhancement in Eu^{3+} doped BMT phosphors for w-LED applications. Ba_3MoTiO_8 phosphors activated with Eu^{3+} ions have been synthesized successfully by three different routes such as solid-state reaction method (SSM), combustion method (CMM), and sol-gel combustion method (SGM) to optimize relatively best synthesis technique and temperature of synthesis. XRD patterns have been used to confirm the phase and crystallinity of the as-prepared phosphor. SEM and Raman spectra have been used to study the morphological behavior and different vibrational bands present in the structure of the titled phosphor respectively. DRS have been recorded to find out the optical band gap of phosphors. PL spectral features recorded under 393 & 465 nm excitation wavelengths reveal an intense red emission at 612 nm corresponding to $^5D_0 \rightarrow {}^7F_2$ transition of the doped Eu^{3+} ions. CMM synthesized sample has shown maximum PL intensity out of the three synthesis methods and further studies have been carried out by preparing a series of europium ions doped BMT phosphors using the CMM technique. The PL decay curves recorded for 612 nm red emission under 393 nm excitation show non-linear double exponential nature with a decrease in an experimental lifetime as Eu^{3+} ions

concentration increases in the as-prepared phosphors. All the morphological and PL studies carried out on the Eu^{3+} ions doped BMT phosphor emphasize the suitability of the as-prepared phosphor for a red component in w-LEDs fabrication.

Chapter 4 contains linear and non-linear PL studies of Ho^{3+}/Yb^{3+} co-doped titanate phosphors for photonic applications. This work presents the morphological and PL studies of the single Ho^{3+} ion doped and Ho^{3+}/Yb^{3+} co-doped BMT: xHo^{3+}/yYb^{3+} phosphors synthesized by conventional SSM reaction method. Phase confirmation of all the as-prepared samples was done by XRD patterns. The morphological behavior and vibrational frequency bands were studied by SEM and FT-IR techniques respectively. DRS has been recorded for the singly doped and co-doped samples to find out the optical bandgap. The linear and non-linear emission spectral studies under 448 & 980 nm excitation wavelengths respectively showed three bands in the green, red, and blue regions. A relatively more intense band observed in the green region under 980 nm excitation shows promising usage of the titled phosphor for non-linear applications. A plot drawn between non-linear PL emission intensity vs pump power reveals the information pertaining to the number of photons involved in the process. In addition, CIE coordinates calculated from the emission spectral features lie in the green region. All the studies show the broad application of the as-prepared phosphors in linear and non-linear luminescence process-based green emitting diodes, display devices, security inks, phototherapy, and SSL applications.

Chapter 5 describes energy transfer induced color tunable PL performance of thermally stable Sm^{3+}/Eu^{3+} co-doped BMT phosphors for w-LED applications. The combustion process has been successfully used to synthesize BMT: Sm^{3+} and BMT: Sm^{3+}/Eu^{3+} co-doped phosphors for w-LED applications. For the as-prepared phosphors, XRD, SEM, FT-IR, DRS, and PL spectroscopy techniques have been used to investigate phase confirmation, morphological analysis, and PL

properties. The PL emission spectra of singly doped Sm^{3+} and Sm^{3+}/Eu^{3+} co-doped phosphors recorded under 409 nm wavelength show intense emission in reddish-orange and red regions, respectively. For Sm^{3+}-Eu^{3+} co-doped phosphors, the intensity of Sm^{3+} peaks show a decrease with an increase in Eu^{3+} ion concentration, demonstrating the energy transfer from Sm^{3+} to Eu^{3+} ions. Quadrupole-quadrupole interaction is the mechanism responsible for energy transfer from Sm^{3+} ions to Eu^{3+} ions according to Dexter's hypothesis as applied to the PL spectra. This result is in consonance with the results of PL decay curves recorded under 409 nm excitation. The Commission Internationale de I' Eclairage coordinates calculated for singly Sm^{3+} doped and Sm^{3+}/Eu^{3+} co-doped phosphors show colour tunability from reddish-orange to pure red regions. All the results obtained finally revealed the utility of the titled phosphors as tunable red emitters needed to fabricate w-LEDs.

Chapter 6 provides structural and luminescence studies on thermally stable Bi^{3+} activated BMT phosphors for near UV pumped w-LED applications. This research presents the outcomes of diverse morphological and PL studies performed on Bi^{3+} ions doped BMT phosphors prepared via conventional SSM method. Phase assessment was carried out via the XRD studies. SEM and EDAX analysis have been used to study the surface morphology and elemental composition. FT-IR was used to study the character and vibrational frequencies of bonds in the titled host lattice. Room-temperature PL was performed under 275 & 386 nm excitations displaying a broad band in the blue region corresponding to $^3P_1 \rightarrow {}^1S_0$ transition of Bi^{3+} ions. The CIE coordinates and correlated colour temperature values show that the as-prepared phosphors emit in the blue vicinity. The PL decay curves under both excitation wavelengths show a single exponential behavior. Temperature-dependent PL studies confirmed the high thermal stability of the phosphor. All the

results obtained endorses the utility of the titled phosphors of this chapter as a blue-emitting component in w-LED and SSL applications.

Chapter 7 summarizes the overall research results presented in this thesis work as well as the specific conclusions drawn from the findings. At the end of this chapter the future scope of the present investigations has been explained.

CONTENTS

Declaration……... iv

Certificate…… v

Acknowledgments……... vi

List of publications……... ix

Abstract…… xii

Contents…… xvii

List of figures……... xxii

List of tables…… xxviii

Chapter 1: Introduction…… 1-28

1.1 Lighting technology…… 2

1.2 Disadvantages of conventional sources of light…….. 2

1.3 Why do we choose w-LEDs over conventional light sources …… 3

1.4 Luminescence and its various forms ……... 4

1.5 A closer look to PL through Jablonski diagram ……. 6

1.6 Phosphor…….. 7

1.6.1 Basic concepts for luminescence and phosphor……. 8

1.6.2 Down- conversion and up-conversion processes…… 10

1.7 Dopants…… 11

1.7.1 Rare Earth (RE) Ions ……..... 11

1.7.2 Post-transition metal ions …… 12

1.7.3 Type of Interactions …….. 13

1.8 Introduction to pc-wLED in the world of solid-state lighting technology…….. 15

1.8.1 Applications of phosphors……. 17

1.9 Spectral analysis…….. 20

1.9.1 Color rendering index…… 20

1.9.2 CIE coordinates & color purity…….. 20

1.9.3 Correlated color temperature……. 23

1.10 Energy transfer mechanism by using theoretical models…….. 23

1.10.1 Dexter theory and Reisfeld's approximation……. 24

1.11 PL decay kinetics……... 25

1.12 Selection of Host lattice……. 26

1.13 Objective of Research Work…….. 28

Chapter 2: Experimental and Characterization Techniques …… 29-55

2.1 Raw materials required …….. 30

2.2 Experimental methods …… 31

2.2.1 Solid-state reaction method…… 33

2.2.2. Combustion method …….. 34

2.2.3 Sol-Gel-Combustion method ……...…….. 34

2.3 Characterization techniques……. 36

2.3.1 Thermal analysis…… 36

2.3.2 XRD for structural investigations……..... 38

2.3.3 SEM and FESEM for morphological investigations…… 41

2.3.4 EDAX…..……... 44

2.3.5 FTIR for the identification of functional groups……... 45

2.3.6 Raman spectroscopy...……... 47

2.3.7 Diffuse reflectance spectroscopy …….. 49

2.3.8 PL Spectroscopy ……... 51

2.3.9 Temperature- dependent PL Spectroscopy ……... 54

Chapter 3: Synthesis optimization and efficiency enhancement in Eu^{3+} doped Barium Molybdenum Titanate phosphors for w-LED applications……..... 56-80

3.1 Introduction…….. 57

3.2 Sample preparation and coding ……..... 59

3.3 Characterization techniques used…… 60

3.4 Results and discussion……. 60

3.4.1 Structure and phase analysis …… 60

3.4.2 Morphological Analysis from SEM …….. 62

3.4.3 Raman spectral analysis …… 65
3.4.4 DRS analysis for band gap measurement…….. 67
3.4.5 PL excitation and emission spectral studies ……. 68
3.4.6 Colorimetric analysis …… 76
3.4.7 PL decay analysis ……. 78
3.5 Conclusions…….. 79
Chapter 4: Linear and Non-linear Photoluminescence studies of Ho^{3+}/Yb^{3+} Co-doped Titanate Phosphors for Photonic Applications……... **81-108**
4.1 Introduction…….. 82
4.2 Experimental ……... 83
4.2.1 Sample preparation via solid-state reaction method…….. 83
4.2.2 Characterization techniques used ……. 84
4.3 Result and discussion …….. 84
4.3.1 Structural measurements ……... 84
4.3.1.1 TGA and DSC analysis…… 84
4.3.1.2 XRD measurements…… 85
4.3.2 Morphological analysis ……. 89
4.3.2.1 SEM …… 89
4.3.2.2 EDX measurements and elemental mapping…… 90
4.3.3 FT-IR spectral analysis ……. 91
4.3.4 DRS analysis for band gap measurement…… 92
4.3.5 Linear (down-conversion) and non-linear (up-conversion) PL behaviour…….. 94
4.3.5.1 Linear PL excitation and emission spectral studies ……... 94
4.3.5.2 Non-linear PL spectral studies……... 97
4.3.5.3 Power dependent non-linear PL studies…… 98
4.3.6 PL lifetime decay measurements ……... 102
4.3.7 CIE and CCT analysis…… 105
4.4 Conclusions…….. 107
Chapter 5: Energy transfer induced colour tunable photoluminescence performance of thermally stable Sm^{3+}/Eu^{3+} co-doped Ba_3MoTiO_8 phosphors for white LED applications…… **109-133**
5.1 Introduction…….. 110
5.2 Experimental method and characterization techniques used …….. 111

5.3 Results and Discussion…… 113
5.3.1 Structural and morphological analysis …….. 113
5.3.2 FT-IR analysis …….. 119
5.3.3 DRS Spectra …….. 120
5.3.4 PL Studies ……. 121
5.3.4.1 PL Studies of BMT: xSm^{3+}(x= 1.5 mol%) phosphor…….. 121
5.3.4.2 PL Studies of single doped Eu^{3+} & Sm^{3+}/Eu^{3+} co-doped BMT phosphors……... 123
5.3.5 PL decay studies ……... 128
5.3.6 Temperature-dependent PL studies……... 129
5.3.7 CIE performance…… 132
5.4 Conclusions…… 132
Chapter 6: Structural and luminescence studies on thermally stable Bi^{3+} activated Ba_3MoTiO_8 phosphors for near UV pumped w-LED applications……..... 134 - 154
6.1 Introduction…….. 135
6.2 Material and Methods ……. 136
6.3 Results and discussion …… 137
6.3.1 Investigations on morphology and structure…….. 137
6.3.1.1 XRD analysis …… 137
6.3.1.2 FE-SEM and EDAX analysis…… 140
6.3.1.3 FT-IR measurement……... 141
6.3.1.4 DRS study……..... 142
6.3.2 PL studies at room temperature …… 143
6.3.2.1 PL excitation and emission studies…… 143
6.3.2.2 Colorimetry analysis…….. 148
6.3.2.3 Decay kinetics…… 150
6.3.3 Temperature-dependent PL Studies…… 152
6.4 Conclusions…….. 153
Chapter 7: Summary and Scope of Future Work…… **155 - 157**
7.1 Summary…….. 155
7.2 Future scope of the work …… 158
- References…… 159
……

List of Figures

1.1	Jablonski diagram.	7
1.2	Absorption of incident energy and luminescence (a1) Host sensitized luminescence (a2) Energy transfer induced luminescence from host to activator (a3) Activator induced luminescence (a4) Host - Sensitizer - Activator induced luminescence.	9
1.3	Representation of stokes (down-conversion) and anti-stokes (up-conversion) shift.	10
1.4	Periodic table comprises RE ions and other transition/post transition metals.	12
1.5	White light generation through Red+ Green + Blue LEDs.	16
1.6	White light generation using phosphors (a) NUV-LED+ RGB phosphors (b) Blue-LED+ Yellow phosphor.	16
1.7	Applications of phosphor materials in various fields.	18
1.8	CIE 1931 Chromaticity Diagram.	21
1.9	Diagrammatic portrayal of PL decay curves.	26
2.1	(a) Flowchart of various steps involved in the synthesis of BMT phosphor by SSR method. (b) Schematic representation of various steps involved in the synthesis of BMT phosphor by SGM and CMM techniques.	33-35
2.2	Perkin Elmer Pyris diamond (TGA/DTA/DSC) system.	37
2.3	Bragg's Diffraction representation from crystal planes.	38
2.4	Bruker D8 Advance X-ray diffractometer.	40
2.5	Zeiss EVO40 Scanning Electron Microscope.	42
2.6	JEOL 7610F Plus Field- Emission Scanning Electron Microscope.	43
2.7	Perkin Elmer spectrum 2 set-up.	46
2.8	Invia Renishaw Raman Spectroscope.	48
2.9	Jasco V-770 Spectrophotometer.	50

2.10	Jasco Spectrophotometer Spectrofluorometer FP-8300.	52
2.11	Horiba PTI Quanta Master equipped with 980 nm solid state laser.	53
2.12	Edinburgh FL920 Fluorescence Spectrometer.	54
2.13	Ocean Optics FLAME-S-XR1-ES Spectrometer.	55
3.1	(a) XRD pattern of BMT sample synthesized by SSM, SGM and CMM technique along with standard diffraction pattern of BMT. (b) XRD pattern of CMM1, SGM1 and SSM1 phosphor with 1 mol% concentration of Europium ion.	61-62
3.2	SEM images were recorded for BMT sample (a (i-iii)) SSM0 (b (i-iii)) SGM0 and (c (i-iii)) CMM0.	63
3.3	SEM images for doped samples (a.1) SSM1 (b.1) SGM1 (c.1) CMM1 and EDAX Spectra for doped BMT phosphor (a.2) SSM1 (b.2) SGM1 (c.2) CMM1.	65
3.4	Raman spectra of SSM0, SGM0 and CMM0 sample.	66
3.5	Diffuse Reflectance Spectrum of CMM0 and CMM2 sample. Inset image shows the assessment of direct band gap using Kubelka- Munk plot.	67
3.6	Excitation spectra of SSM1, SGM1 and CMM1 phosphor with 1 mol% Eu^{3+} ion at 612 nm emission wavelength.	68
3.7	(a) Emission spectra of SSM1, SGM1 and CMM1 phosphor with 1 mol% Eu^{3+} ion at 393 nm excitation wavelength. (b) Emission spectra of SSM1, SGM1 and CMM1 phosphor with 1 mol% Eu^{3+} ion at 465 nm excitation wavelength.	69-70
3.8	(a) Emission spectra of CMM synthesized BMT: xEu^{3+} (x=1, 2, 3 and 4 mol%) phosphors at 393 nm excitation wavelength. (b) Emission spectra of CMM synthesized BMT: xEu^{3+} (x=1, 2, 3 and 4 mol%) phosphors at 465 nm excitation wavelength.	72-73
3. 9	Energy level diagram for various transitions in europium ion.	74
3.10	Dexter Plot of log (I/x) vs. log (x), (a) under 393 nm (b) under 465 nm, excitation wavelengths.	75

3.11	CIE chromaticity diagram of BMT: xEu^{3+} (x= 1, 2, 3, 4 mol%) phosphors synthesized by CMM method, under the excitation wavelength of (a) 393 nm (b) 465 nm.	77
3.12	Decay profile of Eu^{3+} ions doped BMT phosphors synthesized by CMM route.	79
4.1	TGA and DSC curves of an un-doped BMT sample.	85
4.2	(a) XRD patterns of an un-doped BMT sample & co-doped $Ba_{3-x-y}MoTiO_8:xHo^{3+}/yYb^{3+}$ (x=11mol% and y=1,3,5 and 7mol%) phosphors series with standard JCPDS data, (b&c) show rietveld refinement treatment recorded for an un-doped and co-doped BMT phosphor respectively.	86
4.3	Scanning electron microscope images (a-b) of xHo^{3+} doped (x=11mol%) and xHo^{3+}/yYb^{3+} (x=11mol% and y=7mol%) co-doped phosphors (c-d) and their corresponding EDX images.	89
4.4	Elemental mapping of xHo^{3+}/yYb^{3+} (x=11 mol%, y=7 mol%) co-doped BMT phosphor in (a) mixed mapping and for individual elements such as Barium (Ba), Titanium (Ti), Molybdenum (Mo), Holmium (Ho) and ytterbium (Yb) from (b) to (f) respectively.	90
4.5	FT-IR spectra of an undoped sample, single Ho^{3+}doped and co-doped Ho^{3+}/Yb^{3+} BMT phosphors.	91
4.6	Diffuse Reflectance Spectra of $Ba_{3-x-y}MoTiO_8:xHo^{3+}/yYb^{3+}$ phosphor (a) x=11mol%, y=0 mol% (b) x=11mol%, y=1,3,5 and 7mol% and their corresponding tau plots (inset figures).	93
4.7	Linear (a) PL excitation spectrum of Ho^{3+} doped (11 mol%) phosphors under 551 nm emission and (b) PL emission spectra of $Ba_{3-x}MoTiO_8:xHo^{3+}$ (x= 1,3,5,7,9,11 and 13mol%) phosphors under 448 nm excitation wavelengths respectively.	95
4.8	Linear PL spectra of $Ba_{3-x-y}MoTiO_8$**:**xHo^{3+}/yYb^{3+} (x=11mol% and y=1,3,5 and 7mol%) phosphors under λ_{ex} = 448 nm.	96

4.9	Non-linear PL spectra of $Ba_{3-x-y}MoTiO_8$**:**xHo^{3+}/yYb^{3+} (x=11mol% and y=1,3,5 and 7mol%) phosphors under 980 nm laser excitation.	97
4.10	(a) Power dependence non-linear PL spectra of $Ba_{3-x-y}MoTiO_8$**:**xHo^{3+}/yYb^{3+} (y= 7mol%) phosphor under 980 nm laser excitation. (b) Ln-Ln plot of UC intensity vs. pump power	99
4.11	Schematic energy level diagram of Ho^{3+} and Yb^{3+} ions and their energy transfer mechanism.	102
4.12	PL decay curves of $Ba_{3-x-y}MoTiO_8$**:**xHo^{3+}/yYb^{3+} (x=11mol% and y=1,3,5 and 7mol%) phosphors under 980 nm laser excitation (a) λ_{em} = 551 nm (b) λ_{em} = 668 nm.	103
4.13	Variation in calculated lifetime of co-doped phosphors with respect to Yb^{3+} content.	105
4.14	CIE plot of **(a)** single Ho^{3+} doped and **(b)** co-doped Ho^{3+}/Yb^{3+} phosphors under linear and non-linear PL spectral studies.	107
5.1	(a-b) XRD patterns of an un-doped, single doped BMT: xSm^{3+}(x= 0.5, 1.0, 1.5, 2.0 and 2.5mol%) and co-doped BMT: xSm^{3+}/yEu^{3+} (x=1.5mol% and y=1, 2, 3, 4, 5 and 6mol%) phosphors with standard JCPDS	114
5.2	Rietveld refinement for BMT: xSm^{3+}(x= 1.5mol%) and BMT: xSm^{3+}/Eu^{3+} (x= 1.5mol%, y= 1.0mol%) co-doped phosphors respectively & **(c-d)** correspondong W-H plots for all concentrations of Sm^{3+} and Eu^{3+} ions.	115
5.3	Scanning electron microscope images (a-b) of BMT: xSm^{3+} doped (x=1.5mol%) and BMT: xSm^{3+}/yEu^{3+} (x=1.5mol% and y=1mol%) co-doped phosphors and (c-d) corresponding EDX images.	117
5.4	Elemental mapping of BMT: xSm^{3+}/yEu^{3+} (x=1.5 mol%, y=1 mol%) co-doped BMT phosphor (a)mixed mapping (b-f) individual of Barium (Ba), Titanium (Ti), Molybdenum (Mo), Samarium (Sm) and Europium (Eu) elements.	118
5.5	FT-IR spectra of an undoped, xSm^{3+} doped (x= 1.5mol%), and co-doped xSm^{3+}/yEu^{3+} (x=1.5mol%, y=1mol%) phosphors.	119

5.6 [F(R)hν]^2 versus hν plot for optical band gap calculation of BMT**:** xSm^{3+}(x= 0.5, 1.0, 1.5, 2.0 and 2.5mol%) and BMT: xSm^{3+}/yEu^{3+} (x=1.5mol% and y=1, 2, 3, 4, 5 and 6mol%) phosphors. 120

5.7 (a) PL excitation spectrum of BMT: xSm^{3+}(x= 1.5mol%) under 596 nm emission (b) emission spectra of BMT: xSm^{3+}(x= 0.5,1.0,1.5,2.0 and 2.5mol%) phosphors under 409 nm excitation wavelength, (c) PL excitation and emission spectrum of BMT: yEu^{3+}(y= 1.0mol%) phosphor under 615 nm emission and 395 nm excitation wavelengths, respectively & (d) PL excitation spectrum of BMT: xSm^{3+}/yEu^{3+}(x= 1.5mol%, y=1mol%) phosphor under 615 nm emission wavelength (inset figure shows the overlapped excitation spectrums of singly Sm^{3+} doped and Sm^{3+}/Eu^{3+} co-doped phosphors at emission wavelengths 596 and 615 nm respectively). 121

5.8 PL emission spectra of BMT**:** xSm^{3+}/yEu^{3+} (x= 1.5mol%, y= 1,2,3,4,5 and 6mol%) co-doped phosphors under excitation wavelengths (a) 381 nm, (b) 409 nm and (c) 465 nm respectively & (d) plot of R/O ratio vs conc. of Eu^{3+} ions under λ_{ex}= 409nm. 124

5.9 Variation of I_{SM}/I_{SU} of Sm^{3+} ion w.r.t. (a) C$^{6/3}$ (b) C$^{8/3}$and (c) C$^{10/3}$ for BMT**:** xSm^{3+}/yEu^{3+} (x= 1.5mol%, y= 1,2,3,4,5 and 6mol%) co-doped phosphors under 409 nm excitation wavelength. 126

5.10 Schematic energy level diagram of Sm^{3+} and Eu^{3+} ions and their energy transfer mechanism. 127

5.11 PL lifetime curves of BMT**:** xSm^{3+}/yEu^{3+} (x=1.5mol% and y=1,2,3,4,5 and 6mol%) phosphors under 409 nm excitation. 128

5.12 Temperature-dependent PL emission spectra (a) of BMT**:** xSm^{3+}/yEu^{3+} (x= 1.5mol%, y= 1,2,3,4,5 and 6mol%) co-doped phosphors under excitation wavelengths 409 nm & (b) Graph of Ln(I_0/I_T-1) vs. 1/K_BT for activation energy. 130

5.13 CIE plot of optimized single Sm^{3+} doped (under 409 nm excitation) and Sm^{3+}/Eu^{3+} co-doped phosphors (under 381, 409, and 465 nm excitation), respectively. 132

6.1 XRD patterns of xBi^{3+} (x= 0.5, 1.0, 1.5, 2.0 and 3.0mol%) doped Ba_3MoTiO_8 phosphors synthesized by solid state reaction method. 137

6.2 Rietveld refinement fitting for xBi^{3+} (x= 0.5, 1.0, 1.5, 2.0 and 3.0mol%) doped Ba_3MoTiO_8 phosphors. 139

6.3 (a) SEM and (b) EDX images of xBi^{3+}(x= 1.0mol%) doped Ba_3MoTiO_8 phosphor. 140

6.4 FTIR Spectra of xBi^{3+} (x= 0.5, 1.0, 1.5, 2.0 and 3.0mol%) doped Ba_3MoTiO_8 phosphors. 141

6.5 Diffuse reflectance spectra (a) of xBi^{3+}(x= 1.0mol%) doped Ba_3MoTiO_8 phosphor along with (b) tau plot for band gap calculation. 142

6.6 Excitation spectra of xBi^{3+}(x= 1.0mol%) doped Ba_3MoTiO_8 phosphor at λ_{em}= 466 nm. 143

6.7 Emission spectra of xBi^{3+} (x= 0.5, 1.0, 1.5, 2.0 and 3.0mol%) doped Ba_3MoTiO_8 phosphor at (a) λ_{ex}= 275 nm & (b) λ_{ex}= 386 nm respectively. 145

6.8 Schematic energy level diagram of excitation & emission mechanism of Bi^{3+} doped phosphors. 145

6.9 Dexter plot of Log(I/x) versus Log(x) at (a) λ_{ex}= 275nm & (b) λ_{ex}= 386nm respectively. 147

6.10 CIE Chromaticity co-ordinates for Ba_3MoTiO_8: xBi^{3+} (x= 0.5, 1.0, 1.5, 2.0 and 3.0mol%) phosphors under (a) 275nm and (b) 386 nm excitation respectively. 150

6.11 Decay curves of xBi^{3+} (x= 0.5, 1.0, 1.5, 2.0 and 3.0mol%) doped Ba_3MoTiO_8 phosphor at (a) λ_{ex}= 275nm & (b) λ_{ex}= 386nm. 151

6.12 (a) Temperature dependent PL spectra of optimized conc. (x= 1.0mol%) of Ba_3MoTiO_8: xBi^{3+} phosphor & (b) Fitting plot of $Ln[(I_0/I_T)-1]$ vs. 1/KT. 153

List of Tables

2.1	List of chemicals used in the present thesis work.	30
3.1	Sample coding for different concentrations of Europium ion doped BMT phosphor.	59
3.2	CIE Coordinates for BMT phosphors prepared by CMM technique.	78
4.1	Rietveld refinement parameters along with JCPDS data.	88
4.2	Lifetime of Ho^{3+} ions in BMT: Ho^{3+}/Yb^{3+} phosphor for λem=551 nm and 668 nm under 980 nm laser excitation.	105
4.3	Variations of CIE Coordinates and CCT values for singly Ho^{3+} ion doped series and co doped Ho^{3+}/Yb^{3+} series of BMT phosphors.	106
5.1	Calculated structural lattice parameters through Rietveld refinement	115
5.2	Lifetime decay values of BMT: xSm^{3+}/yEu^{3+}(x= 1.5mol%, y= 1,2,3,4,5 and 6mol%) co-doped phosphors for λex=409 nm.	129
6.1	Calculated structural lattice parameters for BMT: xBi^{3+} (x= 0.5, 1.0, 1.5, 2.0 and 3.0mol%) through Rietveld refinement	137
6.2	Calculated CCT values for Bi^{3+} ions doped Ba_3MoTiO_8 phosphors under λex=275 nm and 386 nm.	149
6.3	Lifetime decay values of BMT: xSm^{3+}/yEu^{3+} (x= 1.5mol%, y= 1,2,3,4,5 and 6mol%) co-doped phosphors for λex=409 nm.	151

CHAPTER 1

Introduction

Worldwide, energy consumption is a serious issue for society leading us to think about how to generate and consume energy efficiently. As most of the conventional energy generated is used in the lighting field, we have to focus on this sector to prepare efficient lighting devices which reduces the power consumption. The system used for white light illumination is collectively said to be solid-state lighting.

1.1 Lighting Technology:

The development of artificial lighting technology dates back to tens of thousands of years, and it is still being improved today [1]. The goal of technological development for artificial lighting is to create light that will mimic daylight. So artificial light can be classified into three generations following its development and technology:

I. **Incandescent sources:** This technology was invented in the nineteenth century by Edison. It works on the method to heat an object at a high temperature till then it emits light, e.g. fire, incandescent bulbs, candles, etc. These light bulbs' filaments turn more than 95% of the energy they receive into heat, and less than 5% of it produces visible light.

II. **Compact Fluorescent Lamps (CFL):** The middle of the 20th century saw the commercialization of this method. In this technique, a low-pressure gas, such as mercury, argon, or a combination of gases, was contained in a glass tube where an electric discharge took place. An ultra violet (UV) light is generated when this electrical discharge excites electrons of the gas present in the tube and this UV light was absorbed by the phosphors coated on the glass tube and gives emission in the visible region.

III. **White Light Emitting Diodes (w-LEDs):** Holonyak and Bevacqua demonstrated this method in the early 1960s. Without producing heat, it converts electricity directly to visible light.

1.2. Disadvantages of conventional sources of light:

Conventional sources of light (fire, incandescent bulbs, and CFLs) have many disadvantages, due to which we have to replace them with another suitable source of light. Some of the major disadvantages are [2]:

- Traditional incandescent and fluorescent lamps rely on either the release of gases or heat.
- Burning fossil fuels like oil, coal, or gases increases the price of fuel and pollutes the atmosphere, which is a serious problem.
- Conventional energies are non-renewable and cannot be used for a longer time.
- Some other disadvantages are ozone depletion, global warming, acid rain, etc. All the various aforementioned implicates leads to an urgent need to replace the conventional lighting devices with suitable lighting devices.

1.3. Why do we choose w-LEDs over conventional light sources?

The advantages of w-LEDs are [3]:

1. By lowering the non-radiative recombination (NRR) of electron-hole pairs and creating a new structure with enhanced efficiency, w-LEDs luminescence efficiency can be significantly increased.
2. The cost of white light generated by w-LEDs has been decreasing day by day, due to this cost-effectiveness, solid-state lighting (SSL) may become the next-generation lighting source.
3. Traditional incandescent bulbs lose a large amount of energy through heat radiation. 3 watts would be enough to power an LED to create the same amount of light as a 60-Watt incandescent bulb.
4. LEDs are environmentally friendly because of their non-toxic nature, less CO_2 emission, and less heat production.
5. Compared to 1000 hours for incandescent light bulbs, LEDs can last 100,000 hours.

1.4. Luminescence and its various forms:

German physicist Eilhardt Wiedemann made the discovery of luminescence in 1888; the Latin translation of the word is "light". In luminescence, some type of excitation energy source was used to gain emission in visible region without any heat production. Excitation process in luminescence can be caused by chemical reactions, electric energy, stress on a crystal, mechanical force, nuclear radiation, etc., which all are ultimately caused by spontaneous emission. Luminescence occurs frequently in everyday objects like lamps for lighting, television displays, and lasers in medical equipment [4].

There are numerous categories of luminescence that vary depending on the excitation source [5,6]:

(a) Photoluminescence (PL): Photoluminescence is light emission caused by excitation from electromagnetic radiation. It can be of two types- Fluorescence and phosphorescence.

✓ **Fluorescence**: When an external radiation is fall on the atoms/molecules present in the ground state, then after absorbing the radiation, theses atoms/molecules moved to higher excited states. After that emission of this absorbed light take place. Fluorescence is the rapid absorption of a single ray of light, immediately followed by the emission of long wavelength light. Absorption and emission occur almost simultaneously. The duration of this process is short, usually in the nanosecond range (10^{-9} seconds). Examples include fluorescent dyes, some minerals, and some biomolecules.

✓ **Phosphorescence:** The word phosphor is the source of the term phosphorescence, which describes the continued emission of light from a substance after the stimulating radiation has stopped. It should be noted that only inorganic materials are covered by these definitions.

Phosphorescence is the absorption of light at one wavelength and the delayed emission of light at a longer wavelength. Latency can range from a few milliseconds to hours. Luminous materials, some types of phosphors used in fluorescent lights, and some foods that have phosphorescence [7].

(b) Chemoluminescence: The conversion of chemical energy into emission of light from a substance as a result of a chemical reaction. The reaction products in this method generate in an excited state and come back to the ground state through the emission of light [8].

(c) Bioluminescence: Bioluminescence is a type of luminescence arising from living organisms through chemical reactions. It can be observed in the deep sea [9].

(d) Electroluminescence: Light emission caused by the action of an electric field on a substance is known as electroluminescence. For instance, a LED can produce electron-hole pairs that, upon recombining, result in luminescence. Cathodoluminescence is the term used to describe excitation by free electrons (an electron beam) [10].

(e) Triboluminescence: When a material is mechanically altered, such as when it is broken or polished, triboluminescence can happen [11].

(f) Thermoluminescence: Thermoluminescence is a thermally activated luminescence. In this instance, thermal stimulation simply causes the release of energy that was already given to the material by other methods, such as ions, α, β, γ and X-rays etc [12].

(g) Piezo-luminescence: By exerting pressure on the solid materials, luminescence is created. It has been discovered that irradiated salts, including NaCl, KCl, KBr, and polycrystalline chips of LiF (TLD-100), display piezoluminescent characteristics [13].

(h) Crystalloluminescence: It is the type of luminescence produced during the crystal growth and destruction [14].

(i) Radio luminescence: Radio luminescence is caused in a material by excitation high energy radiations like nuclear radiation (α, β, γ or ions) or X-rays [15].

(j) Mechanoluminescence: Mechanoluminescence is the term for light emission that happens as a result of any form of mechanical action on a substance [16].

(k) Sonoluminescence: In this phenomenon, light is produced with ultrasonic waves as the excitation source [17].

1.5. A closer look to PL through Jablonski diagram:

PL takes place when energy in the form of photons is absorbed, and then there is a subsequent emission of light, preferably in the visible spectrum. The Jablonski diagram (an energy state diagram) is used to depict the creation and decay of excited states as shown in Fig. 1.1.

Some basic terms that have been used in this phenomenon are:

Singlet states: Electrons present in the atom has some specific spin associated to them. When electrons with opposite spin pair up then net spin will be zero. This state is called singlet state.

Triplet states: When both electrons which pair up have same spin, then the state arising is called triplet state.

Due to the vibronic motions of the atoms that make up a molecule, the ground state S_0, singlet states (S_1 and S_2), and triplet states (T_1 and T_2) are all composed of a variety of vibrational states. When an external radiation falls on the molecule present in the ground state S_0, it gets absorbed and due to this absorption, an electronic transition takes place. As a result of which electrons moves to higher excited states either S_1 or S_2. When a transition take place from higher vibronic state to lower vibronic state within a singlet state, it is called a vibrational relaxation. The internal conversion (IC) procedures are used by non-radiative singlet states, namely S_2 and S_3, to relax to the S_1 state.

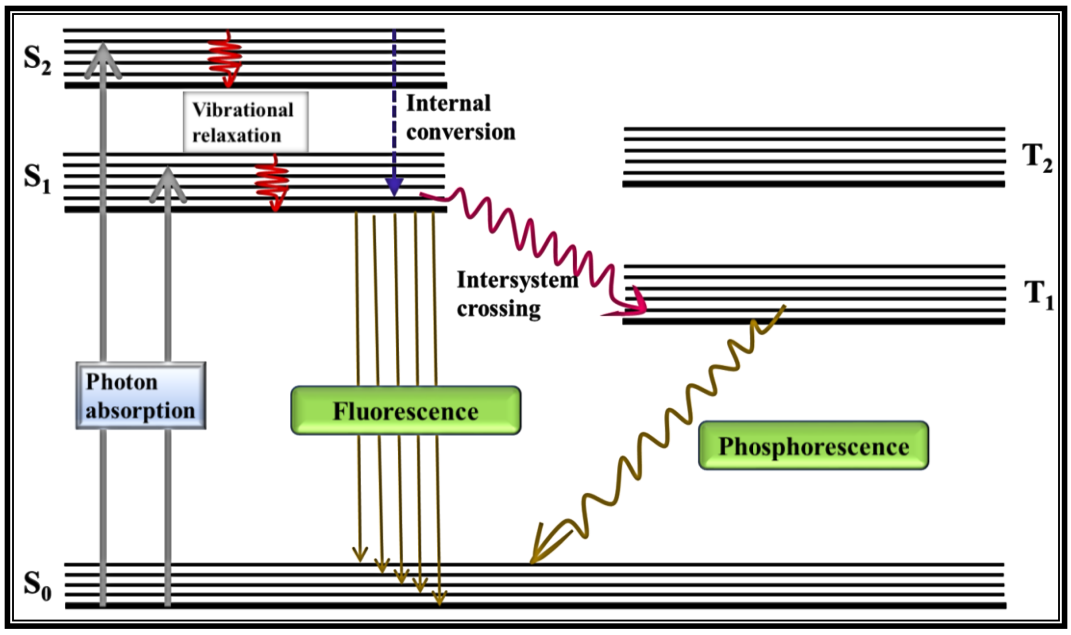

Fig. 1.1. Jablonski diagram

Typically, an intersystem crossing (ISC) procedure from S_1 to T_1 results in triplet states. As a result, electronic transitions between the ground state S_0 and the lowest excited states S_1 or T_1 result in radiative transitions. Fluorescence is the name used to describe the radiative transition from S_1 to S_0, which is categorized as a spin-allowed transition and has a time scale of a few nanoseconds. On the other hand, in the spin-forbidden process known as phosphorescence, the time scale for the T_1 to S_0 transition is substantially longer, ranging from micro- to milliseconds.

1.6. Phosphor:

The meaning of the word phosphor has not changed since it was first used in the early 17th century. A massive, glossy, crystalline stone with a shine was allegedly discovered by an alchemist named Vincentinus Casciarolo in Bologna, Italy. He burned the stone in a charcoal kiln with the goal of turning it into a noble metal. No metals were identified by Casciarolo, but he did discover that the sintered stone produced red light in the dark after being exposed to sunlight. The "Bolognian stone" was the name given to this rock. According to what is now

known, the stone that was discovered may have been barite (BaSO4), and the outcome of the firing was BaS, which is now recognized as a host for phosphor compounds. Following this discovery, several locations throughout Europe reported similar findings, and these light-emitting stones were given the term phosphors.

Phosphors contain a host material and an activator. As a host material, we can use various inorganic oxides such as phosphates, silicates, aluminates, titanates, molybdates etc. As an activator, rare earth (RE) or transition/post transition metal ions are used. Due to their high luminescence efficiency, colour purity, extended lifetime, etc., inorganic oxide-based host materials have garnered a lot of attention. These host materials are crucial for the phosphors luminescence.

1.6.1. Basic concepts for luminescence and phosphor:

Four kinds of luminous materials can be distinguished based on their chemical makeup :

(1) Luminescent centers are already existent in some host materials where they absorb exciting radiation to produce radiative emission. Such hosts are known as luminophores as shown in Fig.1.2 (a1). Host material may give off its exciting energy non-radiatively which subsequently looses it as heat.

(2) When host material absorbs the exciting energy and migrate it to the activator, then activator ions goes to higher excited state by absorbing this energy and later de-excite to ground by giving emission as represented in Fig. 1.2 (a2).

(3) Some luminescent materials contain inactive hosts and activators as luminescent centers. These are called ‘‘host and activator’’ type as represented in Fig.1.2 (a3). The excited state is increased when the activator absorbs the exciting radiation. The emission of light, or a photon, causes this excited state to return to the ground state.

(4) In some luminescent materials, sensitizers are also used to improve or enhance the luminescent properties of activators. We define them ‘‘host-sensitizer-activator’’ type. The incident radiation is absorbed by the sensitizer ion, which then transfers its energy to the activator ion. In this instance, activator ion emission is seen, as indicated in Fig. 1.3 (a4). Activator is referred to as a killer site because it works to quench luminescence in the case where energy transfer to the activator is followed by non-radiative decay.

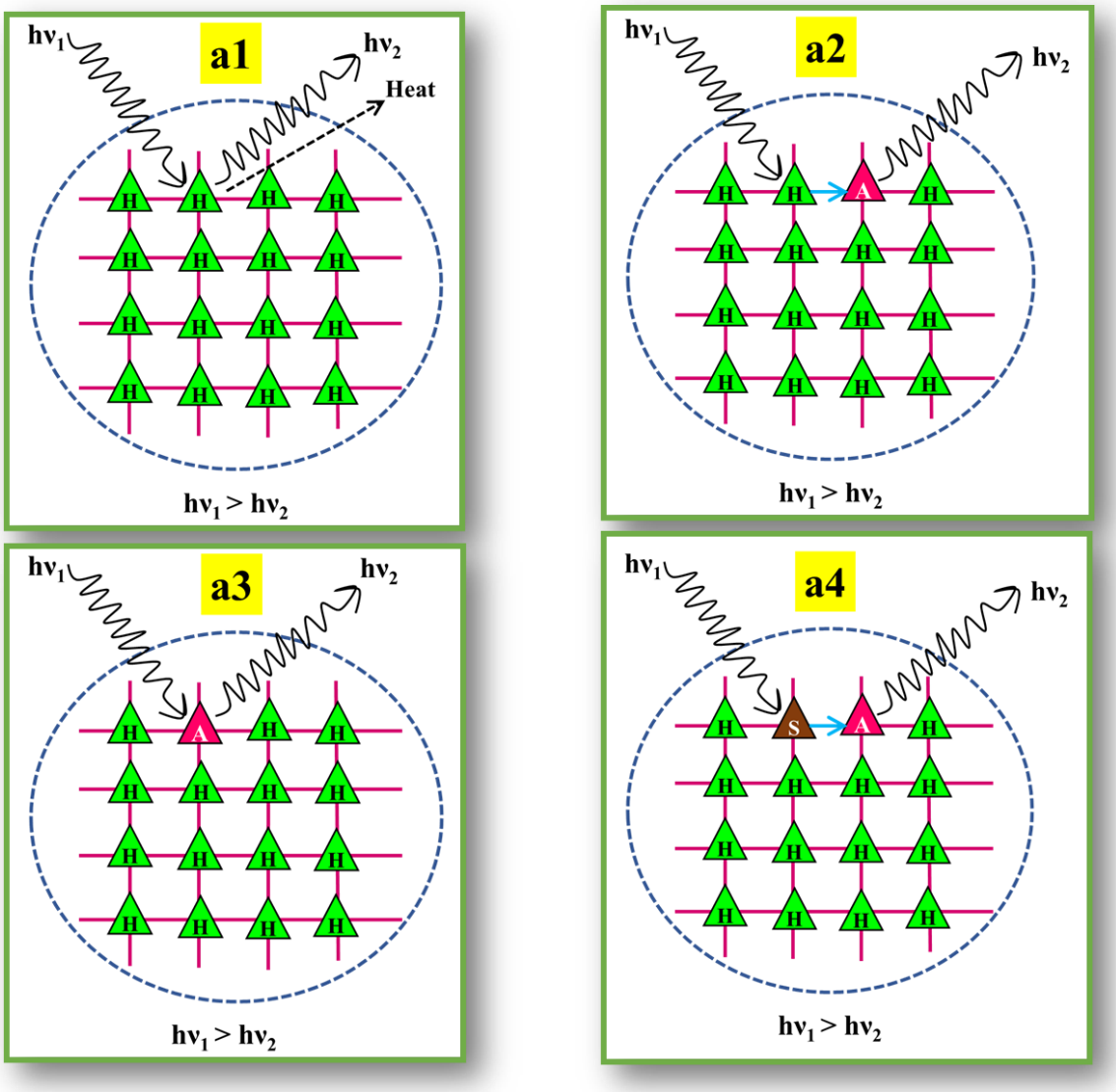

Fig. 1.2. Absorption of incident energy and luminescence (a1) Host sensitized luminescence (a2) Energy transfer induced luminescence from host to activator (a3) Activator induced luminescence (a4) Host - Sensitizer - Activator induced luminescence.

1.6.2. Down- conversion and Up-Conversion processes:

When radiation in the form of high-energy photons (in the UV or n-UV range) strikes a material, some of its energy is absorbed before the material re-emits the energy in the form of two low-energy photons (in the visible or NIR range), which is controlled by Stokes law. The term "down-conversion" also applies to this process [18]. On the other hand, when one high energy photon comes out as one low energy photon, then the emission process is called down-shifting. The Stokes shift is the energy difference between the excitation and emission wavelengths caused by the excitation energy's earlier non-radiative loss. However, it may be possible that two or more low energy photons (in NIR range) are absorbed and subsequently high energy visible or ultraviolet photons are released. This phenomenon is known as up-conversion or anti-Stokes emission [19,20]. Figure 1.3 show the down-conversion and up-conversion processes.

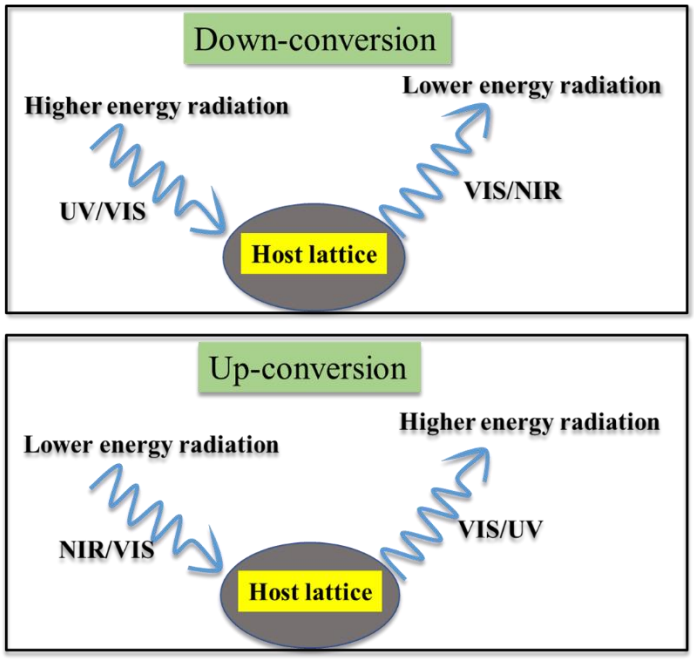

Fig. 1.3. Representation of stokes (down-conversion) and anti-stokes (up-conversion) shift.

1.7. Dopants:

1.7.1. Rare Earth (RE) Ions:

In recent years, the development of effective phosphors with broad applicability has resulted in the extensive usage of RE elements as luminous centers or activators in diverse host lattices. These have served as activators, enabling the utilization of extremely focused spectrum distributions with the effectiveness needed for commercial applications. Although expensive, these RE doped phosphors provide advantages for luminous materials, which justifies their use in production. The market for RE doped luminous materials has been steadily expanding in recent years. They have undergone extensive research and are frequently utilized due to their high quantum efficiency and good stability.

As indicated in Fig.1.4, the RE elements typically consist of 17 elements, with the 15 lanthanides [from La (Atomic no. 57) to Lu (Atomic no. 71)], Sc (Atomic no. 21), and Y (Atomic no. 39) making up the majority of the elements. From Ce^{3+} to Lu^{3+}, the lanthanides have one to fourteen extra 4f electrons in their inner shell configuration. The 4f orbitals of the lanthanide ions from Ce^{3+} to Yb^{3+} are only partially filled, which results in luminescence in the visible region that is unique to each ion energy level. Numerous of these luminous ions can be employed as dopants in different host phosphor lattices. Despite their name, RE elements are quite common in the Earth's crust (apart from the radioactive promethium), with cerium being the 25^{th} most common element. The geo-chemical characteristics of RE elements, however, make them usually distributed and less frequently discovered in concentrated and commercially viable forms. RE minerals are the few resources that can be profitably extracted. The phrase "rare earth" originated from the fact that these minerals, which were once known as "earths," are extremely rare [21].

The light RE elements (REEs), which include lanthanum to europium (Z = 57–63), and the heavy REEs, which include gadolinium to lutetium (Z = 64–71), have historically been separated into two classes. Despite being the lightest REE, yttrium is typically classed with the heavy REEs because of their similar chemical and physical properties.

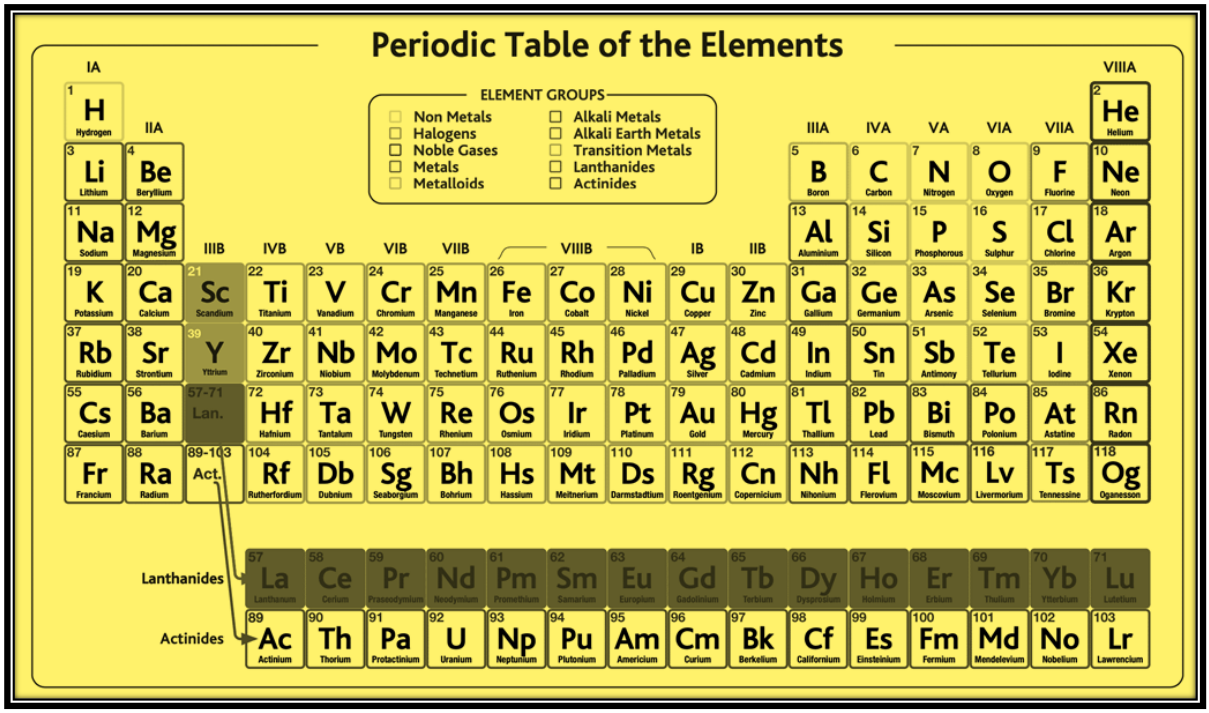

Fig. 1.4. Periodic table comprises RE ions and other transition/post transition metals.

1.7.2. Post-transition metal ions:

Post-transition metal ions are elements to the right of transition metals in periodic table. These elements are found in groups 13 to 17 and show properties between metals and non-metals. We choose bismuth (Bi^{3+}) ions as additives in the matrix for the following reasons-

1. Bismuth-doped phosphors exhibit enhanced fluorescence when exposed to ultraviolet (UV) or near ultraviolet (NUV) light. This is good for getting better colors and making the lighting better suited to specific needs.

2. By adjusting the dopant concentration or changing the material, bismuth-doped phosphors can be designed to emit light of various colors.

3. Bismuth-doped phosphors generally have a broad emission spectrum covering a wide range of wavelengths in the visible spectrum**.**

4. Compared to other materials in the world that are rarely used as additives, bismuth is abundant and relatively inexpensive.

5. Bismuth has a unique electronic structure that makes it a unique optical property. The introduction of bismuth ions into the lattice of phosphor materials can lead to electronic changes that lead to desired luminescence properties.

1.7.3. Type of Interactions:

Broadly, the interaction between two different levels is classified based on the transition between f-f levels and $4f^{n-1}$-$4f^{n}5d^{0}$.

a) Intra-configurational (*f-f*) transition: The electronic transitions from the $^{2S+1}L_J$ to the free ion level or J manifolds in the 4f sub shell are responsible for the wide range of thin lines seen in materials doped with RE ions. They are not allowed to spin. Excitation and emission energies in the f-f transition are efficiently protected from 5s and 5p shells, remaining independent of the host material doped with activator ions. The narrow line width in these spectra is caused by the shielding effect. Different sorts of transitions, including those listed below, result from the interaction of the RE ions in the host with the light.

(i) Magnetic dipole (MD) transitions: A weakly intense transition known as a magnetic dipole (MD) transition is seen when the magnetic field factor of the incident light interacts with the RE ion through a magnetic dipole. MD transition happens when the charges are rotated in a different direction while still rotating in the same direction under inversion through a point.

The MD transition exhibits even parity and possesses even transformation under inversion, allowing transition between states with the same parity. Therefore, a MD transition is endorsed by the Laporte's selection rule ($|\Delta l| = \pm 1$, $|\Delta s| = 0$, $|\Delta L| \leq 0$, $|\Delta J| = 0$; $J = 0 \leftrightarrow 0$ transition is forbidden).

(ii) Electric dipole (ED) transitions: When RE ions interact with electromagnetic radiation's electric field vector via an electric dipole, an ED transition takes place. The parity-permitted transitions between the 4f and 5d states are as follows. Odd parity charge must move linearly in order for an electric dipole to arise. As a result, when the electric dipole operator is inverted, it exhibits peculiar transformation features with respect to an inversion centre. These transitions are subjected to the selection rules as ($|\Delta s| = 0$, $|\Delta l| = \pm 1$, $|\Delta L| \leq 6$, $|\Delta J| \leq 6$).

(iii) Electric quadrupole (EQ) transitions: The EQ transitions, which are substantially weaker than the ED and MD transitions, are produced by the displacement of quadrupole charges. These are parity allowed transitions with selection rules ($|\Delta S| = 0$, $|\Delta L| \leq 2$ and $|\Delta J| \leq 2$).

(b) Interconfigural (f-d) interaction: The transport of 4f electrons to the 5d shell is parity permitted in these transitions. Compared to the 4f-4f transition, the transition between the $4f^{n-1}5d^1$-$4f^n5d^0$ levels gives rise to a wide range of wavelengths. The host ions gave the doped RE ions such a setting, and the crystal field splitting caused the 5d energy levels to separate. The length, type, and environment of the bond between the acceptor ion and the ligand, as well as the acceptor ions' site symmetry, all affect how much of a crystal field effect there is. These changes involve a lot of energy.

1.8. Introduction to pc-wLED in the world of Solid-State lighting (SSL) technology:

The already over burdened global energy infrastructure continues to be under pressure from the rising demand for fossil fuels and their negative environmental impact. Using blue InGaN LED chips with a yellow phosphor coating, Nichia Chemical Co. created a completely new lighting technology in 1996. (YAG: Ce). SSL is the term used to describe lighting applications that make use of LEDs, organic LEDs, or light-emitting polymers. Today, SSL technology is gaining popularity as a potential replacement for traditional lighting sources. Due to their distinctive optical characteristics, phosphor-converted white LEDs are quickly becoming a vital SSL source for the coming generation.

There are many methods to generate white light. But mainly the following three approaches are important to generate white light:

1) **RGB LED method:** In this, red, green, and blue light from three monochromatic LED sources are combined directly to create white light (Fig. 1.5). But the disadvantage of this method is that we require different driven currents for individual LEDs. Although the colour rendering index (CRI) and luminous efficacy of these LEDs are good, but the driving circuit utilised to create white light is complicated, which drives up the price of LEDs and complicates manufacture. Additionally, varying driving currents causes the degradation of various colour LEDs and instability in colour temperature [22].
2) **UV/NUV LED+ RGB phosphor:** In this method, UV LEDs are coated with tricolor RGB phosphor and this combination gives white light (Fig. 1.6(a)). However, the fundamental drawback of this approach is the inconsistent rate at which various components deteriorate, which causes colour shifts over time.

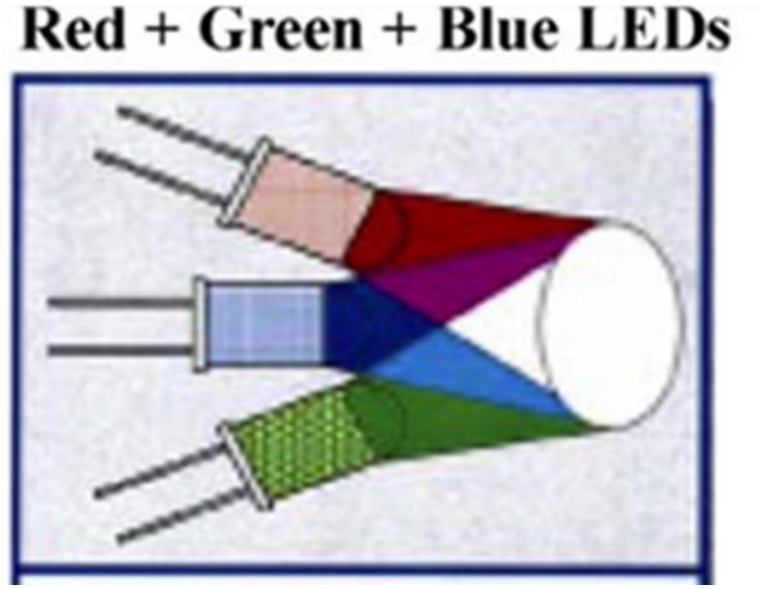

Fig. 1.5. White light generation through Red+ Green + Blue LEDs..

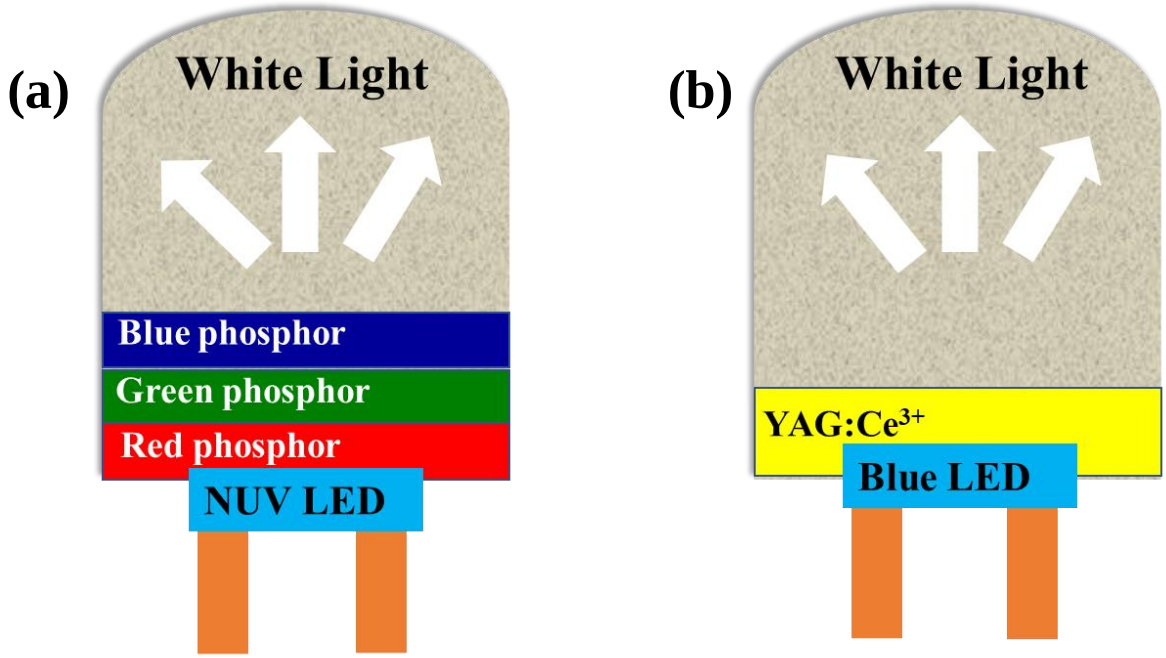

Fig. 1.6. White light generation using phosphors (a) NUV-LED+ RGB phosphors (b) Blue-LED+ Yellow phosphor

3) **Blue LED+ Yellow phosphor:** This technique involves coating a blue LED with yellow phosphor, which is subsequently excited by blue light from the LED to produce white light (Fig. 1.6(b)). Due to the lack of red components, this method's white light has a poor colour rendering index, a strongly correlated colour temperature, and a low chromatic stability, which is one of its drawbacks [23]

1.8.1. Applications of phosphors:

Phosphors are used in more and more technologies, which calls for greater study to advance these technologies and make them more affordable and efficient. Phosphors are employed as light sources in display devices, fluorescent lamps, detectors, and other simple applications like luminous paint with long-lasting phosphorescence, long-lasting phosphors coated pointers, light switches, etc. Some of these uses are shown in Fig. 1.7. Numerous phosphor materials based on RE ions have considerably improved the performance of the devices in which they are utilised. Significant progress has been made in the field of phosphors by purposely introducing trivalent RE ions as light centres in different host matrices to produce RE activated phosphors. RE based phosphors have been crucial in the operation and commercial success of numerous lighting and display products during the past few years. The two most popular display types are liquid crystal displays (LCD) and cathode ray tube (CRT) panels [24].

However, typical CRTs are excessively big and heavy, while LCDs are constrained by their slow response times and narrow viewing angles. Field emissive displays (FED) are regarded as an excellent model of flat panel display (FPD) technology for the upcoming generation of display technology because of their expected high brightness, high contrast ratio, light weight, and low power consumption.

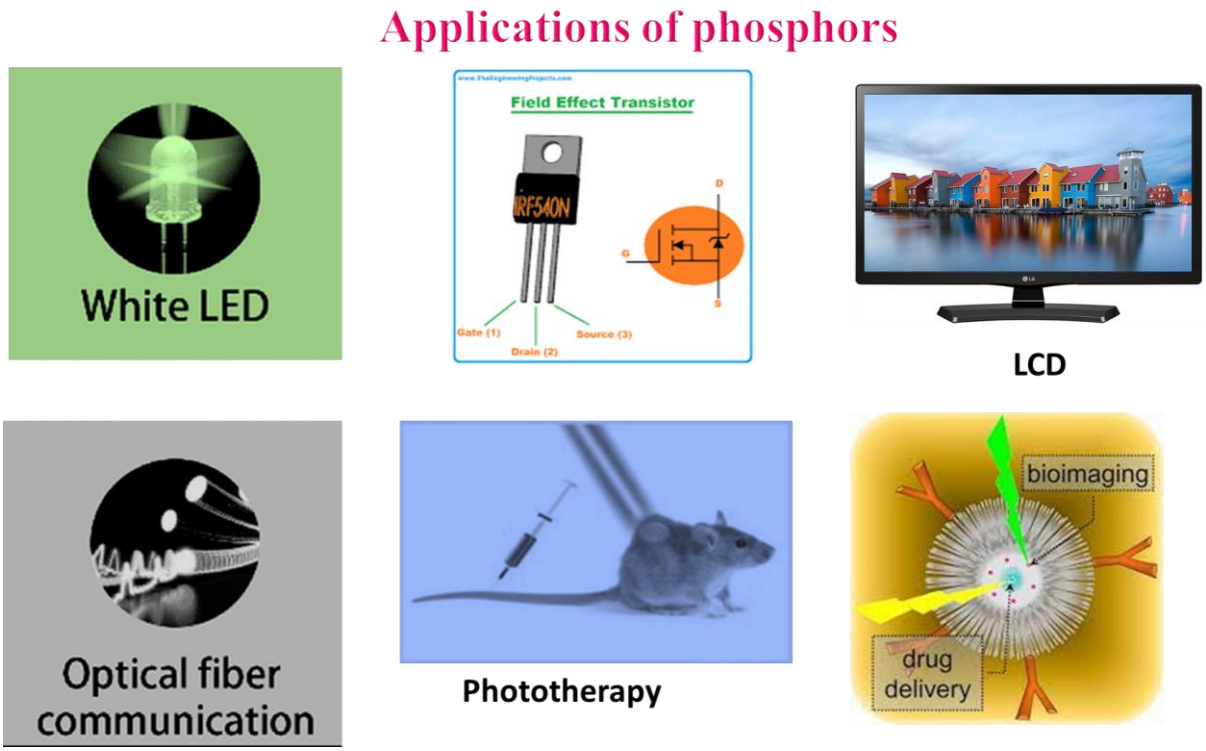

Fig. 1.7. Applications of phosphor materials in various fields.

For instance, Y_2O_3:Eu^{3+} (red), $Y_3Al_5O_{12}$:Tb^{3+} (green), and Y_2SiO_3:Ce^{3+} are commercial phosphor layers used in FEDs. The majority of luminous substances, also known as phosphors, are solid inorganic substances with a host lattice and luminescent core that have been purposefully doped with small amounts of specific impurities. The luminescence is mostly caused by a small amount of purposely added impurities, or "activators." When excitation light from an external source strikes the host, either the host or contaminants absorb the energy. By absorbing energy from impurities, excited photoelectrons are created, which are then reduced in energy by emitting photons or heat to the host matrix. Almost all emissions come from impurity atoms that have been purposefully doped.

The structure and abnormalities in biological tissues and living cells at the organ level are frequently examined in medical diagnosis using biological imaging techniques like X-ray, CT scan, and MRI. These techniques do have certain drawbacks, though. Ionizing radiation has negative side effects, cannot differentiate between benign and malignant cancers, and does not have a real-time reaction. Therefore, a better bio-imaging technique is required, one that can effectively and with high resolution examine what is happening at the cellular and molecular levels.

These limitations of traditional bio-imaging methods can be overcome by an up-conversion fluorescent method used in contemporary bio-imaging. Up-conversion fluorescence techniques with excitation in the near infrared (NIR) region can be used for imaging biological cells and tissues due to their many advantages, such as the fact that they do not cause photodamage to living things, have very low auto-fluorescence, cause no harm, respond instantly, have a high detection sensitivity, and have a high penetration depth in biological tissues. Customized nano dimensional up-conversion phosphor materials are used in this method.

Phosphors within the cell or tissue begin to shine instantly upon 980 nm infrared excitation and produce the visible fluorescence from that specific cell or tissue, which can then be caught by the CCD camera with an advanced optical microscopy equipment. In contrast to typical ultraviolet (UV) excitation, these nano-phosphors exhibit intense visible emission under NIR stimulation, which renders them less damaging to biological samples and increases sample penetration depths.

1.9. Spectral Analysis:

1.9.1. Color rendering index (CRI):

CRI is a metric used to assess a light source's capacity to accurately depict an object's colour. The difference between a set of test colours when illuminated by the source and the same test colours when illuminated by the standard illuminant having the same correlated colour temperature is measured by this unit-less number. It is assessed on a scale from 1 to 100. When the light source and the standard illuminant render colours are identical, then the CRI will be high. Low CRI values indicated that colour reproduction would be less accurate.

1.9.2. CIE coordinates & color purity:

The range of wavelengths where the human eye reacts to light is about between 400 and 750 nm. The Commission Internationale de l'Eclairage [International Commission for Illumination, or (CIE)] standardised colorimetry for photopic (bright-light) vision in 1931, as indicated by the CIE diagram (Fig.1.8). CIE system is commonly used to describe the colour of a light source. The chromaticity coordinates x and y on the CIE chromaticity diagram can be used to represent any colour. By using this technique, the three primary colours that make up any colour are described. X, Y, and Z stand for synthetic colours, often known as tristimulus values. Due to a mathematical trick, the three quantities (x, y, and z) are always made to add up to 1, hence in order to designate a colour, the quantity of two of the reference stimuli is required.

The chromaticity coordinates are the ratios of the light's X, Y, and Z values to the total of the three tristimulus values. The spectral power density $P(\lambda)$ of the light source and the colour matching functions $x(\lambda)$, $y(\lambda)$, and $z(\lambda)$ established in CIE 1931 were used to obtain the CIE chromaticity coordinates from emission spectra.

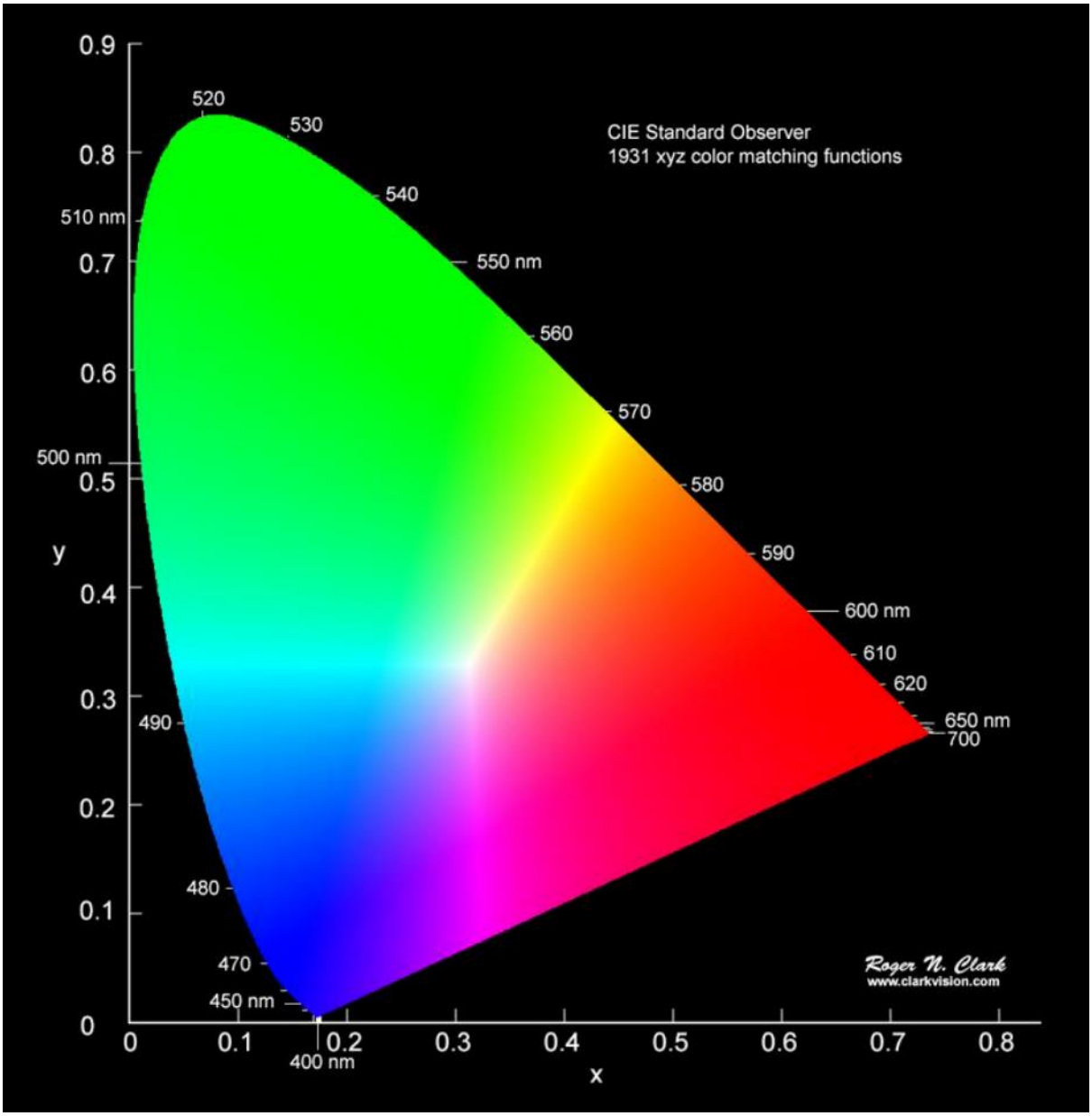

Fig. 1.8. CIE 1931 Chromaticity Diagram

The tri-stimulus values X, Y, and Z can be used to get the chromaticity coordinates, as -

$$x = \frac{X}{X+Y+Z} \quad (1)$$

$$y = \frac{Y}{X+Y+Z} \quad (2)$$

$$z = \frac{Z}{X+Y+Z} \quad (3)$$

where the following equations provide the level of stimulation necessary to match the colour of P(λ). Here, P(λ) is the spectral power density of the light source and the colour matching functions are x(λ), y(λ), and z(λ).

$$X = \int \bar{x}(\lambda)P(\lambda)d\lambda \quad (4)$$

$$Y = \int \bar{y}(\lambda)P(\lambda)d\lambda \quad (5)$$

$$Z = \int \bar{z}(\lambda)P(\lambda)d\lambda \quad (6)$$

The monochromaticity is indicated by the value of the CIE coordinates around the CIE diagram's edge. Therefore, the colour purity can be assessed by utilizing the expression as follows to determine the monochromaticity of the material under investigation using the CIE coordinates as obtained.

$$colour\ purity = \frac{\sqrt{(x-x_{ee})^2+(y-y_{ee})^2}}{\sqrt{(x_d-x_{ee})^2+(y_d-y_{ee})^2}} \quad (7)$$

where (x_{ee}, y_{ee}) are the coordinates of the white point, (x_d, y_d) are the coordinates of the dominant wavelength point, and (x, y) are the coordinates of the sample under consideration. The monochromatic emitters should have a 100% colour purity.

1.9.3. Correlated color temperature (CCT):

CCT is a numerical scale that quantifies a light source's colour. The temperature in Kelvin of a hypothetical black body emitter whose spectral properties most closely match those of the lamp is known as the CCT of a white light source. Cool white (2700K) is brighter than warm white (4100 K). The uses of white light sources are impacted by their colour temperature. A typical incandescent bulb's colour temperature ranges from 2800 to 3000 K, while daylight's is around 6400 K. The CCT range for high-quality white light lighting should be between 2500 K and 6500 K. The correlate colour temperature, which measures the absolute temperature of an ideal blackbody radiator whose colour matches that of the light source, is used to describe the colour of emitted light.The typical CCT of the white region diagram is in the 2000–10000 K range. The McCamy equation can be used to calculate the CCT-

$$CCT = -437\left[\frac{x-x_e}{y-y_e}\right]^3 + 3601\left[\frac{x-x_e}{y-y_e}\right]^2 - 6861\left[\frac{x-x_e}{y-y_e}\right] + 5514.31 \quad (8)$$

Here, the sample under consideration's CIE coordinates are (x, y), and the epicenter's coordinates are (x_e =0.3320, y_e =0.1858) **.**

1.10. Energy transfer mechanism by using theoretical models:

Energy can only be transferred between two neighboring ions only if the resonance occurs between the energy differences of their ground and excited states and there is some proper interaction exists between them. The two nearby ions may interact via multipolar interaction

or exchange interaction. From the emission spectral data, Dexter theory and Reisfeld's approximation can be used to determine the nature of multipolar interaction.

1.10.1. Dexter theory and Reisfeld's approximation:

According to Dexter theory, the luminescence quantum efficiency can be used to determine the type of multipolar interaction by correlating it to the concentration of RE ions as follows:

$$\frac{\eta_0}{\eta} \alpha\, C^{n/3} \tag{9}$$

where C denotes the overall concentration (in moles percent of donor and activator ions), n the kind of interaction, and η_0 and η the luminescence quantum efficiencies of donor ions in the absence and presence of acceptor ions, respectively. The exchange interaction, dipole-dipole (d-d), dipole-quadrupole (d-q), and quadrupole-quadrupole (q-q) interactions, respectively, are represented by the n = 3, 6, 8, and 10 numbers, respectively. With reference to their respective emission intensities, it is possible to approximate the ratio of quantum efficiencies of the donor in the absence and presence of the acceptor. Thus, the relationship described above can be expressed as -

$$\frac{I_{S0}}{I_S} \alpha\, C^{n/3} \tag{10}$$

where I_{s0} and I_s are, respectively, the integrating emission intensities of the RE ions' hypersensitive transitions in the presence and absence of co-dopant ions. I_{s0}/I_s vs $C^{n/3}$ plots for n = 6, 8, and 10 are drawn. The energy transfer mechanism can be investigated by examining the linear fitting factor R^2 for the plot obtained as described previously. The sort of interaction

between the sensitizer and activator is shown by the high value of R^2 obtained for the appropriate "n" number.

1.11. PL decay kinetics:

The lifespan of the excited state, which is the average amount of time the molecules spend in the excited state before returning to the ground state, can be measured experimentally using the analysis of the PL decay curve. The lifetime of a population of excited phosphor is the amount of time it takes for the number of excited molecules to decrease to 1/e, or 36.8% of the initial population. A schematic illustration of PL intensity declining as a function of time is shown in Fig.1.9. The excited state of an atom decays to the ground state using the following equation if decay is single exponential:

$$I = I_0 exp.\left(\frac{-t}{\tau}\right) \quad (11)$$

Where, I is the intensity at time t, I_0 is constant, and τ is the decay constant. The following equation can be used to represent the decay of an atom from its excited state to its ground state if the decay profile is double exponential:

$$I = I_0 + A_1\, exp.\left(\frac{-t}{\tau_1}\right) + A_2\, exp.\left(\frac{-t}{\tau_2}\right) \quad (12)$$

Where I represent the intensity at time t, A_1 and A_2 are constants, and τ_1 and τ_2 are the decay constants that represent the exponential components with quick and gradual decay, respectively. High grade materials typically have a longer emission period, making PL decay curve analysis a very valuable tool for determining material quality. When a sample is excited, its internal electrons travel to a higher excited energy level before relaxing to the state with the lowest vibration. An electron emits a photon to transition to the ground state after a

predetermined amount of time. The duration of the delay is known as the material's excited state lifetime, and it may be calculated using the PL decay curve analysis.

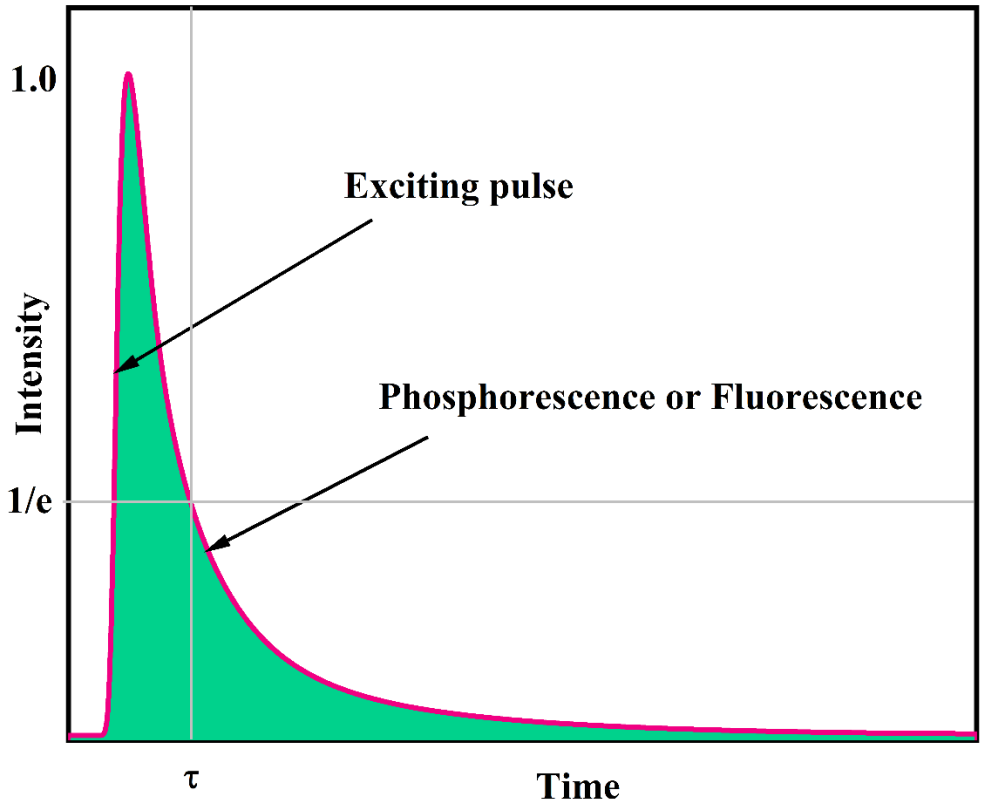

Fig. 1.9. Diagrammatic portrayal of PL decay curves.

In PL decay curve analysis, the material is excited to a higher excited energy state using light with short pulse duration, and the PL emission intensity is then measured as a function of time. A measurement of excited state lifetime is provided by the PL 's decline in intensity over time.

1.12. Selection of Host lattice:

Solid state lighting technology with its tremendous advantages can reach the theoretical limit of luminescence efficiency. The key elements of this SSL technology, which is mostly utilised in lighting, imaging, and display applications, are phosphors. The choice of host material has a notable impact on the luminous qualities displayed by the phosphor when creating an

effective single-phase phosphor-based LED. Therefore, it is crucial to choose a suitable host material. New materials are being searched by many researchers in support of this lighting technology but still there are many challenges to reach the criteria for an efficient host matrix. A good host should have (1) higher absorption in blue and near UV spectral range (2) high thermal and chemical stability, (3) narrow band width emission in visible region, (4) high luminescence energy transfer efficiency and quantum efficiency.

Recent research has shown that inorganic oxides are ideal host materials because of their unique benefits, including affordability, ease of preparation, environmental friendliness, outstanding stability, and strong chemical, thermal, and photo-stability. In general, as a host material binary or ternary compounds of oxides, nitrides, molybdates, titanates, sulfates, etc. are used. Among all these compounds, titanate-based phosphors have attracted much attention because of the alluring properties like high thermal and chemical stability, high mechanical strength, wide bandgap and high refractive index due to which emission intensity increases. The chromaticity of titanate-based system can be controlled by adjusting some of the synthesis parameters and by doping them with a 3d or 4f system. When these lattices doped with RE ions or any other impurity ion, give tremendous luminescence results when excited by either UV or NIR radiations.

Therefore, based on the literature survey, we have selected barium molybdenum titanate (Ba_3MoTiO_8, abbreviated as BMT in further chapters) as a host material for our research work. it is a novel ternary compound and its structural and PL properties are not so much explored. The transition metal Mo, which is present in this lattice, has a broad excitation band in the UV area, which has an impact on the BMT phosphor's luminous behavior [25,26]. The introduction of barium into the compound can affect its optical properties, such as refractive index and

optical transparency. This is valuable in applications like optics, photonic devices, and sensors. The aforementioned scientific patronages offered by barium, molybdenum and titanate have prompted us to prepare an inorganic host lattice by name BMT doped with various RE ions.

1.13. Objective of Research Work:

- To synthesize RE doped BMT phosphors by using different chemical routes to achieve pure phase and homogeneous crystal structure and then optimization of the synthesis technique.
- To perform structural, morphological and vibrational investigations using techniques such as XRD, SEM, Raman and FT-IR.
- To study the luminescent properties (up/down-conversion) of the RE ions doped phosphors and to enhance the luminescence intensity by co-doping with suitable activator/sensitizer so as to understand the host as well as its dependency on concentration of RE ions.
- To prepare phosphors for red, green and blue component of w-LEDs.
- To project these phosphors for utilization in SSL and up-conversion applications

CHAPTER 2

Experimental and Characterization Techniques

The creation of high-quality materials necessitates thorough familiarity with the various synthesis procedures as well as the pertinent characterisation techniques. This chapter's goal is to describe the synthesis techniques used in the current study. The synthesised powder phosphor samples have undergone various characterizations of their structural, morphological, vibrational, and photoluminescent characteristics using techniques like XRD, scanning electron microscope (SEM), field emission scanning electron microscopy (FE-SEM), Fourier transform infrared spectroscopy (FT-IR), UV-Vis spectrophotometer, and spectrofluorometer, among others. This chapter also provides an explanation of the operational principles and experimental equipment employed in the current work.

2.1 Raw materials required:

Modern display technologies, solid-state lighting, cathode ray tubes, nuclear medical diagnostics, X-ray detectors, LEDs, etc. all frequently use phosphor compounds. Inorganic phosphors typically consist of an activator ion and a host material. The right host and dopant must be chosen in order to produce phosphors with a strong PL response and greater chemical, physical, and thermal stability. The RE ions/transition metal ions/post transition metal ions can be used as dopants in these phosphor materials. Both radiative and non-radiative decay are possible for the excited activator ion. For the manufacture of phosphors, various host lattice, such as nitrides, oxides, oxynitrides, sulphides, molybdates, titanates, silicates, or aluminates doped with RE metal ions, are typically used. Among them, host lattices based on molybdates and titanates have stable crystal structures and a lot of light output. Pure synthesis of materials is necessary since the host lattice's structure affects the emission intensity and wavelength. The highly pure raw ingredients that were used to make phosphors are mentioned in Table 2.1.

Table 2.1. List of chemicals used in the present thesis work.

Sr. No.	Chemical Name	Chemical Formula	% Purity	Supplier
1.	Barium Carbonate	$BaCO_3$	99.9	Fisher Scientific
2.	Molybdenum Trioxide	MoO_3	99	Loba Chemie Pvt. Ltd.
3.	Titanium Di-oxide	TiO_2	99.5	Fisher Scientific
4.	Europium Oxide	Eu_2O_3	99.9	Sigma-Aldrich
5.	Ammonium Molybdate	$((NH_4)_6Mo_7O_{24}*4H_2O)$	98	CDH
6.	Barium Nitrate	$(BaNO_3)_2$	99	Fisher Scientific
7.	Titanium (IV) Oxyacetylacetonate	$C_{10}H_{14}O_5Ti$	90	Sigma-Aldrich

8.	Holmium Oxide	Ho_2O_3	99.9	CDH
9.	Ytterbium Oxide	Yb_2O_3	99.9	Sigma-Aldrich
10.	Samarium Nitrate	$Sm(NO_3)_3$	99.9	Sigma-Aldrich
11.	Bismuth Oxide	Bi_2O_3	99	CDH
12.	Citric Acid (CA)	$C_6H_8O_7$	99.5	Fisher Scientific
13.	Nitric Acid	HNO_3	69.71	Fisher Scientific
14.	Glycine	$C_2H_5NO_2$	98	Fisher Scientific
15.	Polyethylene Glycol (PEG)	$H\text{-}(O\text{-}CH_2\text{-}CH_2)_n\text{-}OH$		Fisher Scientific

2.2 Experimental methods:

Numerous parameters, including the choice of host, activator, purity of the chemicals used, sintering temperature, sintering time, stirring of chemical solutions, choice of complexing agents, surfactants, and many more must be carefully taken into account while preparing phosphors. According to the literature, there are many different physical and chemical methods for making phosphors. Physical methods include ball milling, while chemical processes include typical solid-state reactions, sol-gel, combustion, molten salt, co-precipitation, spray pyrolysis, and hydrothermal. The synthesis pathway is a necessary constraint to control the size, shape, distribution, and morphology of the particles. Furthermore, by altering the process used to synthesize the phosphor, the light characteristics and quantum efficiency can be improved. Since the solid-state method approach is a good example of solvent-free synthesis of solid products with excellent yield, it has been used to prepare the majority of bulk powder phosphors. However, it necessitates a considerable amount of time and energy for the tedious grinding of the sample and higher temperature sintering. Additionally, this method of synthesis has some severe drawbacks, such as the introduction of flaws that have an unfavourable effect

on the luminous qualities of the produced phosphor. Rapid diffusion of the reactive species causes the reaction to not finish completely, leaving some residue that causes some flaws. Following the grinding of the raw materials, sintering is done in order to evaporate the residue and obtain the pure phase. Additionally, the produced particles' size distribution is unpredictable and is in the micrometre range. Due to consistent mixing of the precursors in the liquid phase during phosphor synthesis via an alternate chemical method and its optimization, size and shape uniformity can be reduced, significantly improving luminous characteristics. For instance, changing the pH value, including complexing agents, and adding surfactants can significantly improve the purity and shape of the sample in the sol-gel process, which further enhances the PL properties of the phosphors as created. The luminous properties of the as-prepared phosphors are enhanced by the improved structure and morphology. Combustion and the pechini sol-gel method were used to synthesise the phosphor in order to optimise its phase and luminous behaviour among other wet chemical synthesis techniques.

2.2.1 Solid-state reaction (SSM) method:

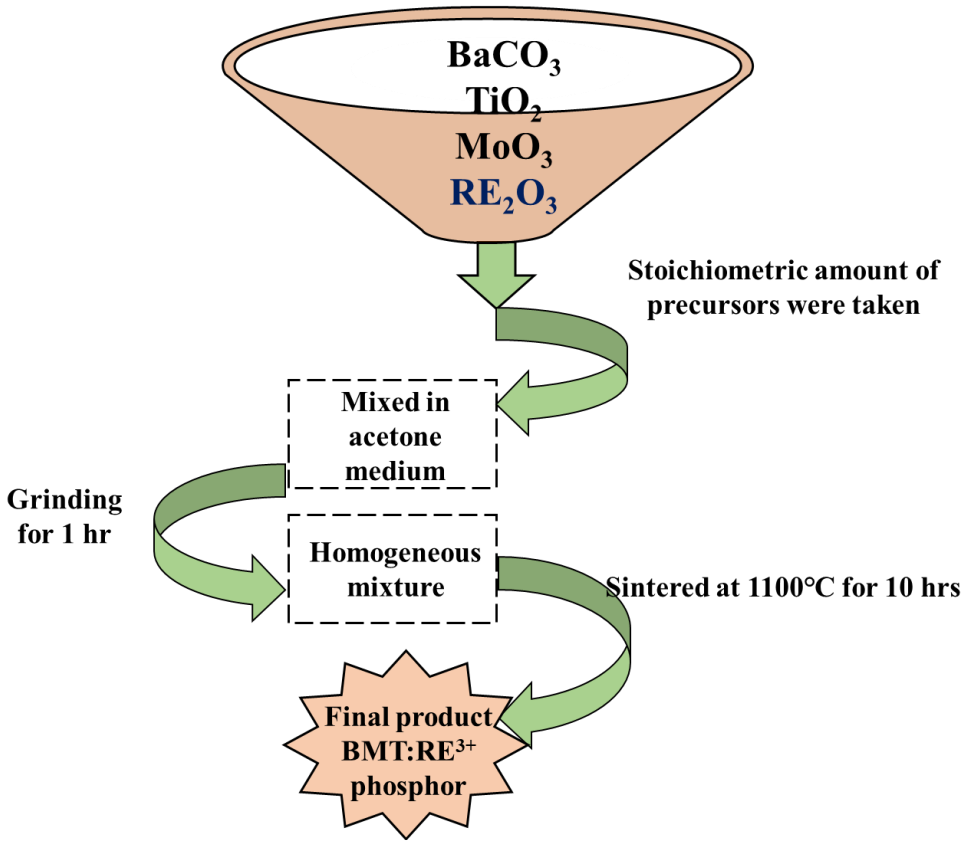

Fig. 2.1(a). Flowchart of various steps involved in the synthesis of BMT phosphor by SSM method.

To create phosphors for industrial usage, where high yield and low cost are crucial in a short amount of time, the SSM method is employed. It uses a dry media reaction where stoichiometrically weighed high purity raw materials are dispersed in volatile solvents like acetone or ethanol, ground, and then heated to promote a diffusion reaction. The temperature necessary for the synthesis of the phosphor is only kept high enough to allow for proper diffusion and complete the reaction in time to prevent precursor materials from melting. Reaction time and temperature are inversely correlated. In order to get the desired phase, the manufacturing of these phosphors occasionally necessitates several heating and grinding

procedures. The resulting phosphor is ground after allowing samples to cool naturally to room temperature. This is followed by other characterizations. Fig. 2.1(a) depicts all synthesis steps involved in this process.

2.2.2. Combustion method (CMM):

The CMM method is a quick and inexpensive synthesis approach that can be used to create a variety of compounds that are useful for industry. The CMM approach is a low temperature synthesis that acts as a self-acting engine to generate heat that is more than what is needed for reactant ignition. The combustion process involves dissolving all of the metal nitrate precursors in DI water, adding RE oxide dispersed in nitric acid to the metal nitrate solution, and stirring the mixture on a magnetic hot plate to ensure uniform mixing. In the CMM method, the oxidizer (nitrate precursors) rapidly breaks down in the presence of an organic fuel (such as urea, hydrazides, glycine, etc.) to produce the product in nano-form. Maintaining an oxidant to fuel ratio of 1 is crucial for successful combustion and can be determined from the valences of the two substances. Metal nitrates and fuel operate as the oxidising and reducing reactants in the CMM reaction, respectively [27]. After the addition of fuel, the solution was placed again on stirring for 2 hours at 120°C. The exothermic reaction's strong energy release raises the temperature of the reacting species and causes a fire to start at 500°C. At this temperature, a grey coloured foamy powder was formed with release of large amount of gases. The CMM reaction is an auto-propagating reaction that uses gas evolution to produce the target product.

2.2.3. Sol-Gel-Combustion method (SGM):

In the Pechini sol-gel process, a metal salt solution reacts with a mildly alkaline or acidic media. A gel with a porous, interconnected network and polymeric chain is created from a sol. Precursors used for this synthesis method were the same as used in the CMM technique. In this

approach, CA is utilized as a chelating agent. A polymeric network of the metal citrate complex is created by using polyethylene glycol and a metal: CA ratio of 1: 2. The CA is added and maintained over a magnetic hot plate under steady heating at 120°C for 4 hours. The homogeneity of the gel and particle size of the resulting powder sample depend heavily on pH in this procedure [28]. It is burnt at 500°C while the gel forms, and the resulting brown foamy solid is ground and sintered at 1000°C for 10h. For characterizations, white powder phosphor that has just been manufactured is used. Figure 2.1(b) depicts the specifics of the combustion and sol-gel synthesis processes used in this paper.

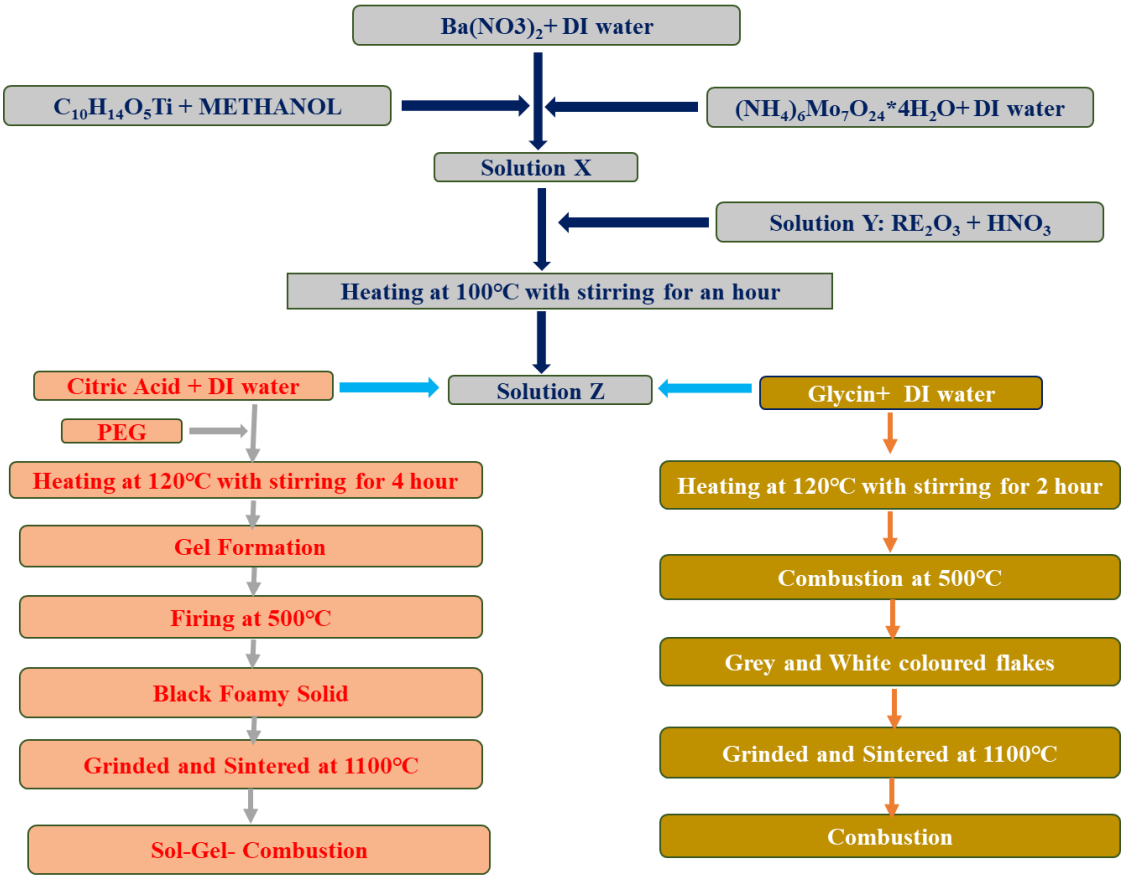

Fig. 2.1(b). Schematic representation of various steps involved in the synthesis of BMT phosphor by SGM and CMM techniques.

2.3. Characterization techniques:

Inherent traits for the optimization and successful use of the as-prepared phosphors in lighting systems must be known in order to apply the appropriate characterization techniques. Using the conventional tools used to determine the structure, morphology, and luminescence behaviour, the as-prepared BMT phosphors have been characterized. The next sections go into great length to explain the experimental methods used to characterize the synthesised phosphors.

2.3.1. Thermal analysis:

The physical characteristics of the reaction products as a function of temperature, stress, and environmental conditions were determined by studying the thermal behaviour of the precursors using thermogravimetric and differential scanning calorimetry (TG-DSC). In order to analyse the substance, the chemical is often heated under regulated conditions. Topography, phase transitions, crystallisation, adsorption, desorption, melting, enthalpy, weight variations, and thermal stability are just a few of the features that may be understood by thermal analysis. However, thermogravimetric-differential scanning calorimetry (TG-DSC) was used in the current thesis work to determine the phosphor's crystallisation temperature.

(i) Thermogravimetric analysis (TGA):

In TGA, a controlled environment and a steady increase in temperature or time are used to measure the mass or weight loss of a precursor. The relationship between weight percentage with respect to time or temperature is known as a thermal decomposition curve. Decomposition, oxidation, vaporisation, sublimation, and desorption are all discussed in this chapter. The weight variation in the TGA curve represents the adsorption or desorption of gases

from the sample under study. While a minor mass change implies the material is stable, a rise in mass shows adsorption and a reduction in mass indicates desorption.

Fig. 2.2. Perkin Elmer Pyris diamond (TGA/DTA/DSC) system.

(ii) Differential thermal calorimetry (DSC): In chemistry and materials research, differential scanning calorimetry (DSC) is a popular thermal analysis method. It is generally used to measure the heat flow into or out of a sample as a function of temperature or time in order to research the thermal properties of substances, including phase transitions, heat capacity, and reaction kinetics. The foundation of DSC is the idea that any physical or chemical change, such as a phase transition (melting, crystallisation, or sublimation), will affect the sample's internal energy balance. When a sample and a reference material are both subjected

to a controlled temperature programme, this causes heat to be released or absorbed, which may be measured as a temperature differential between the sample and the reference material. As indicated in Fig. 2.2, TG-DSC were performed in the current thesis utilizing the Perkin Elmer Pyris diamond (TGA/DTA/DSC) system.

2.3.2. X-ray diffraction (XRD) for structural investigations:

One of the most fundamental and potent technologies for analysing and determining the structure of both bulk materials and nano-structures is X-ray diffractometry (XRD). The phase orientation, geometry, and lattice constants of a crystal structure can all be ascertained using this method. The method can also be used to assess a material's stress and strain. Since XRD is based on the diffraction principle, when X-ray waves with wavelength 0.01- 10 nm are impinged on a crystal, the crystal planes cause them to be diffracted since the interplanar spacing is similar to the wavelength of x-rays. Crystal planes behave similarly to mirrors and can therefore reveal information about the crystal structure. Every crystal's diffraction pattern is distinct, just like a person's fingerprint. Bragg's equation can be used to describe the diffraction of a crystal, and the diagram in Fig. 2.3 that explains this phenomenon.

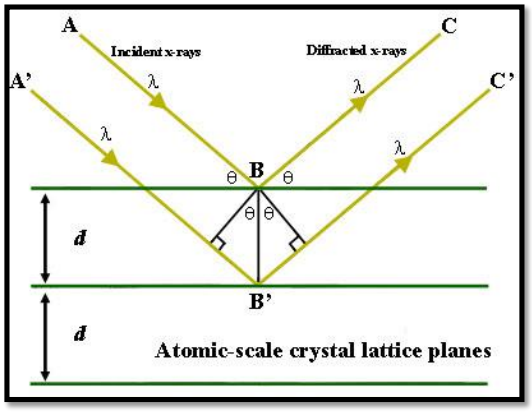

Fig. 2.3. Bragg's Diffraction representation from crystal planes.

$$2d_{hkl}sin\theta_{hkl}= n\lambda \quad (13)$$

where the incident light's wavelength is λ, the interplanar distance is d, the diffraction angle is θ, the Miller indices for the crystals' planes are h, k, and l, and the order of diffraction is n.

The XRD setup consists of a fixed sample holder assembly, a high-speed energy-dispersive compound silicon detector with an automatically adjustable window that can measure patterns in the angular range of 0.1° to 90°, and a moveable copper [Cu-(K)] source for the emission of X-ray spectrum at wavelength 1.54 Å. The high voltage electron beam from the source tube strikes an anode metal target, such as copper (Cu), molybdenum (Mo), iron (Fe), or chromium (Cr), in a vacuum atmosphere to produce a highly collimated X-ray. Cu is the target material most frequently employed for single-crystal diffraction. The sample is exposed to an X-ray beam, which is then detected as the sample and detector rotate. When the incident X-ray strikes the sample and causes constructive interference before an intensity peak develops, the Bragg equation is satisfied. A detector is used to both capture and process this radiation. The output is then taken through a printer or computer monitor after the signal has been converted to a count rate.

A wide range of details concerning the crystal structure, orientation, average crystalline size, and stress in the films are revealed by XRD examinations. The sample's experimentally obtained diffraction patterns are compared to the published Joint Committee on Powder Diffraction Standards diffraction files (JCPDS).

The peak width of the materials can be used to calculate the crystallite size 'D' using Scherer's formula-

$$D=s\lambda/\beta cos\theta \quad (14)$$

Where θ is the Bragg angle, β is the peak's full width at half maximum (FWHM), and s is the constant based on the material's geometry.

The material to be examined may be in the shape of a powder, pellet, or even a thin film that contains crystallites, which are microscopic crystals. The X-Ray diffractometer used in the current thesis work is shown in Fig. 2.4.

Fig. 2.4. Bruker D8 Advance X-ray diffractometer.

2.3.3. Scanning electron microscopy (SEM) and field emission scanning electron microscopy (FE-SEM) for morphological investigations:

A sophisticated type of microscope called a SEM uses electrons rather than light to examine the three-dimensional structure of solid materials. The SEM technique can be used to gather a lot of data about a sample, including the topography, composition, and morphological aspects of the solid sample. It can be considered the most effective method for examining the morphology of organic and inorganic materials on scales ranging from nano to micro scale. SEM provides incredibly accurate images of a range of materials with high magnification up to 30kx and even 1000kx in some modern versions. An electron beam is focused onto a specimen using electromagnetic "lenses" in a SEM (which can be a metal, metal oxide, ceramic, or biological sample). By observing how the electron beam reacts with the specimen surface, an image is created. Different kinds of electrons are deflected when the electron beam strikes the material.

Fig. 2.5. Zeiss EVO40 Scanning Electron Microscope.

In order to create a sample for SEM examination, conducting carbon tape is covered with powder samples, thin films, or pellets, which are then coated with conducting metals like gold (Au) or platinum (Pt). To prevent the concentration of incident electrons at a specific location in the sample, the sample is coated with conducting metals. Now the electron beam is switched on the electrons and their interaction take place with the specimen. This interaction takes place in the form of their scattering from the surface thereby producing secondary electrons along with backscattered electrons (BSE) and these are used to visually inspect the sample's surface. Although secondary electrons are produced throughout the whole volume of interaction, they only escape from a few surface layers and have an energy of less than 50 eV, providing morphological data about the sample. BSE have an energy more than 50 eV and are elastically scattered from the surface, allowing them to travel farther than secondary electrons. Bright

spots can be seen in SEM pictures because high atomic number elements produce more BSE than low atomic number ones do. Because of this, contrast in the pictures produced by BSE can be used to visualise various chemical compositions of the surface elements. While the intensity of the signal is inversely proportional to the concentration of secondary electrons, the dark contrasted image of the surface correlates to the concentration of BSE.

Fig. 2.6. JEOL 7610F Plus Field- Emission Scanning Electron Microscope.

FE-SEM is a type of microscopy that scans the material in a zigzag pattern using a field emission source. When compared to a tungsten filament used in a typical SEM, the electron emitters of a field emission gun have an emission capacity up to 1000 times more. Similar to SEM, secondary electrons are also gathered here by a scintillator detector that generates

photons. Additionally, FE-SEM requires higher vacuum levels, and to prepare the sample, a very thin layer of palladium or Au is coated on it. After leaving the electron gun, the electrons are next focused into a tiny, monochromatic beam using metal apertures and magnetic lenses. Signals from detectors for each sort of electron are gathered to form an image of the item. With nearly infinite depth of field and extremely high magnification, FE-SEM provides information on topography and elements. When it comes to creating clearer images with spatial resolution down to 1/2 nanometers and less electrostatic distortion, it is three to six times more successful than standard SEM. Since structures as small as cell nuclei and microchips may be seen, FE-SEM is a particularly popular technology among physicists, chemists, biologists, material scientists, and electronic engineers. The microscopes used for these morphological studies are shown in Fig. 2.5 and 2.6.

2.3.4. Energy dispersive X-ray spectroscopy (EDAX):

Energy Dispersive X-ray analysis is known as EDAX Analysis. Additionally, it may also be referred to as EDS or EDAX analysis. It is a method for determining the specimen's elemental composition or a region of interest therein.

The specimen is blasted with an electron beam within the SEM during EDAX analysis. The specimen atom's own electrons are hit by the bombarding electrons and some of them are dislodged as a result. A higher-energy electron from an outer shell eventually fills the space left vacant by an ejected inner shell electron. However, the transferring outer electron must sacrifice some of its energy by generating an X-ray in order to accomplish this.

Depending on which shell the transferring electron is transferring to as well as from, the amount of energy produced by the electron varies. Additionally, each element's atom releases

X-rays with a different amount of energy throughout the transfer process. Thus, the identity of the atom from which the X-ray was emitted can be determined by measuring the energies present in the X-rays being released by a specimen during electron beam bombardment. The EDAX spectrum is nothing more than a graph showing the frequency of X-rays at various energies. Peaks in an EDAX spectrum typically correspond to the energies for which the greatest number of X-rays were detected. Since each of these peaks is specific to each atom, they each represent a separate element. The more a peak in a spectrum correlates to a single element, the higher it is. The concentration of the element in the material increases with increasing peak height in a spectrum [37].

The type of X-ray that each peak on an EDAX spectrum plot relates to is also known, in addition to the element that each peak corresponds to. For instance, a peak known as a K-Alpha peak is the energy level of the X-rays produced when an electron in the L-shell descends to the K-shell. The peak corresponding to the X-rays released by M-shell electrons moving into the K-shell is known as the K-Beta peak. EDAX operates on the same fundamental tenet as electron probe microanalysis. A portion of the incident electrons from an electron beam excite the specimen's atoms, which cause them to release X-rays when they return to their ground state. The electron microscope's elemental analysis is based on the detection of these X-rays because their energy is directly correlated with the atomic number of the excited elements.

2.3.5. Fourier transform infrared spectroscopy (FT-IR) for the identification of functional groups:

FT-IR spectroscopy, which is mostly used in research labs to detect various substances present in a given sample, uses infrared radiation with a broad spectrum that ranges from 400 to 4000 cm^{-1}. The examination of thin films and coatings to identify the functional groups is one

application for this approach. The FT-IR spectroscopy method offers a number of benefits, including its quick scanning rates when compared to other dispersive methods and its suitability for usage with solids, liquids, and gases.

Fig. 2.7. Perkin Elmer spectrum 2 set-up.

The molecular bonds of the substances present in the sample determine how the procedure works. The atoms that make up a molecule determine the type of molecular bonds that exist in various compounds. Following their absorption by the IR radiation, the molecules of these compounds in a sample reach a higher energy state. As soon as these molecules reach their initial, or de-excited, state, they emit radiation with an energy equal to the difference between their excited and de-excited energies. From the numerous available wavelengths present in the incident light, each substance absorbs a particular wavelength of IR light. The nature of the substance and its bonds can be ascertained using the FT-IR, which measures these absorbed wavelengths. The IR radiation's "transmittance" or "absorption" can be plotted on the y-axis against the wavenumber on the x-axis in the ensuing graph. Depending on the molecule's characteristics, the graph may contain numerous peaks. The functional groups present in the sample are then identified by comparing these peaks to known standard IR peaks for various materials and bonds. For FT-IR spectroscopy, the Michelson interferometer is frequently

employed. The beam splitter divides the incident beam into two after the light from the IR radiation source in the interferometer setup passes through a collimator. The two beams then move to the interferometer's two mirrors, one of which is always moving. Every wavelength contained in the incident beam is modulated at a different frequency as a result of the introduction of a path difference between the two beams. After being reflected by the mirrors, the beams combine to create a sophisticated interferogram. The sample, as previously mentioned, will absorb light of a certain wavelength from among the many available wavelengths in the light incident on it. The sample is then made incident on the interferogram. The detector counts the number of photons at each wavelength that are being sent. The resulting signal is subsequently processed and transformed using the "Fourier transform method" into useful data. The final graph produced by the Fourier transform approach aids in identifying the various functional groups that are present in the data under consideration. The set-up used for recording FT-IR spectra is shown in Fig. 2.7.

2.3.6. Raman spectroscopy:

Raman spectroscopy is used to look at the specimen's rotational, vibrational, and other frequency modes. It provides information on the bonds and atomic structure of molecules. This technique also offers a fingerprint that can be used to recognise compounds. This spectroscopy is based on the Raman Effect, which is the inelastic scattering of light. When incident monochromatic radiation strikes the sample, it interacts with it differently and either gets scattered, reflected, or absorbed. Information on the molecular structure is gathered using scattered radiation. A common laser is employed as the coherent source in Raman spectroscopy to analyse specimens. Most of the energy that enters the room disperses elastically, creating Rayleigh scatter light. Stokes and anti-Stokes lines make up the majority of the small

percentage, or about 1 in 10^6, that is inelastically scattered, and it is this little fraction that is employed to gather data about the specimen. The frequency of the incident and scattered light are identical in Rayleigh Raman scattering. In anti-Stokes Raman scattering, the frequency of the scattered light is higher than the incident light's frequency, whereas in Stokes Raman scattering, the frequency of the scattered beam light is lower than the incident beam light's frequency.

Fig. 2.8. Invia Renishaw Raman Spectroscope.

The Raman spectrum is displayed between the brightness of the scattered light and the so-called Raman shift in energy. When the photon interacts with the molecule, the electric field, denoted by E, induces a dipole moment, denoted by P.

$$P = \alpha . E \qquad (15)$$

where α is a proportionality constant that explains how the electron cloud around a molecule is distorted. Raman active modes are created by these chemical bonds that undergo certain energy transitions that correspond to changes in polarizability. A laser source, a system for illuminating the sample, and a suitable spectrometer are the three essential components of a modern Raman spectrometer. Lasers are the most popular sources used to analyse Raman

spectra because of their monochromaticity and high-intensity beams, which have good signal-to-noise (S/N) ratios. Raman spectroscopy is frequently superior to IR spectroscopy because it may be utilized to study inorganic systems in an aqueous solution. It has been widely applied to study biological systems. Analysis using Raman spectroscopy requires a small sample quantity, further liquid and film samples can also be analysed. It can detect molecular impurities and additives. For quantitative and qualitative analysis in many settings, Raman spectroscopy has emerged as a non-corrosive technique. Fig. 2.8 shows the Raman spectrometer used in this work.

2.3.7. Diffuse reflectance spectroscopy (DRS):

In DRS, the light reflected off the material is measured rather than the transmitted beam through it. This is a form of absorption spectroscopy. It is a typical technique for determining opaque substances whose absorption is too high to be determined through transmission. Both quantitative and qualitative analysis of materials can be done using the information in a diffuse reflectance spectrum. The resulting spectrum, which is often measured using visible or near-infrared light, gives details on the electronic or possibly vibrational structure of the item being examined. Improved signal-to-noise and sensitivity compared to transmission measurements are some benefits of measuring spectra in reflecting geometries, however this comes at the expense of harder to record and more complicated spectra to comprehend.

Fig. 2.9. Jasco V-770 Spectrophotometer.

The specimen is illuminated with photons of a specific energy, and the relative transmissions of the various photons are monitored. The experiment provides a precise measurement of the band gap because photons with energies greater than the band gap are absorbed and photons with energies lower than the band gap are transmitted. Understanding the scattering and absorbance properties of the sample being examined typically involves applying the Kubelka-Munk theory. To find out the optical band gap, the DRS spectral data was converted into the Kubelka–Munk function using the following equation [29]:

$$F(R) = \frac{(1-R)^2}{2R} = \frac{\alpha}{S} \quad (16)$$

In this equation, R is Reflectance, α is absorption coefficient and S is Scattering coefficient. The tauc equation gives the relation between energy band gap (E_g) and absorption coefficient (α) as shown below:

$$F(R)h\upsilon = C(h\upsilon - E_g)^n \quad (17)$$

Here hυ belongs to photon energy, C is energy independent constant and n can take values depend upon the type of transition which is 1/2 and 2 for direct and indirect allowed transitions. Since F(R) is directly proportional to α, the above equation can be rewrite as:

$$F(R)h\upsilon = C(h\upsilon - E_g)^n \quad (18)$$

In the current thesis, a Jasco V-770 UV-Visible/NIR spectrophotometer was employed to record DRS (shown in Fig. 2.9). It has an exceptional linearity of absorbance and a singular monochromator design for optimal light throughput. The V-770 is capable of measuring wavelengths between 190 and 2700 nm. Even with a small spectral bandwidth, the single monochromator design delivers a substantially higher energy throughput than a double-monochromated system, improving the S/N ratio across the whole spectrum range.

2.3.8. Photoluminescence (PL) Spectroscopy:

The process through which light energy, or photons, promote the emission of a photon from any substance is known as PL spectroscopy, or PL for short. It is a non-contact and non-destructive method to detect objects. Essentially, light hits the sample and gets absorbed and a process called photoexcitation occurs. When the material relaxes and return to lower energy after light stimulation, it releases energy of photons. Light excitation causes the material to transition to a higher state. PL is the light or brightness emitted as a result of this process.

Fig. 2.10. Jasco Spectrophotometer Spectrofluorometer FP-8300.

The excitation and emission spectra as well as the lifespan of the excited state of the samples are all measured using PL spectroscopy. A PL spectrometer, which consists of an excitation source, monochromator, sample holders, and detector, can be used to measure the PL properties. The PL spectrophotometer uses a variety of excitation sources, including mercury lamps, tungsten lamps, and xenon arc lamps. Because it possesses an energy continuum spanning from the ultraviolet into the near infrared, the xenon arc lamp is frequently utilised. The excitation monochromator, which has gratings for high resolution and spectrum purity, receives the light emitted from the source. The down-conversion PL spectra as displayed in Fig. 2.10 were recorded using a Jasco FP-8300 spectrofluorometer in this study.

Fig. 2.11. Horiba PTI Quanta Master equipped with 980 nm solid state laser.

The source of excitation, the sample cell, and the detector are the three main parts of this apparatus. It comes from a xenon lamp. The sample cell should be constructed of a material that barely absorbs the desired wavelength. A good grade of glass is usually sufficient, although quartz cells should be used for wavelengths below 250 nm. The entry slit of the excitation monochromator receives concentrated light from the lamp after it has been gathered. The excitation monochromator and lamp housing are separated by a quartz window. By exhausting the heat from the instrument, this protects against bulb failure. The monochromators' entry and exit parts are managed by the loaded software which controls themovable slits. The band pass of light incident on the sample is determined by the width of the slits on the excitation monochromator. The emission monochromator's slits regulate how strongly the fluorescence signal is detected by the signal detector.

A 980 nm solid state laser-equipped Horiba PTI Quanta Master has been used for an up-conversion PL investigation displayed in Fig. 2.11. By substituting a xenon lamp for the 980 nm laser, certain up-conversion PL tests have also been carried out with this apparatus.

A 150 MHz digital oscilloscope (HM 1507, Hameg Instruments) and an Edinburg FL920 spectrometer were used to perform time-resolved PL (TRPL), as illustrated in Fig 2.12.

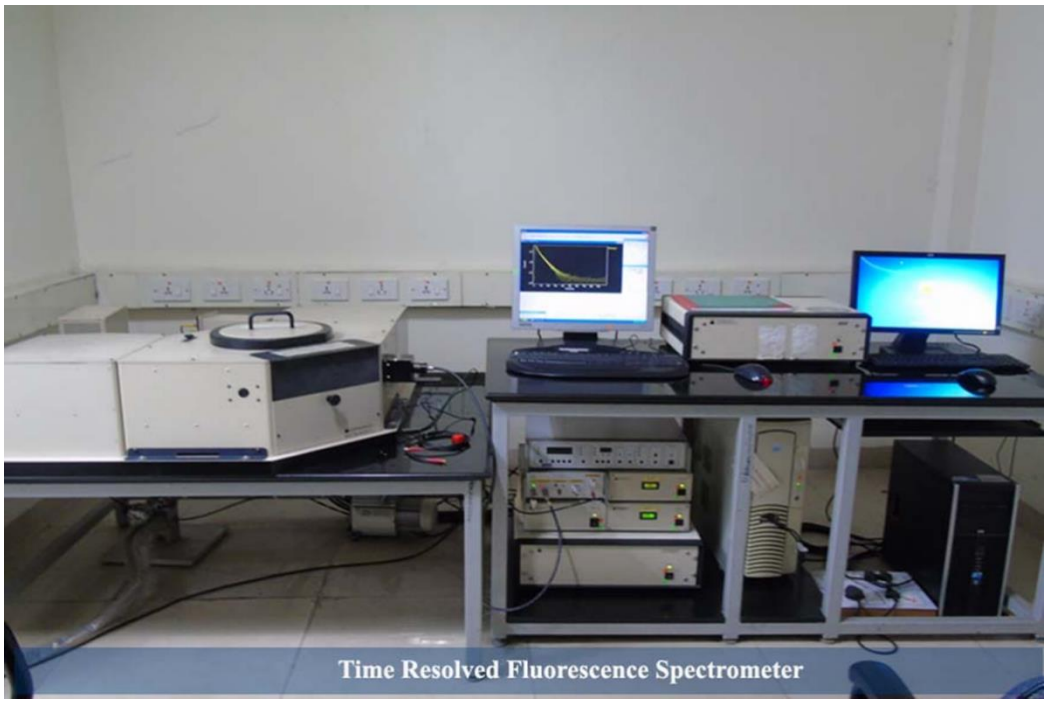

Fig. 2.12. Edinburgh FL920 Fluorescence Spectrometer.

2.3.9. Temperature- dependent PL Spectroscopy:

Materials science and solid-state physics use temperature-dependent PL to examine the characteristics of materials and their light emission (PL) as a function of temperature. Understanding the electrical and optical characteristics of phosphors, semiconductors,

quantum dots, nanomaterials, and other materials that exhibit PL is made possible by this technique. For lighting applications, the phosphor must be thermally stable, which can be determined by observing PL spectra at high temperatures. In general, the PL profile shouldn't change at high temperatures, however thermal quenching could cause the intensity to drop. The thermal quenching should be as low as possible for a better phosphor, suggesting greater thermal stability of the phosphors at high temperatures. Fig. 2.13 depicts the setup used to record temperature-dependent PL.

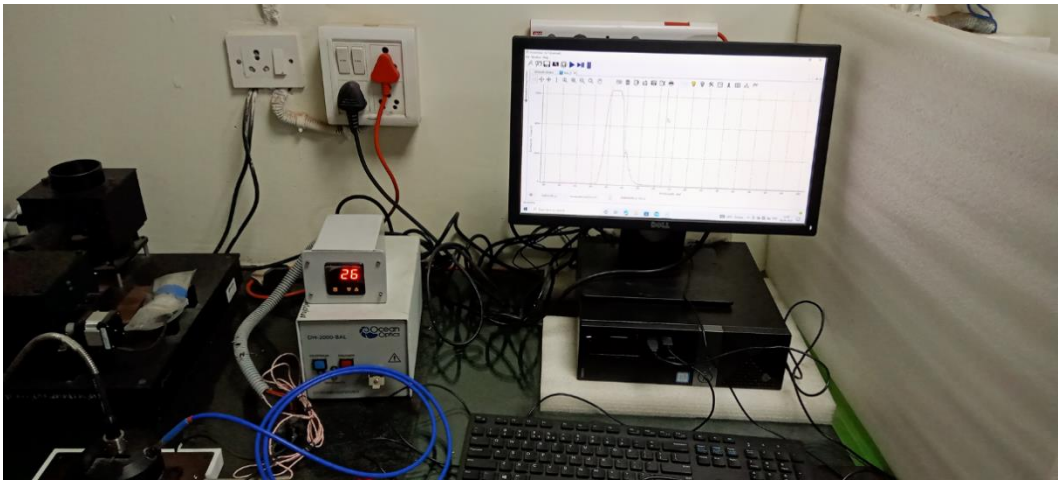

Fig. 2.13. Ocean Optics FLAME-S-XR1-ES Spectrometer.

CHAPTER 3

Synthesis optimization and efficiency enhancement in Eu^{3+} doped Barium Molybdenum Titanate phosphors for w-LED applications

Ba_3MoTiO_8 phosphor activated with Eu^{3+} ions have been synthesized successfully by three different routes such as SSM, CMM and SGM to optimize relatively best synthesis technique and temperature of synthesis. XRD pattern has been used to confirm the phase and crystallinity of the as prepared phosphor. SEM and Raman spectra have been used to study the morphological behaviour and different vibrational bands present in the structure of the titled phosphor respectively. DRS have been recorded to find out the optical band gap of phosphors. PL spectral features recorded under 393 nm and 465 nm excitation wavelengths reveal an intense red emission at 612 nm corresponding to $^5D_0 \rightarrow {}^7F_2$ transition of the doped Eu^{3+} ions. CMM synthesized sample has shown maximum luminescence intensity out of the three methods and further studies have been carried out by preparing a series of europium ions doped Ba_3MoTiO_8 phosphor using the CMM technique. All the morphological and PL studies carried out on the Eu^{3+} ions doped Ba_3MoTiO_8 phosphor contemplate the suitability of the as prepared phosphor for red component in w-LEDs applications.

The content of this chapter has been published in an international journal - **Materials Research Bulletin, 150 (2022) 111753**.

3.1 Introduction:

In this digitalized world, energy plays an important role in various sectors affecting the social and economic development. The ever-increasing demand of energy causes irreversible changes in our surrounding environment. Among the total energy produced from various sectors, major share is utilized for indoor as well as outdoor lighting purpose. Huge mismatch in energy production and consumption is being caused that may be due to the inefficiency of gadgets which gave low output yield and exhaust huge amount of energy. The conventional sources of energy including fossil fuels, incandescent and fluorescent lamps cause large loss of energy in the form of heat and radiation, while also not being environment friendly. It is important to utilize the available energy in efficient, sensible and sustainable way. Thus, developing alternate devices and technology such as SSL devices is showing possibility of excellence in next generation illumination sources when compared to fluorescent and incandescent lamps due to their high efficiency, larger lifetime, low cost of preparation and eco- friendly behaviour. The commercial method that we use currently to generate white light is coating of yellow phosphor (YAG: Ce^{3+}) on blue LED chip. But the light generated from this method have low CRI) and high CCT due to deficiency of red component. Another prominent method used to generate white light is coating of RGB (red, green and blue) phosphors on n-UV LED chip or coating of R/G phosphor on blue LED chip. Usage of these techniques can effectively improve CRI and CCT values in comparison to usage of yellow phosphor with blue LED chip. White light can also be generated by the combination of n-UV LED + RGB phosphor. This technique is not a widely used one because the commercial red phosphor ($Y_2O_2S:Eu^{3+}$) used in this technique is not a good absorbent of light generated by n-UV chip. Moreover, it has poor lifetime under UV excitation and is chemically unstable. RE ions are used as an excellent

dopant in host lattices due to their high luminescence efficacy, high solubility and large stokes shifts. In addition, these ions are easily getting excited by absorbing UV or n-UV radiations and gives emission in visible region through down shifting process. Out of the various RE ions, europium ion is one of the most promising lanthanide ion and gives red emission due to its prominent $^5D_0 \rightarrow {}^7F_2$ transition. Europium ion exhibits narrow band and has higher lifetimes as compared to other luminescent materials. So, it is relevant to prepare Eu^{3+} doped BMT phosphor as an efficient red emitting phosphor which can overcome the limitations of currently used host lattices.

In this context, an un-doped BMT sample has been prepared by three different synthesis methods like SSM, SGM and CMM to optimize the best synthesis method useful for showcasing relatively better luminescence efficiency. SSM is a commonly used synthesis method for phosphors but it has its own drawbacks such as requirement of high sintering temperature, non-uniform mixing of precursors, vast size distribution and ensuing grinding which out-turn in damaging of phosphor surface and reduction of luminescence intensity. So, it is obligatory to focus on other chemical methods like combustion, Sol-gel, hydrothermal, wet chemical route etc. to curb these limitations. Sol-gel process generally involves formation of organic/inorganic network through a chemical reaction at low temperature, transition of this solution to colloidal sol and then transition of this colloidal sol to gel form. Pechini-type sol-gel, also known as polymerizable-complex technique, is a vastly used technique for metal-complex formation with the addition of citric acid (CA) and polyethylene glycol (PEG). Combustion method is an unadorned, safe and energy frugalite method. In this technique, chemical reaction takes place at relatively low temperature.

The present work includes the synthesis of BMT: Eu^{3+} phosphor for better luminescence property using three different techniques (SSM, SGM and CMM) and characterization of the as prepared phosphor using XRD, Raman, SEM to check the crystallinity, morphology and phase formation. Raman spectra and SEM studies have been compared for different samples synthesized by different techniques to optimize synthesis technique for better morphology. Further DRS, PL and PL decay spectral analysis have been conducted on the as prepared phosphors. The CIE coordinated have also been evaluated using the PL spectral information.

3.2 Sample preparation and coding:

Eu^{3+} doped BMT phosphor was prepared by three different techniques mentioned in section 2.2 of chapter 2 along with Fig. 2.1 (a&b). Table 3.1 depicts sample coding for different concentrations of europium ion.

Table 3.1. Sample coding for different concentrations of Europium ion doped BMT phosphor.

Synthesis Method	Eu^{3+} ion concentration (mol%)	Sample Code
Solid state Reaction (SSM)	0	SSM0
	1.0	SSM1
Sol-gel Combustion (SGM)	0	SGM0
	1.0	SGM1
Combustion (CMM)	0	CMM0
	1.0	CMM1
	2.0	CMM2
	3.0	CMM3
	4.0	CMM4

3.3 Characterization techniques used:

XRD was carried out using the Bruker D8 Advanced powder X-ray diffractometer via Cu-Kα radiation (1.54Å). For surface morphology, SEM recordings were done by using the instrument Zeiss EVO40. DRS study was conducted by using the JASCO V–770 Spectrophotometer. To study the PL properties, JASCO made Spectrofluorometer (FP-8300) has been employed. Raman Spectra was recorded with the help of Invia Renishaw Raman Spectroscope. To study the PL decay profiles, Edinburgh FL920 Fluorescence spectrometer was used.

3.4 Results and Discussion:

3.4.1 Structure and phase analysis:

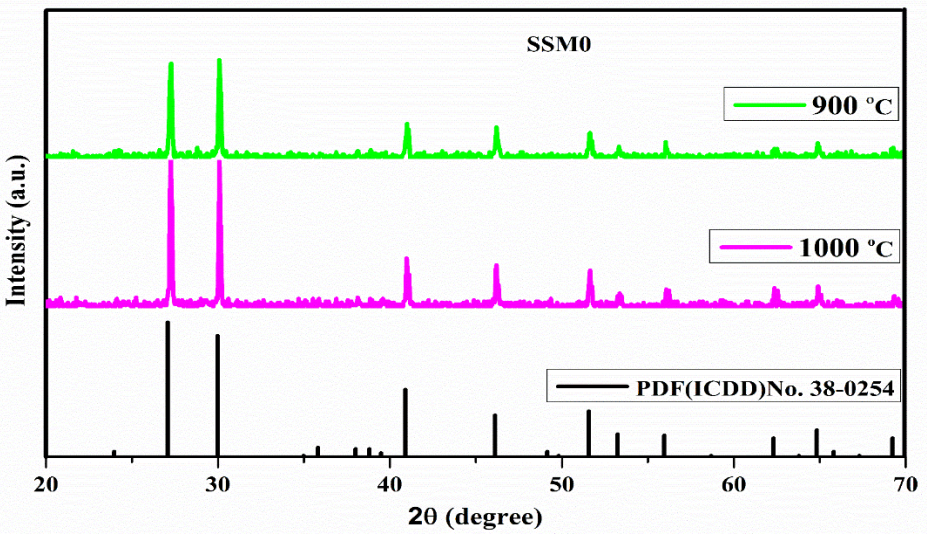

Fig. S1. XRD pattern of SSM sample sintered at temperature 900℃ and 1000℃ along with standard diffraction pattern of BMT.

For structure and phase analysis, XRD pattern of BMT sample was examined for differently synthesizing methods. SSM synthesized sample was sintered at different temperatures to optimize the suitable temperature for this method (Fig. S1). But the sample sintered at 1100℃ has the single-phase confirmation with standard ICDD card no.00-038-0254 with a space group R-3m (166), and lattice parameters a= 5.9570Å, b=5.9570Å and c=21.290Å. Fig. 3.1(a)

manifests the XRD pattern of SSM0, SGM0 and CMM0 samples along with the standard JCPDS data. As shown in Fig. 3.1(a) the diffraction patterns of SSM0, SGM0 and CMM0 samples are perfectly matching with the standard JCPDS data (00-038-0254). Fig. 3.1(b) shows the XRD pattern of SSM1, SGM1, CMM1 samples with 1 mol% of europium ion. With the incorporation of europium ion, no mismatch of phase was found.

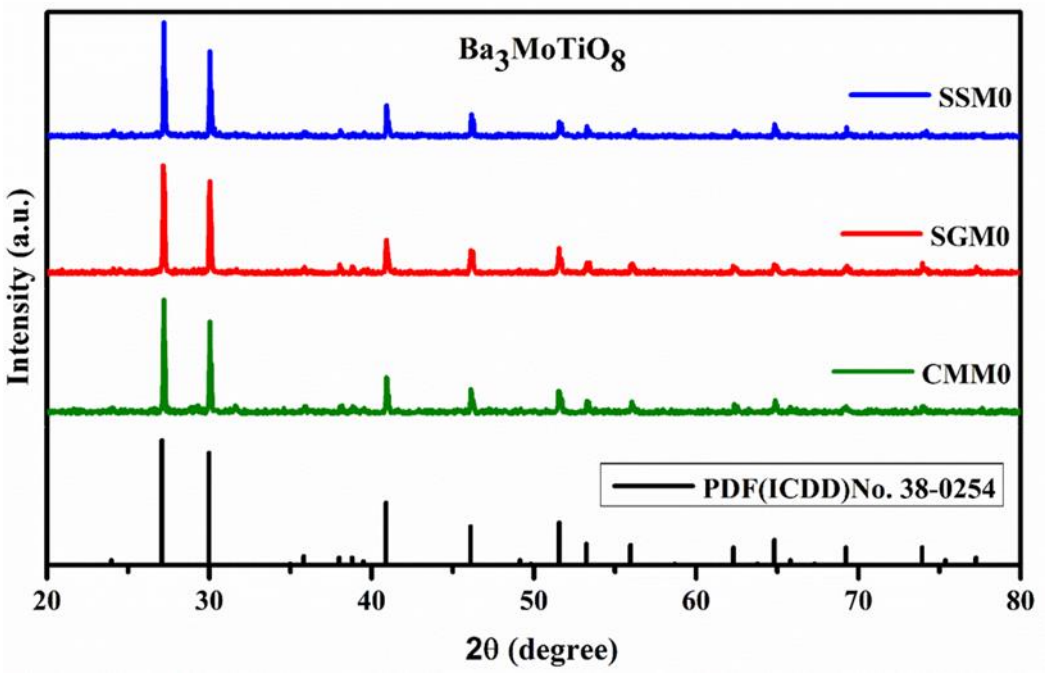

Fig. 3.1(a). XRD pattern of BMT sample synthesized by SSM, SGM and CMM technique along with standard diffraction pattern of BMT.

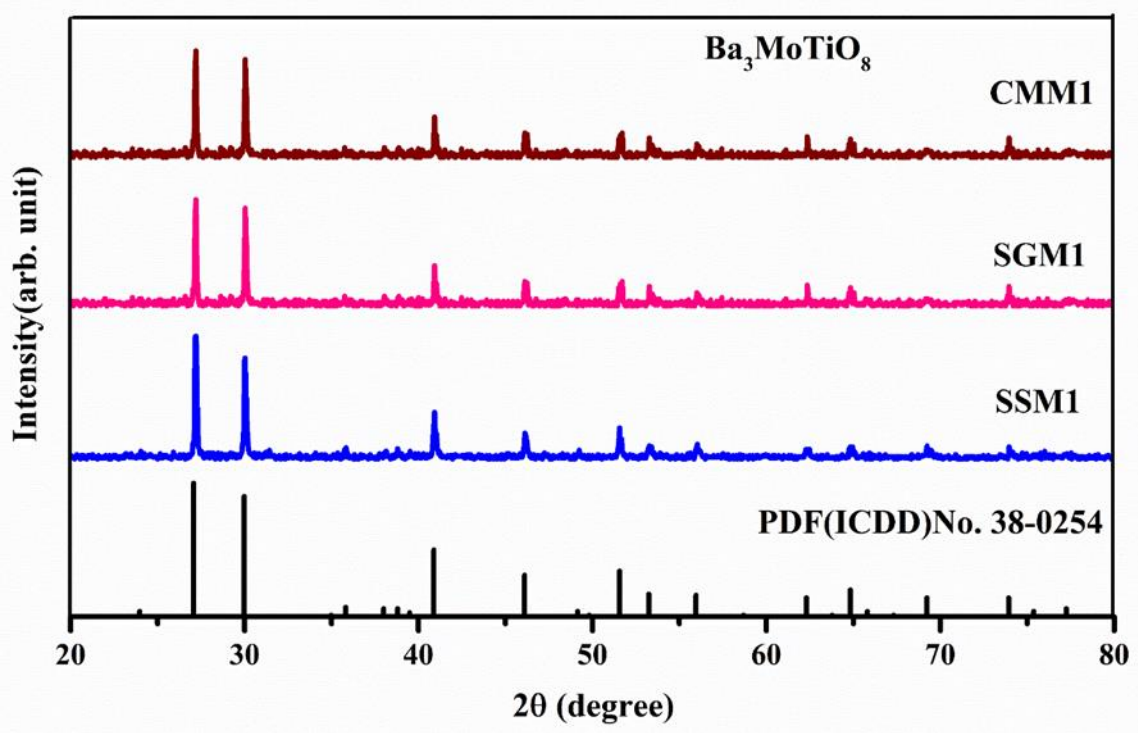

Fig. 3.1(b). XRD pattern of CMM1, SGM1 and SSM1 phosphor with 1 mol% concentration of Europium ion.

This shows that, Eu^{3+} ions (ionic radii 1.08 Å) are successfully replacing Ba^{2+} ions (ionic radii 1.4 Å) due to their proximity in ionic radii. In addition to this their charges are also getting compensated ($3Ba^{2+}$ ions replaced for $2Eu^{3+}$ ions). Crystalline size was calculated by using the Debye-Scherer formula given in eq. (14) described in chapter 2. The crystalline size estimated using the Debye-Scherer formula was found to be 140 nm, 71nm, 65 nm for SSM1, SGM1and CMM1 samples respectively.

3.4.2. Morphological Analysis from SEM:

To elucidate the information pertaining to morphology of the as prepared phosphors, the SEM images are recorded for BMT phosphors prepared by three different techniques such as SSM, SGM and CMM. Fig. 3.2 shows the SEM images of SSM0, SGM0 and CMM0 samples taken at different magnifications.

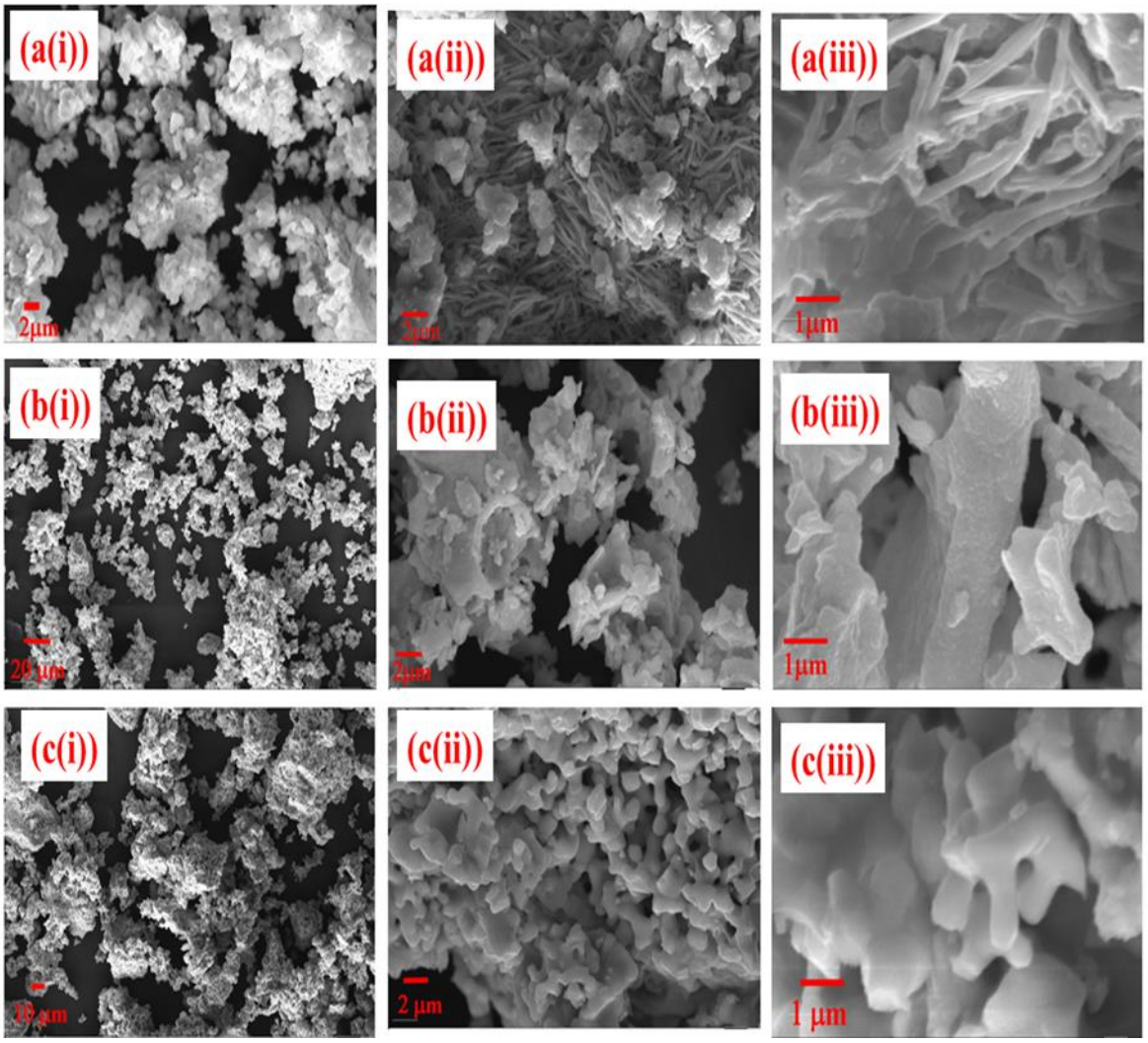

Fig. 3.2. SEM images were recorded for BMT sample **(a (i-iii))** SSM0 **(b (i-iii))** SGM0 and **(c (i-iii))** CMM0.

Fig. 3.2(a(i)) shows the image of SSM0 sample taken at 5.0 KX magnification and it is conspicuous from the same figure that, particles are agglomerated and non-uniformly distributed. Fig. 3.2(a(ii)) & 3.2(a(iii)) show the images recorded for the same sample with a magnification of 10.0 KX and 35.0 KX respectively. Fig. 3.2(a(ii)) show flowery morphology with some rod like fibrous structure and such rod like shape appears relatively clear in Fig. 3.2(a(iii)). Particle size for SSM0 sample lies in the range of 5-7 µm. Fig. 3.2(b(i)) and 3.2(c(i)) are the SEM images recorded for SGM0 and CMM0 samples respectively with 5.0 KX

magnification and illustrate that cluster formation is more for CMM0 sample as compared to the SGM0. Due to more aggregation in CMM0 sample, they can absorb more excitation energy and useful in showcasing relatively high luminescence [30]. Fig. 3.2(b(ii)) and 3.2(c(ii)) are the images recorded for SGM0 and CMM0 samples with 10.0 KX magnification and illustrate that the particles are non-uniform in size and shape in SGM0 sample. In case of CMM0 sample, the particles attain dumbbell like shape with a uniform size. Fig. 3.2(b(iii)) and 3.2(c(iii)) are the SEM images pertaining to SGM0 and CMM0 samples respectively with 35.0 KX magnification. In the SEM image of SGM0 sample, the particles are appearing with some elongation in a particular direction. On the other hand, the SEM image of CMM0 sample show the particles distributed uniformly with relatively better morphology and useful in enhancing its luminescence performance. This difference in morphology may be due to the difference in reaction essence with varying the synthesis method [31]. The aforementioned SEM analysis performed for BMT sample synthesized by using different techniques allows us to contemplate that, the morphology of the particles is improving gradually from SSM to CMM synthesis route via SGM method. The particle size for SGM0 and CMM0 samples lie in the range of 3-4μm and 1-2μm respectively. Fig. 3.3 shows the SEM images and EDAX spectra for doped samples. Fig. 3.3(a.1), 3.3(b.1) and 3.3(c.1) shows the morphology of SSM1, SGM1 and CMM1 phosphors and Fig. 3.3(a.2), 3.3(b.2) and 3.3(c.2) manifests all the constituent elements present in the phosphor lattice [19,32]. The particle size for all the BMT samples prepared by using three different techniques are in micro meter range and quite suitable for coating in w-LEDs and other display devices [33,34].

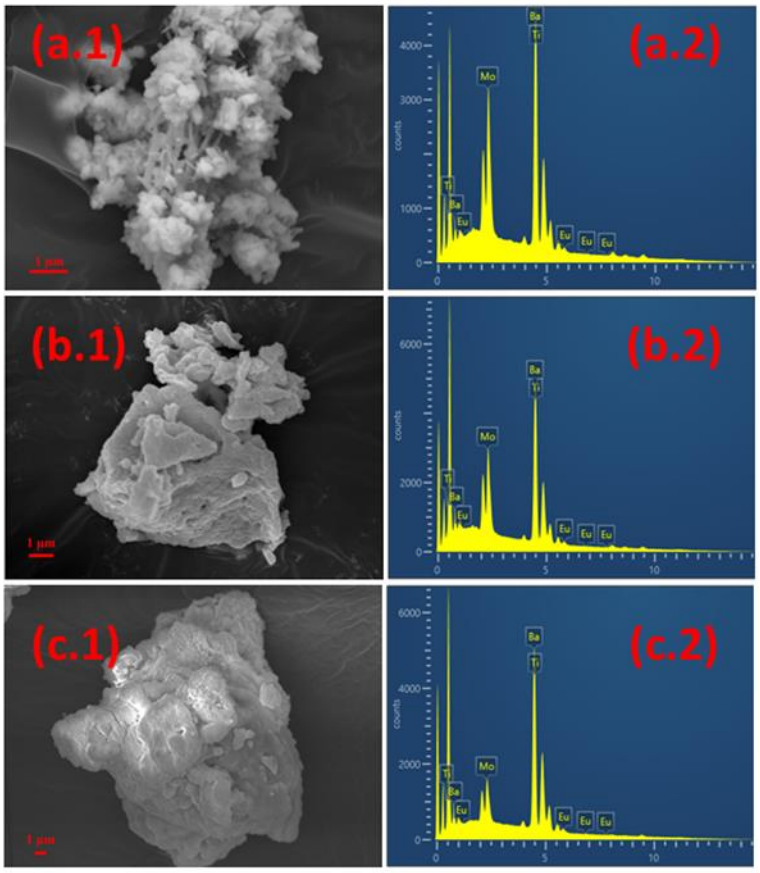

Fig. 3.3. SEM images for doped samples (a.1) SSM1 (b.1) SGM1 (c.1) CMM1 and EDAX Spectra for doped BMT phosphor (a.2) SSM1 (b.2) SGM1 (c.2) CMM1.

3.4.3. Raman spectral analysis:

In the process of knowing the information pertaining to different vibrational modes present in the as synthesized BMT samples, the Raman spectra was recorded for BMT phosphors synthesized by different techniques under 488nm excitation. Fig. 3.4 manifests the different Raman vibrational peaks observed for BMT sample prepared by different methods at wavenumbers 326, 526, 792, 841, 892 and 1042 cm^{-1}.

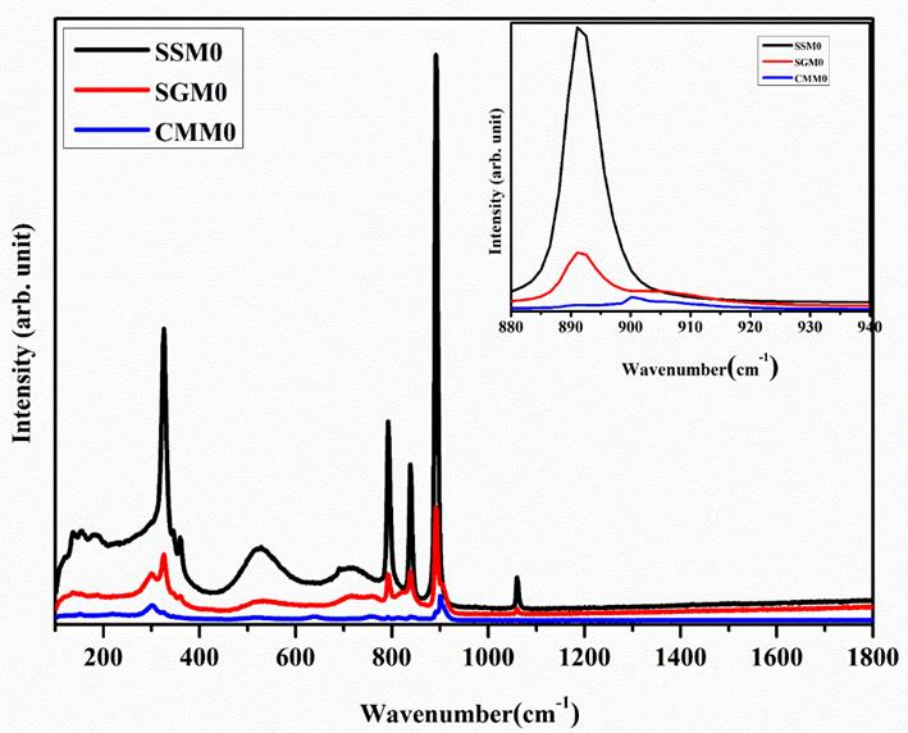

Fig. 3.4. Raman spectra of SSM0, SGM0 and CMM0 sample.

The band at 326 cm^{-1} describes the bending vibration modes of Mo-O bonds and the band observed at 526 cm^{-1} (between the range 450-600 cm^{-1}) belongs to the bond vibrations between Ti and oxygen atoms [35,36]. Vibrational bonds present at 792 and 841 cm^{-1} are in good agreement with anti-symmetric stretching bonds with tetrahedral O-Mo-O molecules [37,38]. Most intense peak observed at 892 cm^{-1} corresponding to the phonon energy of the as prepared compound. It is well known that a host lattice with relatively less phonon energy gives emission more in radiative form than non-radiative. The phonon energy observed for this lattice is relatively low when we compared with the phosphors reported earlier [35,39,40]. Fig.3.4 represents the comparison of Raman spectra observed for SSM0, SGM0 and CMM0 samples. Among all the three samples prepared by using three different methods, a sample prepared by CMM method show relatively intense PL when compared with the other methods. As the

particle size decreases from solid state to combustion method, shifting in Raman peaks are observed towards higher wavenumber side (as shown in inset of Fig. 5) and intensity of the peaks decreased gradually [41].

3.4.4. Diffuse Reflectance Spectra (DRS) analysis for band gap measurement:

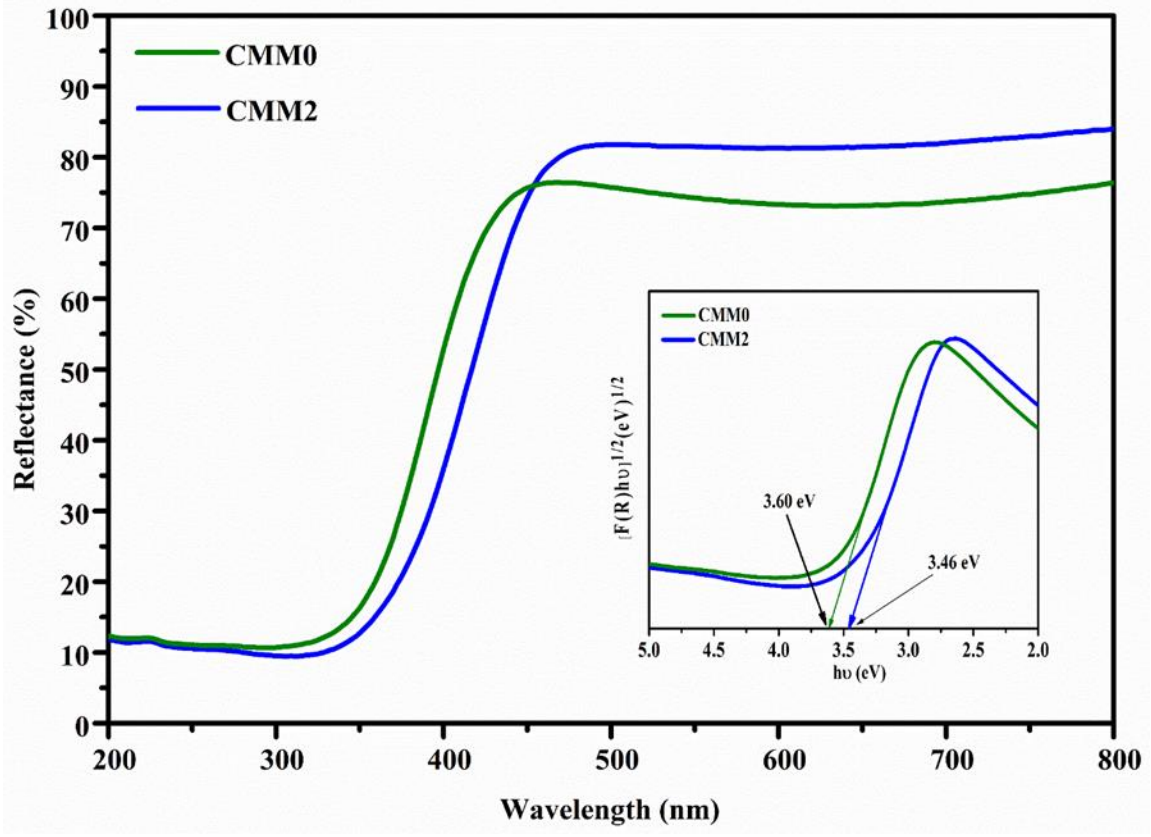

Fig. 3.5. Diffuse Reflectance Spectrum of CMM0 and CMM2 sample. Inset image shows the assessment of direct band gap using Kubelka- Munk plot.

Fig. 3.5 displays the DRS of CMM0 and CMM2 phosphor recorded in the range 200-800 nm. To find out the optical band gap the DRS spectral data was converted into the Kubelka–Munk function using the following equation (16), (17) and (18) described in chapter 2:

To calculate the band gap of the aforementioned mentioned phosphors (CMM0 and CMM2), a graph has been plotted between the $[F(R)h\upsilon]^{1/2}$ and hυ as shown in inset of Fig. 3.5 [42,43].

Direct band gap for CMM0 and CMM2 was found to be 3.60 and 3.46 eV respectively by extrapolating the slope as shown in the inset of Fig. 6.

3.4.5. PL excitation and emission spectral studies:

To study the luminescent properties of europium doped BMT phosphors, PL spectral features were investigated at room temperature. PL excitation spectra of BMT phosphors with 1 mol% of Eu^{3+} ions (prepared by different synthesizing techniques) are shown in Fig.3.6 The spectra were recorded in the wavelength range 260-500 nm.

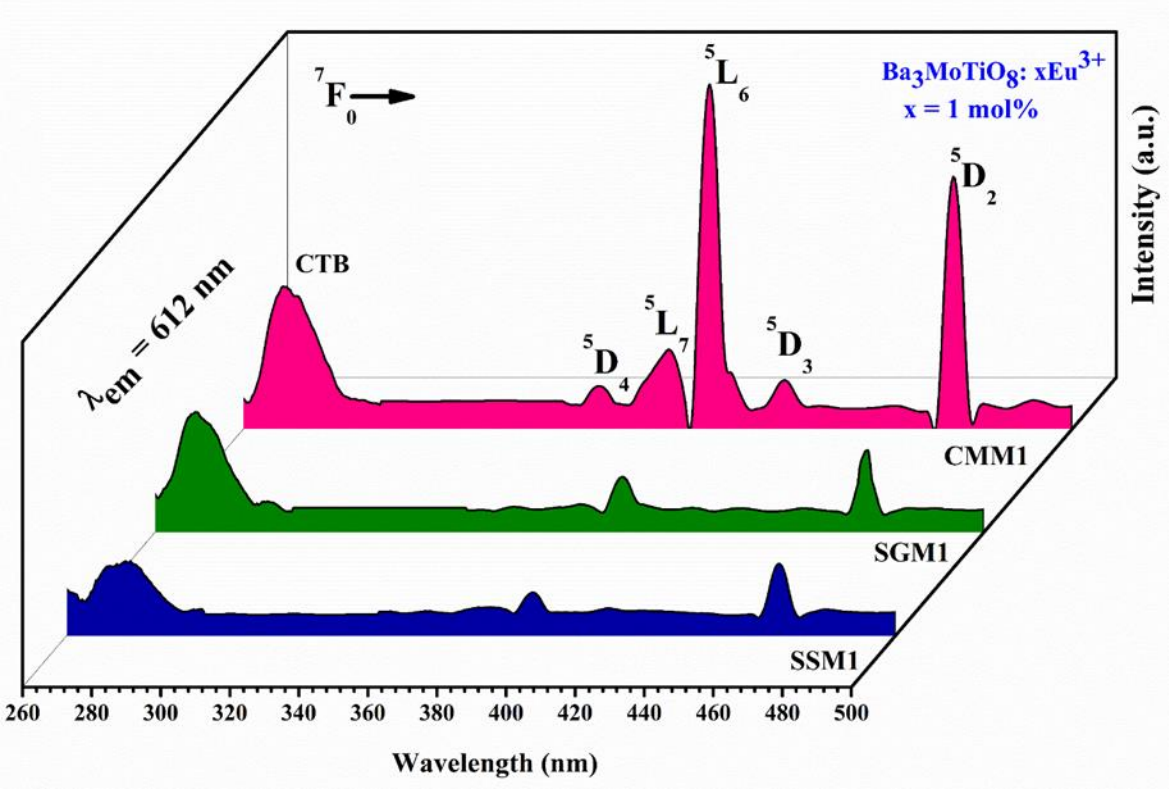

Fig. 3.6. Excitation spectra of SSM1, SGM1 and CMM1 phosphor with 1 mol% Eu^{3+} ion at 612 nm emission wavelength.

The spectra comprise of one broad charge transfer band (CTB) between the range 260-290 nm and several peaks in the region between 350-500 nm at wavelengths 360, 381, 393, 414, 465 nm and the transitions corresponding to these peaks are $^7F_0 \rightarrow {}^5D_4$, $^7F_0 \rightarrow {}^5L_7$, $^7F_0 \rightarrow {}^5L_6$, $^7F_0 \rightarrow {}^5D_3$, $^7F_0 \rightarrow {}^5D_2$ respectively. CTB is in agreement due to the transition from 2p orbital of O^{2-} to the

empty 4f shell of the Eu^{3+} ion[44]. Out of these peaks, two main peaks of comparatively high intensity are present at wavelengths 393nm and 465nm and were used as an excitation wavelength to record the PL emission spectra. The PL emission spectra has been recorded for 1 mol% Eu^{3+} doped samples (SSM1, SGM1, CMM1) under 393 and 465 nm excitation wavelengths. For comparison purpose, the PL emission spectra recorded under the two intense excitation wavelengths are shown in Fig. 3.7(a) (under 393 nm excitation) and Fig. 3.7(b) (under 465 nm excitation) between the region 550-750 nm.

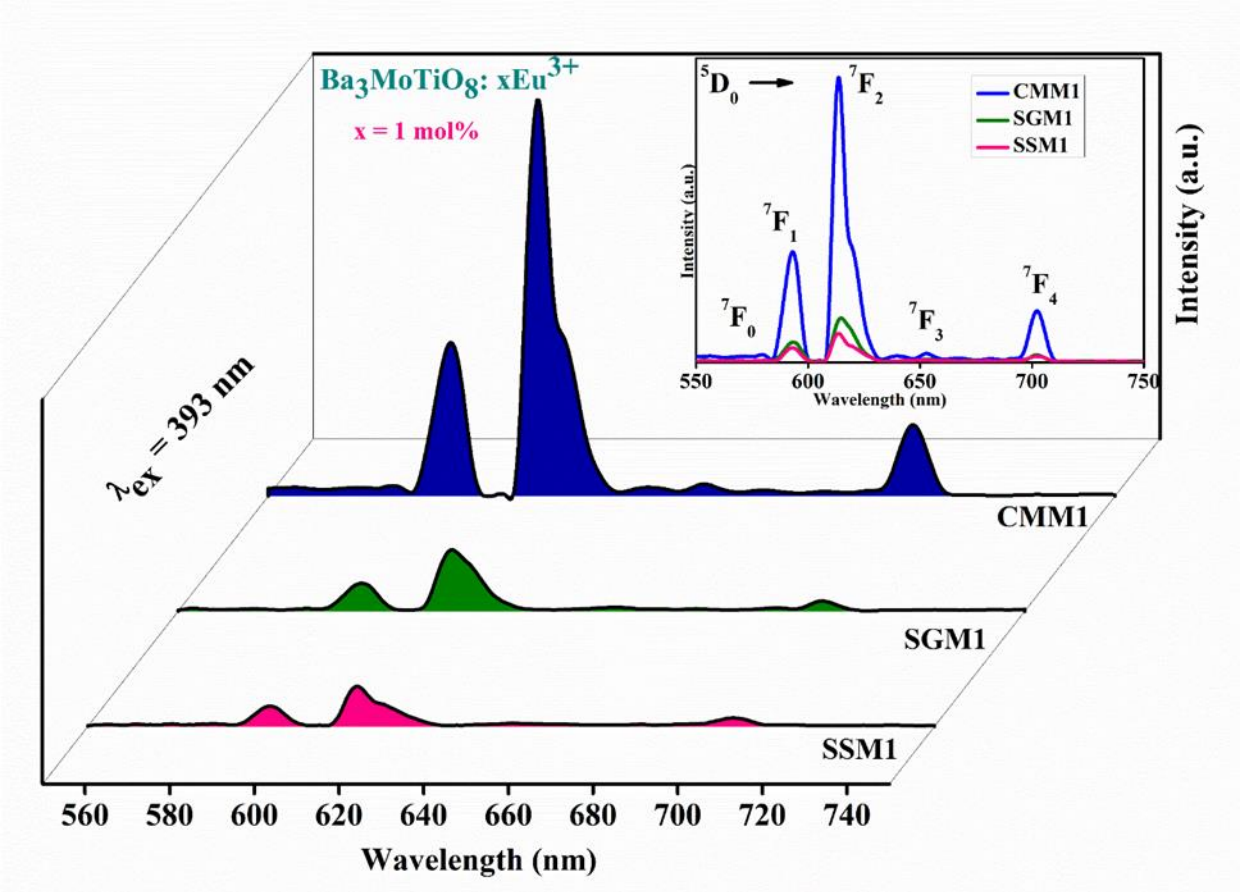

Fig. 3.7(a). Emission spectra of SSM1, SGM1 and CMM1 phosphor with 1 mol% Eu^{3+} ion at 393 nm excitation wavelength.

These two PL emission spectra comprises same peaks at wavelengths 582, 593, 612, 658 and 704 nm accompanying the transitions $^5D_0 \rightarrow {}^7F_0$, $^5D_0 \rightarrow {}^7F_1$, $^5D_0 \rightarrow {}^7F_2$, $^5D_0 \rightarrow {}^7F_3$ and $^5D_0 \rightarrow {}^7F_4$

respectively [45–47]. A comprehensive analysis of both the figures (Fig. 3.7(a) & 3.7(b) allows us to contemplate that, the BMT phosphor prepared by employing combustion technique is yielding good luminescence when compared with the remaining two techniques. Relatively high luminescence intensity in case of CMM1 sample may be due to the improved morphology and smaller size particles that can be seen from the SEM images. Particles with relatively smaller in size can minimize scattering and yields relatively intense luminescence [48]. Low luminescence intensity in case of SSM synthesized sample may be due to high agglomeration in particles due to which luminescence intensity decreased.

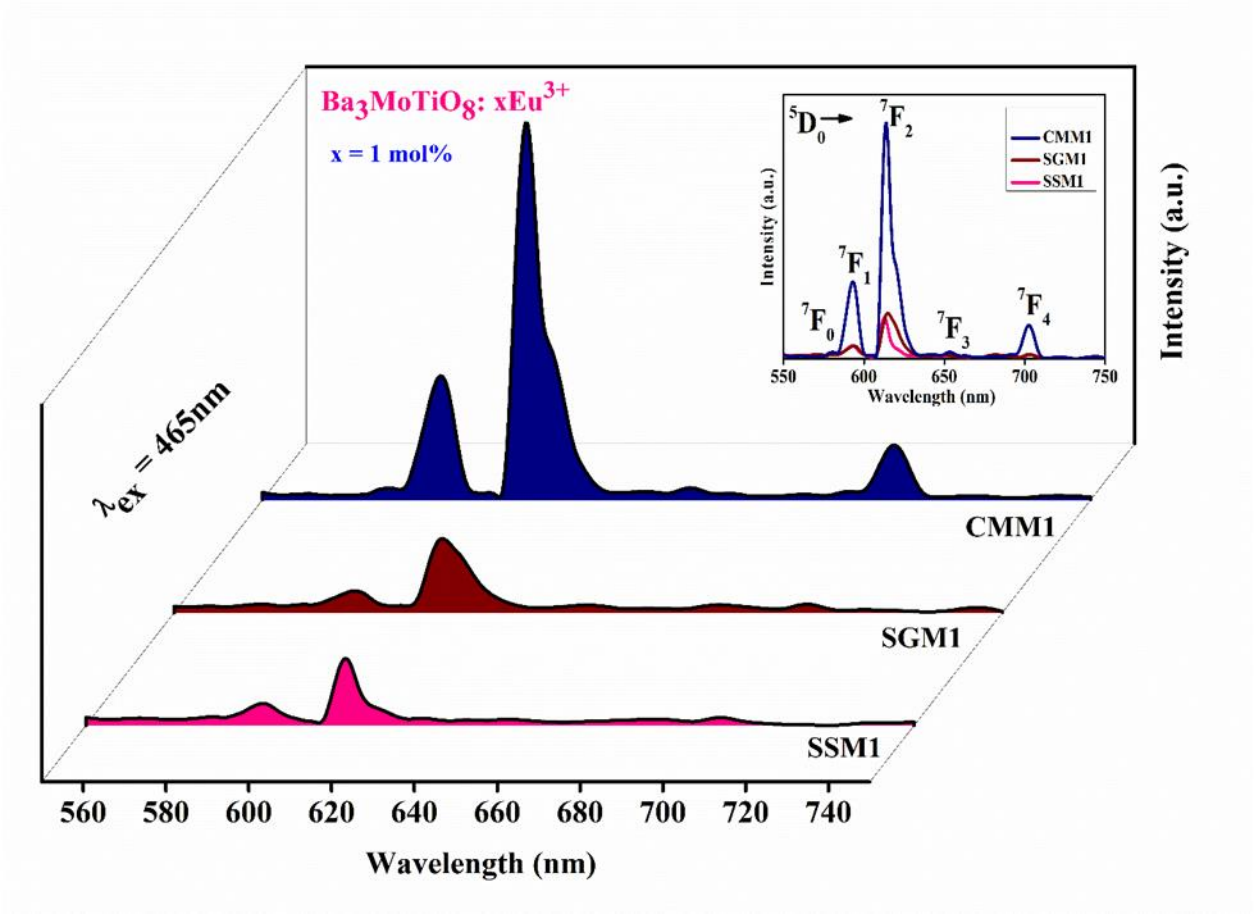

Fig. 3.7(b). Emission spectra of SSM1, SGM1 and CMM1 phosphor with 1 mol% Eu^{3+} ion at 465 nm excitation wavelength.

So, on that behalf it is contemplated that, CMM technique is the optimized one among the three techniques used to prepare BMT: Eu^{3+} phosphor.

Fig. S2 shows the comparative emission spectra recorded for CMM1 sample at different excitation wavelength 393nm and 465nm. Spectra recorded at 393 nm showed a little higher intensity as compared to 465 nm. Intense luminescence possessed by BMT: xEu^{3+} phosphor under 393 nm excitation wavelength promotes its usage in visible red photonic device applications under n-UV LED/blue LED excitation sources.

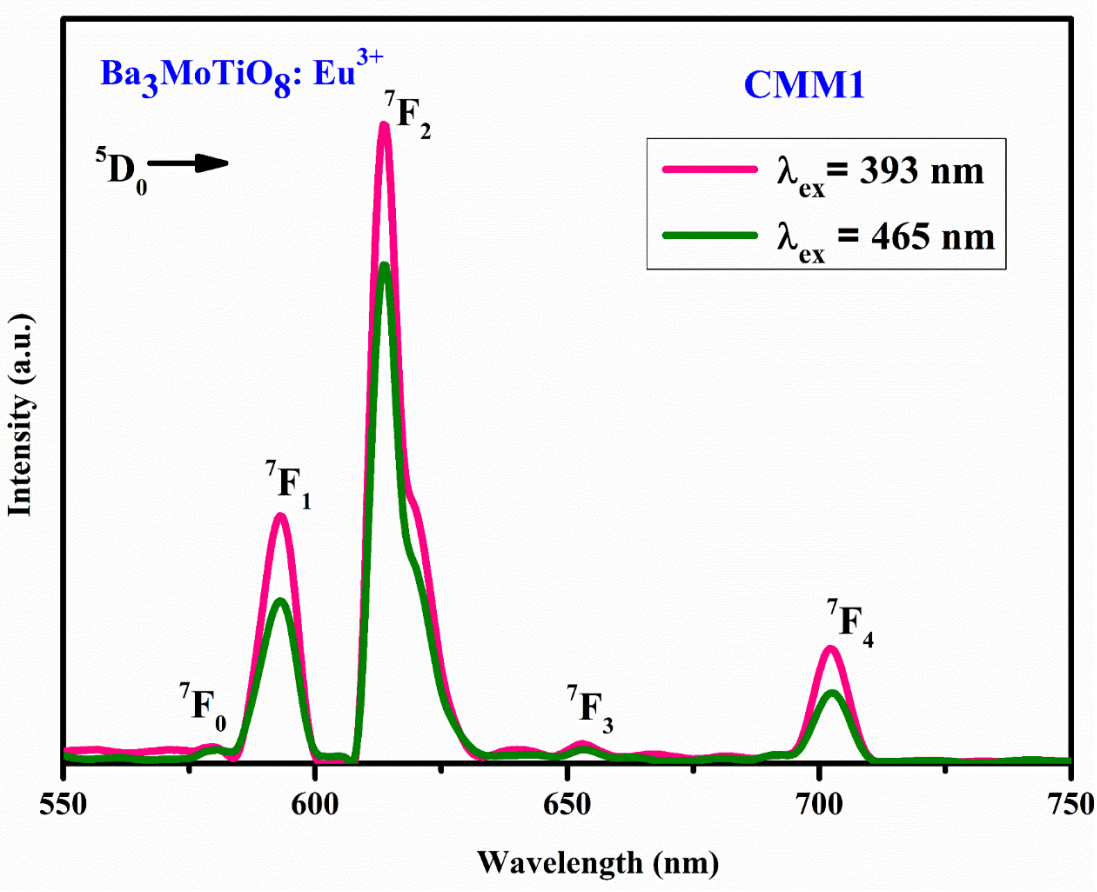

Fig. S2. Emission spectra of CMM1 phosphor with 1 mol% Eu^{3+} ion at 393nm and 465 nm excitation wavelength.

Relatively higher luminescence exhibited by BMT phosphor prepared by using CMM technique prompted us to prepare a series of europium ion doped BMT: xEu^{3+} phosphors (x=

1, 2, 3, 4 mol%) using the CMM technique for the optimization of the doped RE ion concentration for better luminescence. Emission spectra was recorded for this CMM synthesized series to check the optimized concentration of activator ion. Spectra was recorded between the wavelength range 550-750 nm by taking the excitation wavelength as 393 nm and 465nm. All the peak positions and transitions are same as mentioned above and there is no shifting in the peaks by changing the excitation wavelength. For both excitation wavelengths, highest luminescence intensity was observed for x = 2 mol% concentration of Europium ion. Beyond 2 mol% of europium ion concentration, the PL intensity decreases for both the cases as shown in Fig. 3.8(a) and Fig. 3.8(b).

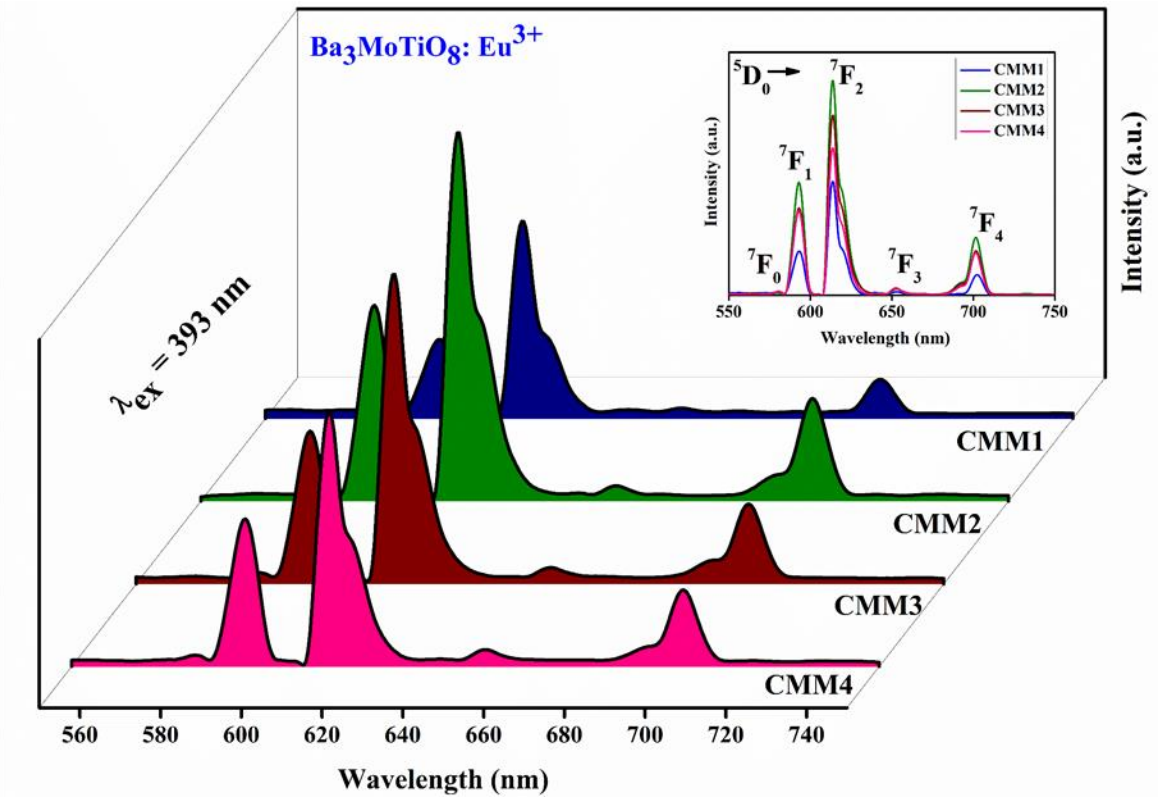

Fig. 3.8(a). Emission spectra of CMM synthesized BMT: xEu^{3+} (x=1, 2, 3 and 4 mol%) phosphor at 393 nm excitation wavelength.

This may be due to concentration quenching produced by a non-radiative energy transfer took place between the activator ions. Therefore, it is concluded that 2 mol% of europium ion concentration is optimum in BMT phosphor to showcase relatively intense luminescence.

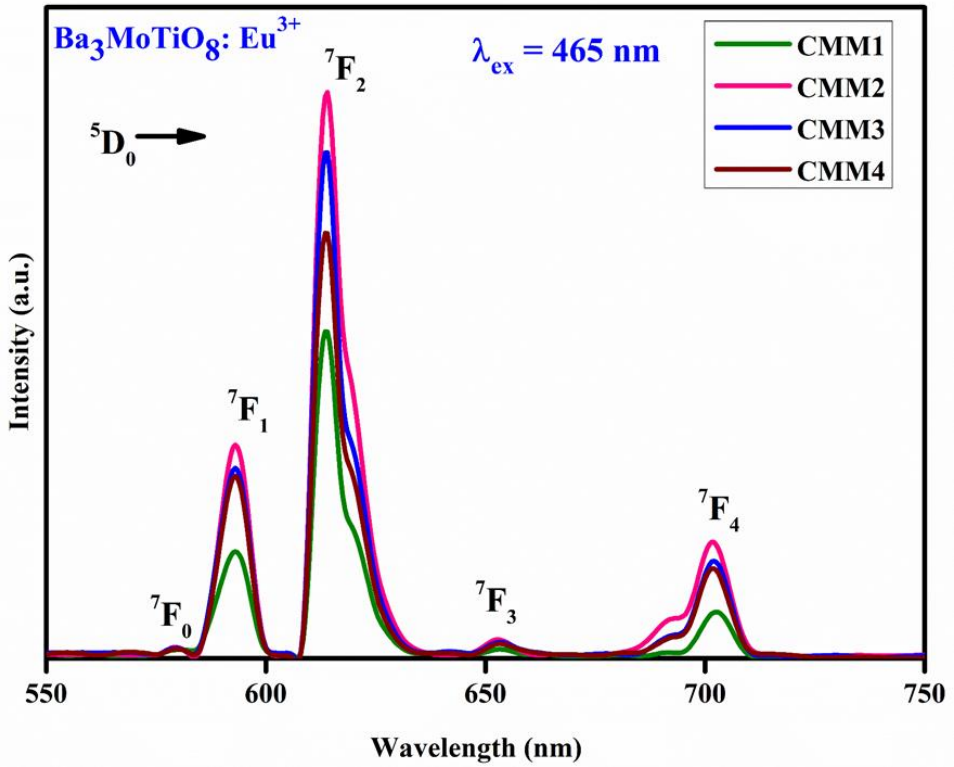

Fig. 3.8(b). Emission spectra of CMM synthesized BMT: xEu^{3+} (x=1, 2, 3 and 4 mol%) phosphors at 465 nm excitation wavelength.

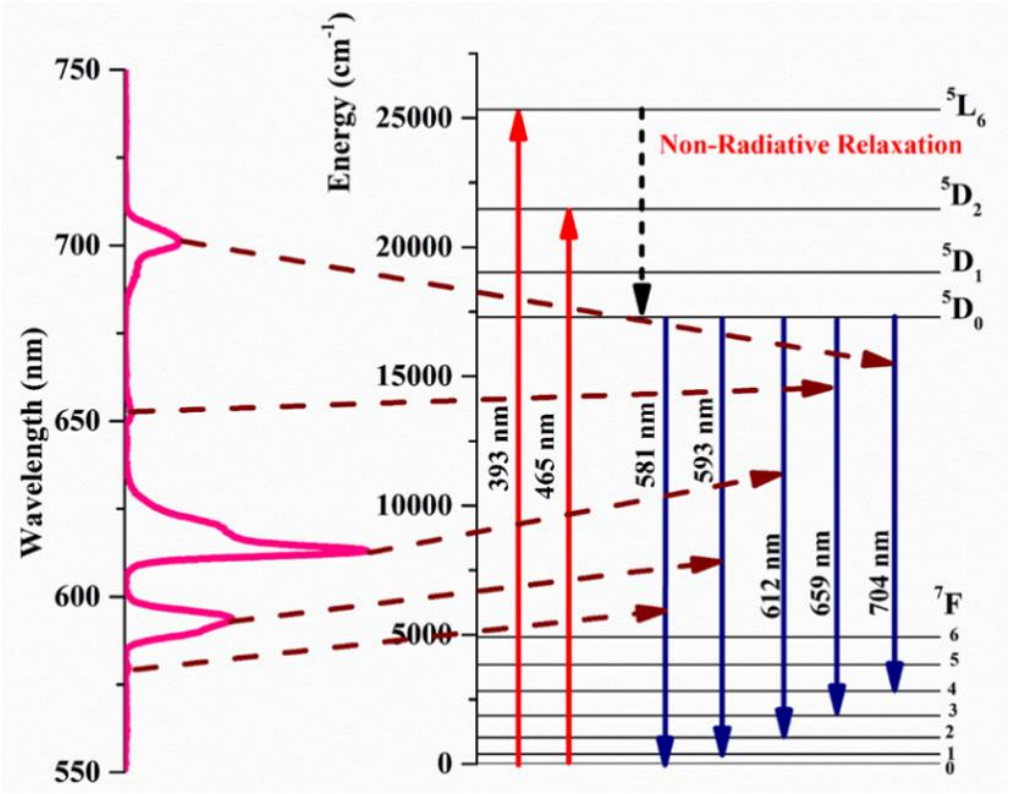

Fig. 3.9. Energy level diagram for various transitions in europium ion.

An energy level diagram has been made to show various transitions of excitation and emission spectra and is shown in Fig.3.9. For the non-radiative relaxation three mechanisms are responsible like radiative re-absorption, exchange interaction and electric multipolar interaction between the activator ions. Critical distance R_c is the average shortest distance on which energy transfer depends between activator ions. To find out the critical distance (distance between two neighbouring ions) the following formula is used [49].

$$R_C = 2[3V/(4\Pi X_C N)]^{1/3} \quad (19)$$

Where X_C is mol concentration of activator ion at which quenching took place. Here X_C=0.02 (2 mol%), V is the volume of unit cell and N is number of cations per unit cell. For this case- V=654.28Å^3, N=3, and Xc = 0.02. The average critical distance calculated by using these

values is 27.51Å which is very large when compared to 5Å designated for exchange interaction. This allows us to contemplate that, exchange interaction is not responsible for energy transfer. This made us to apply Dexter theory further to check the type of multipolar interaction responsible for energy transfer.

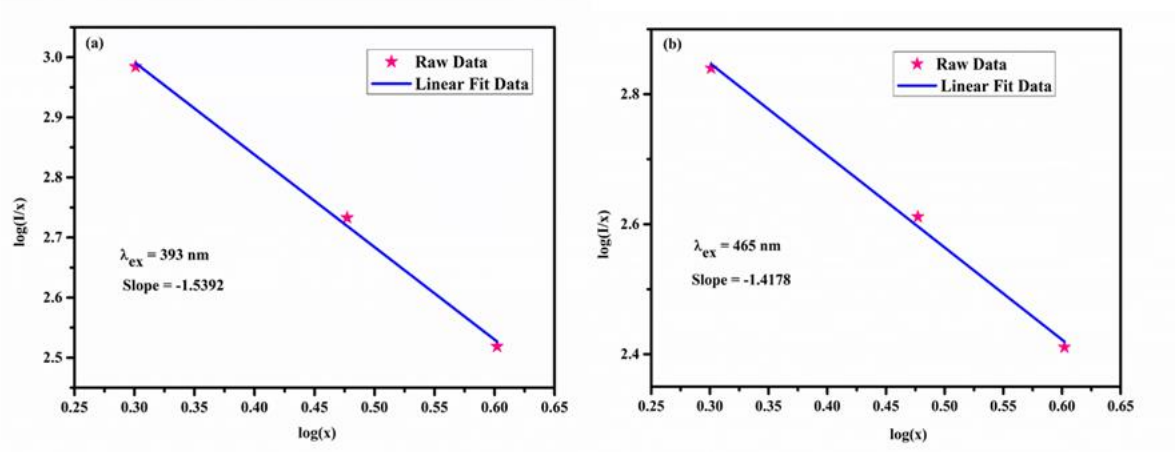

Fig. 3.10. Dexter Plot of log (I/x) vs. log (x), (a) under 393 nm (b) under 465 nm, excitation wavelengths.

The relation between emission intensities and doping concentration is given as [42,50]-

$$I/x = K\,[1+\beta(x)^{Q/3}]^{-1} \qquad (20)$$

Here x is the mole concentration of europium ion, Q determines the type of interaction (Q=6, 8 and 10 are corresponding to electric dipole-dipole interaction, dipole-quadrupole interaction and quadrupole - quadrupole interaction respectively), I is luminous intensity, K and β are constants. According to Huang's theory, relation between luminous intensity and mole fraction of activator ions is given as [51]-

$$log\frac{I}{x} = A - \frac{Q log x}{3} \qquad (21)$$

where A is independent of doping concentration. Fig. 3.10(a) and 3.10(b) shows the graph between log (I/x) and log(x) using Dexter theory under 393 nm and 465 nm excitation wavelength. The Q value estimated from the slope of the graph was found out 4.617 and 4.253 which are close to 6 indicating electric dipole-dipole interaction as the responsible mechanism for energy transfer and the subsequently observed concentration quenching effect.

3.4.6. Colorimetric analysis:

Commission Internationale de I'Eclairage was used to find out the colorimetric performance of BMT: Eu^{3+} phosphor by using the emission spectral date recorded under 393 nm and 465 nm excitation wavelength. The CIE coordinates calculated for CMM synthesized BMT: xEu^{3+} phosphor (x= 1, 2, 3, 4 mol%) were depicted in Table 3.2. The CIE coordinates of CMM synthesized BMT: xEu^{3+} phosphor is falling in pure red region as shown in Fig. 3.11(a) and 3.11(b).

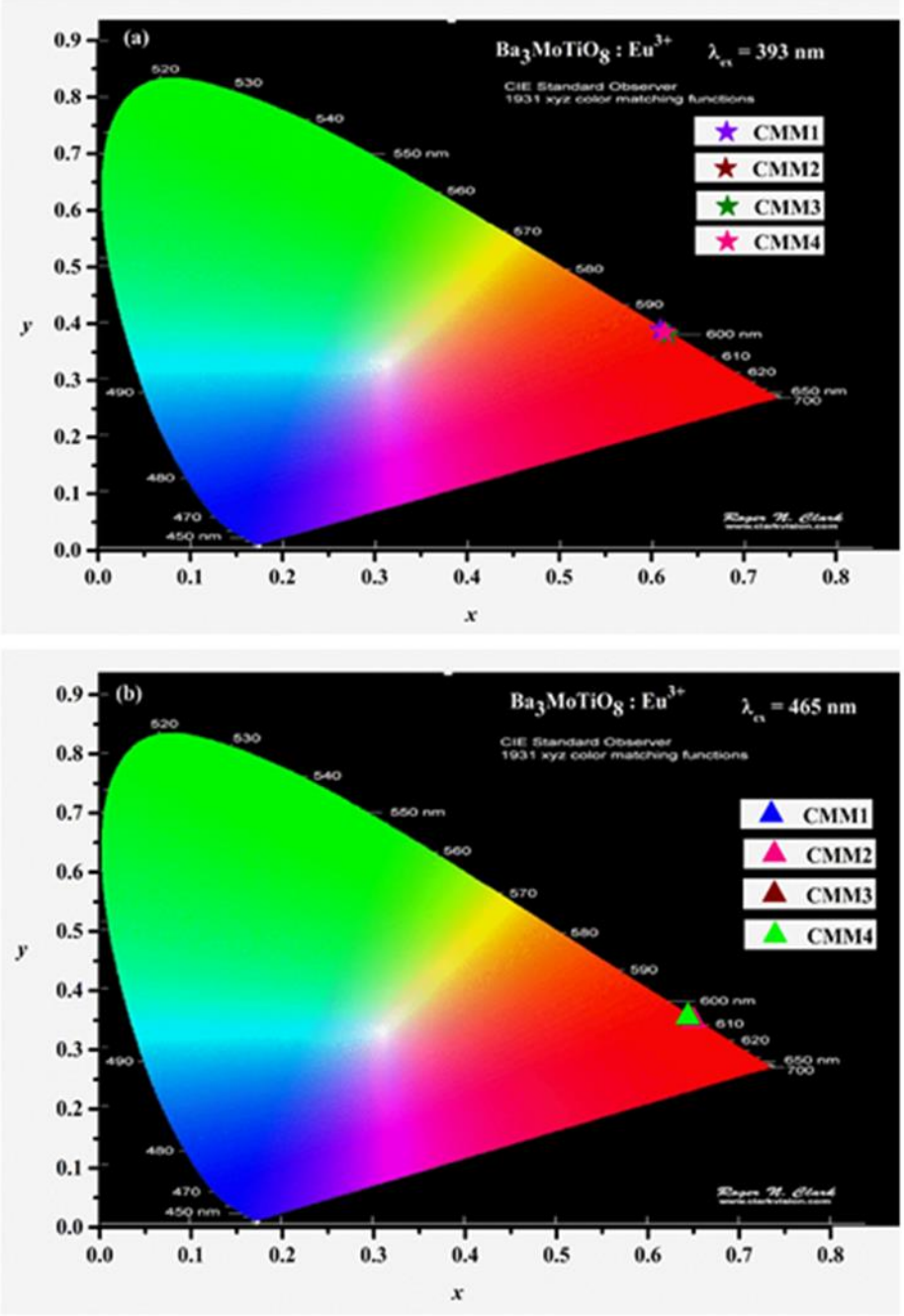

Fig. 3.11. CIE chromaticity diagram of BMT: xEu^{3+} (x= 1, 2, 3, 4 mol%) phosphors synthesized by CMM method, under the excitation wavelength of (a) 393 nm (b) 465 nm.

The correlated colour temperature (CCT) was calculated using the McCamy empirical theoretical equation (8) given in chapter 1 [52,53]:

The CCT values determined for BMT phosphor were 1756.17, 1827.94, 1822.68, 1791.86 K for the PL spectra recorded under 393 nm excitation wavelength and for 465 nm excitation wavelength were 2410.72, 2582.46, 2415.68 and 2357.34 K corresponding to 1.0, 2.0, 3.0 and 4.0 mol% of Eu^{3+} ion concentration, respectively. This allows us to authenticate the superior nature of BMT: xEu^{3+} phosphor for intense red emission required for the fabricating w-LEDs.

Table 3.2. CIE Coordinates for BMT phosphors prepared by CMM technique

Sample	CIE Co-ordinates (x, y) Under 393 nm excitation	CIE Co-ordinates (x, y) Under 465 nm excitation
CMM1	(0.6097, 0.3895)	(0.6454, 0.3542)
CMM2	(0.6182, 0.3811)	(0.6501, 0.3495)
CMM3	(0.6178, 0.3816)	(0.6455, 0.3540)
CMM4	(0.6146, 0.3847)	(0.6438, 0.3558)

3.4.7. PL decay analysis:

PL decay measurements were carried on combustion synthesized BMT: xEu^{3+} phosphor (x= 1, 2, 3, 4 mol%) for 612 nm red emission under 393 nm excitation and is shown in Fig. 13. From Fig. 3.12 it is conspicuous that, all the decay curves recorded are showing non-linear bi-exponential behaviour and obeys the following by-exponential equation (12) given in chapter 1 [47,54]:

Then, the average experimental lifetime was calculated by using the expression:

$$\tau = (A_1\tau_1^2 + A_2\,\tau_2^2) / (A_1\tau_1 + A_2\,\tau_2) \qquad (22)$$

The average experimental lifetime values are found be 1.89, 1.77, 1.55 and 1.35 ms, for CMM1, CMM2, CMM3 and CMM4 phosphors respectively [55]. These results showed that, with increase in the concentration of europium, experimental decay times are decreasing. This happened because of increase in non- radiative recombination resulting in energy transfer between the activator ions itself [55–57].

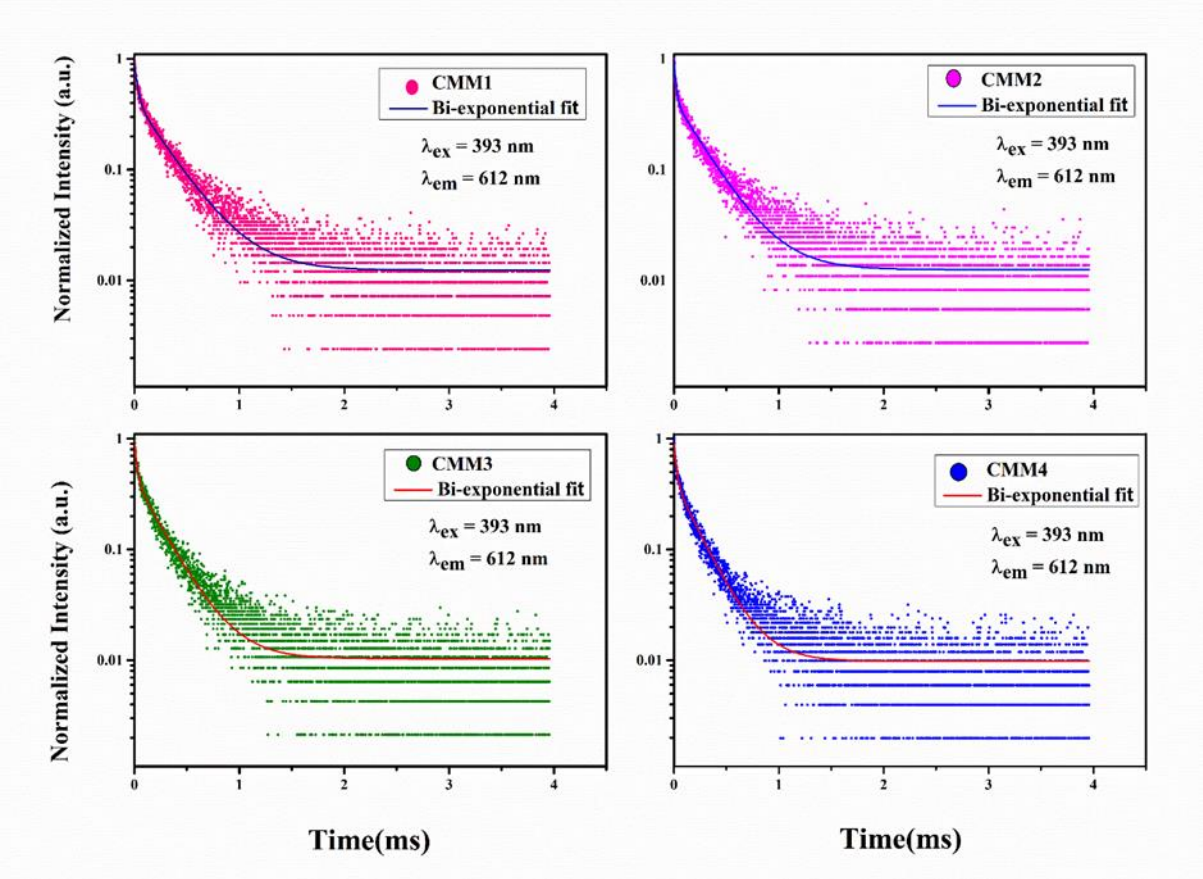

Fig. 3.12. Decay profile of Eu^{3+} ions doped BMT phosphors synthesized by CMM route.

3.5. Conclusions

BMT: xEu^{3+} phosphor was successfully synthesized by three different methods- Solid state, Sol-gel and Combustion method. A comparative Raman Analysis was also carried out for undoped samples of three techniques which shows that by varying the synthesis route, peaks position shifts toward higher wavenumber side and this happens because the decrease in

particle size when we go from SSM technique to SGM and then to CMM. The XRD pattern confirmed the phase and crystallinity of all the samples. Comparison of morphology was done by SEM micrographs. In case of combustion synthesized samples, morphology of particles gets improved, and this improved morphology enhances the luminescence intensity as evident from the PL spectra. A comparative PL spectrum recorded for 1 mol% europium ion doped BMT phosphor prepared by using SSM, SGM and CMM techniques demonstrates the superiority of CMM technique in showcasing relatively intense red emission. This prompted to have further investigations on a BMT phosphor prepared by CMM technique with different concentrations of europium. All the BMT phosphors prepared by CMM techniques are displaying red emission under 393 and 464nm as excitation wavelengths. This has been further confirmed by CIE chromaticity diagram also. And lastly, time decay analysis was carried out which shows that 2 mol% is the optimum concentration of Europium ion for combustion synthesized series and after that energy transfer take place between the activator ions itself through dipole-dipole interaction which can be confirmed from the Dexter theory. CIE points calculated for combustion synthesized samples lies in pure red region. So above results indicate that combustion method synthesized BMT phosphor can act as an efficient red phosphor in w-LEDs applications under n-UV or Blue radiation excitation.

CHAPTER 4

Linear and Non-linear Photoluminescence studies of Ho^{3+}/ Yb^{3+} Co-doped Titanate Phosphors for Photonic Applications

This work presents the morphological and PL studies of the single ion Ho^{3+} doped and Ho^{3+}/Yb^{3+} co-doped $Ba_{3-x-y}MoTiO_8:xHo^{3+}/yYb^{3+}$ phosphors synthesized by conventional solid-state reaction method. Phase confirmation of all the as-prepared samples was done by XRD patterns. The morphological behavior and vibrational frequency bands were studied by SEM and FT-IR techniques respectively. DRS has been recorded for the singly doped and co-doped samples to find out the optical bandgap. The linear and non-linear emission spectral studies under 448 and 980 nm excitation wavelengths respectively showed three bands in the green, red, and blue regions. A relatively more intense band observed in the green region under 980 nm excitation shows promising usage of the titled phosphor for non-linear applications. A plot drawn between non-linear luminescence emission intensity Vs pump power reveals the information pertaining to the number of photons involved in the process. In addition, CIE coordinates calculated from the emission spectral features lie in the green region. All the studies show the broad application of the as-prepared phosphors in linear and non-linear luminescence process-based green emitting diodes, display devices, security inks, phototherapy, and SSL applications.

The content of this chapter has been published in an international journal - **Journal of Alloys and Compounds, 928 (2022) 167156**.

4.1. Introduction

The RE doped materials are fascinating to the researchers due to their multifold applications in the field of solid-state lighting, bio-imaging, security inks, phototherapy, display devices, drug delivery, lasers, and many more via linear (down-conversion) and non-linear (up-conversion) processes [3,20,58]. Up-Conversion (UC) is the process in which absorption of two or more low-energy photons results in a single high-energy photon. In medical fields such as bio-imaging and drug delivery, conventionally organic dyes and quantum dots are used. However, the usage of organic dyes and quantum dots has pitfalls like photo bleaching, a weak signal to noise ratio and auto fluorescence. Moreover, for the aforementioned medical applications, organic dyes and quantum dots needs to be excited with high-energy UV radiation. Longer exposure of high-energy UV radiation damages the healthy tissues. So RE doped UC phosphors have more advantages over the traditional sources due to their high stokes shift, low cytotoxicity, high photo stability and low synthesis cost, etc. Recently, RE doped UC materials have been used in photocatalytic systems also [59,60]. In addition, if a material has the capability to convert the NIR radiation into visible light, then it can be used in security inks to hide a document for security purposes [61]. So these days, RE ions doped phosphors can be used as a substitute for these UC applications [19,62]. On the flip side, down-conversion (DC) is the reverse process of UC and a suitable host lattice doped with RE ions has various applications in SSL, plasma devices, lasers, optoelectronic devices etc. SSL technology is becoming the future generation demand in the field of illumination technology as conventional sources of energy like fossil fuels, incandescent and fluorescent lamps are very limited in quantity and have drawbacks like exhaustion of energy in the long run and unfriendly behaviour towards the environment. In comparison to other materials, RE doped phosphors

have advantages like photo stability, low production cost and ease of synthesis. These RE ions have good electronic and optical properties, wide emission range (UV-vis-NIR) [63–66]. So, pc-w-LEDs can emerge as an energy saving device for next generation with their higher luminous efficacy, longer lifetime and good optical performance.

In the present work, a series of Ho^{3+} ion doped phosphor and another series for Ho^{3+}/Yb^{3+} co-doped phosphors have been prepared to understand the suitability of BMT phosphor for green light emission. Relatively less phonon energy observed for the BMT phosphor (890 cm^{-1}) prompted us to explore the possible usage of this host for visible photonic device applications through DC and UC studies [67]. Here Yb^{3+} ion act as a suitable sensitizer as it has larger cross-section in the NIR region and no reabsorption process in the excited state which upgrades the light absorption and expands the population of activator ions by effective transfer of gathered energy. Ho^{3+} ion has more energy levels, longer excited state lifetime and visible emission in red and green region. However, Ho^{3+} ion is often selected as an activator ion in the study of UC materials as it has almost negligible UC efficiency on 980 nm excitation as a singly doped ion [68–72]. This BMT phosphor with doping of Ho^{3+} ion (as an activator) shows intense green emission under blue excitation (λ_{ex}= 448 nm) and can be used as a green emitting component in w-LEDs. Co-doping of Yb^{3+} ion (as a sensitizer) was done by optimizing the concentration of Ho^{3+} ion and then by varying the mol% concentration of sensitizer ion (Yb^{3+} ion).

4.2. Experimental

4.2.1. Sample preparation via solid-state reaction method:

A series of single Ho^{3+} ions doped and Ho^{3+}/Yb^{3+} co-doped BMT phosphors were prepared by the solid-state reaction method as discussed in section 2.2 of chapter 2. Flow chart of all the steps involved in the synthesis is shown in Fig. 2.1.

4.2.2 Characterization techniques used:

BMT sample has been characterized for thermo-gravimetric (TGA) and differential scanning calorimetry (DSC) analysis under Ar gas atmosphere at a heating rate of 10℃/min using the instrument Setaram labsys evo. For structural investigations, Bruker D8 Advanced Powder X-ray diffractometer has been used with Cu-Kα radiation (λ= 1.54 Å) under working voltage and tube current 40kV and 40mA respectively. To understand the morphological behaviour, SEM micrographs have been recorded using JEOL 7610F Plus machine. FT-IR spectra were recorded by using the Perkin Elmer spectrum 2 instrument. To investigate the down conversion PL spectra, Jasco FP-8300 spectrofluorometer has been used (Xe lamp as an excitation source) and for up-conversion PL, Horiba PTI Quanta Master equipped with 980 nm solid state laser has been employed. The UV-vis-NIR absorption spectra was recorded with Jasco V-770 Spectrophotometer. PL lifetime decay curves were recorded by using 150 MHz digital oscilloscope (HM 1507, Hameg Instruments).

4.3. Result and discussion

4.3.1. Structural measurements:

4.3.1.1.TGA and DSC analysis:

Fig. 4.1 shows the TGA and DSC analysis recorded for an un-doped BMT sample precursor ($BaCO_3$, TiO_2 and MoO_3) sintered from room temperature to 1100℃. DSC curve shows three endothermic peaks at 590, 810 and 918℃. The total weight loss (15.3%) of the sample was occurred into two stages. The first stage was between the temperature range 450-620℃. This weight loss of about 5.1% was because of the evaporation of water and decomposition of organic species such as acetone used during the synthesis. The first endothermic peak at 590℃ describes the same.

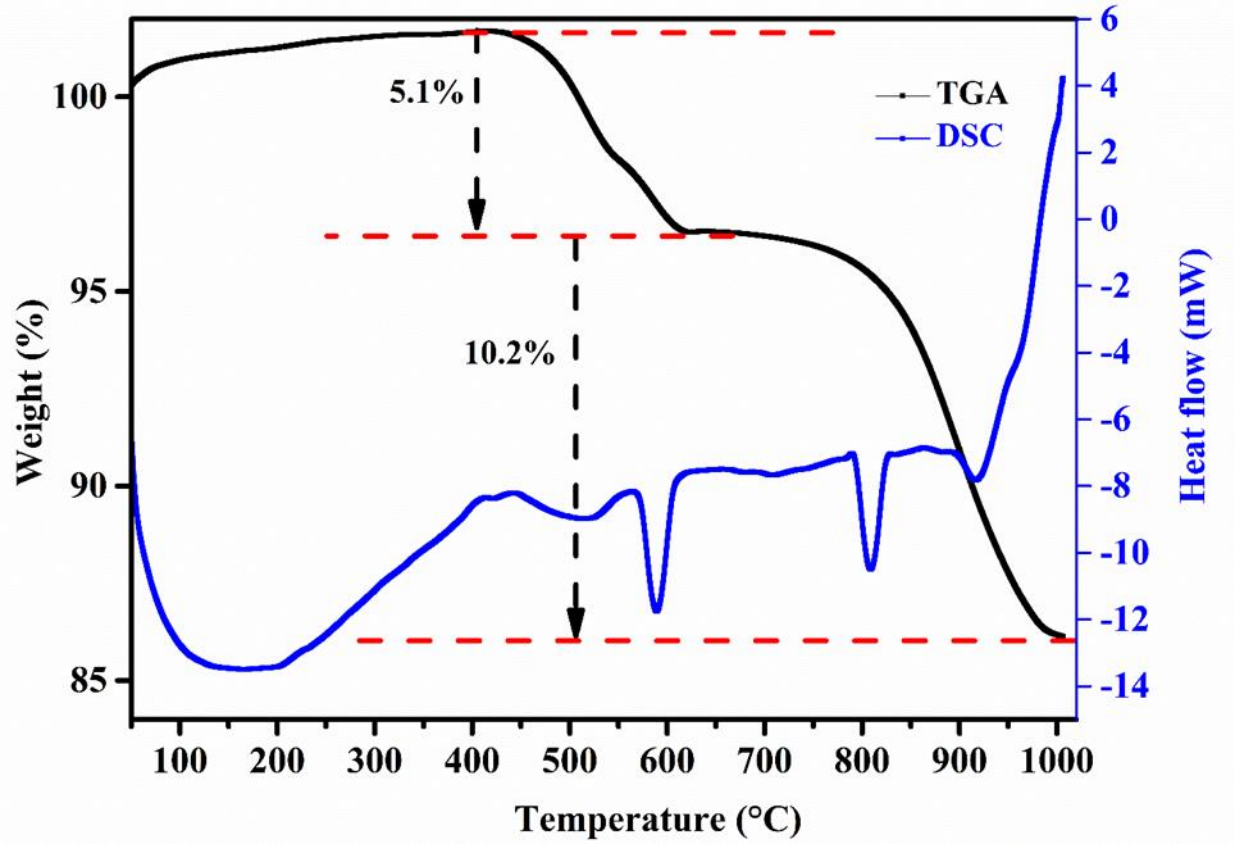

Fig. 4.1. TGA and DSC curves of an un-doped BMT sample.

The second weight loss of about 10.2% was observed in the temperature range 670-980℃ which may be due to degradation of CO_2 and H_2O molecules. After that weight loss curve tends to straight that means sample had enough weight loss and sample will go from amorphous nature to crystalline after that temperature. So the endothermic peak at 810℃ can be attributed to the melting and decomposition of carbonate and oxide precursors and the peak at 918℃ may be due to the phase transformation into crystalline form[55,73].

4.3.1.2. XRD measurements:

Fig. 4.2(a) represents the XRD patterns recorded for the un-doped BMT sample and Ho^{3+}/Yb^{3+} co-doped BMT phosphors. Diffraction peaks of all samples were found to be matching perfectly with the standard JCPDS file 38-0254 and no impure phase was recorded.

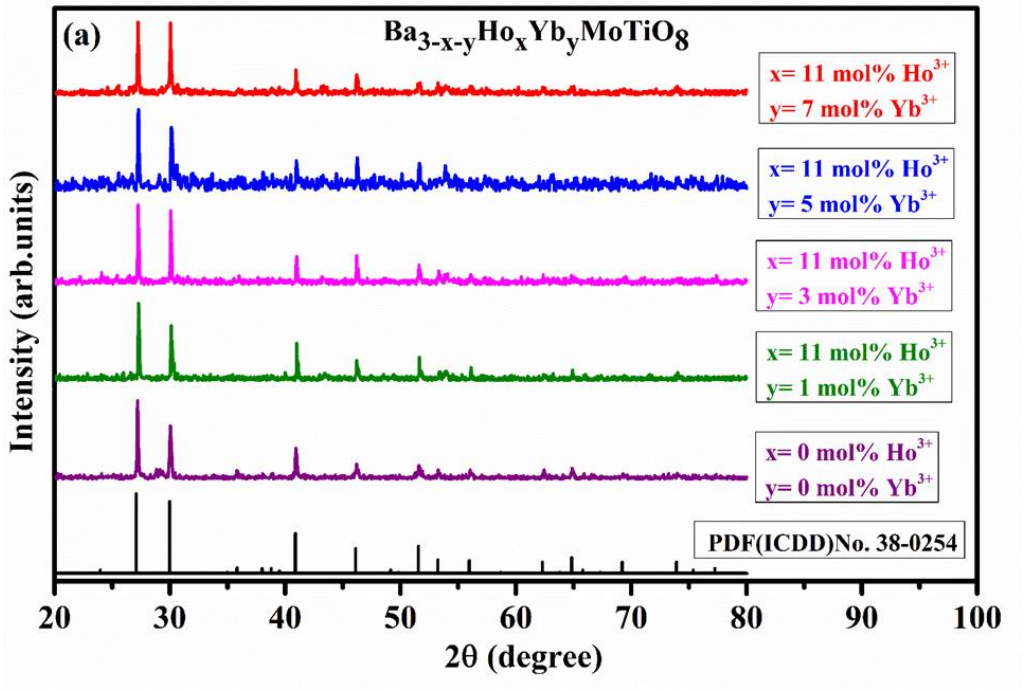
(a)
$Ba_{3-x-y}Ho_xYb_yMoTiO_8$
x= 11 mol% Ho^{3+}
y= 7 mol% Yb^{3+}
x= 11 mol% Ho^{3+}
y= 5 mol% Yb^{3+}
x= 11 mol% Ho^{3+}
y= 3 mol% Yb^{3+}
x= 11 mol% Ho^{3+}
y= 1 mol% Yb^{3+}
x= 0 mol% Ho^{3+}
y= 0 mol% Yb^{3+}
PDF(ICDD)No. 38-0254
Intensity (arb.units)
20 30 40 50 60 70 80 90 100
2θ (degree)

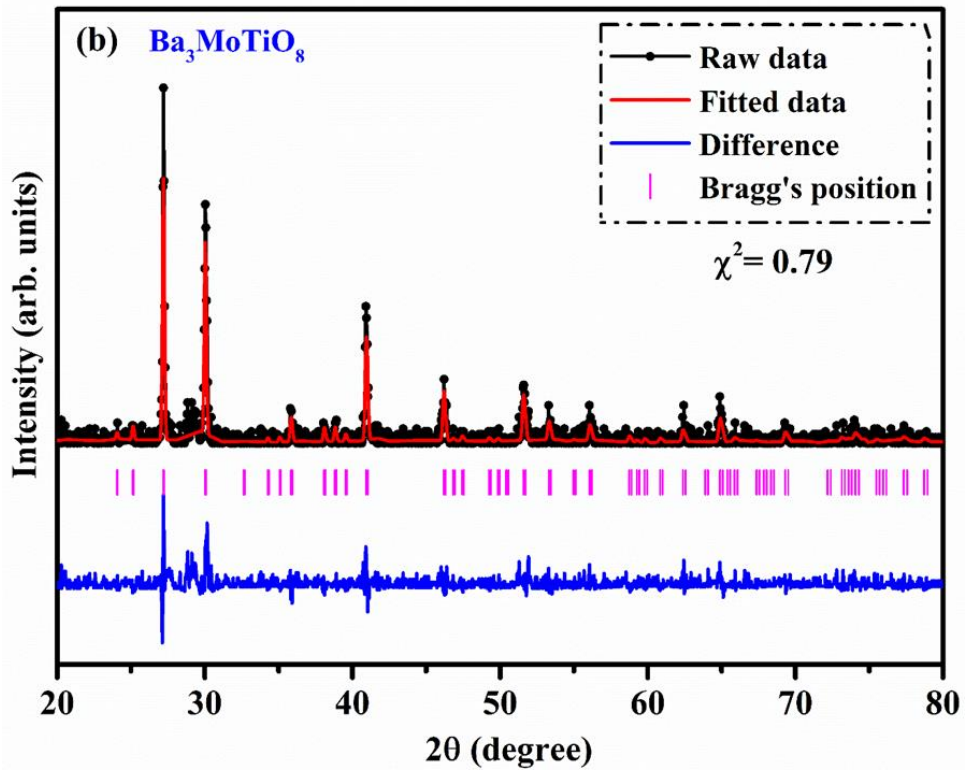
(b) Ba_3MoTiO_8
Raw data
Fitted data
Difference
Bragg's position
χ^2= 0.79
Intensity (arb. units)
20 30 40 50 60 70 80
2θ (degree)

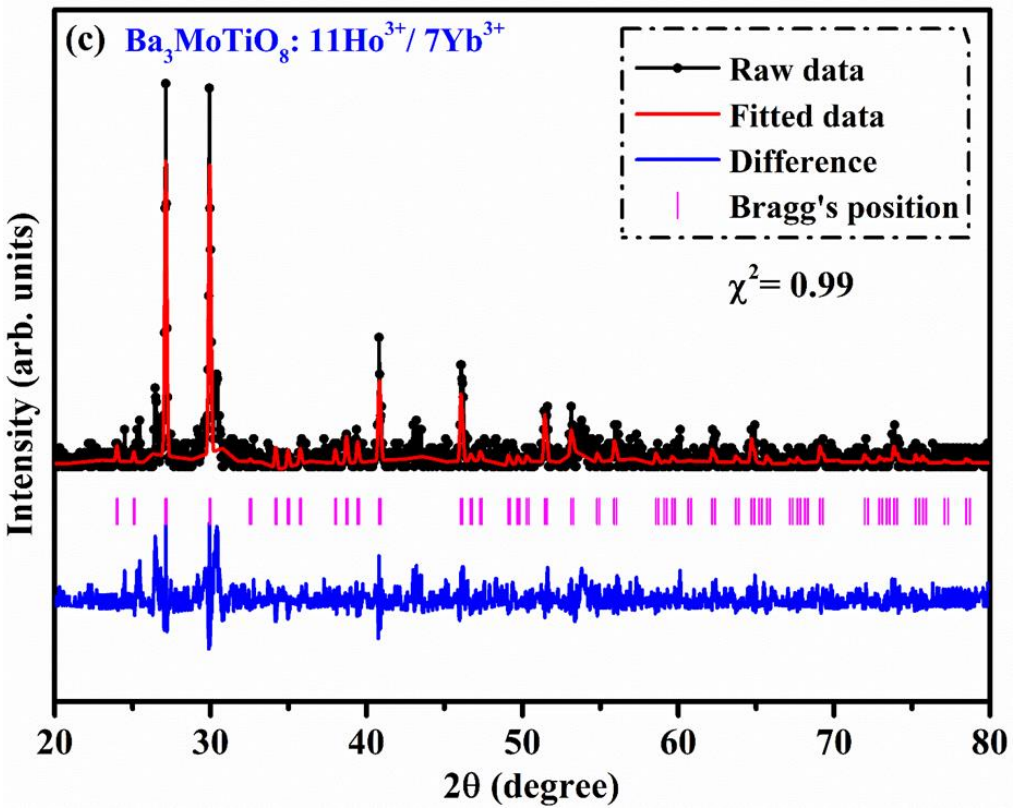

Fig. 4.2(a). XRD patterns of an un-doped BMT sample & co-doped $Ba_{3-x-y}MoTiO_8$**:**xHo^{3+}/yYb^{3+} (x=11mol% and y=1,3,5 and 7mol%) phosphors series with standard JCPDS data**. Fig. 4.2(b)** & **Fig. 4.2(c)** show reitveld refinement treatment recorded for an un-doped and co-doped BMT phosphor respectively.

This implied the single-phase formation of all the samples. This single-phase formation may be perhaps due to the exact matching of ionic radii of Ba^{2+} ions (1.49 Å) with Ho^{3+}(1.04 Å) and Yb^{3+} ions (1.01 Å) and replacement of Ba^{2+} ions with either Ho^{3+} and Yb^{3+} ions. The phase of BMT samples were found to be rhombohedral with a space group R-3m and space group number 166. Crystallographic axes and angles were provided to be a=5.95Å, b=5.95Å, c=21.29Å, α=90º, β=90º, γ=120º respectively. Average crystallite size of all the samples were calculated by using Debye-Scherrer equation (14) given in chapter 2. Average crystallite sizes for co-doped samples (Ho^{3+}/Yb^{3+}) using equation (14) were found to be in the range of 80-90 nm for 1, 3, 5 and 7 mol% concentration of Yb^{3+} ions respectively.

Fig.4.2 (b &c) shows the Rietveld refinement profile fitting of an un-doped BMT sample and BMT: xHo^{3+}/yYb^{3+} (x= 11mol%, y= 7mol%) phosphor by using FullProf suite software. The black solid line with dot and red line in the graph tells the raw and fitted data respectively. The blue line refers to the difference between raw and fitted data. The pink colour vertical line gives the information pertaining to Bragg's positions. The Gaussian function was used for peak shape fitting and linear interpolation function was used between background points. Initially, the values of lattice parameters (a, b, c, α, β, γ) and space group were fed in the software given in the JCPDS file. The refinement results were listed in Table 4.1 and confirmed the pure phase formation of samples as there was no significant change in lattice parameters after refinement. The goodness of fit (χ^2) values were found 0.79 and 0.99 for un-doped BMT sample and doped BMT phosphor respectively. These results indicate the successful synthesis of BMT phosphor by solid state reaction method.

Table 4.1. Rietveld refinement parameters along with JCPDS data.

Parameters	**Standard data JCPDS (038-0254)**	**BMT (un-dope)**	**BMT: xHo^{3+}/ yYb^{3+} x = 11mol% y = 7mol%**
a (Å)	5.9570	5.9493	5.9669
b (Å)	5.9570	5.9493	5.9669
c (Å)	21.2900	21.2473	21.296
α = β	90	90	90
γ	120	120	120
χ^2	-	0.79	0.99
Cell volume($Å^3$)	654.28	651.26	656.6

4.3.2. Morphological analysis:

4.3.2.1. SEM:

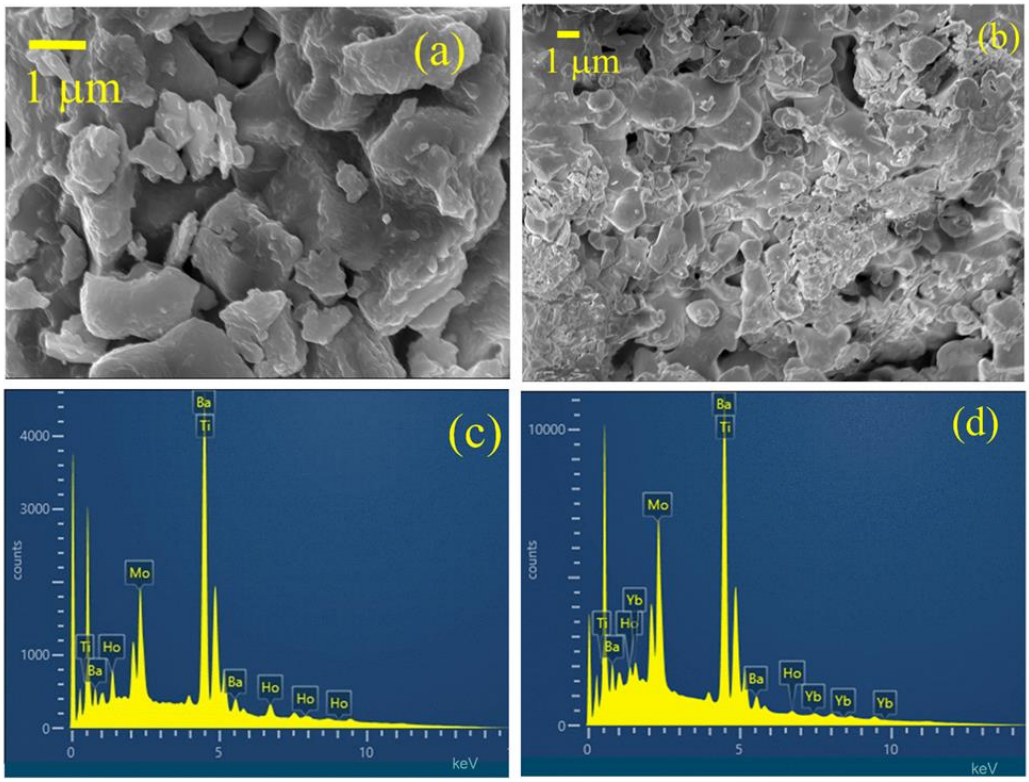

Fig. 4.3. Scanning electron microscope images **(a-b)** of xHo^{3+} doped (x=11mol%) and xHo^{3+}/yYb^{3+} (x=11mol% and y=7mol%) co-doped phosphors **(c-d)** and their corresponding EDX images.

Fig. 4.3(a) and 4.3(b) shows the morphology of particles for Ho^{3+} doped and Ho^{3+}/Yb^{3} co-doped samples. Particles were very much agglomerated in both the cases with a non-uniformity in size and shape. This difference in size of particles may be due to the manual grinding during the synthesis process, due to which there was random distribution of particles. The average particle size was found out in the range of 1-8 μm for singly doped sample and in the range of 1-5 μm for co-doped samples [74].

4.3.2.2. EDX measurements and elemental mapping:

Energy dispersive x-ray analysis is the technique used to recognize the elemental composition of materials. Fig. 4.3(c) shows the EDX spectra of singly Ho^{3+} ion doped sample and 4.3(d) shows the spectra of co-doped Ho^{3+}/Yb^{3+} sample. In the EDX analysis of Ho^{3+} ion doped sample, Ba, Mo, Ti and Ho elements were present and in co-doped sample, Ba, Mo, Ti, Ho and Yb elements were present. Thus, the EDX recorded confirms the elements that were used in the preparation of these samples.

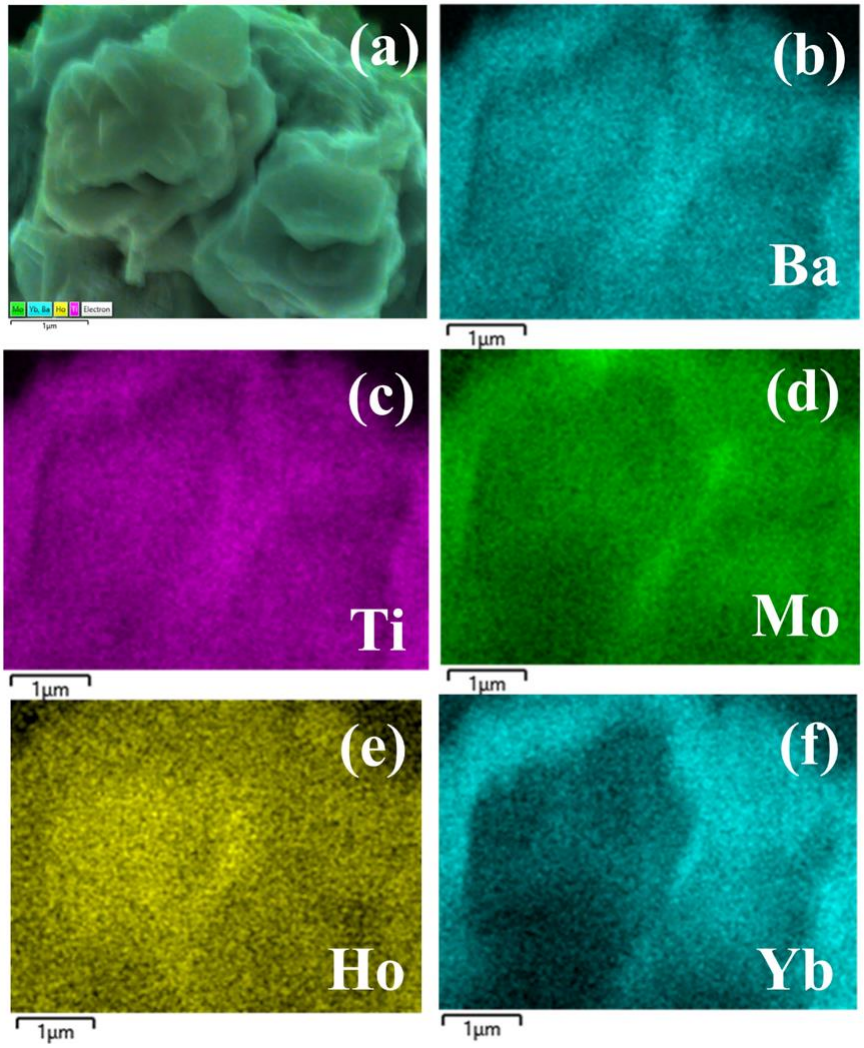

Fig. 4.4. Elemental mapping of xHo^{3+}/yYb^{3+} (x=11 mol%, y=7 mol%) co-doped BMT phosphor in (a) mixed mapping and for individual elements such as Barium (Ba), Titanium (Ti), Molybdenum (Mo), Holmium (Ho) and ytterbium (Yb) from (b) to (f) respectively.

Fig. 4.4 shows the elemental mapping of the co-doped phosphor. From the elemental mapping it is evident that all the elements are present in host lattice and the dopant elements are uniformly distributed all over the surface.

4.3.3. FT-IR spectral analysis:

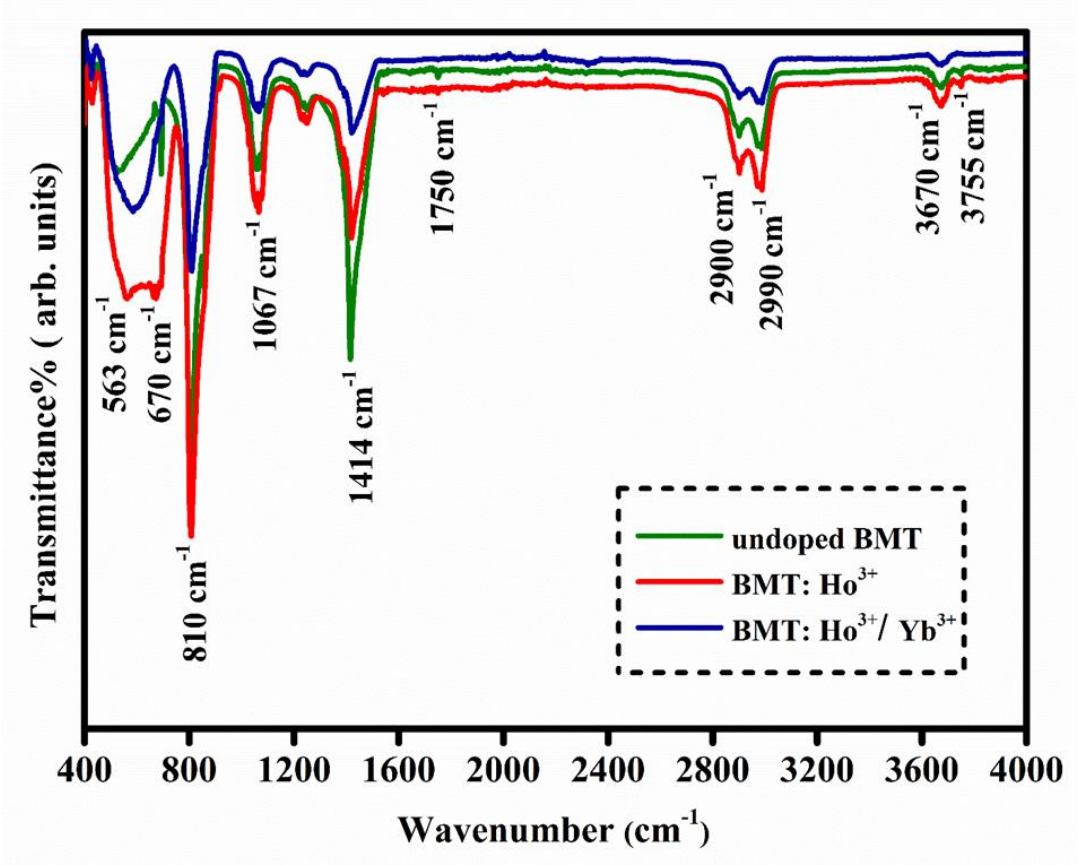

Fig. 4.5. FT-IR spectra of an undope sample, single Ho^{3+}doped and co-doped Ho^{3+}/Yb^{3+} BMT phosphors.

FT-IR technique was used to find out the vibrational groups present in the host lattice. Fig.4.5 shows the FT-IR analysis of an un-doped BMT sample, 11 mol% Ho^{3+} ions doped BMT phosphor and Yb-Ho co-doped (7 mol% Yb^{3+}/11 mol% Ho^{3+}) BMT phosphor in the range of 400-4000 cm^{-1}. The absorption bands present in the region between 500-800 cm^{-1} generally correspond to the metal oxygen bonds. A band observed at 563 cm^{-1} represents the stretching

vibrations of Ti-O groups in the host lattice [75]. In addition to this, 670 cm^{-1} and 810 cm^{-1} bands belong to the Mo-O and Mo-O-Mo stretching vibrations respectively in MoO_4^{2-} tetrahedrons [76]. The deeper shoulder between the region 780-830 cm^{-1} is due to the host phonon frequency as MoO_4^{2-} group vibrations of lattice which are very strong and broad in this region [77]. The bands at 1067 and 1414 cm^{-1} accredited to the stretching vibrations of C-O due to the $BaCO_3$ and H-O-H blending vibrations respectively [78,79]. The spectra between the region 1700-4000 cm^{-1} assigned to the presence of stretching vibrations of hydroxyl groups and hydrogen bonding [36–38]. The different functional groups identified are same in an un-doped as well as doped BMT phosphors.

4.3.4. DRS analysis for band gap measurement:

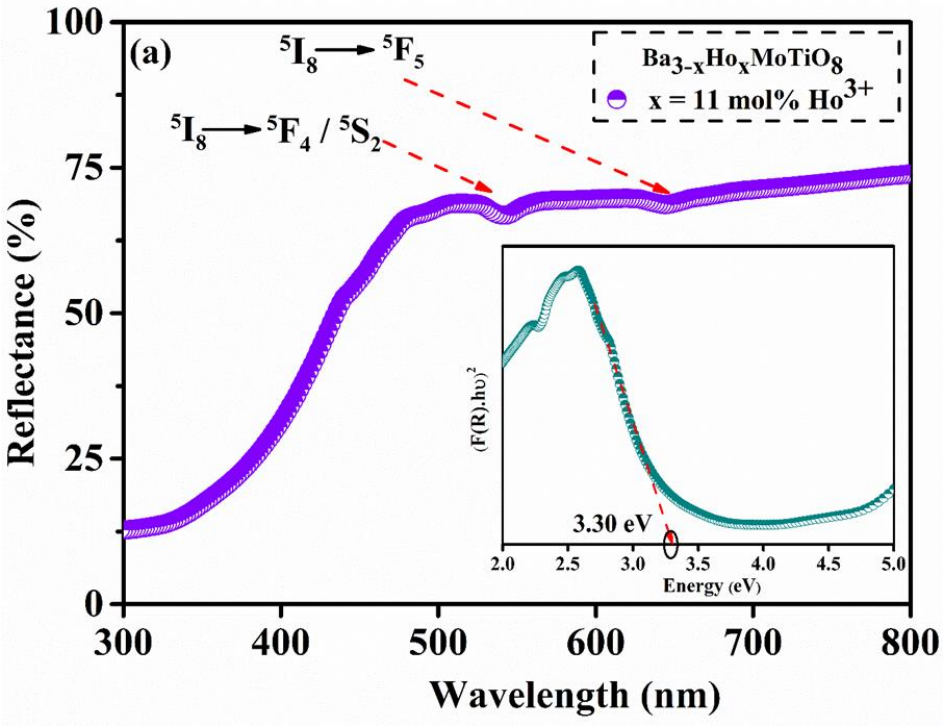

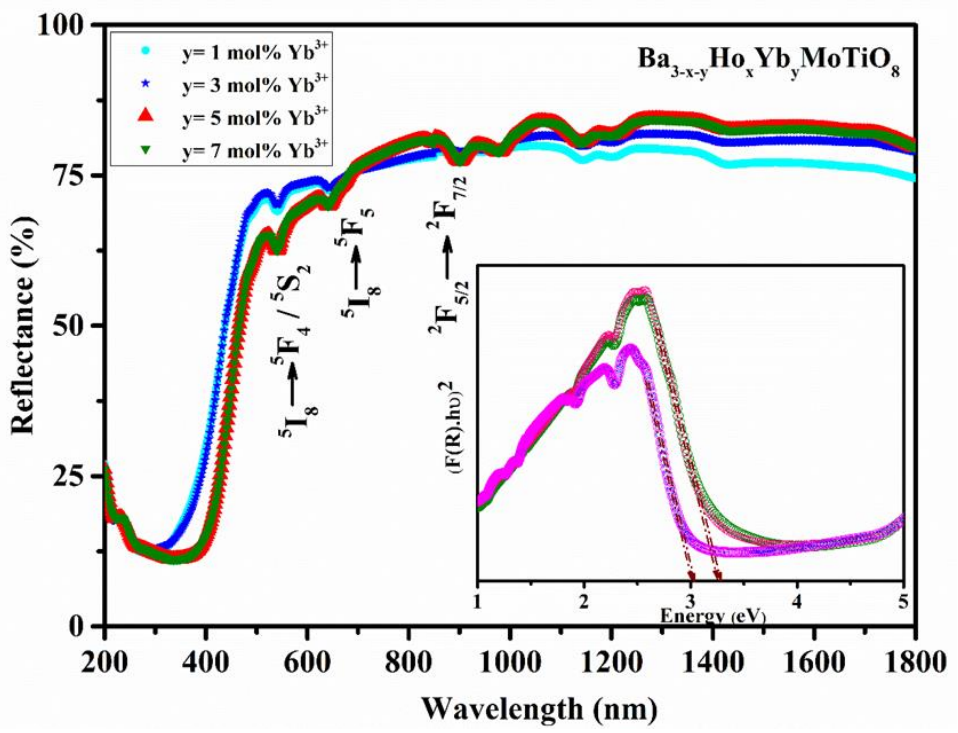

Fig. 4.6. Diffuse Reflectance Spectra of $Ba_{3-x-y}MoTiO_8$**:**xHo^{3+}/yYb^{3+} phosphor **(a)** x=11mol%, y=0 mol% **(b)** x=11mol%, y=1,3,5 and 7mol% and their corresponding tau plots (inset figures).

Fig. 4.6(a) shows the UV-vis DRS spectra of a Ho^{3+} ion doped BMT phosphor in the range of 300-800 nm wavelength. In this spectra, two bands are observed in the visible region at wavelengths 544 nm and 645 nm when transitions take place from ground state $^5I_8$ of Ho^{3+} ion to the excited states $^5F_4/^5S_2$ and $^5F_5$ of Ho^{3+} ion respectively [75,77,83]. On the other hand, Fig. 4.6(b) shows the absorption spectra of Ho^{3+}/Yb^{3+} co-doped phosphors in the UV-vis-NIR range. In this spectra, an additional absorption band was observed in NIR region due to the incorporation of Yb^{3+} ions at wavelength 948 nm corresponding to transition $^2F_{5/2} \rightarrow {}^2F_{7/2}$ [84]. As Yb^{3+} is having larger cross-section in NIR region, 980 nm laser source was used to record the UC PL spectra and its corresponding lifetime curves. The optical band gap has been calculated for the above two series using the kubelka-munk function described in chapter 2, eq. (16(, (17) and (18)-

In this case we have calculated the allowed direct band gap by using m=1/2. Inset figures of 4.6(a) and 4.6(b) show the $(\alpha h\upsilon)^2$ versus $h\upsilon$ plot for the single Ho^{3+} ion doped and Ho^{3+}/Yb^{3+} co-doped phosphors. The value of optical band bap was calculated to be 3.30 eV for singly Ho^{3+} doped sample and in the range of 3.00-3.27 eV for the co-doped samples by extrapolating the slope of tau plot. The obtained values are satisfactorily matching with the previous reported values [62,85]. Lower value of band gap promotes large number of ions to excited state and results in enhancement of PL intensity [86].

4.3.5. Linear (down-conversion) and non-linear (up-conversion) PL behaviour:

4.3.5.1. Linear PL excitation and emission spectral studies:

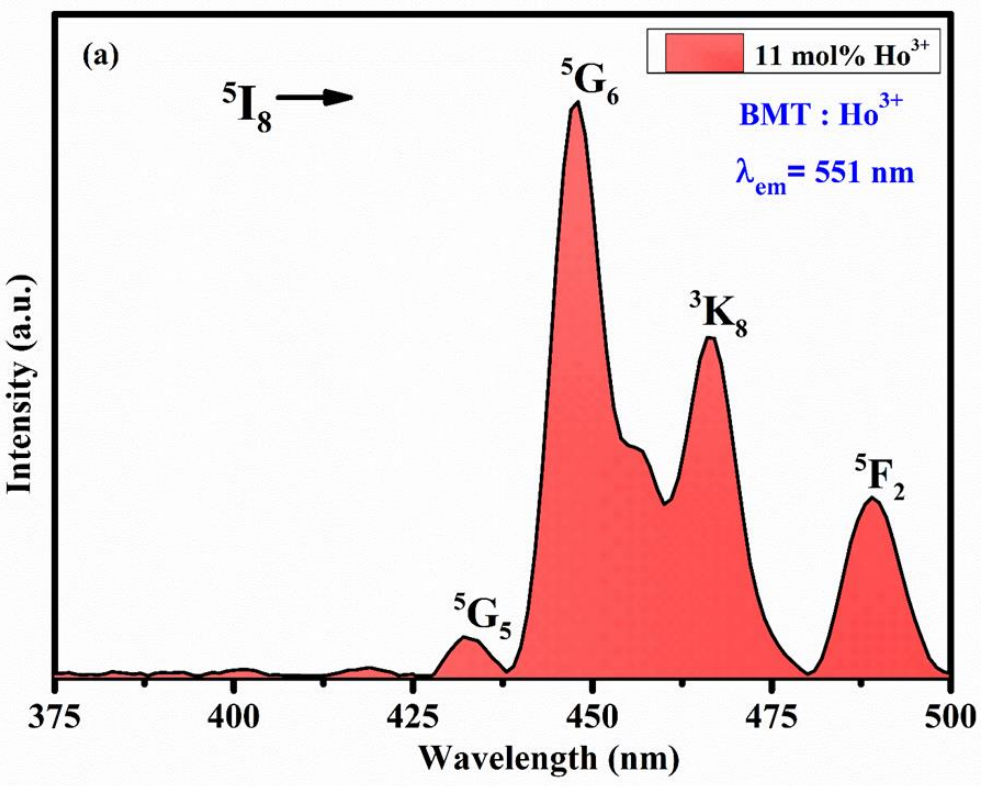

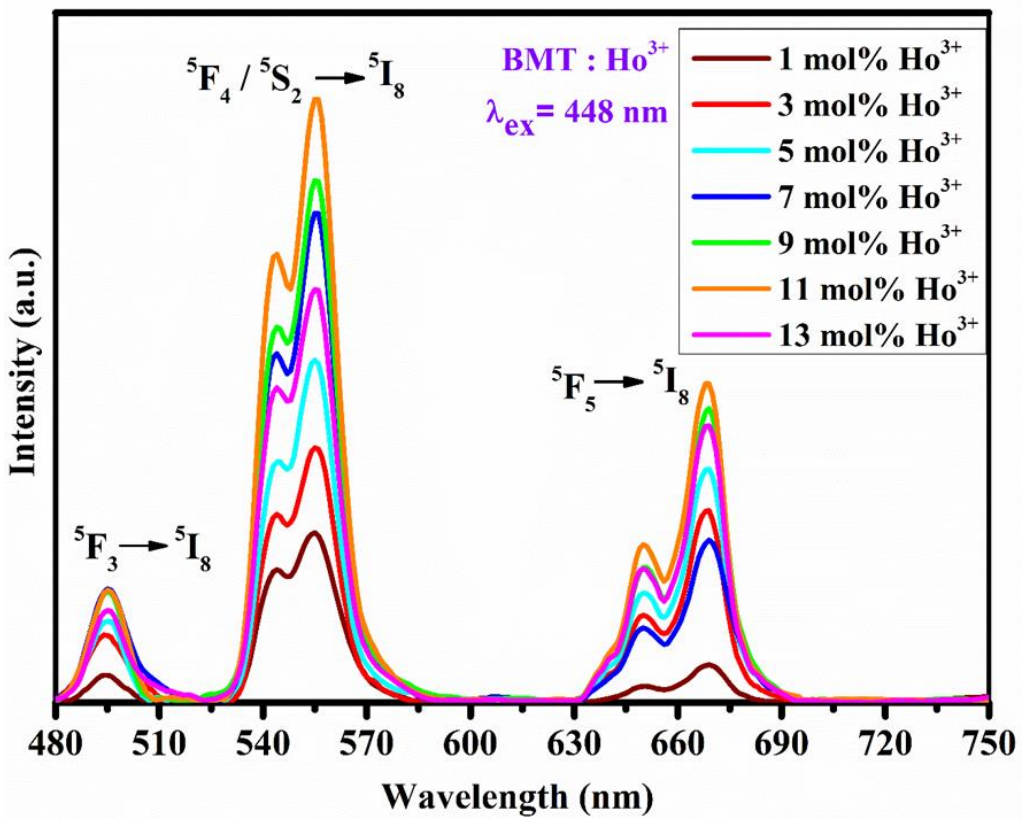

Fig. 4.7. Linear **(a)** PL excitation spectrum of Ho^{3+}doped (11 mol%) phosphor under 551 nm emission and **(b)** PL emission spectra of $Ba_{3-x}MoTiO_8$**:**xHo^{3+}(x= 1,3,5,7,9,11 and 13mol%) phosphors under 448 nm excitation wavelengths respectively.

Fig.4.7 (a) & (b) shows the PL excitation spectrum (under 551nm emission) and PL emission spectra (under 448nm excitation) of Ho^{3+} ion doped BMT phosphors respectively. In the excitation spectrum shown in Fig. 4.7 (a), four peaks were observed at 432 nm, 448 nm, 466 nm and 489 nm corresponding to the transitions from ground state $^5I_8$ to excited states $^5G_5$, $^5G_6$, $^3K_8$ and $^5F_2$ of Ho^{3+} ions respectively. The highest intense peak found at 448 nm was used as an excitation wavelength to record the emission spectra of BMT: x Ho^{3+}(x= 1, 3,5,7,9,11 and 13 mol%) phosphors in the range between 480-750 nm wavelength. In the emission spectra shown in Fig.4.7 (b), three bands were observed at wavelengths 492, 551 and 668 nm pertaining to the transitions $^5F_3 \rightarrow {}^5I_8$, $^5F_4/{}^5S_2 \rightarrow {}^5I_8$ and $^5F_5 \rightarrow {}^5I_8$ respectively [87]. The most intense band in this emission spectra was corresponding to green emission at 551nm

wavelength. Spectra shows that increase in the concentration of Ho^{3+} ions, the PL intensity increases up to 11mol % and after that drops suddenly due to the phenomena of concentration quenching. Fig.4.8 shows the linear emission spectra recorded for the $Ba_{3-x-y}MoTiO_8$**:**xHo^{3+}/yYb^{3+} (x=11mol%, y=1, 3, 5 and 7mol%) phosphors under 448 nm excitation. The co-doped BMT phosphors also show visible emission under blue excitation and contains two emission peaks at wavelengths 551 and 668 nm pertaining to transitions $^5F_4/\,^5S_2 \rightarrow {}^5I_8$ and $^5F_5 \rightarrow {}^5I_8$ respectively.

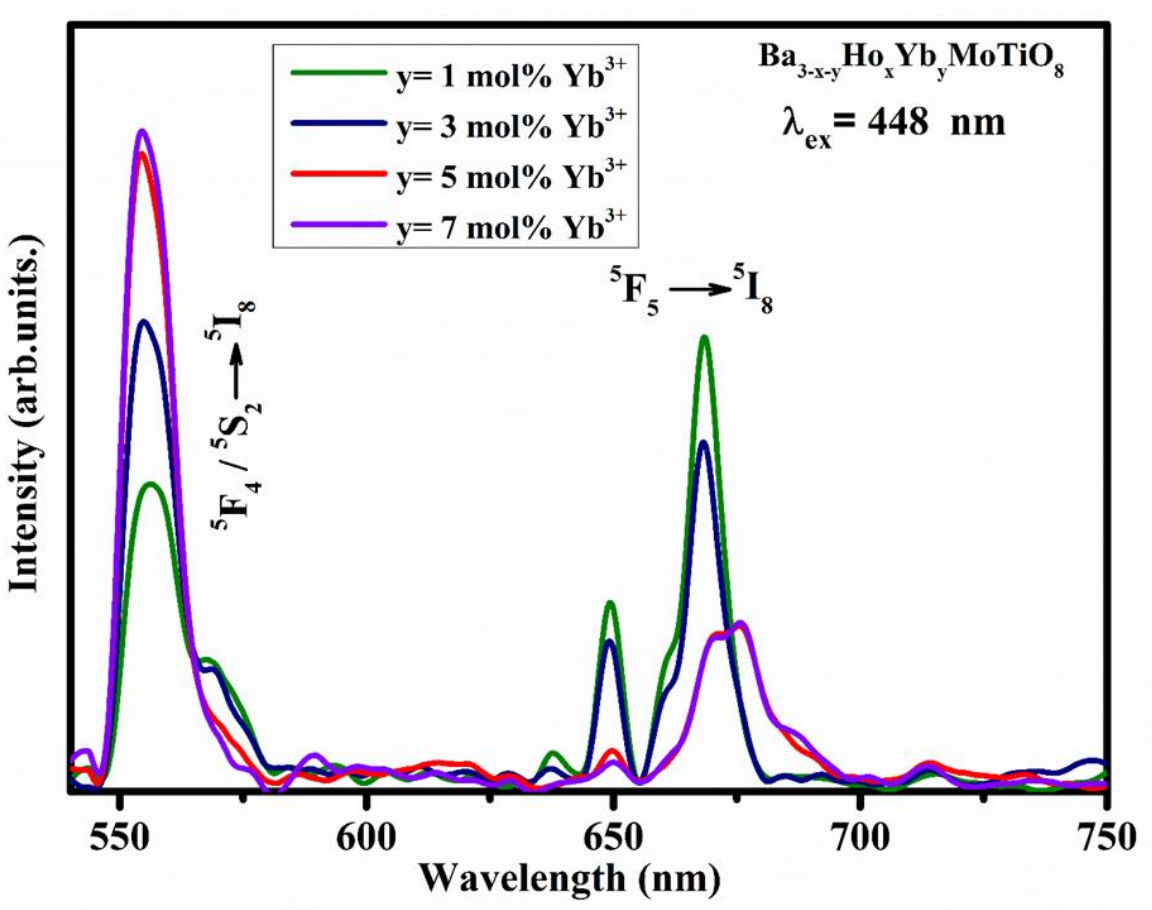

Fig. 4.8. Linear PL spectra of $Ba_{3-x-y}MoTiO_8$**:**xHo^{3+}/yYb^{3+} (x=11mol% and y=1,3,5 and 7mol%) phosphors under λ_{ex} = 448 nm.

From Fig. 4.8 it is conspicuous that, intensity of green emission increases with increase in Yb^{3+} content. Contrarily on the opposite side, the emission corresponding to red region decreases with increase in Yb^{3+} ion concentration. This may be due to the cross relaxation energy transfer observed between Ho^{3+} and Yb^{3+} ions and energy transfer from Yb^{3+} ions to Ho^{3+} ions in case of green emission [57,88]. As the Ho^{3+} ions show very weak or negligible non-linear emission under 980 nm excitation, a series of Ho^{3+}/Yb^{3+} co-doped samples were prepared to study the Up-conversion behaviour of BMT phosphors.

4.3.5.2. Non-linear PL spectral studies:

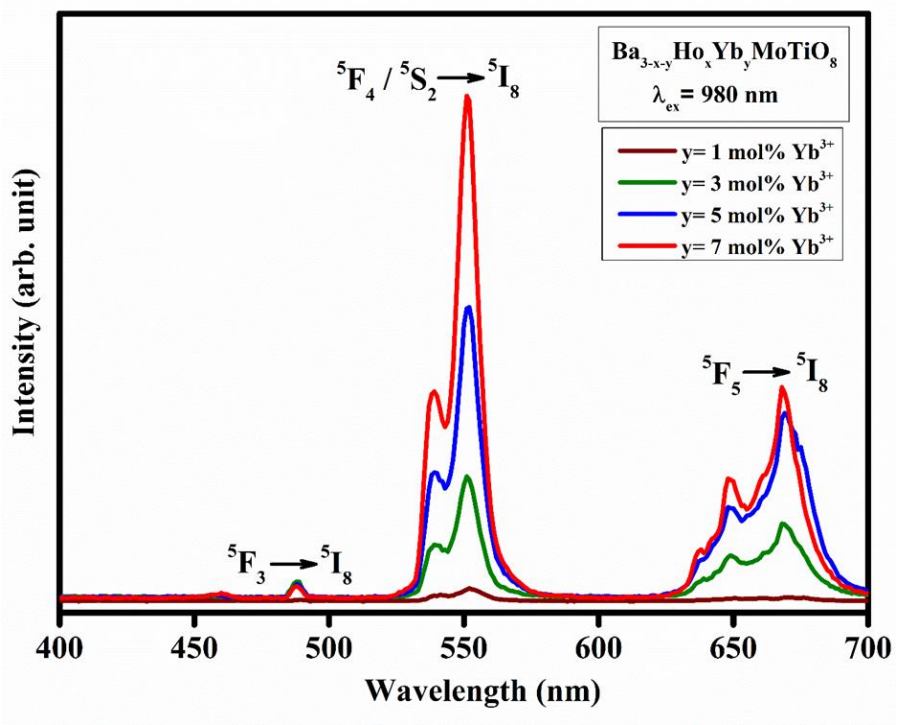

Fig. 4.9. Non-linear PL spectra of $Ba_{3-x-y}MoTiO_8$**:**xHo^{3+}/yYb^{3+} (x=11mol% and y=1,3,5 and 7mol%) phosphors under 980 nm laser excitation.

The non-linear PL spectra for the co-doped Ho^{3+}/Yb^{3+} phosphors were recorded under 980 nm laser excitation in the range of 400-700 nm. In this spectra, three different bands were observed at wavelengths 488, 551 and 668 nm in blue, green and red regions respectively. These blue, green and red bands are the resultant transition of the Ho^{3+} ions from its $^5F_3$, $^5F_4$/ $^5S_2$ and $^5F_5$

excited states to the $^5I_8$ ground state respectively [70,85,89]. From Fig. 4.9, it is observed that the intensity of green band is approximately double as compared to red band and 15-20 times higher than that of blue band. It is well known that Ho^{3+} ion has very weak absorption cross-section for 980nm laser excitation. Therefore, in the present work, Yb^{3+}ions are acting as sensitizer and transferring energy to Ho^{3+} ion (activator) and results in the up-conversion PL observed in Fig.10. Moreover, from Fig.4.9 it is conspicuous that, with increase in the concentrations of Yb^{3+} ion (1,3,5 and 7mol%) the non-linear emission shown by Ho^{3+} ions are increasing continuously up to 7mol%. This gradual increase in Ho^{3+} ions emission with increase in the concentration Yb^{3+} ions is due to continuous energy transfer from Yb^{3+} ions to Ho^{3+} ions. To have further conformation for this up-conversion process observed, we have studied the power dependence non-linear PL studies.

4.3.5.3. Power dependent non-linear PL studies:

Fig.4.10(a) shows the variation in intensity of green and red bands with respect to the input pump power. The intensity of green band dominates over the red band and blue band has lowest intensity in this up-conversion spectra. With increase in pump power, initially the up-conversion intensity increases for green band up to 480 mW and then slightly decreases or saturates beyond. This decrease or saturation in intensity may be due to the heating of the material at higher pump power.

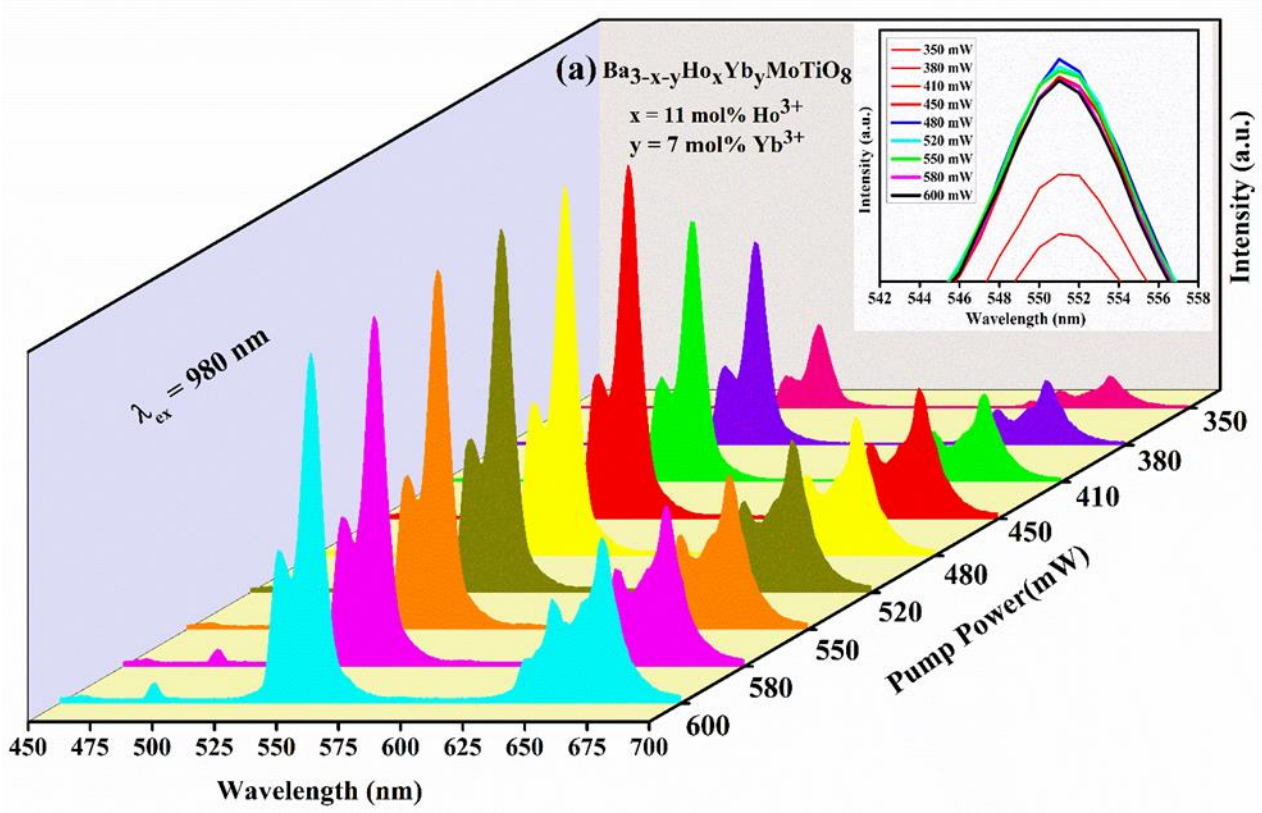

Fig. 4.10(a). Power dependence non-linear PL spectra of $Ba_{3-x-y}MoTiO_8$:xHo^{3+}/yYb^{3+} (y= 7mol%) phosphor under 980 nm laser excitation.

On the flip side, intensity of red band increases continuously with increasing pump power up to 600 mW power, but the dominancy of green emission is still present. This dominancy in green emission may be because of direct excitation of Holmium ions in $^5F_4$/ $^5S_2$ state through excited state absorption (ESA) and energy transfer (ET) from Yb^{3+} ions as shown in energy level diagram of Fig. 12. But at higher pump powers, photon density increases in $^5F_4$/ $^5S_2$ level and they start to relax through non-radiative relaxations (NRR) in $^5F_5$ level. Additionally, excitation of Ho^{3+} ions through energy transfer from Yb^{3+} ions still remain continue. Due to these factors the population of ions in $^5F_5$ level increases and continuous enhancement in red emission takes place at higher pump powers [87].

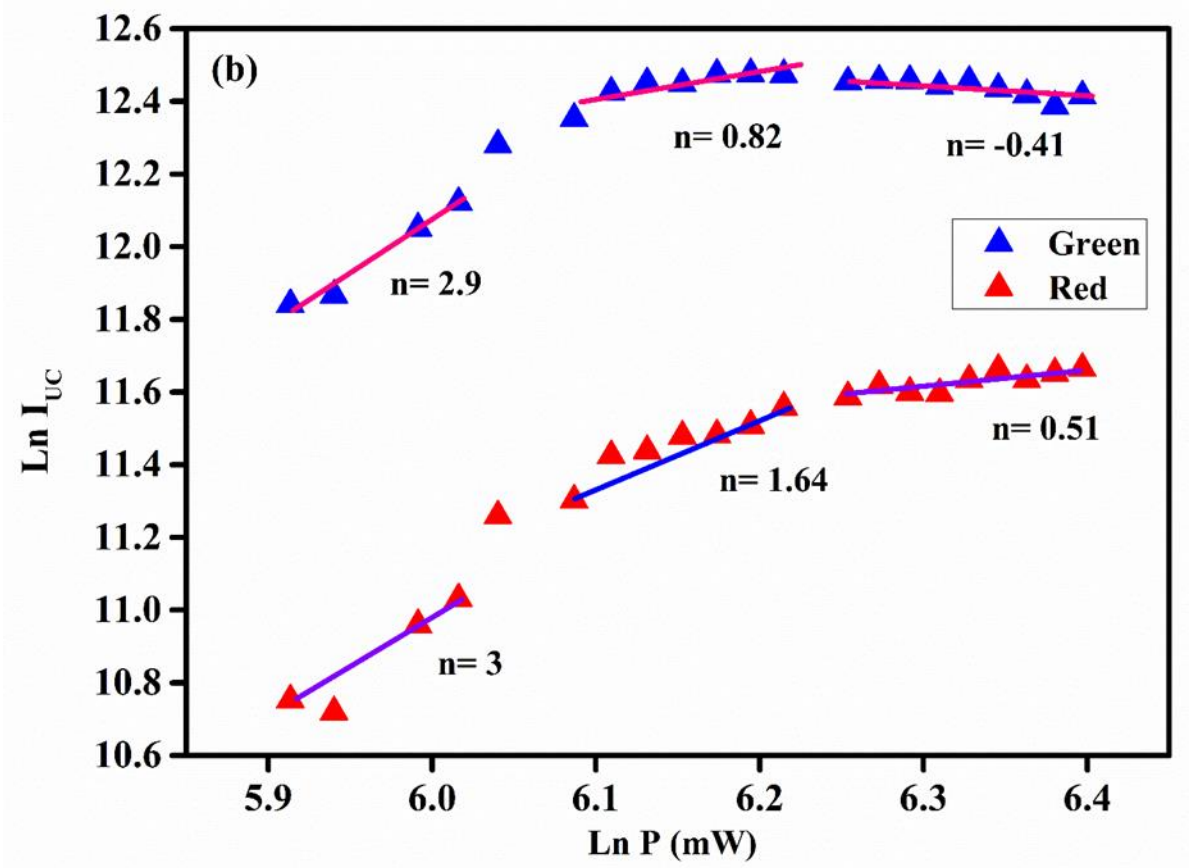

Fig. 4.10(b). Ln-Ln plot of UC intensity vs. pump power.

It was already known that the up-conversion luminescence intensity is directly proportional to the n^{th} power of the input pump power.

$$I_{UC} \alpha (P_{in})^n \quad (23)$$

Where n is an integer and gives the information about the number of photons involved in the up-conversion process. When the plot of up-conversion intensity vs. input pump power was plotted, the value of slope i.e., n gives the detail of number of photons involved in UC process. Fig.4.10(b) shows the plot of $Ln(I_{UC})$ versus $Ln(P_{in})$. From this plot, we calculated the slope value and the value of n comes out nearly 3 up to 480 mW power and beyond that it is approximately equal to 2. So initially 3 photons are involved in the UC process up to 480mW power and beyond that the pump power is lost due to heating effect. In order to describe the

mechanism of energy transfer, an energy level diagram has been plotted for Ho^{3+} and Yb^{3+} ions as shown in Fig. 4.11. On 980 nm laser excitation, Yb^{3+} ions make transition from ground state $^2F_{7/2}$ to excited state $^2F_{5/2}$. Then Yb^{3+} ions act as a sensitizer and transfer their energy through phonon assisted energy transfer to Ho^{3+} ions and by gaining energy, Ho^{3+} ions reach to $^5I_6$ state. After reaching $^5I_6$ level, some Ho^{3+} ions further move to excited states $^5F_4$, $^5F_5$ states through ESA or ET from Yb^{3+} ions. The cooperative energy transfer (CET) also takes place in which two Yb^{3+} ions cooperatively transfer their energy to $^3K_8/^5F_2$ or higher levels. From these higher levels Ho^{3+} ions relax non-radiatively to lower states and the transition from $^5F_{3,}$ $^5F_4/$ $^5S_2$ and $^5F_5$ levels to $^5I_8$ level results in blue, green and red bands respectively with the involvement of 2 or 3 photons. The mechanism behind the involvement of 3 photons is the accumulation of large number of photons in the $^5F_4/$ $^5S_2$ and $^5F_5$ levels through sequential ESA, ET and CET phenomena as shown in Fig.4.11 [90–92].

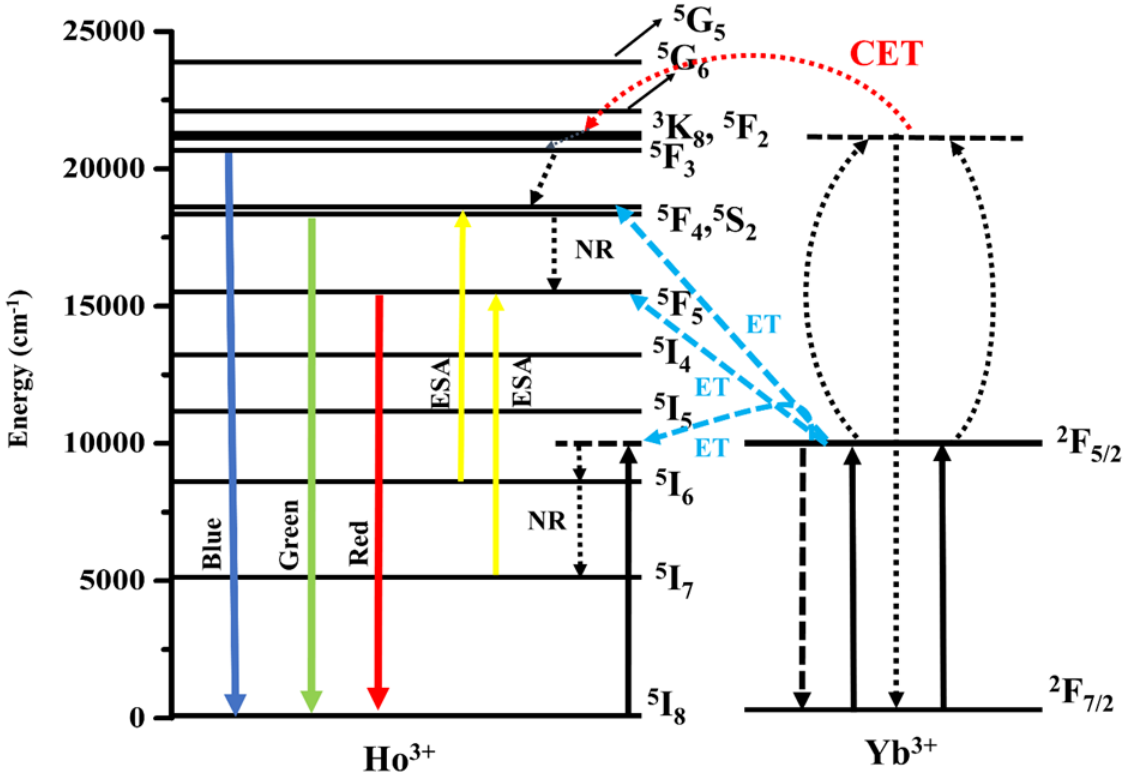

Fig. 4.11. Schematic energy level diagram of Ho^{3+} and Yb^{3+} ions and their energy transfer mechanism.

4.3.6. PL lifetime decay measurements:

The PL lifetime curves of $^5F_4/^5S_2$ and $^5F_5$ levels in Ho^{3+}/Yb^{3+} co-doped samples corresponding to transition $^5F_4/^5S_2 \rightarrow {}^5I_8$ and $^5F_5 \rightarrow {}^5I_8$ were recorded under 980 nm laser source excitation. The decay curves were shown in Fig. 4.12(a) & (b) at λ_{em}=551 nm and λ_{em}=668 nm respectively. The decay curves of these phosphors were fitted by single exponential function using eq. (11) as described in chapter 1.

The value of all lifetimes were calculated and written in Table 4.2.

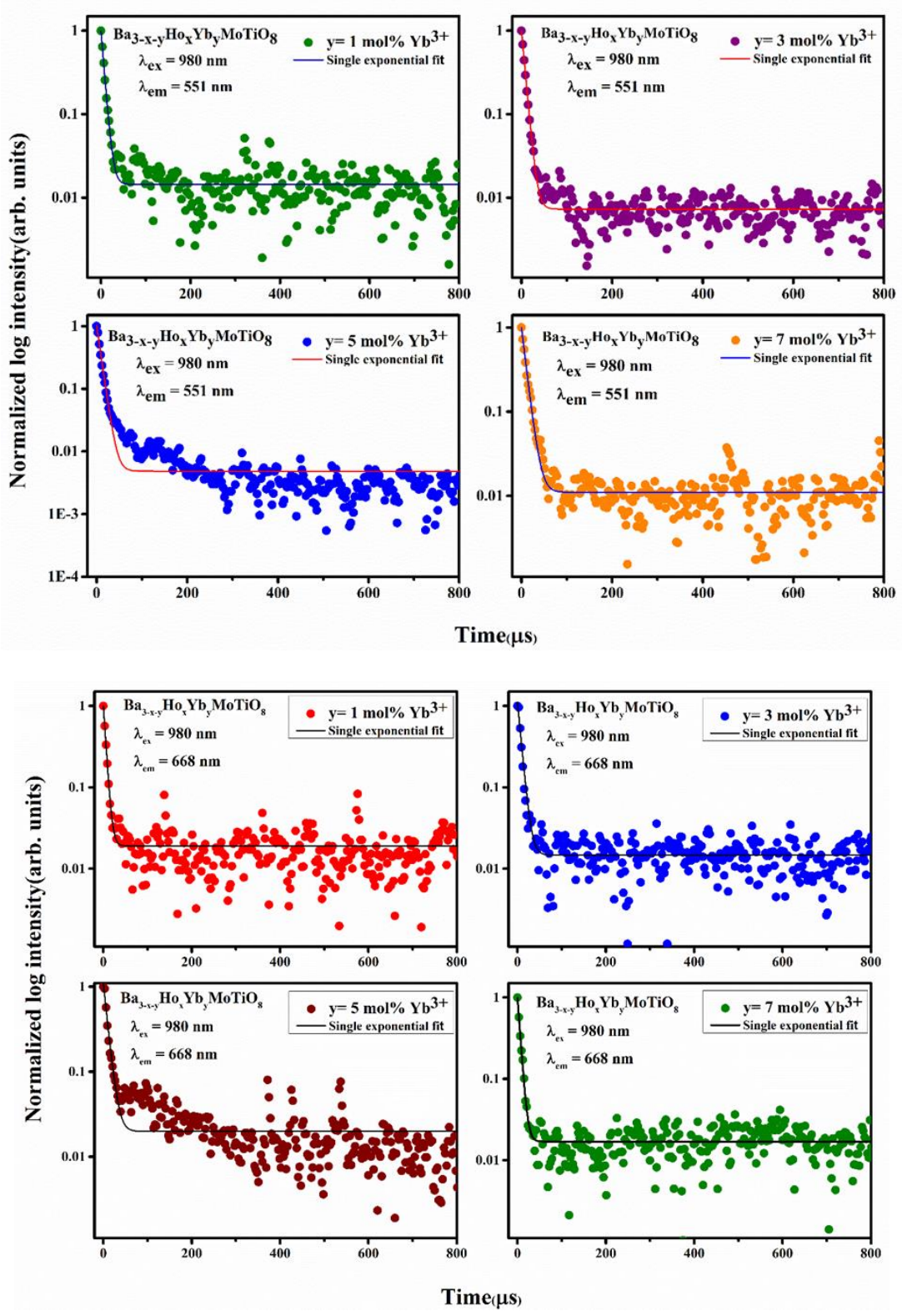

Fig. 4.12. PL decay curves of $Ba_{3-x-y}MoTiO_8$:xHo^{3+}/yYb^{3+} (x=11mol% and y=1,3,5 and 7mol%) phosphors under 980 nm laser excitation (a) λ_{em} = 551 nm (b) λ_{em} = 668 nm.

It is observed that, the lifetime values corresponding to λ_{em}=551 nm are relatively larger than that of λ_{em}=668 nm. This supports the relatively more intensity observed for green bands when compared to the red bands in UC emission spectra by varying the Yb^{3+} content. The estimated lifetime values with λ_{em}=551nm show continuous increase with increase in Yb^{3+} concentration. This supports the continuous transfer of energy from Yb^{3+} ions to Ho^{3+} ions up to 7 mol% concentration in the present work [62,84]. On the other side, calculated lifetime values corresponding to λ_{em}=668 nm, initially show increment up to 5 mol% Yb^{3+} content and then show a decrement. This may be due to the fact that after a certain concentration of Yb^{3+} ion, energy transfer saturates down or become less which can also be confirmed from the UC PL spectra.

From the UC PL spectra shown in Fig. 4.9, it is conspicuous that, the intensity of green band increases with increase in Yb^{3+} ion concentration (maximum doped Yb^{3+} concentration is 7 mol%) continuously. This increase in luminescence intensity demonstrate transfer of energy from Yb^{3+} ions to Ho^{3+} ions. This is further supported by increase in experimental lifetime values of green band (551 nm) with increase in Yb^{3+} ion concentration. However, intensity of red band firstly increases sharply with Yb^{3+} content up to 5 mol% and reaches almost saturation up to 7mol%. This is well supported by increase in lifetime values of red band (668 nm) with increase in Yb^{3+} ion concentration up to 5 mol% and decreases slightly at 7 mol%. This also further supports transfer of energy from Yb^{3+} ions to Ho^{3+} ions. The variation of lifetime values with Yb^{3+} content in case of green and red bands is shown in Fig. 4.13.

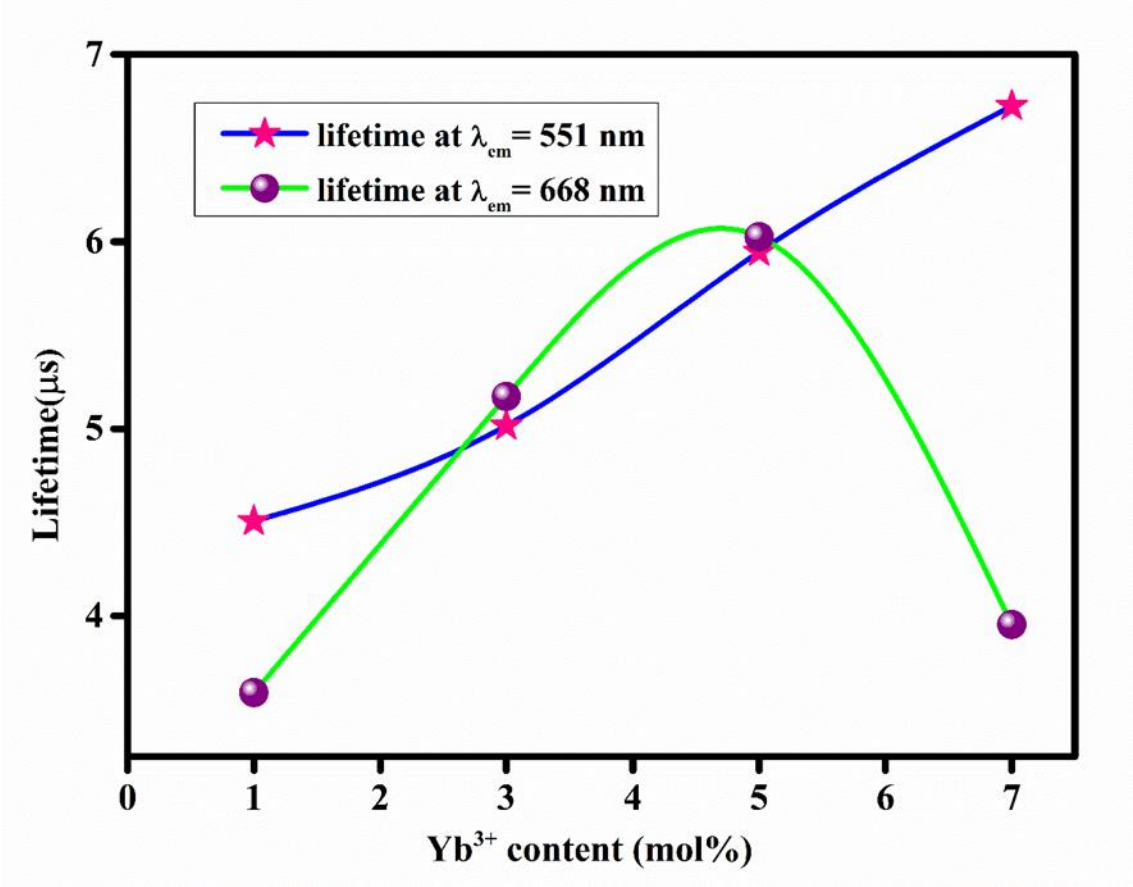

Fig. 4.13. Variation in calculated lifetime of co-doped phosphors with respect to Yb^{3+} content.

Table 4.2. Lifetime of Ho^{3+} ions in BMT: Ho^{3+}/ Yb^{3+} phosphor for λ_{em}=551 nm and 668 nm under 980 nm laser excitation.

Sample ID (Yb^{3+} series)	**Lifetime values (μs) λ_{em}=551 nm**	**Lifetime values (μs) λ_{em}=668 nm**
1mol% Yb^{3+}	4.51	3.59
3mol% Yb^{3+}	5.02	5.17
5mol% Yb^{3+}	5.94	6.03
7mol% Yb^{3+}	6.73	3.96

4.3.7. CIE and CCT analysis: The colorimetric performance of the as prepared phosphors was shown in Fig. 4.14 (a) & (b) using the DC and UC PL emission data respectively. CIE

coordinates were calculated for the singly Ho^{3+} ion doped series and co doped Ho^{3+}/Yb^{3+} series and are listed in Table 4.3. Fig.4.14 (a) & (b) shows that, all the CIE coordinates are falling in green region. Correlated colour temperature (CCT) values are estimated by using the McCamy equation (8) given in chapter 1.

The CCT values are also listed in Table 4.3. All these results of CIE coordinates and CCT values show that the as prepared phosphors are useful in solid state lighting applications [77,84].

Table 4.3. Variations of CIE Coordinates and CCT values for singly Ho^{3+} ion doped series and co doped Ho^{3+}/Yb^{3+} series of BMT phosphors.

Sample ID (Ho^{3+} series)	**CIE Co-ordinates (Ho^{3+}series) λ_{ex}=448 nm**	**CCT(K) (Ho^{3+}series)**	**Sample ID (Yb^{3+} series)**	**CIE Co-ordinates (Yb^{3+}series) λ_{ex}=980 nm**	**CCT(K) (Yb^{3+} series)**
1mol% Ho^{3+}	(0.3290,0.6427)	5569.1	1mol% Yb^{3+}	(0.3326,0.4725)	5509.6
3mol% Ho^{3+}	(0.3432,0.6094)	5344.4	3mol% Yb^{3+}	(0.3520,0.5180)	5123.3
5mol% Ho^{3+}	(0.3487,0.6140)	5261.7	5mol% Yb^{3+}	(0.3604,0.5697)	5035.4
7mol% Ho^{3+}	(0.3290,0.6303)	5569.4	7mol% Yb^{3+}	(0.3440,0.608)	5331.2
9mol% Ho^{3+}	(0.3446,0.6221)	5328.5			
11mol% Ho^{3+}	(0.3419,0.6257)	5370.7			
13mol% Ho^{3+}	(0.3447,0.6200)	5326.0			

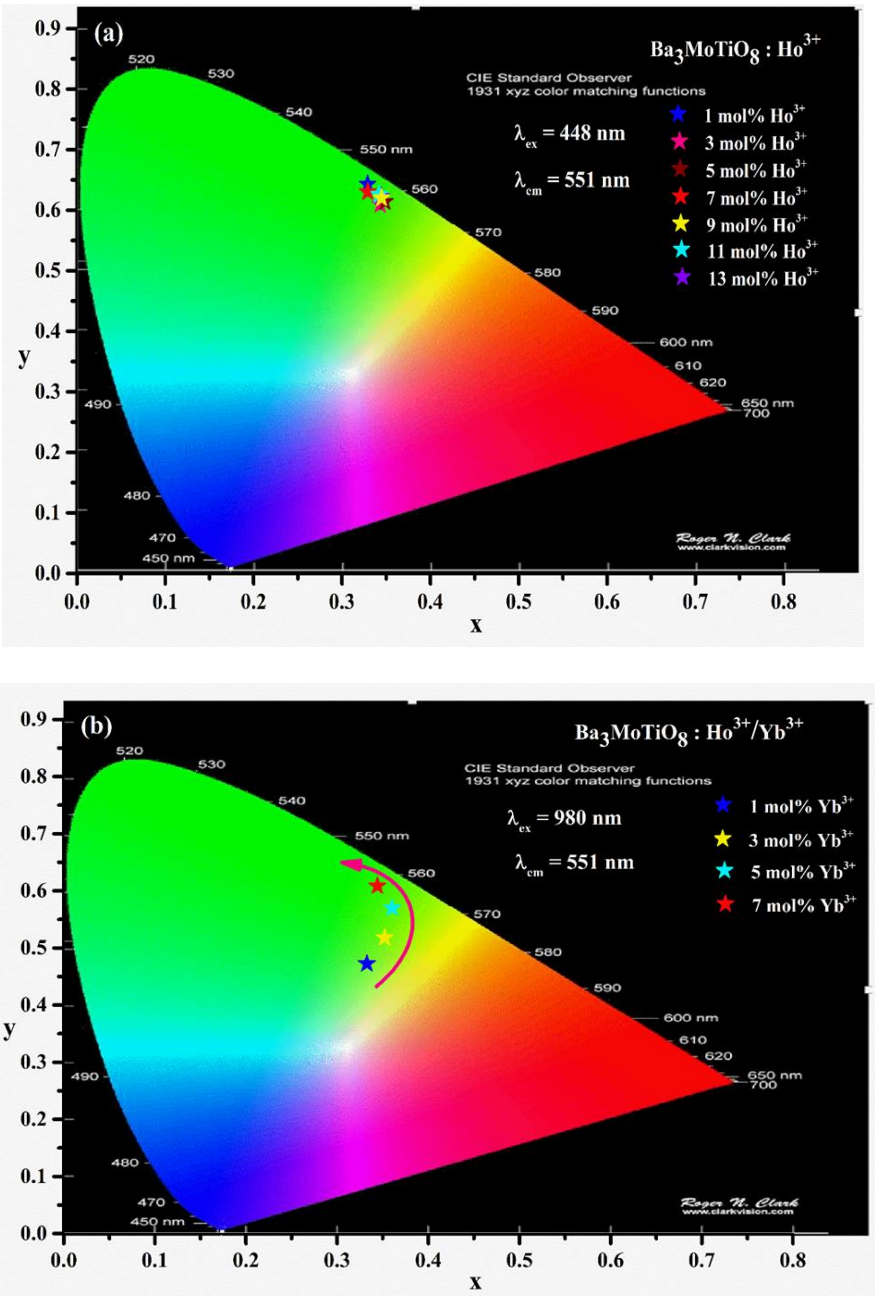

Fig. 4.14. CIE plot of **(a)** single Ho^{3+} doped and **(b)** co-doped Ho^{3+}/Yb^{3+} phosphors under linear and non-linear PL spectral studies.

4.4. Conclusions

A series of single Ho^{3+} ion doped and Ho^{3+}/Yb^{3+} co-doped BMT phosphors were prepared by solid state reaction method. XRD technique confirmed the pure phase and crystallinity of the as prepared phosphors. Morphological studies show that particle size of phosphors lie in the

micro meter range and elemental mapping shows the presence of all the constituent elements that are used during the synthesis process. It was also found that the constituent elements are uniformly distributed all over the surface of the as prepared phosphor. FT-IR spectra describes the presence of various metal oxide bands and hydroxyl groups present in the titled phosphor. The UC and DC PL emission show intense green emission (at 551 nm) under 980 nm laser excitation as well as under 448 nm xenon lamp excitation. The variation in UC intensity with pump power reveal the information pertaining to the number of photons involved in the UC process. PL lifetime decay curves recorded under 980 nm excitation show continuous increment under λ_{em}=551 nm and in case of λ_{em}=668 nm, lifetime values first increasing and then decreasing. The CIE coordinates of all samples lie in green region. All these results indicate that the as prepared phosphor can be a promising candidate for application in UC & DC based green emitting diodes, display devices, security ink, phototherapy and SSL applications.

CHAPTER 5

Energy transfer induced colour tunable photoluminescence performance of thermally stable Sm^{3+}/Eu^{3+} co-doped Ba_3MoTiO_8 phosphors for white LED applications

The combustion process has been successfully used to synthesize $Ba_3MoTiO_8:Sm^{3+}$ and $Ba_3MoTiO_8:Sm^{3+}/Eu^{3+}$ co-doped phosphors for w-LED applications. For the as-prepared phosphors, XRD, SEM, FT-IR, DRS, and PL spectroscopy techniques have been used to investigate phase confirmation, morphological analysis, and PL properties. The PL emission spectra of singly Sm^{3+} doped and Sm^{3+}/Eu^{3+} co-doped phosphors recorded under 409 nm wavelength show intense emission in reddish-orange and red regions, respectively. For Sm^{3+}-Eu^{3+} co-doped phosphors, the intensity of Sm^{3+} peaks show a decrease with an increase in Eu^{3+} ion concentration, demonstrating the energy transfer from Sm^{3+} to Eu^{3+} ions. Quadrupole-quadrupole interaction is the mechanism responsible for energy transfer from Sm^{3+} ions to Eu^{3+} ions according to Dexter's hypothesis as applied to the PL spectra. This result is in consonance with the results of PL decay curves recorded under 409 nm excitation. CIE coordinates calculated for singly Sm^{3+} doped and Sm^{3+}/Eu^{3+} co-doped phosphors show colour tunability from reddish-orange to pure red regions. All the results obtained finally revealed the utility of the titled phosphors as tunable red emitters needed to fabricate w-LEDs.

The content of this chapter has been published in an international journal - **Journal of Materials Science: Materials in Electronics, 34 (2023) 1662**.

5.1 Introduction

In the current era, increasing human power consumption by humankind is taking a toll on natural resources. Most of the electricity produced is consumed by lighting devices and traditional lighting sources are being replaced by w-LEDs, which are more efficient than the traditionally used incandescent and fluorescent lamps [93–96]. Researchers working in the field of phosphors are fiercely searching for novel and more efficient phosphor materials for the replacement of traditionally used materials in LEDs. Blue chips made of InGaN and yellow phosphor (YAG: Ce^{3+}) are used to create the commercially available white LEDs. [97,98]. But the light produced through this method has some shortcomings, such as a poor colour rendering index, a high correlated colour temperature, and mismatched warm white light due to the deficiency of the red component [99,100]. The introduction of red/orange emitting phosphors can improve these limitations. So, another approach that can be used for white light generation is either a combination of blue LED chips coated with green and red phosphors or UV LED chips coated with orange and cyan emitting phosphors. So, an orange-emitting phosphor in combination with a cyan-emitting phosphor under UV excitation can be a promising choice for researchers [101].

Recently, RE doped phosphor/glasses materials have been finding immense attention in the scientific community because of their vast applications in the fields of SSL technology, display devices, solar cells, etc. [102–105]. RE ion doping is usually preferred in phosphors due to their magnificent properties like high solubility, high luminescence efficacy, and large Stoke shifts [21,106–109]. Commercially, the red phosphor is fabricated with the sulfide-based Y_2O_2S: Eu^{3+} material, which is excited in the near-UV range [110]. The material Y_2O_2S: Eu^{3+}

is chemically unstable, decreasing its luminous efficiency [42]. Therefore, as a replacement for this, the development of a highly efficient red phosphor is required. Among all the RE ions, the Eu^{3+} and Sm^{3+} ions show promising results and give emission in the reddish-orange and pure red regions, respectively [20–23]. In a broad emission range that spans the UV to visible regions, they exhibit good electrical and optical properties. Here, optical transitions occur between a variety of f states, and the filled 5s and 5p subshells effectively shield the f electrons from their surroundings. [11, 24–26]. The Eu^{3+} is an effective activator ion due to its high colour purity and its intense red emission (615 nm) corresponding to transition $^5D_0 \rightarrow {}^7F_2$ [111]. The Sm^{3+} ion can act as a good sensitizer because of the lower energy difference between Sm^{3+} ($^4G_{5/2}$) and Eu^{3+} ($^5D_0$) and can transfer its excitation energy to Eu^{3+}. So, co-doping of Sm^{3+}/Eu^{3+} ions in a host lattice can broaden the excitation bands and helps in enhancing the luminescence efficiency for the red color emission in w-LEDs. Sm^{3+} ions can also act as a good activator when doped singly in some host compounds and gives orange-reddish emission. Such singly Sm^{3+} ions doped phosphors are used in such devices where the emission corresponding to the reddish-orange regions is needed. Therefore, in this article, we have reported our work on singly Sm^{3+}doped and Sm^{3+}/Eu^{3+} co-doped barium molybdenum titanate (BMT) based host lattice Ba_3MoTiO_8.

5.2. Experimental method and characterization techniques used:

The preparation of the BMT phosphor was done through the combustion method. In our previous work, we have reported the superiority of the combustion method used to prepare BMT phosphor because of relatively high luminescence efficiency, crystallinity, and better morphology [67]. This has prompted us to use the combustion method to prepare BMT

phosphor co-doped with samarium and europium ions to study color tunability. All the synthesis steps involved are discussed in section 2.2 and Fig. 2.1 (b).

The phase identification and confirmation of all the as-synthesized BMT phosphors was determined by an X-ray diffractometer (Bruker D8 Advanced X-Ray Diffractometer) with Cu-Kα radiation (λ = 1.54 Å) in the range of 2θ= 20º-70º. To analyze the structural parameters, Rietveld refinement was done using Full-Prof Suite software. The surface morphology and elemental distribution were checked by SEM on a JEOL 7610F Plus operated at 5 kV. To determine the various vibrational functions and groups present in the system, FT-IR was performed by Perkin Elmer spectrum 2. The diffuse reflectance spectral (DRS) studies were conducted on a Jasco-made V-770 Spectrophotometer at room temperature. A Jasco FP-8300 spectrofluorometer was used to record the PL excitation and emission spectra with a Xenon lamp serving as the excitation source. On a Hameg Instruments HM 1507 digital oscilloscope operating at 150 MHz, PL decay curves were captured. The ocean optics setup was used to record the temperature-dependent PL experiments with a resolution of 0.1 nm under a Xenon lamp excitation source.

5.3. Results and Discussion:

5.3.1. Structural and morphological analysis:

Figs. 5.1(a) and (b) show the XRD patterns of un-doped, single-doped BMT: xSm^{3+} (x= 0.5, 1, 1.5, 2, and 2.5mol%) and co-doped BMT: xSm^{3+}/yEu^{3+} (x=1.5mol%, y=1, 2, 3, 4, 5, 6mol%) phosphors along with standard JCPDS data (JCPDS No. 38-0254). From Fig. 5.1, it can be seen that all the diffraction patterns were in good agreement with the standard JCPDS patterns with rhombohedral crystal structure and space group R-3m (166) without the formation of any secondary crystallite phase. This shows the successful incorporation of dopant ions into the host lattice and single-phase confirmation of all the phosphors. By zooming in on the main intense peak of the XRD data, it is found that there is some shifting in the peak position towards the higher angle side with the introduction of Sm^{3+} and Eu^{3+} ions in the host lattice when compared with the un-doped sample. This shifting may be caused by the difference in the ionic radii of the Ba^{2+} ions (ionic radii =1.49 Å) in comparison to the dopant ions Sm^{3+} (ionic radii =1.09 Å) and Eu^{3+}(ionic radii =1.08Å). Fig. 5.2(a-b) shows the Rietveld refinement fitting for the xSm^{3+} (x= 1.5mol%) and xSm^{3+}/yEu^{3+} (x= 1.5mol%, y=1mol%) doped BMT phosphors using Full Proof suite software. In our earlier work, we performed Rietveld refinement on an un-doped BMT sample [112]. All the structural parameters extracted from the refinement fitting were listed in Table 5.1. The goodness of the fit (χ^2) value is less than 1, indicating no significant deviation in lattice parameters and the successful formation of single phase.

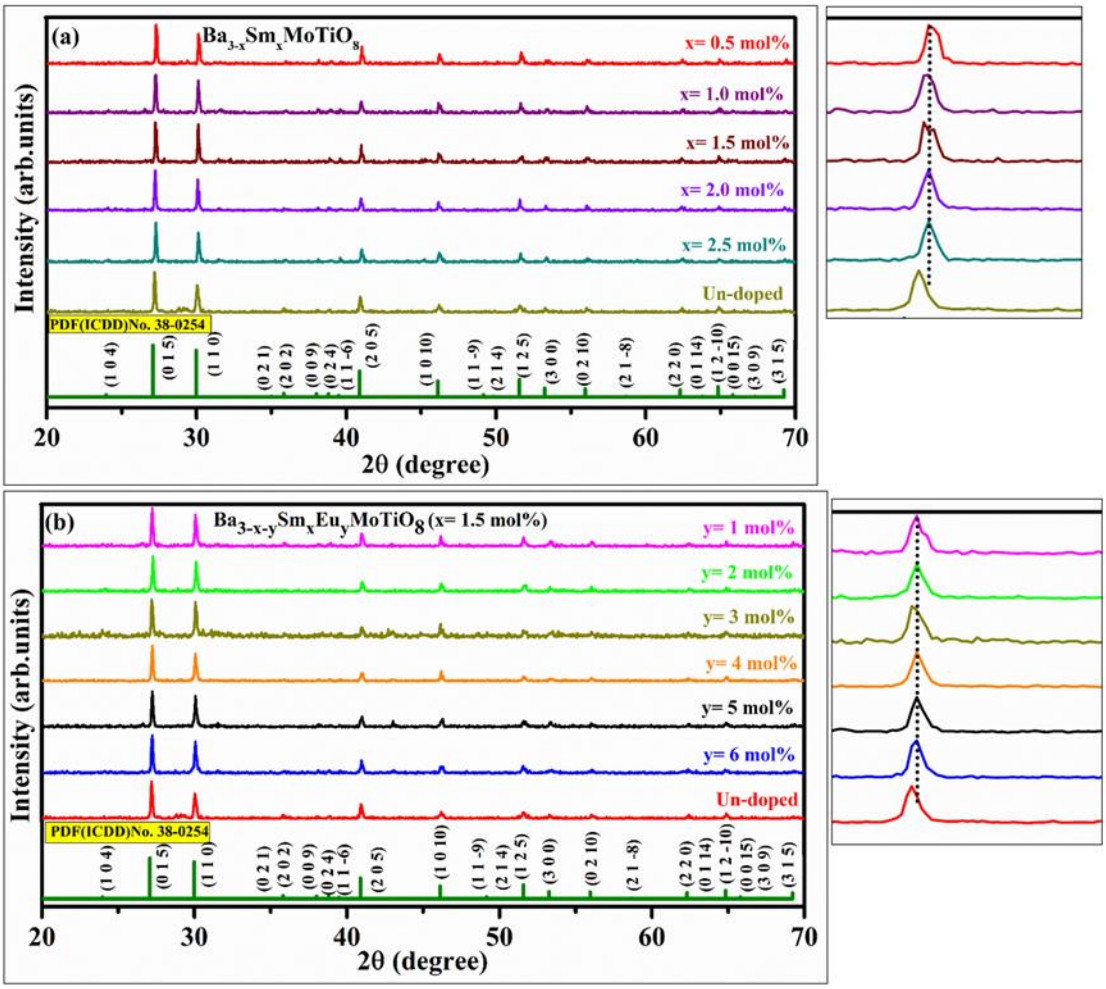

Fig. 5.1(a-b). XRD patterns of an un-doped, single doped BMT: xSm^{3+}(x= 0.5, 1.0, 1.5, 2.0 and 2.5mol%) and co-doped BMT: xSm^{3+}/yEu^{3+} (x=1.5mol% and y=1, 2, 3, 4, 5 and 6mol%) phosphors with standard JCPDS.

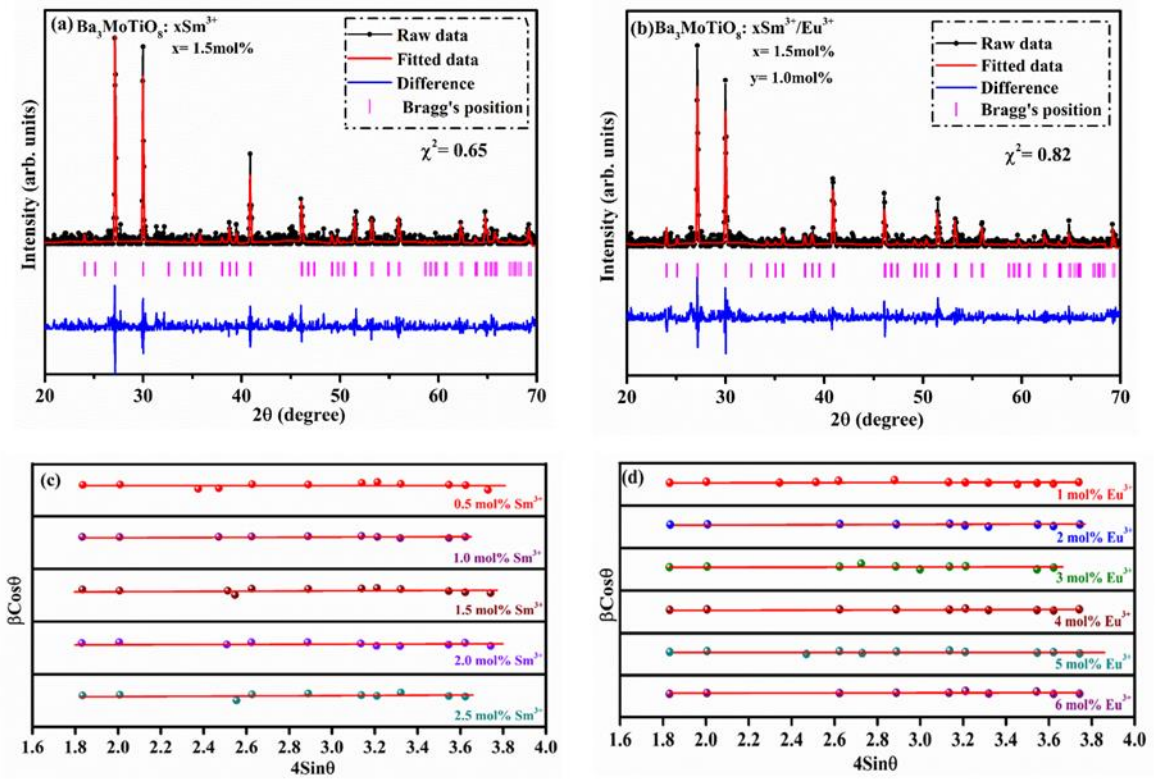

Fig. 5.2(a-b) Rietveld refinement for BMT: xSm^{3+}(x= 1.5mol%) and BMT: xSm^{3+}/Eu^{3+} (x= 1.5mol%, y= 1.0mol%) co-doped phosphors respectively & **(c-d)** correspondong W-H plots for all concentrations of Sm^{3+} and Eu^{3+} ions.

Table 5.1. Calculated structural lattice parameters through Rietveld refinement.

Parameters	**Standard data JCPDS (038-0254)**	**BMT: xSm^{3+} x = 1.5mol%**	**BMT: xSm^{3+}/ yEu^{3+} x = 1.5mol% y = 1mol%**	**BMT (un-doped)**
a (Å)	5.9570	5.9596	5.9568	Ref. [23]
b (Å)	5.9570	5.9596	5.9568	
c (Å)	21.2900	21.2903	21.2936	
α = β	90	90	90	
γ	120	120	120	
χ^2	-	0.65	0.82	
Cell volume($Å^3$)	654.28	654.84	654.32	

The average crystallite size of the single and co-doped phosphors was calculated by the Debye- Scherrer formula given by eq. (14) in chapter 2.

The crystallite size corresponding to the most intense peak calculated for single Sm^{3+} ion-doped phosphors lies in the 60-70 nm range, and for Sm^{3+}/Eu^{3+} co-doped phosphors, it lies in the range of 62-72 nm. As we know, the broadening of the XRD peak is due to the crystallite size in addition to the strain present in it. To calculate the lattice strain present in the crystal, a Williamson-Hall plot has been used using the equation [113]-

$$\beta_T \, Cos\theta = \frac{s\lambda}{D} + \varepsilon(4Sin\theta) \qquad (24)$$

The symbol ε represents the strain present in the lattice, and the other symbols have the exact same meaning as discussed above. A linear graph has been plotted between $4Sin\theta$ and $\beta_T Cos\theta$ by considering the major peaks in the XRD data, as shown in Fig.5.2(c&d). The slope of the fitted line gives the value of strain, and from the intercept value, we calculate the crystallite size. The average crystallite size for singly Sm^{3+} doped and Sm^{3+}/Eu^{3+} co-doped phosphors was found to be 98 nm and 88 nm, respectively. The value of strain was found in the range of 0.000170-0.000353 for Sm^{3+} doped phosphors, and for Sm^{3+}/Eu^{3+} co-doped phosphors, it lies in the range of 0.000267-0.0007.

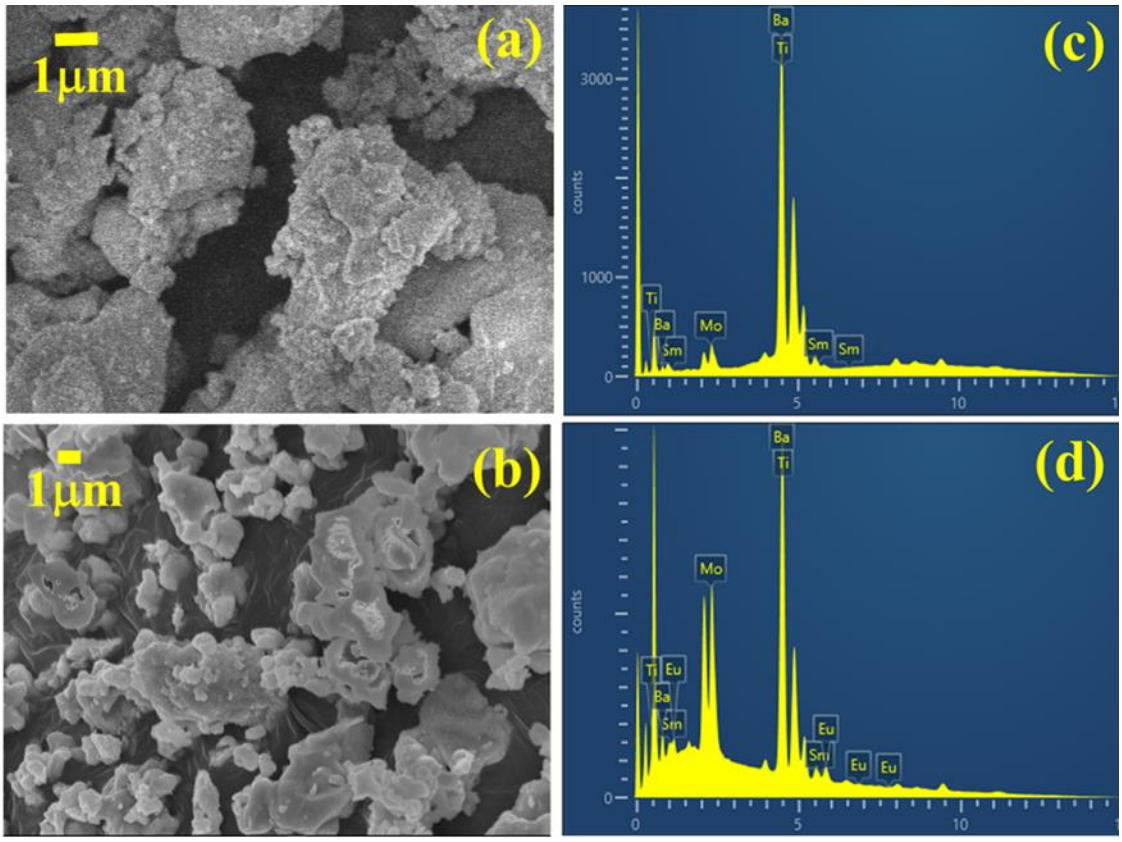

Fig. 5.3. Scanning electron microscope images (a-b) of BMT: xSm^{3+} doped (x=1.5mol%) and BMT: xSm^{3+}/yEu^{3+} (x=1.5mol% and y=1mol%) co-doped phosphors and (c-d) corresponding EDX images.

Additionally, SEM and energy dispersive X-ray analysis (EDX) have been performed to further investigate the microscopic morphology and elemental composition of the prepared phosphors. Figs. 5.3(a&b) represent the SEM micrographs of single doped BMT: xSm^{3+}(x=1.5mol%) and co-doped BMT: xSm^{3+}/yEu^{3+} (x=1.5mol%, y= 1mol%) phosphors. The particles of these phosphors are irregular in shape with much agglomeration. These irregularities in shape and size may be due to the unequal distribution of mass and temperature during the sintering as well as due to the manual crushing of phosphor after sintering [114]. The size of particles for single-doped and co-doped phosphors are in the range of 0.5-5.0 μm and 0.1-6.0 μm respectively. Fig. 5.3 (c&d) demonstrate the corresponding EDAX images of

these phosphors. It can be seen from both the EDX images that all elements are present in the phosphor lattice that have been used during synthesis.

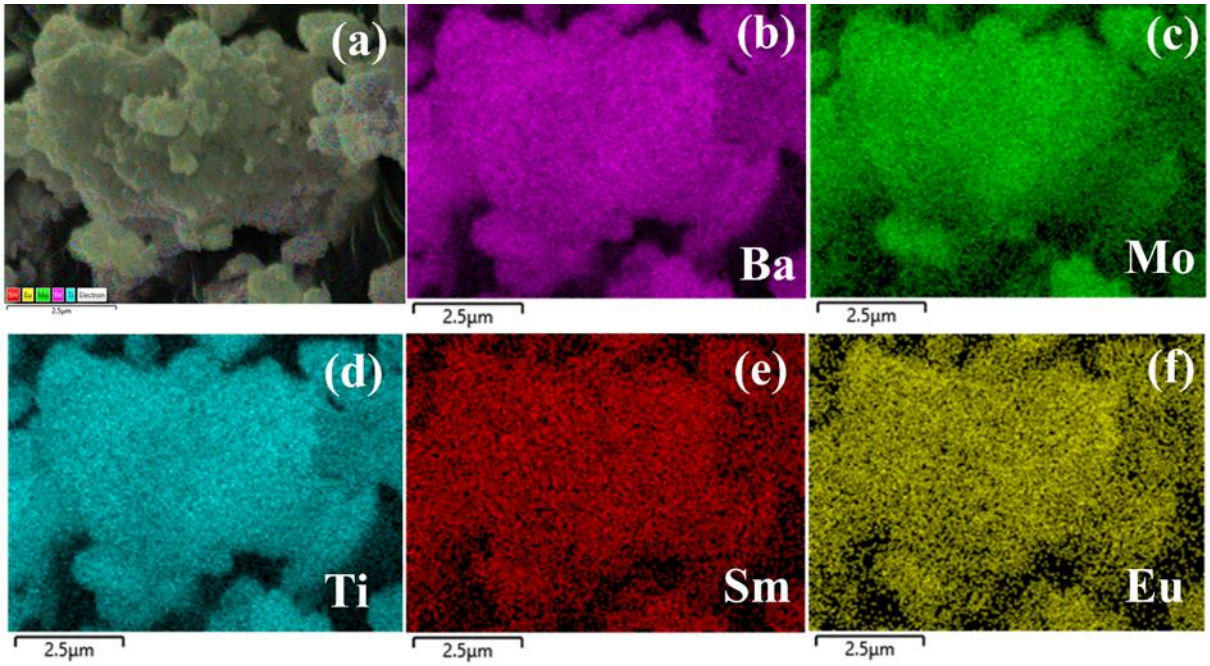

Fig. 5.4. Elemental mapping of BMT: xSm^{3+}/yEu^{3+} (x=1.5 mol%, y=1 mol%) co-doped BMT phosphor (a)mixed mapping (b-f) individual of Barium (Ba), Titanium (Ti), Molybdenum (Mo), Samarium (Sm) and Europium (Eu) elements.

Fig. 5.4 shows the elemental mapping of co-doped BMT: xSm^{3+}/yEu^{3+} (x=1.5mol%, y= 1mol%) phosphor. From the elemental mapping images, it was clear that barium, molybdenum, titanium, samarium, and europium elements were uniformly distributed in the particles, which shows the successful synthesis of phosphor.

5.3.2. FT-IR analysis:

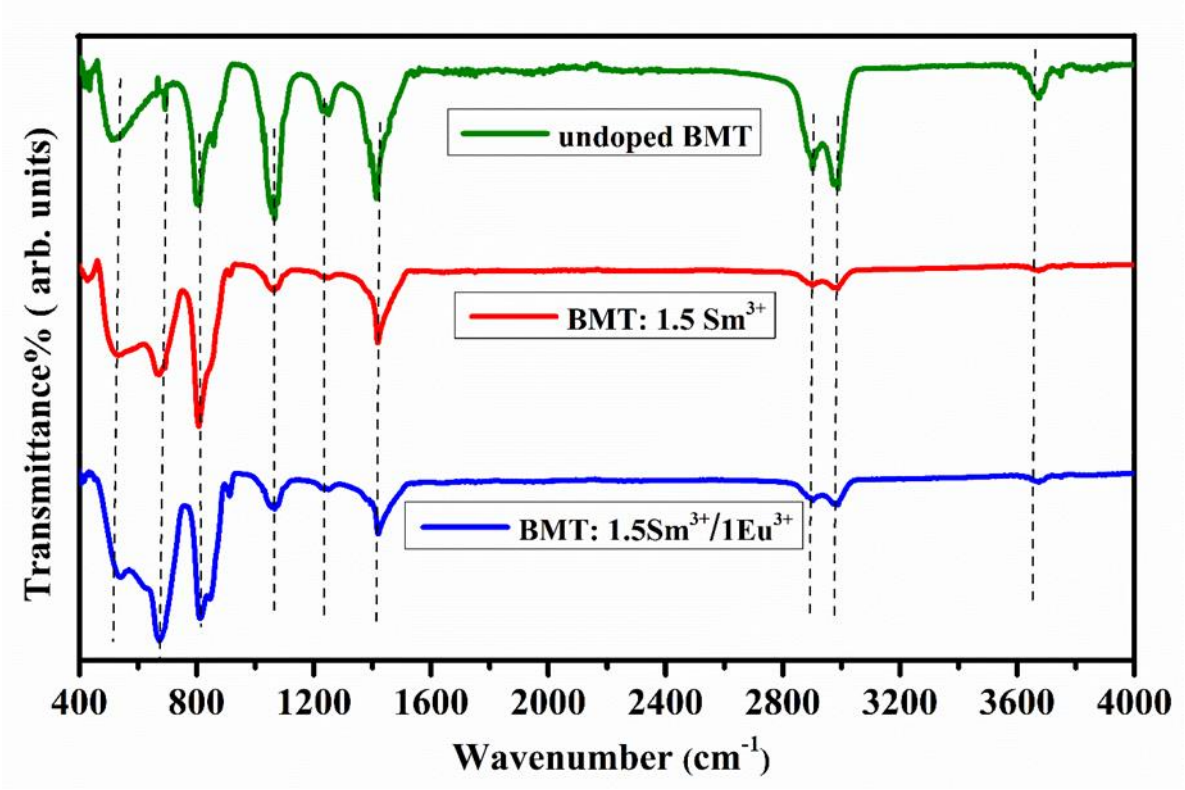

Fig. 5.5. FT-IR spectra of an undoped, xSm^{3+} doped(x= 1.5mol%), and co-doped xSm^{3+}/yEu^{3+} (x=1.5mol%, y=1mol%) phosphors.

FT-IR spectra of un-doped, singly doped BMT: xSm^{3+} (x=1.5mol%) and co-doped BMT: xSm^{3+}/yEu^{3+} (x=1.5mol%, y=1mol%) phosphors were recorded in attenuated total reflectance mode (ATR), as shown in Fig. 5.5. The spectra were in the range 400-4000 cm^{-1} to analyse the different functional groups that are present along with their stretching and bending vibrations. The infrared bands of all the phosphors occupy an almost similar position with or without doping. The absorption band at 530 cm^{-1} belongs to the stretching vibrations of Ti-O groups present in the system [85]. The bands at 678 and 818 cm^{-1} are due to the MoO_4^{2-} tetrahedrons ascribed to their Mo-O and Mo-O-Mo stretching vibrations [76,77]. The bands at 1068 and 1421 cm^{-1} demonstrate C-N stretching and C=C stretching, respectively [115,116]. The band

at 1230 cm-1 describes the N-H bending absorption [117]. The two bands at 2897 and 2996 cm^{-1} represent C-H bonding [118]. The shortest absorption band at 3670 cm^{-1} can be assigned to the stretching mode of O-H groups in absorbed water molecules [119].

5.3.3. DRS Spectra:

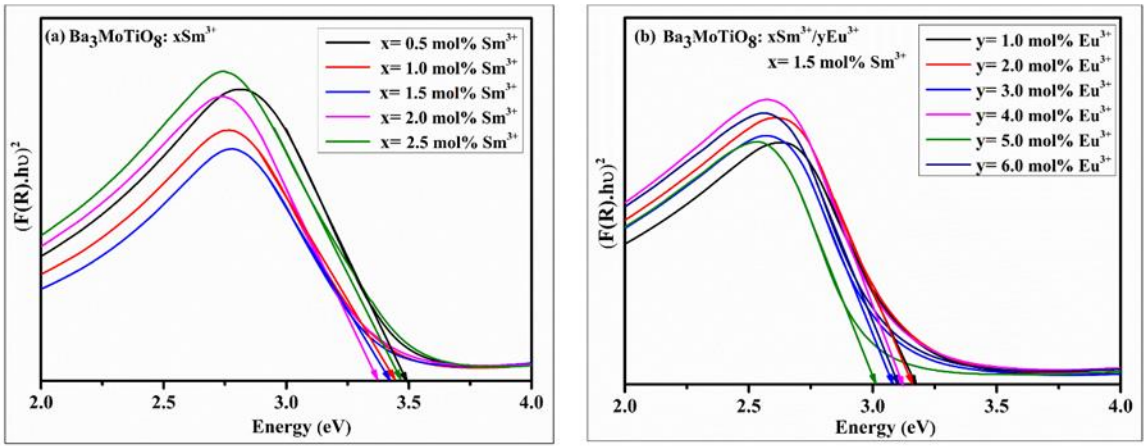

Fig. 5.6. $[F(R)h\nu]^2$ versus hν plot for optical band gap calculation of BMT**:** xSm^{3+}(x= 0.5, 1.0, 1.5, 2.0 and 2.5mol%) and BMT: xSm^{3+}/yEu^{3+} (x=1.5mol% and y=1, 2, 3, 4, 5 and 6mol%) phosphors.

Diffuse reflectance spectra were recorded for the BMT: xSm^{3+} (x= 0.5, 1, 1.5, 2 and 2.5mol%) and co-doped BMT: xSm^{3+}/yEu^{3+} (x=1.5mol%, y=1, 2, 3, 4, 5, 6mol%) phosphors. To find the optical band gap, the Kulbelka-Munk function was applied to the DRS data given by equation (16) and (17) in chapter 2 [120].

In that equation, n is a transition dependent constant with values of 1/2, 2, 1/3, and 3 for direct allowed, indirect allowed, direct forbidden, and indirect forbidden, respectively.

Now a graph was plotted between $[F(R)h\upsilon]^2$ vs. energy hυ for the n=1/2 transition, as shown in Fig.5.6. By extrapolating from the linear section of the figure, the intercept on the x-axis provides an approximation of the band gap value. The approximate band gap values for singly Sm^{3+} doped BMT phosphors lie in the range 3.3-3.5 eV, and for co-doped BMT:

Sm^{3+}/Eu^{3+} phosphors lie in the range 3.0-3.25 eV, respectively [121]. The band gap energy decreases with the addition of co-doping of Eu^{3+} ions. This results in a greater number of atoms getting excited to the upper states and thereby resulting a stronger emission when they fare falling down to the lower energy states. The band gap values obtained in the present work are in consonance with the values reported for other phosphors doped with Sm^{3+} and Eu^{3+} ions [122,123].

5.3.4. PL Studies:

5.3.4.1. PL Studies of BMT: xSm^{3+}(x= 1.5 mol%) phosphor:

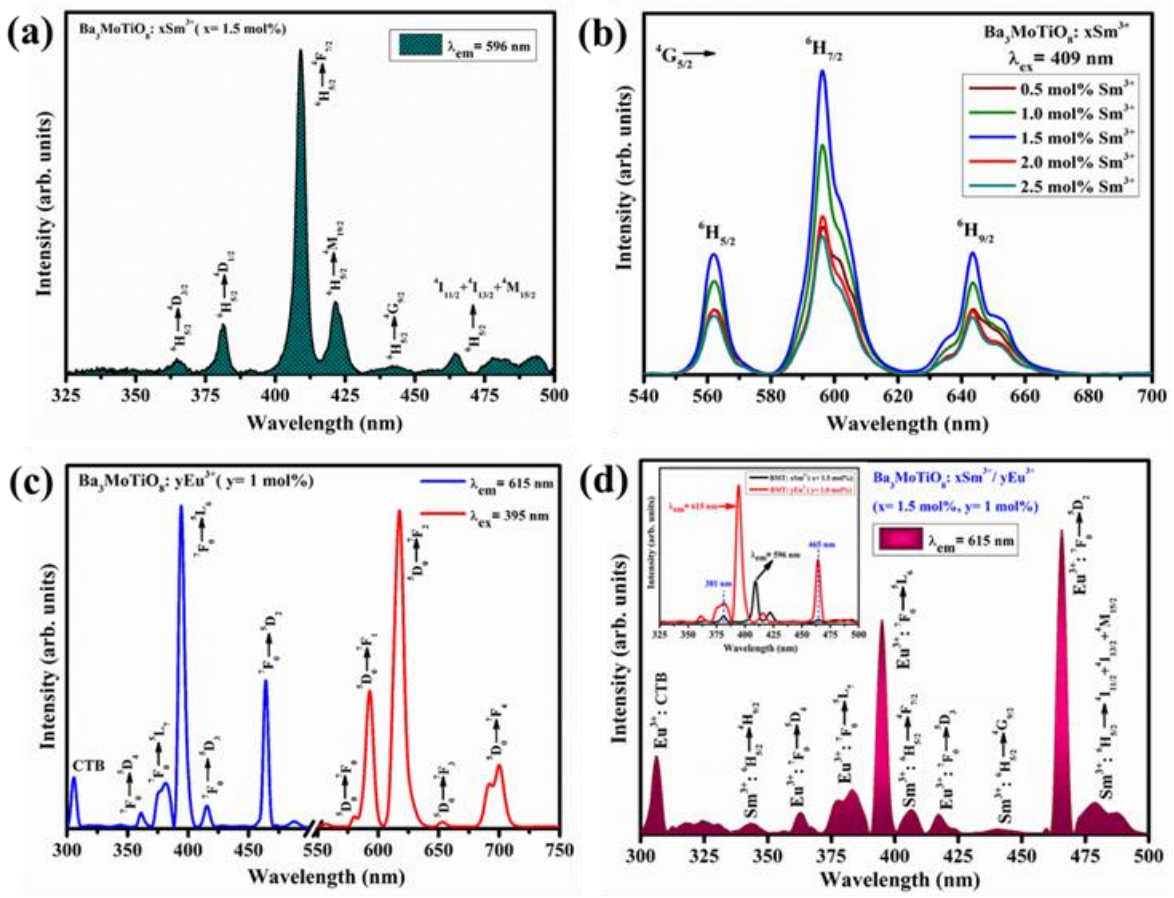

Fig. 5.7. (a) PL excitation spectrum of BMT**:** xSm^{3+}(x= 1.5mol%) under 596 nm emission **(b)** emission spectra of BMT**:** xSm^{3+}(x= 0.5,1.0,1.5,2.0 and 2.5mol%) phosphors under 409 nm excitation wavelength, **(c)** PL excitation and emission spectrum of BMT**:** yEu^{3+}(y= 1.0mol%) phosphor under 615 nm emission and 395 nm excitation wavelengths, respectively & **(d)** PL

excitation spectrum of BMT**:** xSm^{3+}/yEu^{3+}(x= 1.5mol%, y=1mol%) phosphor under 615 nm emission wavelength (inset figure shows the overlapped excitation spectrums of singly Sm^{3+} doped and Sm^{3+}/Eu^{3+} co-doped phosphors at emission wavelengths 596 and 615 nm respectively).

Fig. 5.7(a & b) show the excitation spectrum and emission spectra of BMT: xSm^{3+}(x= 1.5mol%) phosphor, respectively. A 596 nm emission wavelength was used to record the excitation spectra, which ranged from 325 to 500 nm. The spectrum comprises several peaks at 364, 381, 409, 421,442 and 465 nm corresponding to the transitions $^6H_{5/2} \rightarrow {}^4D_{3/2}$, $^6H_{5/2} \rightarrow {}^4D_{1/2}$, $^6H_{5/2} \rightarrow {}^4F_{7/2}$, $^6H_{5/2} \rightarrow {}^4M_{19/2}$, $^6H_{5/2} \rightarrow {}^4G_{9/2}$ and $^6H_{5/2} \rightarrow {}^4I_{11/2} + {}^4I_{13/2} + {}^4M_{15/2}$ respectively [124–127]. Out of these peaks, the most intense peak in the excitation spectrum is at 409 nm, so we recorded the emission spectra for BMT: xSm^{3+}(x= 0, 1, 1.5, 2 & 2.5mol%) series at this excitation wavelength. The emission spectra of this series recorded in the range of 540-700 nm comprise three bands at wavelengths 562, 596, and 643 nm corresponding to a transition from the excited state $^4G_{5/2}$ of Sm^{3+}ions to ground states $^6H_{5/2,}$ $^6H_{7/2}$ and $^6H_{9/2}$ respectively [128,129]. The intensity of emission peaks increases with Sm^{3+}ions concentration up to 1.5mol%; beyond that, emission intensity decreases, which is attributed to the phenomenon of concentration quenching. Concentration quenching is the phenomenon in which if we increase the activator ions higher than a certain value, the number of non-radiative transitions rises through cross-relaxation processes and results in low PL intensity. In the present work, it was observed that, 1.5 mol% of Sm^{3+} ions produce concentration quenching as shown in Fig. 5.7 (b). The most intense band at 596 nm wavelength corresponds to reddish-orange emission under UV excitation. So Sm^{3+} doped BMT phosphors can be used with cyan-emitting phosphors by coating them with UV LED as reddish-orange colour emitting devices, and by co-doping them with Eu^{3+} ions, they can be used to obtain pure red emission.

5.3.4.2. PL Studies of single doped Eu^{3+} & Sm^{3+}/Eu^{3+} co-doped BMT phosphors:

The PL excitation and PL emission spectra of BMT: yEu^{3+}(y= 1mol%) phosphor were reported in Fig. 5.7(c) at λ_{em}= 615 nm and λ_{ex}= 395 nm, respectively. The excitation spectrum recorded in the range 300-550 nm comprises peaks at wavelengths 306, 360, 381, 395, 415, and 465 nm corresponding to the charge transfer band (CTB), $^7F_0 \rightarrow {}^5D_4$, $^7F_0 \rightarrow {}^5L_7$, $^7F_0 \rightarrow {}^5L_6$, $^7F_0 \rightarrow {}^5D_3$, and $^7F_0 \rightarrow {}^5D_2$ transitions of Eu^{3+} ions respectively [130]. The emission spectrum was recorded using the most intense peak of the excitation spectrum (λ_{ex}= 395 nm) in the range of 550-750 nm. The emission spectrum consists of five peaks at wavelengths 579, 596, 615, 653, and 701nm corresponding to the transition of Eu^{3+} ions from excited state $^5D_0$ to $^7F_0$, $^7F_1$, $^7F_2$, $^7F_3$, and $^7F_4$ states, respectively [131]. The transition $^5D_0 \rightarrow {}^7F_1$ is a magnetic dipole (MD) in nature, whereas $^5D_0 \rightarrow {}^7F_2$ is an electric dipole (ED). In the emission graph, if the ED transition is ruling over the MD transition, that means the Eu^{3+} ion occupies anti-inversion symmetry and gives red emission corresponding to transition $^5D_0 \rightarrow {}^7F_2$ with high colour purity [132].

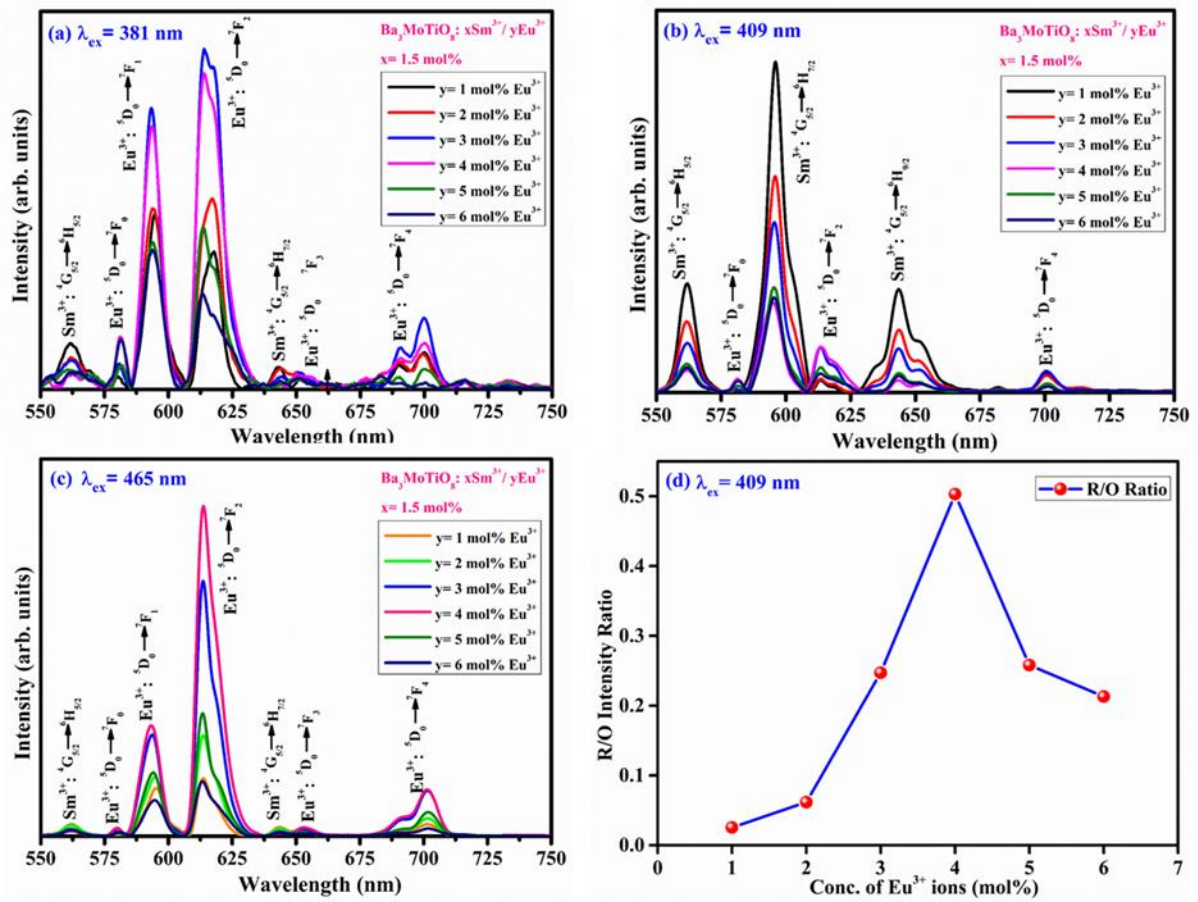

Fig. 5.8. PL emission spectra of BMT**:** xSm^{3+}/yEu^{3+} (x= 1.5mol%, y= 1,2,3,4,5 and 6mol%) co-doped phosphors under excitation wavelengths (a) 381 nm, (b) 409 nm and (c) 465 nm respectively & (d) plot of R/O ratio vs conc. of Eu^{3+} ions under λ_{ex}= 409nm.

The PL excitation spectrum of BMT: xSm^{3+}/yEu^{3+} (x=1.5mol%, y=1mol%) co-doped phosphor is shown in Fig. 5.7(d) in the wavelength range 300-500 nm by keeping λ_{em}= 615 nm. In the spectrum, the highest number of peaks are due to Eu^{3+} ions, and some peaks are due to Sm^{3+} ions. The Sm^{3+} ion peaks at 343, 406, 440, and 480 nm are due to the transitions $^6H_{5/2} \rightarrow {}^4H_{9/2}$, $^6H_{5/2} \rightarrow {}^4F_{7/2}$, $^6H_{5/2} \rightarrow {}^4G_{9/2}$ and $^6H_{5/2} \rightarrow {}^4I_{11/2} + {}^4I_{13/2} + {}^4M_{15/2}$ respectively. Eu^{3+} ion peaks are present at 306, 362, 382, 395, 417, and 465 nm, corresponding to transitions CTB, $^7F_0 \rightarrow {}^5D_4$, $^7F_0 \rightarrow {}^5L_7$, $^7F_0 \rightarrow {}^5L_6$, $^7F_0 \rightarrow {}^5D_3$ and $^7F_0 \rightarrow {}^5D_2$ respectively. The inset of Fig. 5.7(d) shows the excitation spectrum of BMT: xSm^{3+} (x=1.5mol%) and BMT: yEu^{3+} (y=1mol%) by keeping

the emission wavelengths at 596 and 615 nm, respectively. By taking into account this inset of Fig. 5.7(d), the emission spectra of BMT: xSm^{3+}/yEu^{3+} (x=1.5mol%, y=1, 2, 3, 4, 5, and 6mol%) co-doped phosphors were recorded at three different excitation wavelengths (381, 409. and 465 nm). Here, 409 nm is the Sm^{3+} ion (sensitizer) excitation wavelength, and 381 and 465 nm are the overlapping wavelengths of Sm^{3+} and Eu^{3+} ions.

Fig. 5.8(a, b & c) show the emission spectra of co-doped BMT: xSm^{3+}/yEu^{3+} (x=1.5mol%, y=1,2,3,4,5 and 6mol%) phosphors at λ_{ex}= 381, 409, and 465nm respectively. The emission spectra at λ_{ex}= 381 nm show seven peaks. Out of these seven peaks, two peaks at 562 nm ($^4G_{5/2} \rightarrow {}^6H_{5/2}$) and 644 nm ($^4G_{5/2} \rightarrow {}^6H_{7/2}$) correspond to the Sm^{3+} ion transitions, and the other five peaks at 581 ($^5D_0 \rightarrow {}^7F_0$), 594 ($^5D_0 \rightarrow {}^7F_1$), 615 ($^5D_0 \rightarrow {}^7F_2$), 652 ($^5D_0 \rightarrow {}^7F_3$) and 700 nm ($^5D_0 \rightarrow {}^7F_4$) due to the Eu^{3+} ion transitions [133]. The spectra given in Fig. 5.8(a, b &c) show that with increasing concentration in Eu^{3+} ions, the emission intensity of Eu^{3+}ion peaks increase while Sm^{3+} ion peak intensity decreases. The emission spectra given in Fig. 5.8(b) were recorded at λ_{ex}= 409 nm. With an increased concentration of Eu^{3+} ions, the emission intensity of Sm^{3+} peaks decreased, and Eu^{3+} ion peaks increased up to 4 mol%. This confirms the energy transfer mechanism of Sm^{3+} ions to Eu^{3+} ions. After a 4 mol% concentration of Eu^{3+} ions, the energy transfer mechanism becomes constant, i.e., it attains saturation. This may be due to the phenomenon of concentration quenching. Fig. 5.8(d) shows the increase in Red to Orange (R/O) emission intensity with different Eu^{3+} ion concentrations at λ_{ex}= 409 nm. The R/O ratio is increasing up to 4mol% concentration of Eu^{3+} ions. Increasing R/O ratio is a clear indication of energy transfer from Sm^{3+} to Eu^{3+} ions [65].

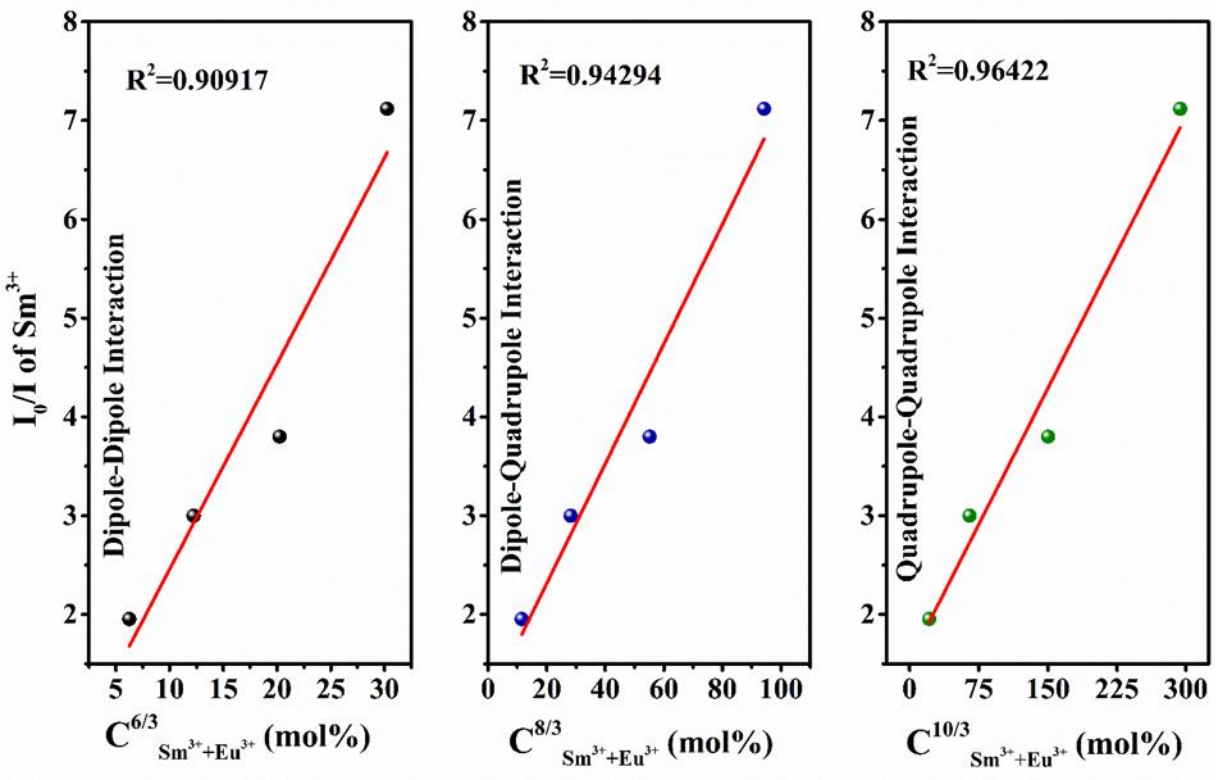

Fig. 5.9. Variation of I_{SM}/I_{SU} of Sm^{3+} ion w.r.t. (a) $C^{6/3}$ (b) $C^{8/3}$and (c) $C^{10/3}$ for BMT**:** xSm^{3+}/yEu^{3+} (x= 1.5mol%, y= 1,2,3,4,5 and 6mol%) co-doped phosphors under 409 nm excitation wavelength.

To explain that energy transfer mechanism via multipolar interaction, Dexter's formula, along with Reisfeld's approximation, was applied as [134] given in eq. (9) of chapter 1-

Where η_0 and η represent the luminescent quantum efficiencies of Sm^{3+} ions without Eu^{3+} ion doping and with Eu^{3+} ion doping, respectively, C is the sum of the concentration of activator (Eu^{3+}) and sensitizer (Sm^{3+}) ions, and n is a number that indicates the type of multipolar interaction (n = 6, 8 and 10 for dipole-dipole, dipole-quadrupole, and quadrupole-quadrupole interaction, respectively). The ratio of luminescence intensities can be used to roughly calculate the ratio of quantum efficiencies given in eq. (10)[135,136]-

$$\frac{I_{SM}}{I_{SU}} \alpha\, C^{n/3}$$

Here I_{SM} is the luminescence emission intensity for the Sm^{3+} ion-doped sample, and I_{SU} is the luminescence emission intensity for the Sm^{3+}/Eu^{3+}co-doped sample. A graph was plotted between I_{SM}/ I_{SU} versus $C^{n/3}$ by taking n = 6, 8, and 10 under λ_{ex}= 409 nm in Fig. 5.9. The best linear regression was found in the case of n=10, which shows that quadrupole-quadrupole interaction is responsible for energy transfer mechanism from Sm^{3+} to Eu^{3+} ions [127].

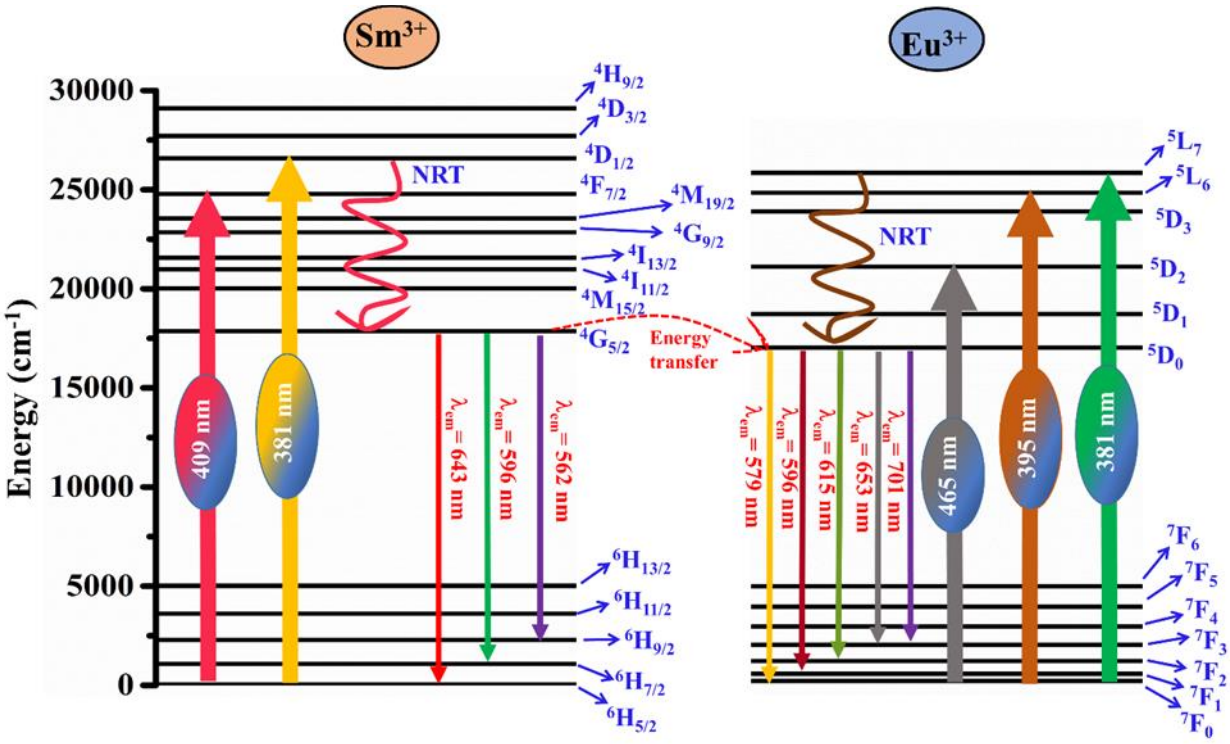

Fig. 5.10. Schematic energy level diagram of Sm^{3+} and Eu^{3+} ions and their energy transfer mechanism.

Fig. 5.10 shows the energy level diagram of Sm^{3+} and Eu^{3+} ions to display the energy transfer mechanism between these two ions. There is a very small energy difference between the energy level $^4G_{5/2}$ of the Sm^{3+} ion and the $^5D_0$ level of the Eu^{3+} ion. Due to this, the Sm^{3+} ion can act as an efficient sensitizer for Eu^{3+} ions [137].

5.3.5. PL decay studies:

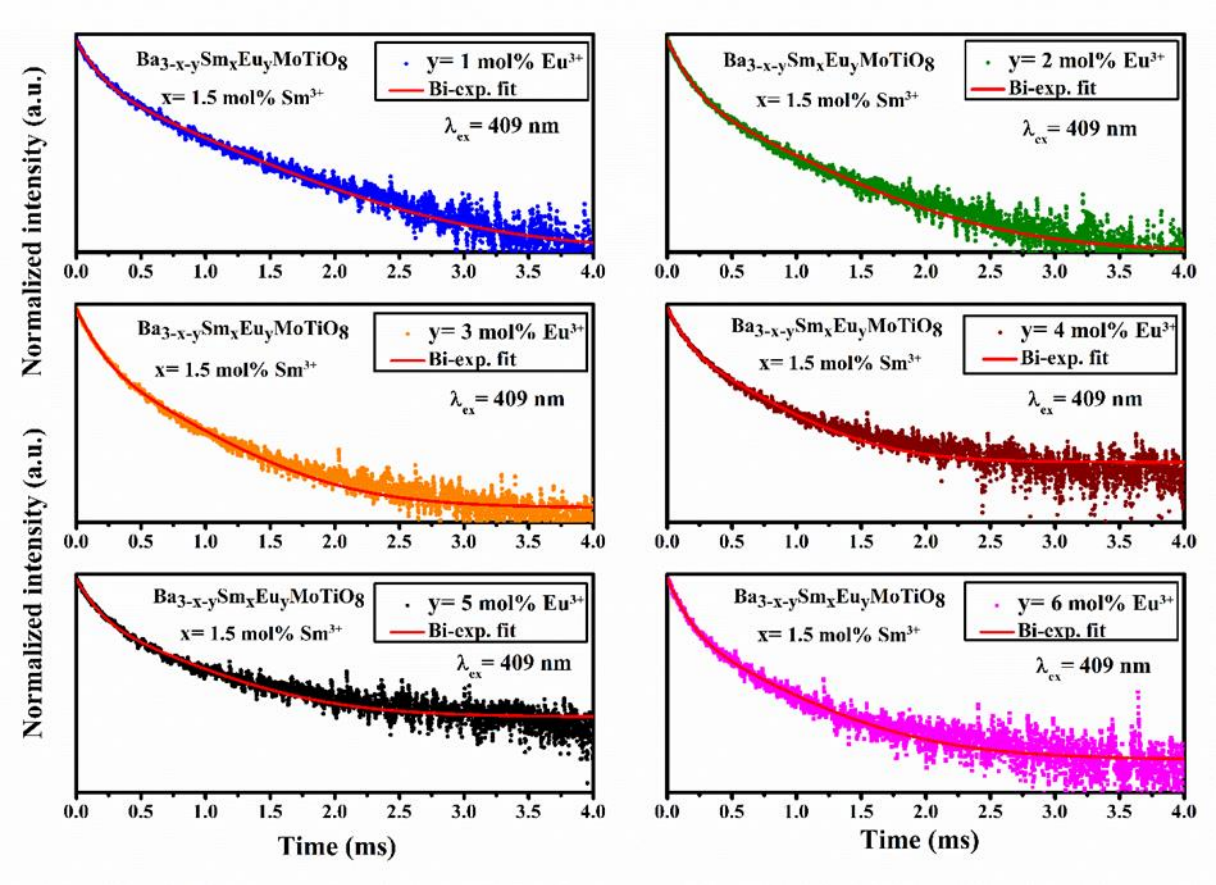

Fig. 5.11. PL lifetime curves of BMT**:** xSm^{3+}/yEu^{3+} (x=1.5mol% and y=1,2,3,4,5 and 6mol%) phosphors under 409 nm excitation.

The PL decay curves of BMT: xSm^{3+}/yEu^{3+} (x =1.5mol%, y =1, 2, 3, 4, 5, and 6mol%) phosphors excited under a 409 nm wavelength have been shown in Fig. 5.11. The PL decay curves show best fitting for a non-linear bi-exponential function given by eq. (12) in chapter 1 [124,138]-

The average lifetime values of the co-doped BMT phosphors are listed in Table 5.2 [124,139,140]. The lifetime values of the Sm^{3+}/Eu^{3+} co-doped BMT phosphors initially decrease up to 4 mol% of Eu^{3+} ions and reach saturation beyond. This indicates energy transfer

from a donor (Sm^{3+} ions) to an acceptor (Eu^{3+}) ion, up to 4 mol% of Eu^{3+} ions in the BMT phosphors. This result is in consonance with the information given by the PL spectral data of Sm^{3+}/Eu^{3+} co-doped BMT phosphors. The PL intensity of the co-doped BMT phosphor increases up to 4mol% of Eu^{3+} ion concentration and decreases further [132,139]. After that concentration, energy transfer saturates and results in an intensity decrement in the PL spectra due to the phenomenon of concentration quenching. As a result of it, lifetime decay curve behaviour also changes.

Table 5.2. Lifetime decay values of BMT: xSm^{3+}/ yEu^{3+}(x= 1.5mol%, y= 1,2,3,4,5 and 6mol%) co-doped phosphors for λ_{ex}=409 nm.

Sample ID (Sm^{3+}/Eu^{3+} series)	**Lifetime values (ms)**
y= 1mol%	0.60 Ref. [40,56,57]
y= 2mol%	0.448
y= 3mol%	0.257
y= 4mol%	0.205
y= 5mol%	0.273
y= 6mol%	0.311

5.3.6. Temperature-dependent PL studies:

Thermal stability is an important parameter for phosphor utilisation in SSL and wLED applications. To check the thermal stability of BMT: xSm^{3+}/yEu^{3+} (x =1.5mol%, y =4mol%) co-doped phosphor, temperature-dependent PL spectra have been recorded by taking the 409 nm excitation wavelength.

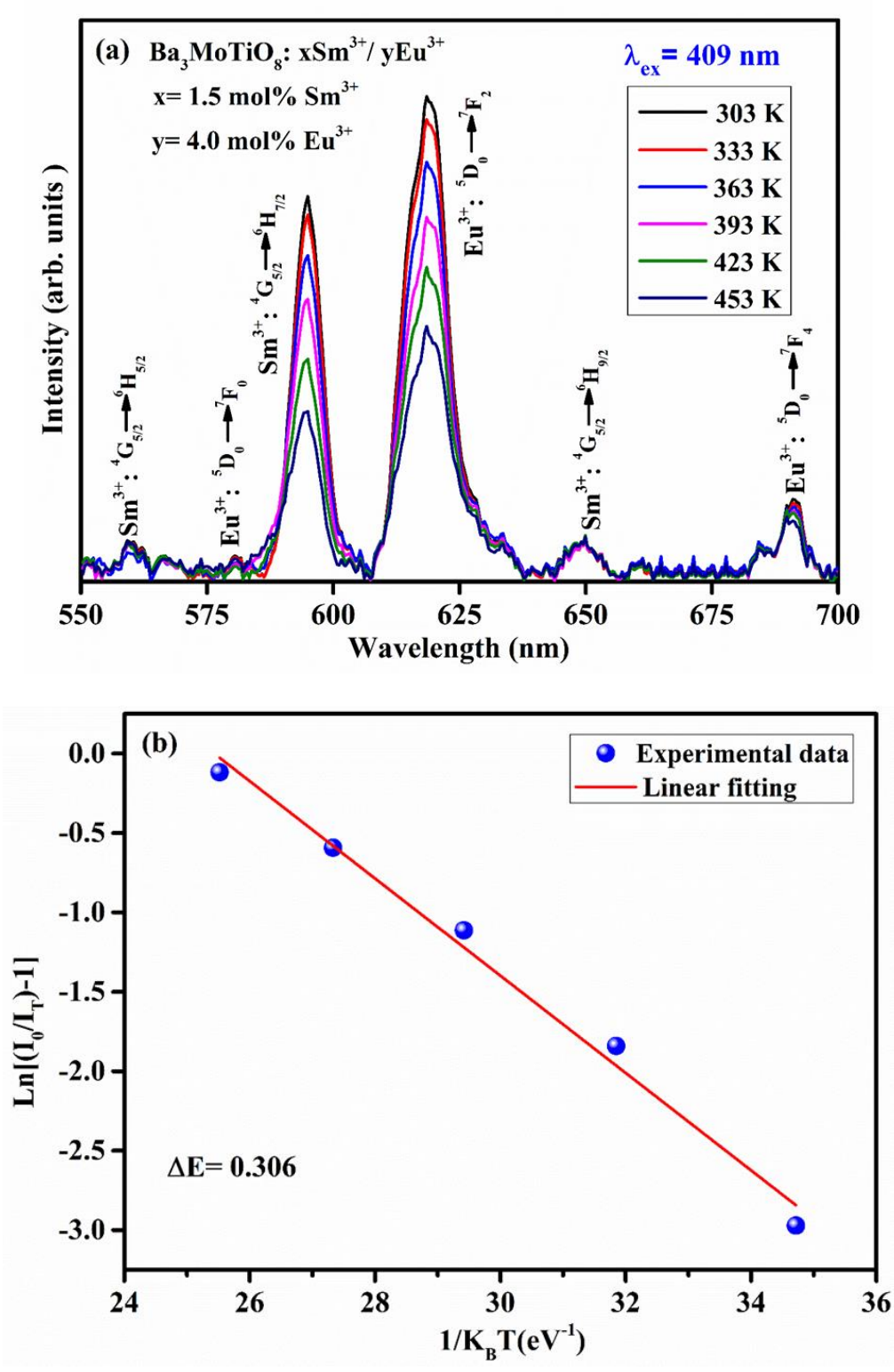

Fig. 5.12. Temperature-dependent PL emission spectra (a) of BMT**:** xSm^{3+}/yEu^{3+} (x= 1.5mol%, y= 1,2,3,4,5 and 6mol%) co-doped phosphors under excitation wavelengths 409 nm & (b) Graph of $Ln(I_0/I_T-1)$ vs. $1/K_BT$ for activation energy.

Fig. 5.12(a)shows the PL spectral curves by varying the temperature from 303 K to 453 K. With variation in temperature, a decrease in the luminescence intensity of the phosphor has been observed without any change in the emission profile. This decrement in intensity may be due to the thermal quenching effect, which increases the non-radiative electronic transitions and results in low luminescence intensity. Up to the 423 K, the phosphor retains approximately 65% of its luminescence intensity, showing the thermal stability of this phosphor. The activation energy of the co-doped phosphor can be calculated using this equation [135]-

$$I_T = \frac{I_0}{1+C\ exp.\left(\frac{-\Delta E}{K_B T}\right)} \quad (25)$$

where I_0 and I_T represent the luminescence intensities at room temperature and at a certain temperature, respectively. Here, C is an equation constant. Fig. 5.12(b) shows a graph plotted between $\ln(I_0/I_T\text{-}1)$ and $1/K_BT$, and linear fitting in this plot gives the value of the slope. The activation energy (ΔE= 0.306) calculated from the slope was compared with the previously reported work and showed the good thermal stability of the co-doped phosphor [141].

5.3.7. CIE performance:

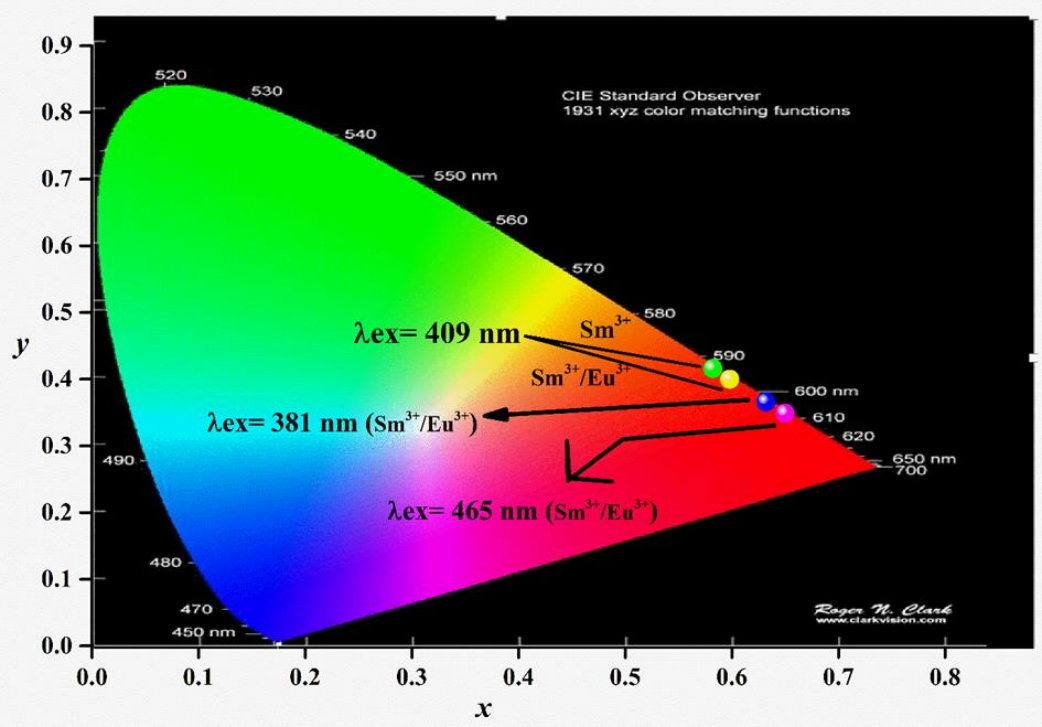

Fig. 5.13. CIE plot of optimised single Sm^{3+} doped (under 409 nm excitation) and Sm^{3+}/Eu^{3+} co-doped phosphors (under 381, 409, and 465 nm excitation), respectively.

Using PL emission spectral data, CIE coordinates were determined for the optimised single- and co-doped BMT phosphors, as shown in Fig. 5.13. The CIE coordinates for the optimised single Sm^{3+} ion (1.5mol% concentration) doped BMT phosphor were (0.582, 0.416) under the 409 nm excitation wavelength, which lie in the orange- reddish region. CIE co-ordinates for the BMT: xSm^{3+}/yEu^{3+} (x =1.5mol%, y =4mol%) phosphor were calculated to be (0.632, 0.36), (0.598, 0.40) and (0.650, 0.349) under 381 nm, 409 nm, and 465 nm excitation wavelengths, respectively. All the CIE coordinates for co-doped phosphors lie in the pure red region.

5.4. Conclusion:

A series of singly Sm^{3+} doped BMT: xSm^{3+} (x =0.5, 1, 1.5, 2 and 2.5mol%) and co-doped BMT: xSm^{3+}/yEu^{3+} (x =1.5mol%, y =1, 2, 3, 4, 5 and 6mol%) phosphors were successfully

synthesized by combustion method. The single-phase confirmation of these singly doped and co-doped phosphors was done by XRD patterns. All the phosphors show sharp XRD peaks without any impurities. Through SEM, morphological analysis has been performed, and particle size was calculated to be in the micrometer range. All the elements were uniformly distributed over the surface of the crystal, and that has been confirmed by EDX. FT-IR spectra recorded for an un-doped, single Sm^{3+} doped, and Sm^{3+}/Eu^{3+} co-doped phosphors show similar vibrational and absorption bands. The optical band gap obtained from the DRS study lies in the range of 3.0 - 3.5 eV for all the concentrations of Sm^{3+} and Sm^{3+}/Eu^{3+} co-doped phosphors. PL spectra recorded under the 409 nm excitation wavelength for the singly Sm^{3+} ion doped phosphors show reddish-orange emission at the 596 nm wavelength, corresponding to transition $^4G_{5/2} \rightarrow {}^6H_{7/2}$. Sharp red emission at 615 nm corresponding to transition $^5D_0 \rightarrow {}^7F_2$ is visible in PL spectra for co-doped BMT phosphors that were taken at three distinct excitation wavelengths (409, 381, and 465 nm). The intensity of the Eu^{3+} peaks increases with an increase in Eu^{3+} ion concentration, while the Sm^{3+} peaks decrease under the 409 nm excitation wavelength, according to PL spectral analyses of co-doped phosphors. This shows the energy transfer mechanism from Sm^{3+} ions to Eu^{3+} ions in the co-doped phosphors. Quadrupole-quadrupole interaction is the basis for this energy transfer process, according to Dexter's theory applied to it. CIE coordinates calculated for optimized single Sm^{3+} ion-doped phosphors lie in the reddish-orange region, and for co-doped phosphors lie in the red region, demonstrating the energy transfer induced colour tunable behaviour from the reddish-orange to red region, respectively. These studies show the application of prepared phosphors in orange and red color-emitting LED devices.

CHAPTER 6

Structural and luminescence studies on thermally stable Bi^{3+} activated Ba_3MoTiO_8 phosphors for near UV pumped w-LED applications

This research presents the outcomes of diverse morphological and PL studies performed on Bi^{3+} ions doped Ba_3MoTiO_8 phosphors prepared via conventional solid-state reaction method. Phase assessment was carried out via the XRD studies. FESEM and EDAX analysis have been used to study the surface morphology and elemental composition. FT-IR was used to study the character and vibrational frequencies of bonds in the phosphor lattice. Room-temperature PL was performed under 275 nm and 386 nm excitations displaying a broad band in the blue region corresponding to $^3P_1 \rightarrow {}^1S_0$ transition of Bi^{3+} ions. The CIE coordinates and correlated colour temperature values show that the as-prepared phosphors emit in the blue vicinity. The decay curves under both excitation wavelengths show a single exponential behaviour. Temperature-dependent PL studies confirmed the high thermal stability of the phosphor. We want to endorse these phosphors as a blue-emitting component in w-LED and SSL applications.

The content of this chapter has been published in an international journal - **International Journal of Applied Ceramic Technology, 21 (2023) 1208-1219.**

6.1. Introduction:

RE doped phosphor materials today find immense usage in various imaging and optoelectronic applications like w-LEDs, SSL, solar cells, display devices, cathode ray tubes, lasers, scintillators, etc. [42,65,149–157,103,142–148]. Although RE materials give sharp luminescence, the w-LEDs built on such phosphor-based platforms have major disadvantages like low CRI and excessively CCT >4500K [103,158–160]. Near UV LED chips integrated with RGB phosphors have been used to construct w-LEDs [161–163]. RE ions like Eu^{3+} and Ce^{3+} are widely used with various host lattices to achieve a tunable emission in the desired wavelength region. This is because the 4f-5d electronic transitions in these RE ions are sensitive to the coordination environment. So, a proper choice of host matrix can indeed affect the luminescence efficiency [164].But it has been observed that RE doped phosphors re-absorb in the blue and green region leading to a decrease in luminescence efficiency [160,164]. Also, high purification and refinement are required for RE based materials. So, it is imperative to formulate RE free phosphors that have excitation in the near UV region and large absorption in the visible range along with a viable and inexpensive synthesis procedure [165].

Bismuth has an electronic configuration of $[Xe]4f^{14}5d^{10}6s^{2}6p^{3}$. There are five valence electrons in the outermost shell of bismuth. Due to this, the bismuth ion can have valence states between -3 and +5, with luminescence properties being dependent on the valence state of bismuth. The Bi^{3+} state is the most stable one [166]. Bismuth is available in abundance at low prices and can be excited in the near UV region (350-400 nm) [167]. Most importantly, there is no reabsorption of Bi^{3+} in the visible region, unlike RE ions, thereby resulting in no loss of reabsorption energy. Also, despite being a single emitting ion, the emission from Bi^{3+} can be tuned to cover emissions from the blue, green, and even red regions of the spectrum. This is

due to the non-radiative transition from $^3P_1 \rightarrow {}^1S_0$ of Bi^{3+} ion [164,167]. Thus, for our research work, we chose Bi^{3+} as an activator for our BMT phosphor.

In the current research work, BMT phosphors doped with Bi^{3+} ions have been synthesized via a solid-state reaction method and various characterization have been performed to check the utility of prepared phosphors in W-LED applications.

6.2. Material and Methods:

A series of xBi^{3+}(x= 0.5, 1.0, 1.5, 2.0, and 3.0mol%) ions doped BMT phosphors was prepared via solid-state reaction method. Fig. 2.1(a) comprises all the synthesis steps involved in the process. The obtained powder was reground again for characterization purposes.

The crystal phase was examined by the Bruker D8 Advanced X-ray Diffractometer by using Cu-Kα radiation (λ= 1.54 Å). For FT-IR spectroscopy, the Perkin Elmer Spectrum 2 instrument was used. SEM and EDX images were taken from the JEOL 7610 F Plus microscope. Diffuse reflectance spectrum (DRS) was recorded on a Jasco V-770 Spectrophotometer . PL excitation and emission studies were taken down by a Horiba PTI Quanta Master Spectrofluorometer equipped with a xenon lamp. PL lifetime curves were obtained from a 150 MHz digital oscilloscope (HM 1507, Hameg Instruments). To record the temperature-dependent PL, a fibre integrated spectrometer (Model: FLAME-S-XR1-ES) from Ocean Optics was employed.

6.3. Results and discussion:

6.3.1 Investigations on morphology and structure

6.3.1.1 XRD analysis

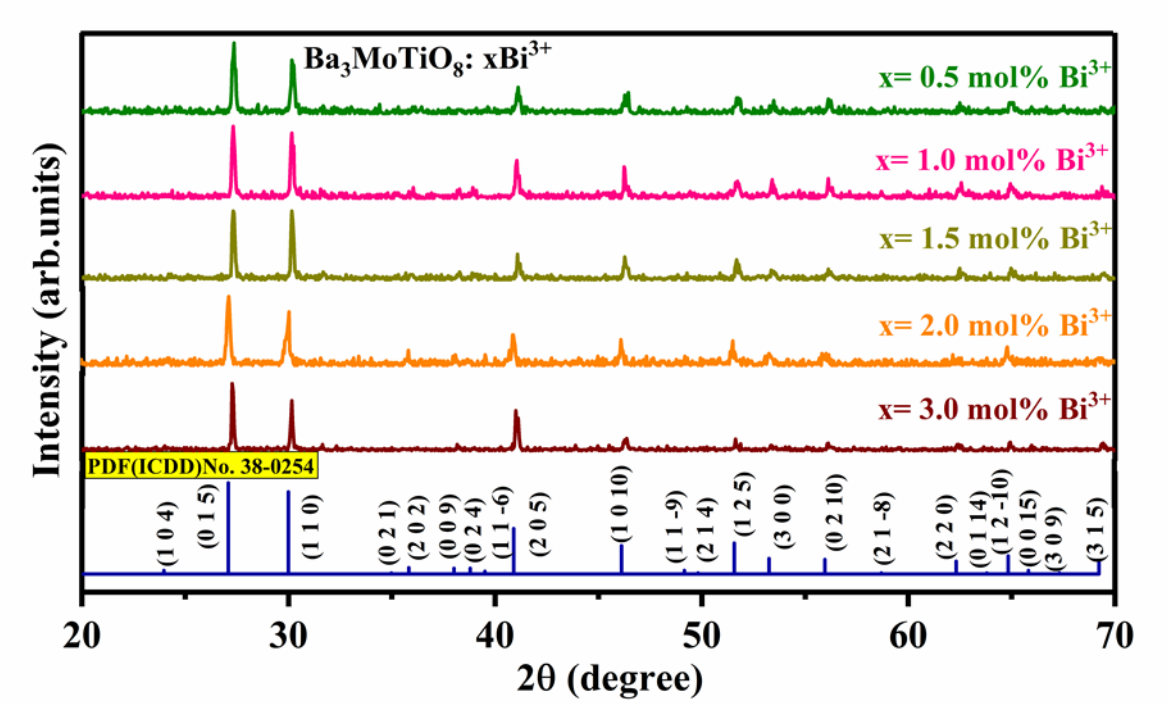

Fig. 6.1. XRD patterns of xBi^{3+} (x= 0.5, 1.0, 1.5, 2.0 and 3.0mol%) doped Ba_3MoTiO_8 phosphors synthesized by solid state reaction method.

Table 6.1. Calculated structural lattice parameters for BMT: xBi^{3+}(x= 0.5, 1.0, 1.5, 2.0 and 3.0mol%) through Rietveld refinement.

BMT: xBi^{3+}	**a (Å)= b (Å)**	**c (Å)**	**α = β**	**γ**	**χ^2**	**Cell volume(Å^3)**
JCPDS	5.9570	21.2900	90	120	-	654.28
x = 0.5mol% Bi^{3+}	5.9578	21.3027	90	120	0.85	654.82
x = 1.0mol% Bi^{3+}	5.9599	21.2870	90	120	1.04	654.80

x = 1.5mol% Bi^{3+}	5.9565	21.2856	90	120	1.14	654.01
x = 2.0mol% Bi^{3+}	5.9558	21.2943	90	120	0.65	654.13
x = 3.0mol% Bi^{3+}	5.9592	21.2952	90	120	0.43	654.90

The XRD patterns of BMT: xBi^{3+}(x= 0.5, 1.0, 1.5, 2.0, 3.0mol %) phosphors are given in Fig. 6.1. It can be seen that the diffraction pattern matches perfectly with standard ICDD card no. 38-0254, with no impurity peaks. The addition of dopant Bi^{3+} has no effect on the phase or structure formation of the phosphors, as Ba^{2+} and Bi^{3+} have nearly similar ionic radii of 135 pm and 138 pm respectively with co-ordination number 6 [168,169]. So, barium ions can easily replace bismuth ions. The phase of the as-prepared phosphors is rhombohedral, the space group being R-3m and 166 being the space group number [112]. The Debye- Scherrer equation was used to evaluate the average crystallite size from the XRD data [57]. The crystallite size of the particles for the most dominant peak ($2\theta = 27.3$) ranges from 50-70 nm. Fig. 6.2 shows the Rietveld Refinement plots for the BMT: xBi^{3+} (x= 0.5, 1.0, 1.5, 2.0, 3.0mol %) phosphors using Full Prof suite software. The lattice parameters, cell volume and χ^2 (goodness of fit) were calculated for the as prepared phosphors and have been listed in Table 6.1.

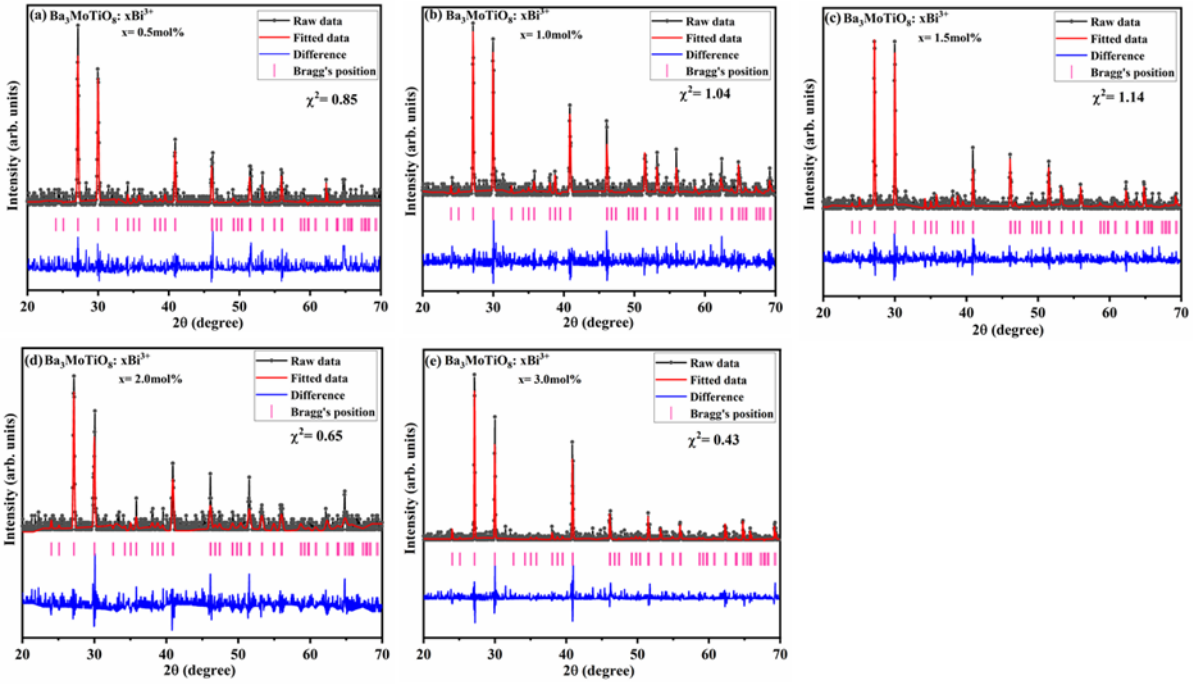

Fig. 6.2. Rietveld refinement fitting for xBi^{3+} (x= 0.5, 1.0, 1.5, 2.0 and 3.0mol%) doped Ba_3MoTiO_8 phosphors.

6.3.1.2 FE-SEM and EDAX analysis

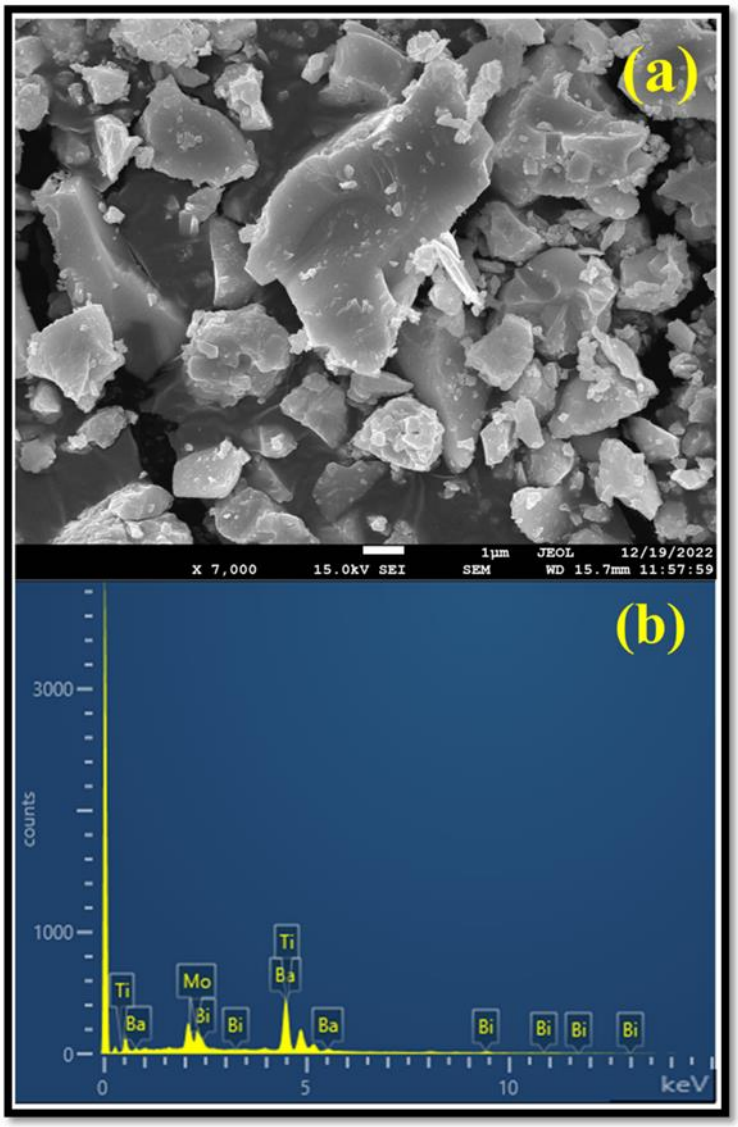

Fig. 6.3. (a) SEM and **(b)** EDX images of xBi^{3+}(x= 1.0mol%) doped Ba_3MoTiO_8 phosphor.

Fig. 6.3(a) displays the FE-SEM image of xBi^{3+}(x= 1.0mol%) doped BMT phosphor. The phosphors do not show any uniform shape, and particle size lies in the range of 0.1-10 μm. Also, some agglomeration can be seen. All of this can be attributed to the manual grinding process involved in the synthesis of the phosphors. The EDAX analysis has been introduced in Fig. 6.3(b). As is evident from spectrum, peaks corresponding to all the elements Ba, Ti,

Mo, and Bi are present, confirming all the precursor elements have been successfully encompassed into the host lattice.

6.3.1.3 FT-IR measurement

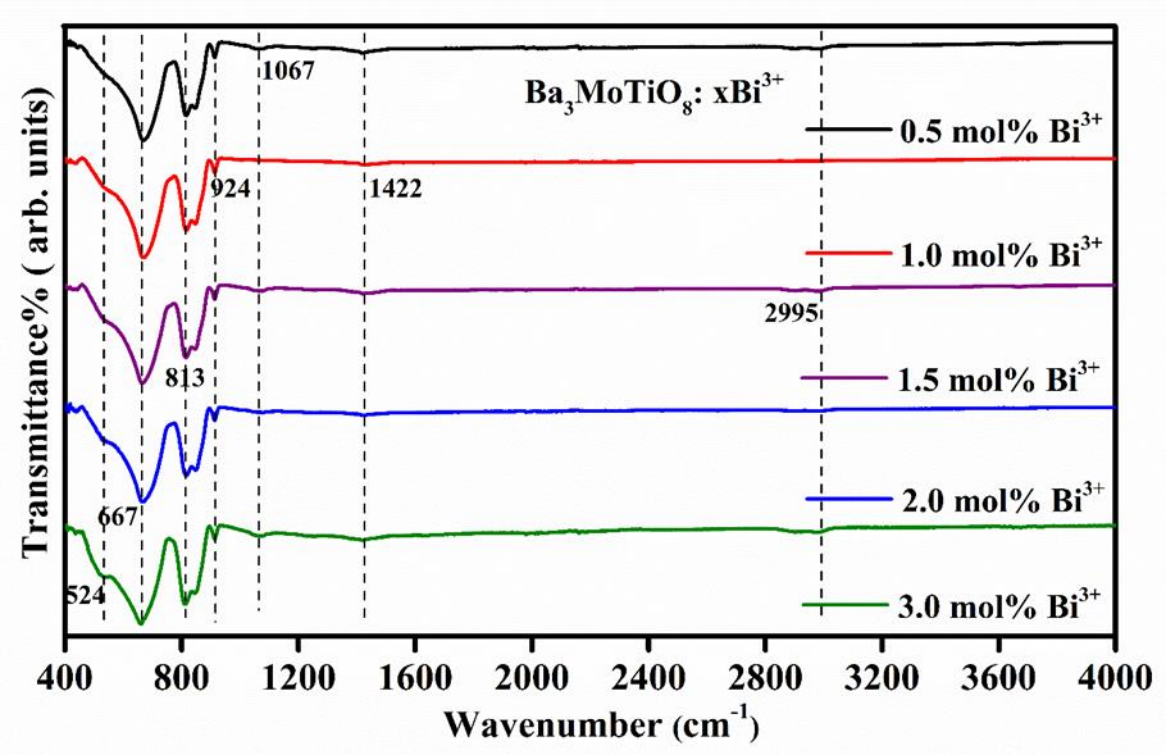

Fig. 6.4. FTIR Spectra of xBi^{3+} (x= 0.5, 1.0, 1.5, 2.0 and 3.0mol%) doped Ba_3MoTiO_8 phosphors.

Fig. 6.4 demonstrates the various vibrational and IR bands present in the prepared BMT: xBi^{3+}(x= 0.5, 1.0, 1.5, 2.0, and 3.0mol%) phosphors. The bands observed at 524 and 667 cm^{-1} define the Ti-O bending mode vibrations and Mo-O vibrations, respectively [170,171] . The IR bands at 813 and 924 are attributed to the stretching vibrations of Mo-O-Mo in MoO_4^{2-}tetrahedrons and Mo=O stretching vibrations in the hexagonal phase, respectively [112,170] . The bands of CO_3^{2-} at 1067 and 1422 cm^{-1} signify the symmetric and asymmetric stretching modes of the C-O bond [172]. A small hump at 2995 cm^{-1} supports the presence of hydrogen bonding [113].

6.3.1.4 Diffuse reflectance spectra (DRS) study

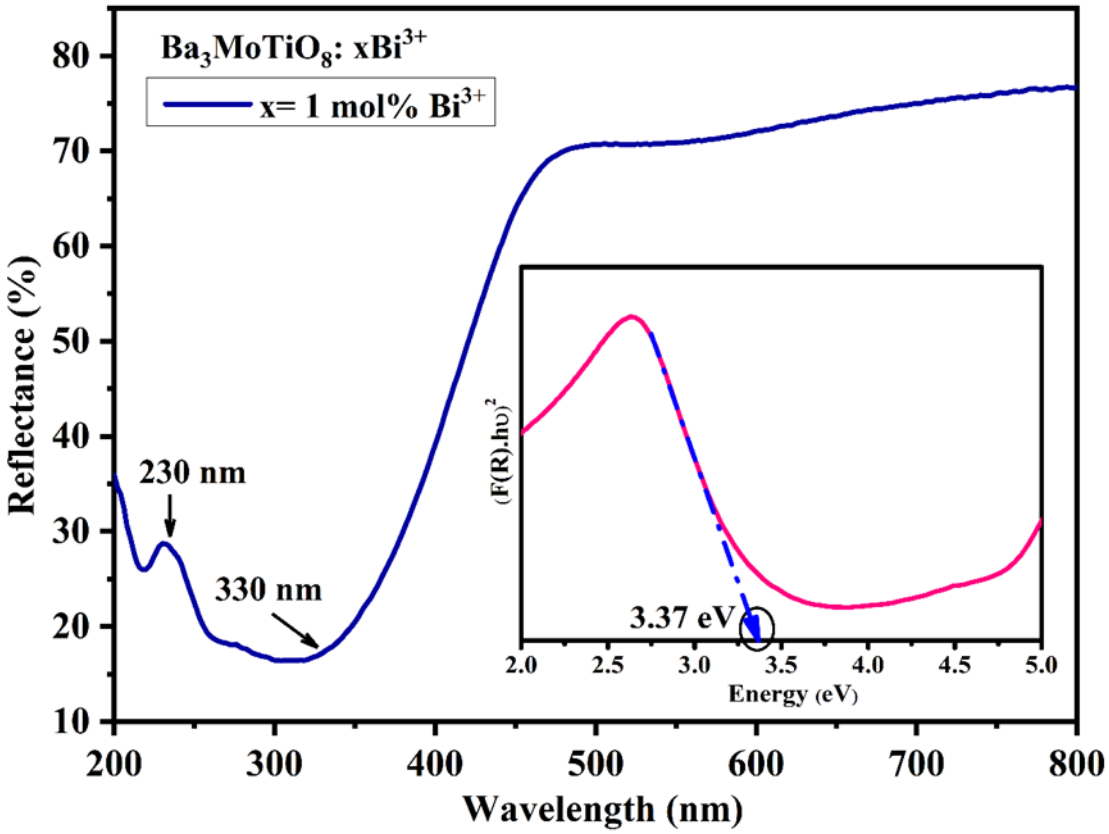

Fig. 6.5. Diffuse reflectance spectra (a) of xBi^{3+}(x= 1.0mol%) doped Ba_3MoTiO_8 phosphor along with (b) tau plot for band gap calculation.

The DRS of xBi^{3+}(x= 1.0mol%) doped BMT phosphor has been presented in Fig. 6.5. Two bands at 230 nm and 330 nm can be observed in the graph. Absorption of Bi^{3+} produces the band corresponding to the shorter wavelength of 230 nm, whereas defects due to Bi ions or Bi based clusters cause the broadband at a longer wavelength of 330 nm [173]. The optical band gap of the sample was determined by converting the diffuse reflectance spectrum data into a Kubelka-Munk function using eq. (16) and (17) as described in chapter 2 [174]:

The value of the direct bandgap corresponding to s= ½ was found to be 3.37 eV for optimised concentration of Bi^{3+} ions.

6.3.2 PL studies at room temperature

6.3.2.1 PL excitation and emission studies

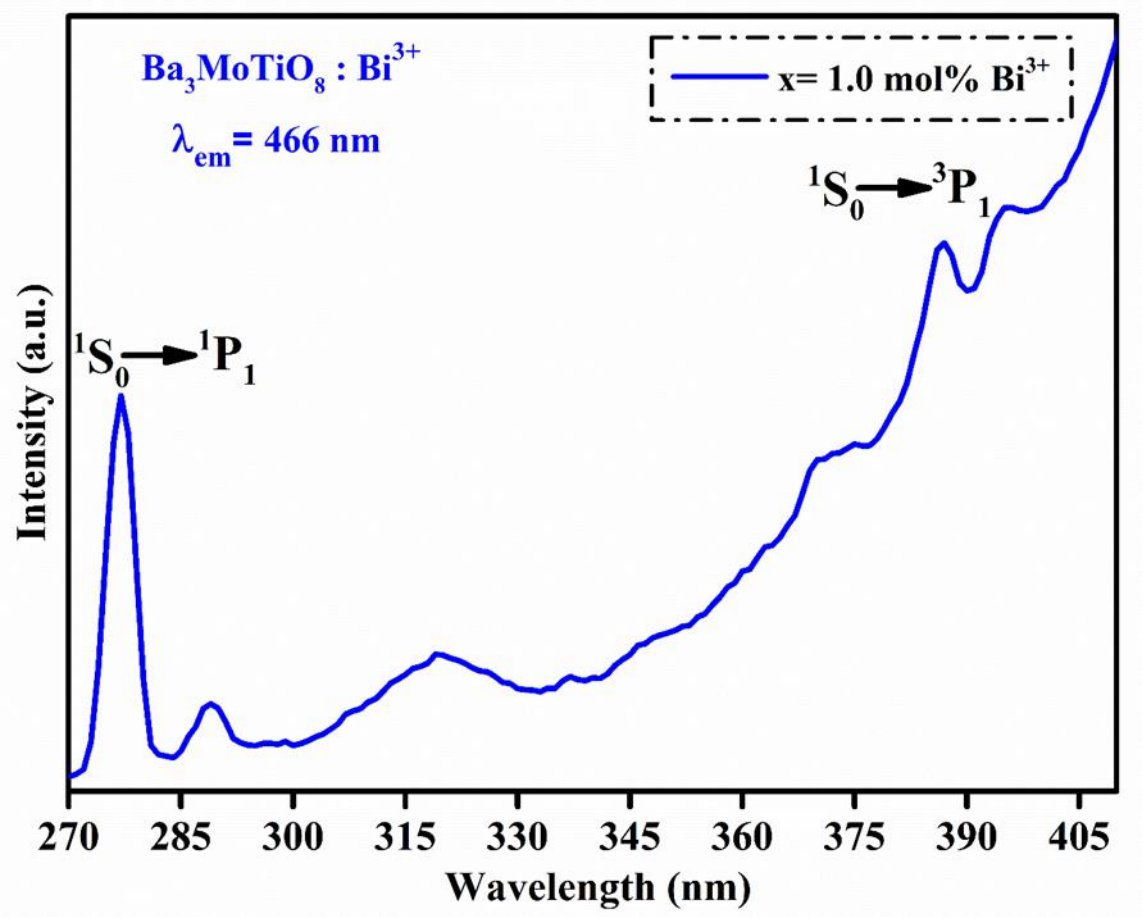

Fig. 6.6. Excitation spectra of xBi^{3+}(x= 1.0mol%) doped Ba_3MoTiO_8 phosphor at λ_{em}= 466 nm.

As mentioned earlier, Bi^{3+} ions have an electronic configuration of $[Xe]4f^{14}5d^{10}6s^2$ having $^1S_0$ ground state and $^1P_1$, $^3P_0$, $^3P_1$, and $^3P_2$ excited states. There are two spin forbidden transitions $^1S_0 \rightarrow {}^3P_0$ and $^1S_0 \rightarrow {}^3P_2$. The only allowed transitions are $^1S_0 \rightarrow {}^1P_1$ and $^1S_0 \rightarrow {}^3P_1$ in the excitation spectrum and $^3P_1 \rightarrow {}^1S_0$ in the emission spectrum. Fig. 6.6 shows the excitation spectrum of xBi^{3+}(x= 1.0mol%) doped BMT phosphor under 466 nm emission. Two bands, $^1S_0 \rightarrow {}^1P_1$ (275 nm) and $^1S_0 \rightarrow {}^3P_1$ (386 nm) can be seen [159]. Both these wavelengths were used to observe the emission spectra of the phosphors. Figs. 6.7(a) and (b) exhibit the PL

emission spectra under 275 nm and 386 nm excitation, respectively. In both cases, a single intense broad band centred at 466 nm can be seen. Thus, the Bi^{3+} ion exhibits the ability to get excited by near UV light and emit in the blue region. The broad excitation spectrum from 275-390 nm for the Bi^{3+} ion coincides with the emission band of a near UV (n-UV) LED chip. Thus, Bi^{3+} doped luminescent materials can be used in white light-emitting LEDs (w-LEDs) [167].

Under 275 nm and 386 nm excitation, the emission spectra of the as-prepared Bi^{3+} doped BMT phosphors are shown in Fig. 6.7(a) and (b), respectively. A single broadband in the blue region centered at around 466 nm is in accordance with the transition $^3P_1 \rightarrow {}^1S_0$ [175].

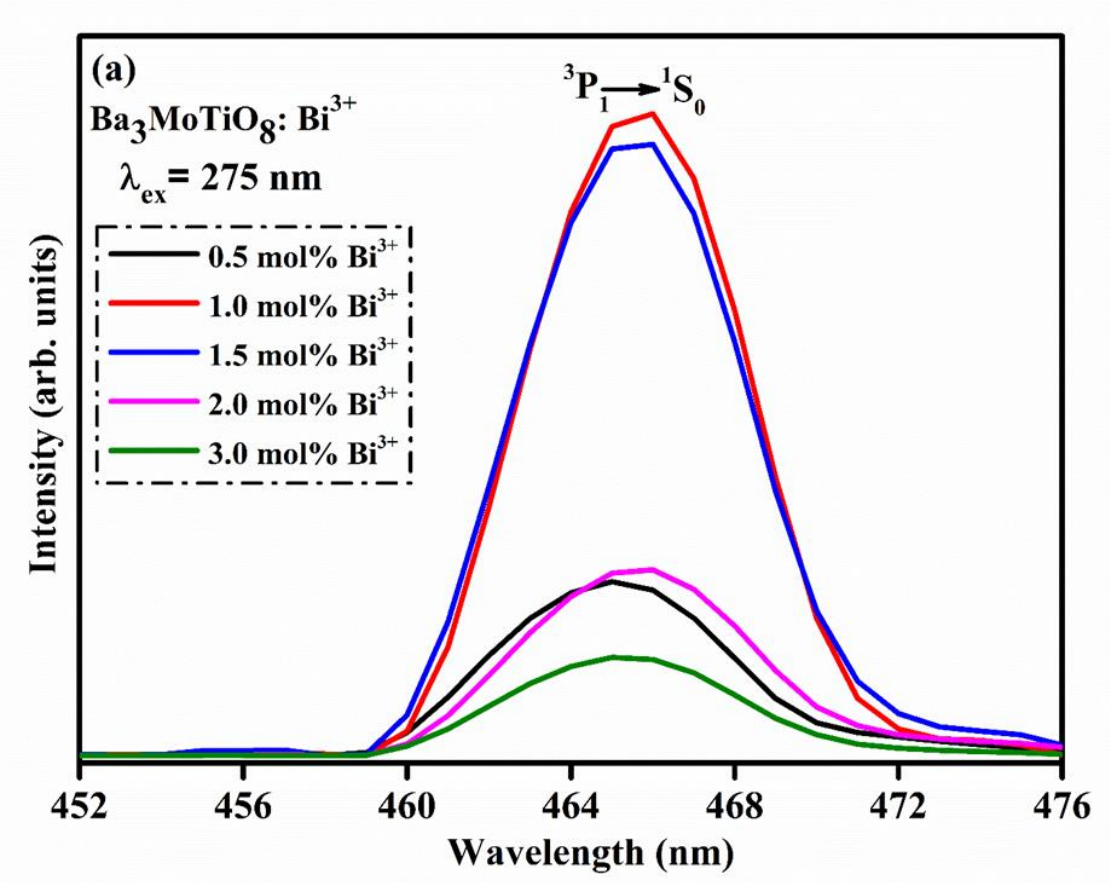

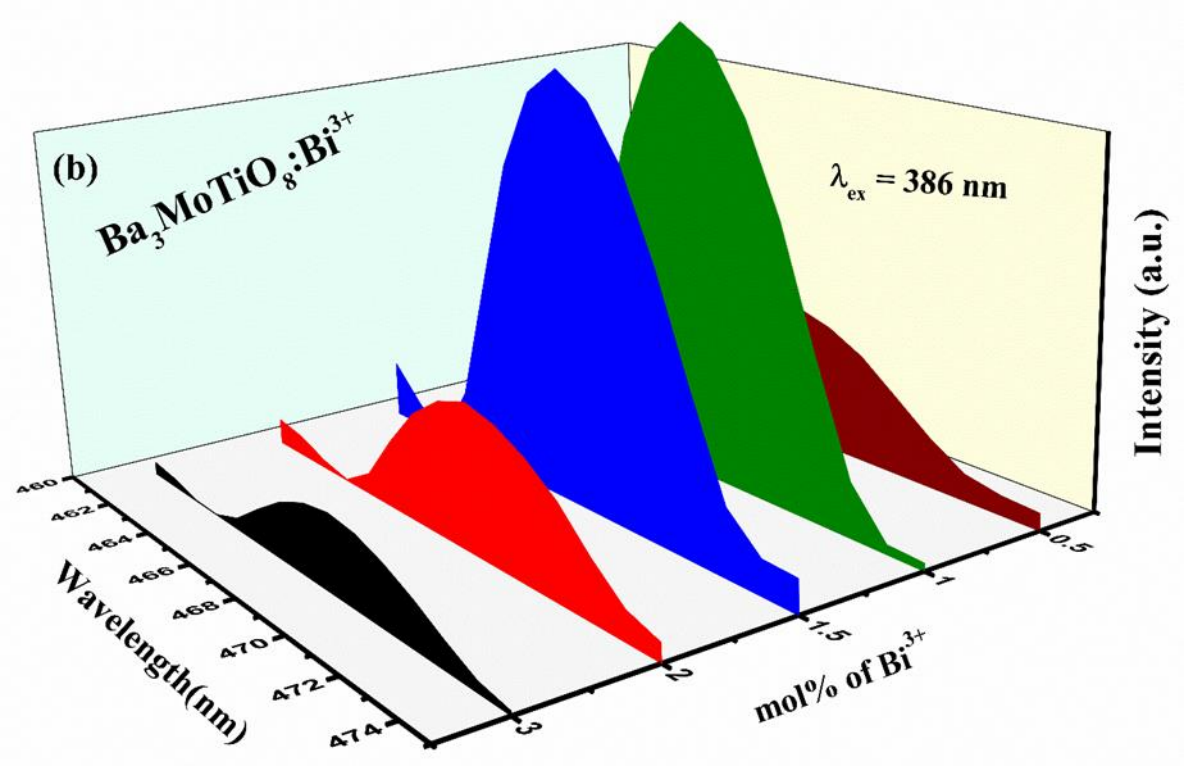

Fig. 6.7. Emission spectra of xBi^{3+} (x= 0.5, 1.0, 1.5, 2.0 and 3.0mol%) doped Ba_3MoTiO_8 phosphor at **(a)** λ_{ex}= 275 nm & **(b)** λ_{ex}= 386 nm respectively.

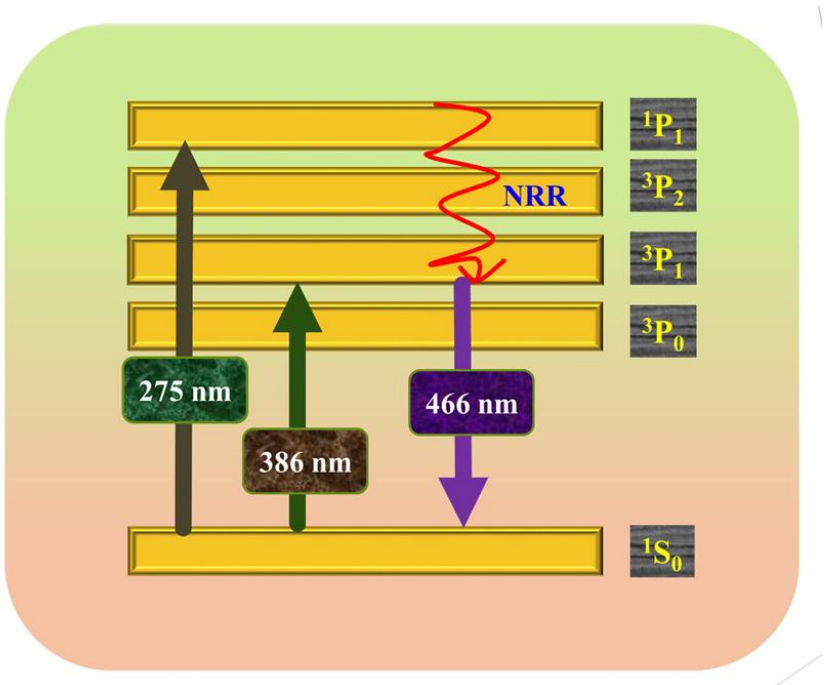

Fig. 6.8. Schematic energy level diagram of excitation & emission mechanism of Bi^{3+} doped phosphors.

Fig. 6.8 manifests the corresponding energy level diagram for the Bi^{3+} ion. The transitions occur from $^1S_0$ to upper excited triplet states ^3P_j (j=0, 1, 2) or singlet $^1P_1$ state[176]. Here, only transitions from $^1S_0 \rightarrow {}^1P_1$ and $^1S_0 \rightarrow {}^3P_1$ are allowed and the other transitions to the upper states are spin forbidden. So, as is evident from the diagram, Bi^{3+} ions transition from the ground level to either the $^1P_1$ or $^3P_1$ states. In the former case, they fall down to the $^3P_1$ state non-radiatively and then to the ground state, thereby emitting luminescence in the blue region. These non- radiative relaxations (NRR) are represented by red arrow in Fig. 6.8.

As is evident, the emission intensity of samples under 275 and 386 nm excitation increases until 1 mol % of Bi^{3+} ions and then decreases. This phenomenon is known as concentration quenching and is produced due to non-radiative interactions between the Bi^{3+} ions [177]. Thus, the BMT phosphor doped with 1 mol% of Bi^{3+} was chosen as the optimized sample for further luminescence studies. Non-radiative relaxation is viable because of three mechanisms, specifically radiative re-absorption, exchange interaction, and activator dependent electric multipolar. The shortest distance among the activator ions on which the energy transfer depends is critical distance R_c. The critical distance can be determined by using the eq. (19) as described in chapter 3 [178]:

The value of R_c then comes out to be 34.66 Å. This value is large as compared to 5 Å ($R_c \leq 5$ Å is ideal for exchange interaction). So, in this case, exchange interaction was not responsible in the mechanism of transfer of energy.

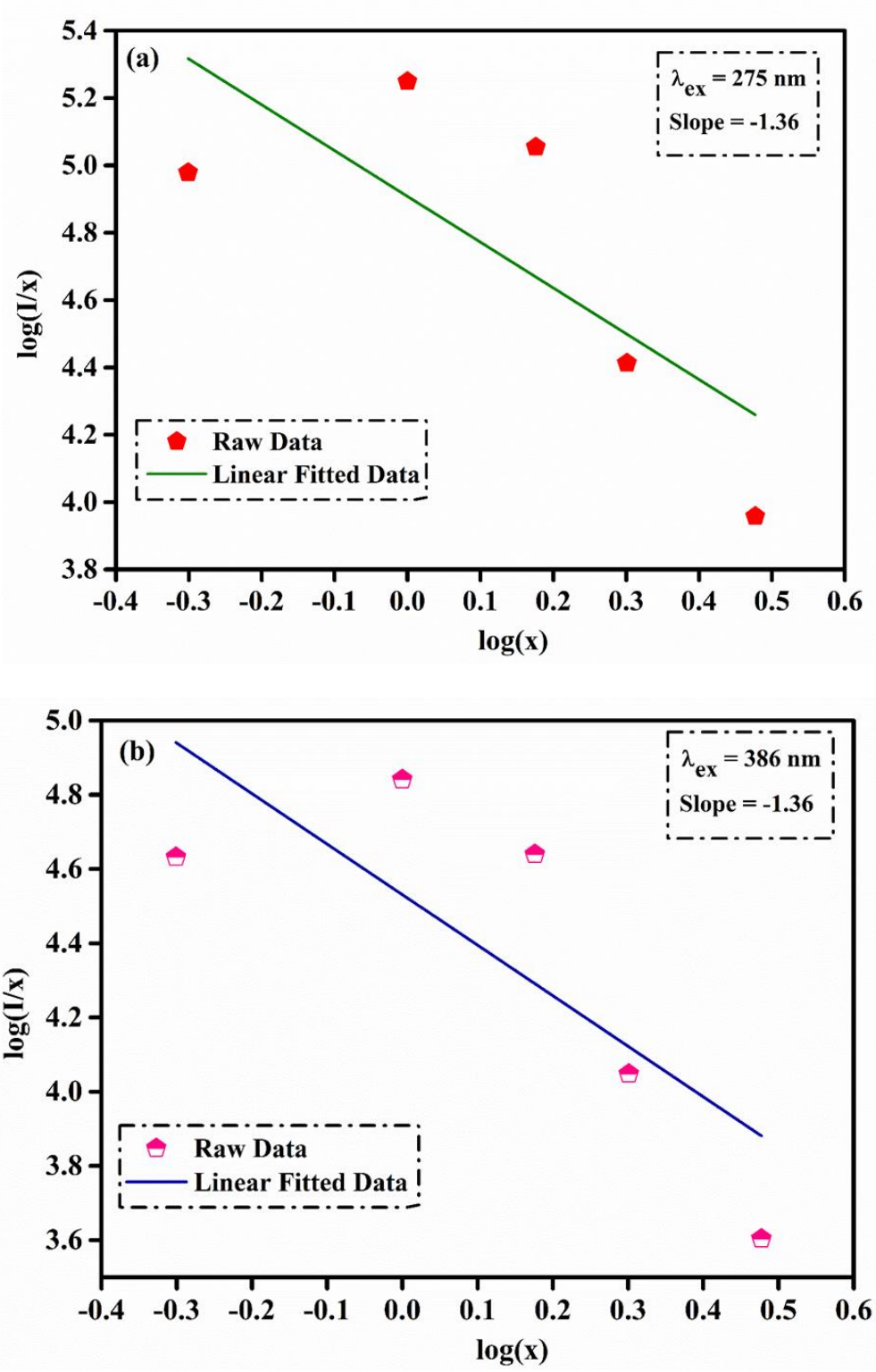

Fig. 6.9. Dexter plot of Log(I/x) versus Log(x) at (a) λ_{ex}= 275nm & (b) λ_{ex}= 386nm respectively.

Therefore, Dexter's theory was used to check the types of multipolar interactions that could be involved in the process of energy transfer. Emission data for the phosphors under 275 and 386 nm was used for Dexter studies, and the plots have been presented in Figs. 6.9(a) and (b). The equation (21) given in chapter 1 used for Dexter's study is defined by [151]:

The kind of interplay between the activator ions is given by the value Q. Here Q is 6 for electric dipole-dipole interaction, 8 for dipole-quadrupole interactions, and 10 for quadrupole-quadrupole interactions. As can be seen in the figures, linear plots between log (I/x) and log (x) were obtained, having slopes equal to -1.36. So, the value of Q calculated from this turned out to be 4.08, which is closest to 6 (when compared with Q= 6,8, and 10 as discussed above) indicating electric dipole- dipole interaction is responsible for the energy transfer between the dopant ions [179]. So, we can conclude that the interaction between Bi^{3+} ions in the phosphor lattice leading to energy transfer and subsequent quenching is electric dipole-dipole in nature.

6.3.2.2 Colorimetry analysis

Figs. 6.10 (a) and (b) show the CIE plots of the BMT: xBi^{3+} phosphors under 275 nm and 386 nm excitations, respectively. All the coordinates lie in the blue region. The McCamy formula gives correlated color temperature (CCT) values as described in eq. (8) [151]:

The calculated values of CCT for all samples under 275 nm and 386 nm excitation are given in Table 6.2. Accordingly, CIE coordinates and CCT values display that Bi^{3+} doped BMT phosphors can be used for blue light generation in w-LEDs and SSL applications.

Table 6.2. Calculated CCT values for Bi^{3+} ions doped Ba_3MoTiO_8 phosphors under λ_{ex}=275 nm and 386 nm.

Sample ID (Bi^{3+} series)	CCT values (K) λ_{ex}=275 nm	CCT values (K) λ_{ex}=386 nm
0.5 mol% Bi^{3+}	1761	1866
1.0 mol% Bi^{3+}	1767	1827
1.5mol% Bi^{3+}	1769	1851
2.0 mol% Bi^{3+}	1779	1907
3.0 mol% Bi^{3+}	1764	1887

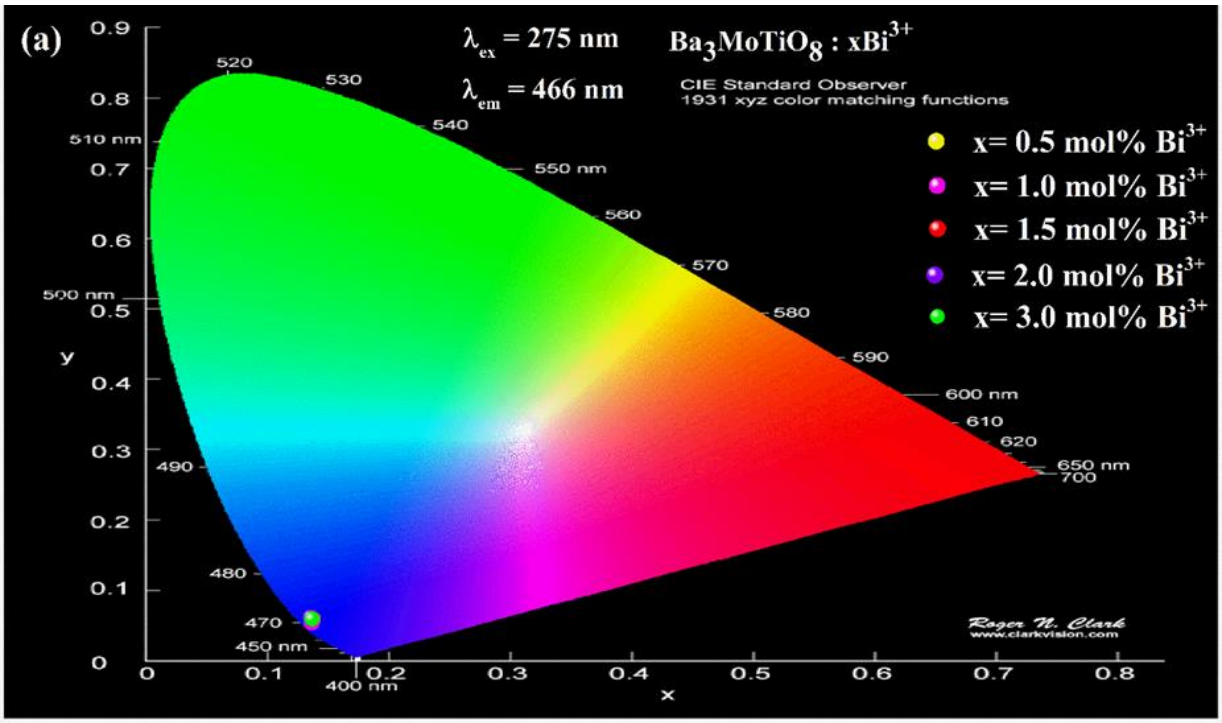

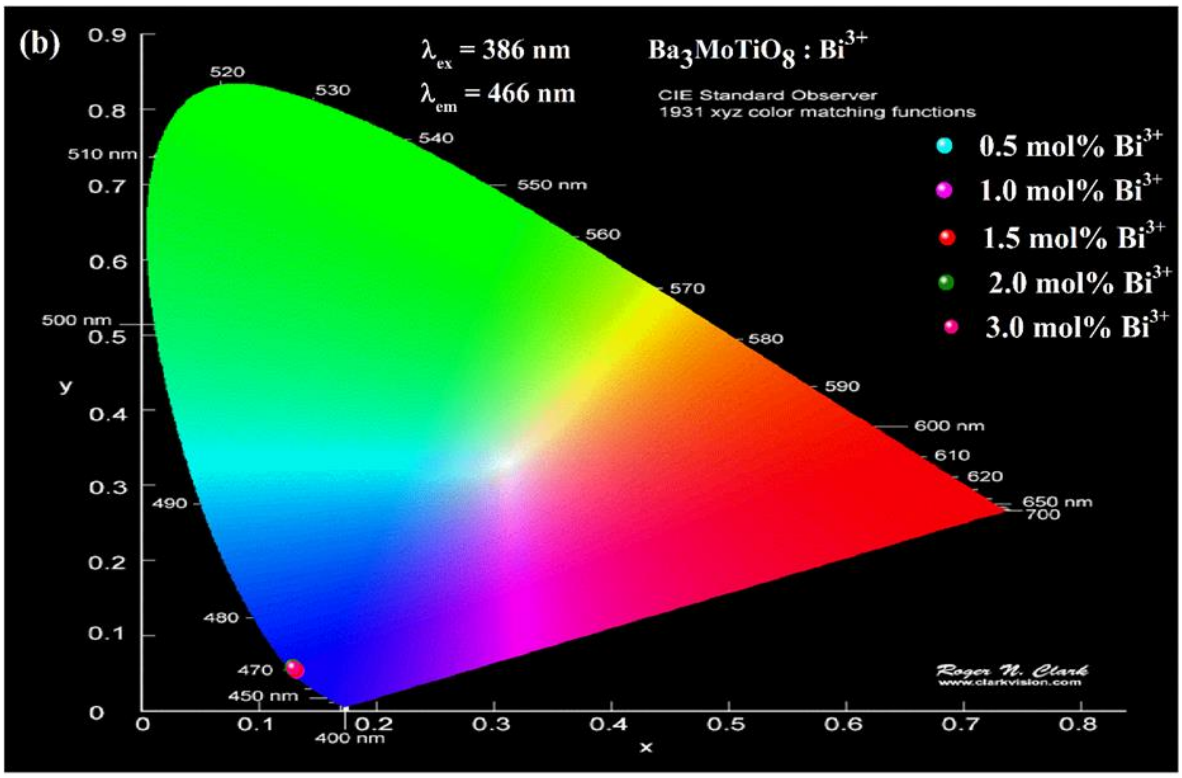

Fig. 6.10. CIE Chromaticity co-ordinates for Ba_3MoTiO_8: xBi^{3+} (x= 0.5, 1.0, 1.5, 2.0 and 3.0mol%) phosphors under (a) 275nm and (b) 386 nm excitation respectively.

6.3.2.3 Decay kinetics

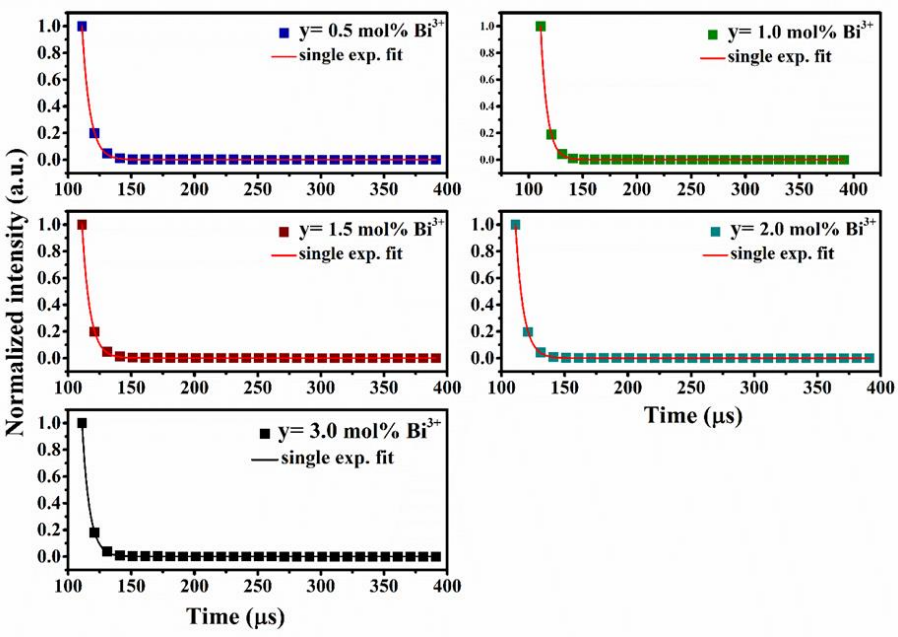

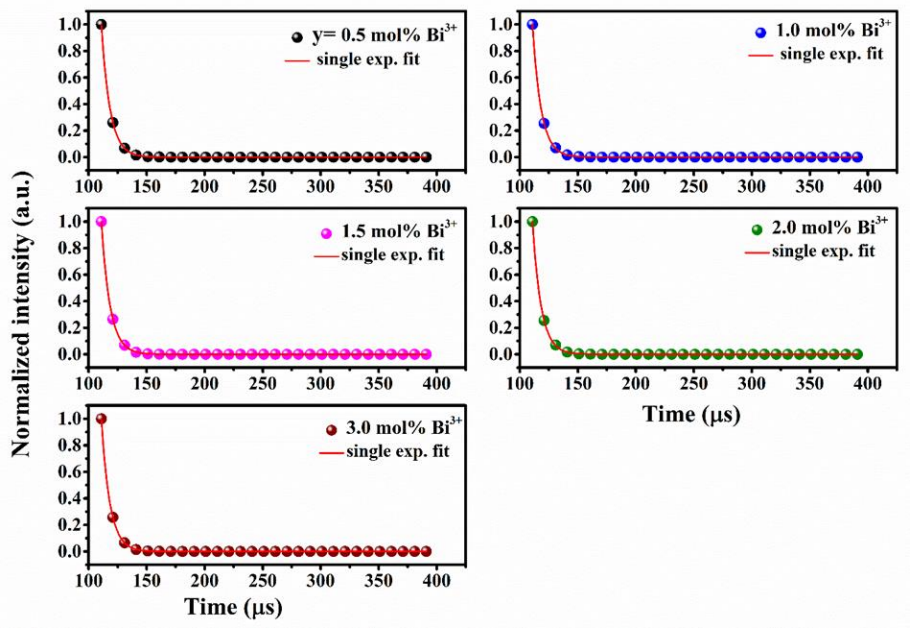

Fig. 6.11. Decay curves of xBi^{3+} (x= 0.5, 1.0, 1.5, 2.0 and 3.0mol%) doped Ba_3MoTiO_8 phosphor at (a) λ_{ex}= 275nm & (b) λ_{ex}= 386nm.

The decay curves for BMT phosphors for 466 nm emission under 275 and 386 nm excitation are presented in Figs. 6.11 (a) and (b). These curves obey a single exponential function given in eq. (11). The lifetime values for all the phosphors under both excitation wavelengths have been presented in Table 6.3. PL lifetime values show a decrement with an increase in Bi^{3+} ion concentration, demonstrating the non-radiative loss of energy between Bi^{3+} ions [167,180].

Table 6.3. Lifetime decay values of BMT: xSm^{3+}/ yEu^{3+}(x= 1.5mol%, y= 1,2,3,4,5 and 6mol%) co-doped phosphors for λ_{ex}=409 nm.

Sample ID (Bi^{3+} series)	**Lifetime values (μs) λ_{ex}=275 nm**	**Lifetime values (μs) λ_{ex}=386 nm**
0.5 mol% Bi^{3+}	4.30	5.20
1.0 mol% Bi^{3+}	4.28	5.15
1.5mol% Bi^{3+}	4.19	5.10
2.0 mol% Bi^{3+}	4.18	5.10
3.0 mol% Bi^{3+}	4.05	5.09

6.3.3 Temperature-dependent PL Studies

The thermal behaviour of the phosphors needs to be analysed if they have to be used for w-LEDs and SSL applications, as the working temperatures of such materials go beyond 470K which can cause significant degradation and defects in the operations of the optoelectronic device [181]. Fig. 6.12(a) shows temperature-dependent PL spectra of the BMT: xBi^{3+} (x=1mol%) sample under 275 nm excitation. As is evident, the luminescence intensity decreases from 25^0C to 175^0C. The phosphor retains 90% of its maximum luminescence intensity at 175^0C proving that the phosphor is highly heat stable. This decrease can be attributed to thermal quenching in the sample due to phonon interactions wherein a crossing point between the ground and excited states leads to activation of a luminescence center. The activation energy required for thermal quenching may be calculated with the use of Arrhenius equation (25) [182].

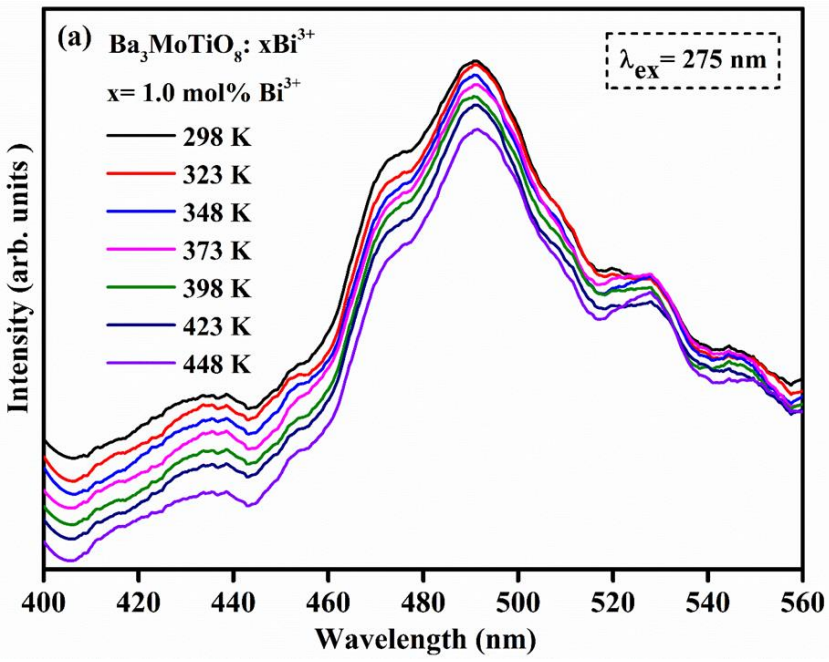

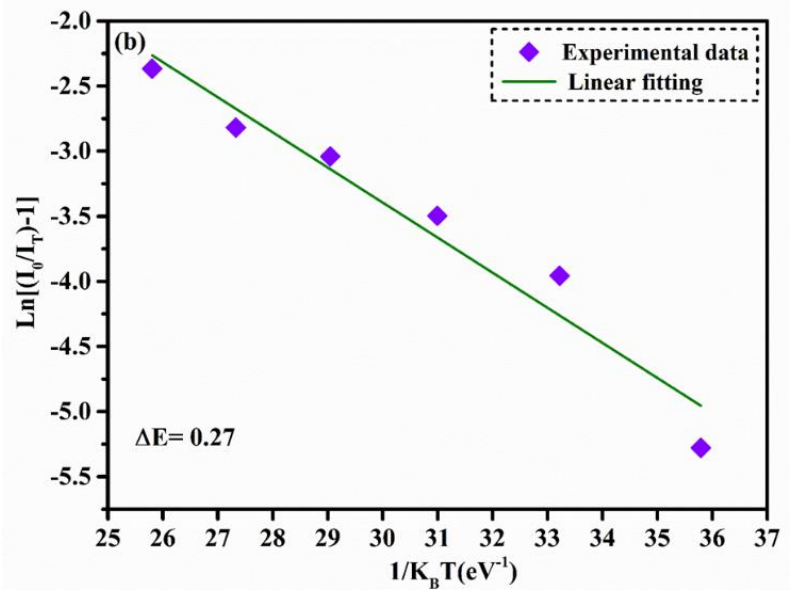

Fig. 6.12(a). Temperature dependent PL spectra of optimized conc. (x= 1.0mol%) of Ba_3MoTiO_8: xBi^{3+} phosphor & **(b)** Fitting plot of $Ln[(I_0/I_T)-1]$ vs. 1/KT.

The activation energy for thermal quenching is denoted by ΔE, b and K, which are independent and Boltzmann constants (8.629 x 10^{-5} eV) respectively. A linear plot among ln[(I_0/I_T) -1] and $1/K_BT$ has been displayed in Fig. 6.12 (b) the slope of which gives the activation energy. The value of activation energy brought out to be 0.27 eV which is notably better than other reported phosphors, thereby signalling high thermal stability and employability in SSL devices and w-LEDs [182–184].

6.4. Conclusions

Bi^{3+} doped Ba_3MoTiO_8 phosphors prepared via a solid-state reaction method have been studied in thorough detail. Various morphological assessments were undertaken, like XRD, FT-IR, FESEM, and EDAX, to establish the phase, structure, and chemical nature of the phosphors. Room temperature PL studies ascertained the luminescent behavior of the materials. Under 275 and 386 nm excitation, a broad band in the blue region centered at 466 nm is seen,

corresponding to $^3P_1 \rightarrow {}^1S_0$ transition. The decay curves for the samples under both excitation wavelengths show a single exponential behaviour. CIE and CCT values confirm the blue-emitting property of the as-prepared phosphors. Temperature-dependant PL studies were performed to assess the thermal stability of the blue-emitting phosphors. It was confirmed that these phosphors indeed possess the high activation energy required for thermal quenching. In light of all the results of our studies, we wish to propose Bi^{3+} doped Ba_3MoTiO_8 phosphors for w-LED and SSL device applications.

CHAPTER 7
Summary and Scope of Future Work

7.1. Summary

The primary goal of this thesis study is to synthesize and analyse RE doped Ba_3MoTiO_8 phosphors for use in general illumination for solid state lighting applications. By adding Eu^{3+}, Sm^{3+}, Ho^{3+}, Yb^{3+}, and Bi^{3+} ions as RE dopants, multicolour (red, orange, green, and blue) emitting pure phase BMT phosphors were successfully synthesized using SSM, CMM, and SGM processes. Significant emphasis has been paid to improving emission qualities by altering the synthesis procedure and increasing the dopant RE ion concentration.

As described in earlier chapters, there has lately been a surge in interest in pc-LEDs because to its unique attributes such as better energy efficiency, lifespan, eco-friendliness, and compelling luminosity features. Such advanced pc-LEDs have a wide range of applications, including display devices, safety signals, bio-sensors, bio-medical therapies, and artificial lighting. In this context, new phosphors with enhanced luminous properties must be created. Following the motivation for developing new phosphors and extensive research on their structural, morphological, and photoluminescent properties, single phase Eu^{3+} doped BMT phosphors were successfully synthesized by SSM, SGM and CMM methods to achieve intense and pure red emission. Out of these methods, a correlatively higher PL intensity and better morphology was observed in case of CMM synthesized phosphors. All the BMT phosphors prepared by CMM techniques are displaying red emission under 393 and 464 nm as excitation wavelengths. This has been further confirmed by CIE chromaticity diagram also. And lastly, time decay analysis was carried out which shows that 2 mol% is the optimum concentration of Europium ion for combustion synthesized series and after that energy transfer take place

between the activator ions itself through dipole-dipole interaction which can be confirmed from the Dexter theory. CIE points calculated for combustion synthesized samples lies in pure red region. These red emitting phosphors can be used in combination with green and blue phosphors by coating them on n-UV LED chips. As another option, these Eu^{3+} doped BMT phosphors can be used by co-doping with commercial YAG: Ce^{3+} phosphor and by coating them on blue (InGaN) chip so that a better CRI and low CCT value can be achieved.

Further, a series of single Ho^{3+} ion doped and Ho^{3+}/Yb^{3+} co-doped BMT phosphors were prepared for the green colour component in w-LED applications. The UC and DC PL emission show intense green emission (at 551 nm) under 980 nm laser excitation as well as under 448 nm xenon lamp excitation. The variation in UC intensity with pump power reveal the information pertaining to the number of photons involved in the UC process. PL lifetime decay curves recorded under 980 nm excitation show continuous increment under λ_{em}=551 nm and in case of λ_{em}=668 nm, lifetime values first increasing and then decreasing. The CIE coordinates of all samples lie in green region. All these results indicate that the as prepared phosphor can be a promising candidate for application in UC & DC based green emitting diodes, display devices, security ink, phototherapy and SSL applications.

In the next chapter, a series of singly Sm^{3+} doped BMT: xSm^{3+} (x =0.5, 1, 1.5, 2 and 2.5mol%) and co-doped BMT: xSm^{3+}/yEu^{3+} (x =1.5mol%, y =1, 2, 3, 4, 5 and 6mol%) phosphors were successfully synthesized. The optical band gap was calculated from the DRS study lies in the range of 3.0 - 3.5 eV for all the concentrations of Sm^{3+} and Sm^{3+}/Eu^{3+} co-doped phosphors. PL spectra recorded under the 409 nm excitation wavelength for the singly Sm^{3+} ion doped phosphors show reddish-orange emission at the 596 nm wavelength, corresponding to transition $^4G_{5/2} \rightarrow {}^6H_{7/2}$. Sharp red emission at 615 nm corresponding to transition $^5D_0 \rightarrow {}^7F_2$ is

visible in PL spectra for co-doped BMT phosphors that were taken at three distinct excitation wavelengths (409, 381, and 465 nm). The intensity of the Eu^{3+} peaks increases with an increase in Eu^{3+} ion concentration, while the Sm^{3+} peaks decrease under the 409 nm excitation wavelength, according to PL spectral analyses of co-doped phosphors. This shows the energy transfer mechanism from Sm^{3+} ions to Eu^{3+} ions in the co-doped phosphors. Quadrupole-quadrupole interaction is the basis for this energy transfer process, according to Dexter's theory applied to it. CIE coordinates calculated for optimized single Sm^{3+} ion-doped phosphors lie in the reddish-orange region, and for co-doped phosphors lie in the red region, demonstrating the energy transfer induced colour tunable behaviour from the reddish-orange to red region, respectively. These studies show the application of prepared phosphors in orange and red color-emitting LED devices.

Finally, Bi^{3+} doped Ba_3MoTiO_8 phosphors have been prepared as a blue colour emitting component in w-LEDs. Under 275 and 386 nm excitation, a broad band in the blue region centered at 466 nm is seen, corresponding to $^3P_1 \rightarrow {}^1S_0$ transition. The decay curves for the samples under both excitation wavelengths show a single exponential behaviour. CIE and CCT values confirm the blue-emitting property of the as-prepared phosphors. Temperature-dependent PL studies were performed to assess the thermal stability of the blue-emitting phosphors. It was confirmed that these phosphors indeed possess the high activation energy required for thermal quenching. In light of all the results of our studies, we wish to propose Bi^{3+} doped Ba_3MoTiO_8 phosphors for w-LED and SSL device applications.

7.2. Future scope of the work

1. To carry out the further literature survey on the aforementioned topic for thorough knowledge and understanding.
2. To synthesize the phosphors with other chemical routes also like Co-precipitation, Hydrothermal to obtain homogeneous and pure crystalline phase. Such techniques may improve the particle morphology and reduce the particle size which in turn further improves the luminescence properties
3. To enhance the luminescence properties of Ba_3MoTiO_8 phosphor by using other suitable dopants/co-dopants (for ex: Bi^{3+} may act as sensitizer for Eu^{3+} ions, Yb^{3+} for Tm^{3+} and Tb^{3+}) so that we can explore our application part in other down-conversion/up-conversion applications.
4. To project these phosphors in device fabrication and other photonic applications.

References:

[1] PERSPECTIVE, (2015). https://doi.org/10.2172/889939.

[2] T.O.F. Contents, Sources and process, (2017) 1–20.

[3] S. Ye, F. Xiao, Y.X. Pan, Y.Y. Ma, Q.Y. Zhang, Phosphors in phosphor-converted white light-emitting diodes: Recent advances in materials, techniques and properties, Mater. Sci. Eng. R Reports. 71 (2010) 1–34. https://doi.org/10.1016/j.mser.2010.07.001.

[4] S.L. Shinde, S. Senapati, K.K. Nanda, Luminescence from wide band gap materials and their applications, Adv. Nat. Sci. Nanosci. Nanotechnol. 6 (2015). https://doi.org/10.1088/2043-6262/6/1/015002.

[5] K. Takayama, S. Hiramatsu, Ion-channel guiding in a steady-state free-electron laser, Phys. Rev. A. 37 (1988) 173–177. https://doi.org/10.1103/PhysRevA.37.173.

[6] J. McKittrick, L.E. Shea-Rohwer, Review: Down conversion materials for solid-state lighting, J. Am. Ceram. Soc. 97 (2014) 1327–1352. https://doi.org/10.1111/jace.12943.

[7] Banwel.Pdf, (n.d.).

[8] T.H. Fereja, A. Hymete, T. Gunasekaran, A Recent Review on Chemiluminescence Reaction, Principle and Application on Pharmaceutical Analysis, ISRN Spectrosc. 2013 (2013) 1–12. https://doi.org/10.1155/2013/230858.

[9] C. Ramesh, R. Mohanraju, A review on bioluminescence and its applications A Review on Bioluminescence and its Applications, 5 (2018) 3–5.

[10] H. Xu, Q. Sun, Z. An, Y. Wei, X. Liu, Electroluminescence from europium(III)

complexes, Coord. Chem. Rev. 293–294 (2015) 228–249. https://doi.org/10.1016/j.ccr.2015.02.018.

[11] Y. Xie, Z. Li, Triboluminescence: Recalling Interest and New Aspects, Chem. 4 (2018) 943–971. https://doi.org/10.1016/j.chempr.2018.01.001.

[12] A.J.J. Bos, Theory of thermoluminescence, Radiat. Meas. 41 (2006). https://doi.org/10.1016/j.radmeas.2007.01.003.

[13] X.-H. Fan, J.-C. Zhang, M. Zhang, C. Pan, X. Yan, W.-P. Han, H.-D. Zhang, Y.-Z. Long, X. Wang, Piezoluminescence from ferroelectric $Ca_3Ti_2O_7:Pr^{3+}$ long-persistent phosphor, Opt. Express. 25 (2017) 14238. https://doi.org/10.1364/oe.25.014238.

[14] Поконова Ю.В., Галоидэфиры. Способы получения, свойства, применение. No Title, 1820 (1966) 340.

[15] T. Lauer, Radioluminescence (rl), 2015. https://doi.org/10.1007/978-94-007-6326-5_104-3.

[16] A. Feng, P.F. Smet, A review of mechanoluminescence in inorganic solids: Compounds, mechanisms, models and applications, Materials (Basel). 11 (2018). https://doi.org/10.3390/ma11040484.

[17] A. Lynn, Undergraduate Honors College Theses Sonoluminescence : Sound And Light, (2017).

[18] R. Bajaj, A.S. Rao, G.V. Prakash, Photoluminescence down-shifting studies of thermally stable Eu3+ ions doped borosilicate glasses for visible red photonic device applications, J. Non. Cryst. Solids. 575 (2022) 121184. https://doi.org/10.1016/j.jnoncrysol.2021.121184.

[19] A. Prasad, A.S. Rao, G.V. Prakash, A study on up-conversion and energy transfer

kinetics of $KGdF_4:Yb^{3+}/Er^{3+}$ nanophosphors, J. Mol. Struct. 1205 (2020) 127647. https://doi.org/10.1016/j.molstruc.2019.127647.

[20] R. Bajaj, A.S. Rao, G.V. Prakash, Linear and nonlinear photoluminescence from thermally stable $KYF_4:Eu^{3+}$ cubic nanocrystals, J. Alloys Compd. 885 (2021) 160893. https://doi.org/10.1016/j.jallcom.2021.160893.

[21] V. Balaram, Rare earth elements: A review of applications, occurrence, exploration, analysis, recycling, and environmental impact, Geosci. Front. 10 (2019) 1285–1303. https://doi.org/10.1016/j.gsf.2018.12.005.

[22] Z.H. Ju, R.P. Wei, J.X. Ma, C.R. Pang, W.S. Liu, A novel orange emissive phosphor $SrWO_4:Sm^{3+}$ for white light-emitting diodes, J. Alloys Compd. 507 (2010) 133–136. https://doi.org/10.1016/j.jallcom.2010.07.138.

[23] Y. Tian, Development of phosphors with high thermal stability and efficiency for phosphor-converted LEDs, J. Solid State Light. 1 (2014) 1–15. https://doi.org/10.1186/s40539-014-0011-8.

[24] C.R. Ronda, T. Jüstel, H. Nikol, Rare earth phosphors: Fundamentals and applications, J. Alloys Compd. 275–277 (1998) 669–676. https://doi.org/10.1016/S0925-8388(98)00416-2.

[25] C.F. Yang, C.Y. Lin, Investigation of luminescent properties of Eu^{3+} doped double perovskite Ba_2ZnMoO_6 phosphors by using solid-state reaction method, Microsyst. Technol. 24 (2018) 4067–4074. https://doi.org/10.1007/s00542-017-3624-1.

[26] Y. Li, X. Liu, Energy transfer and luminescence properties of $Ba_2CaMoO_6:Eu^{3+}$ phosphors prepared by sol-gel method, Opt. Mater. (Amst). 42 (2015) 303–308. https://doi.org/10.1016/j.optmat.2015.01.018.

[27] X. Ye, W. Zhuang, Y. Hu, T. He, X. Huang, C. Liao, S. Zhong, Z. Xu, H. Nie, G. Deng, Preparation, characterization, and optical properties of nano- and submicron-sized Y_2O_3: Eu^{3+} phosphors, J. Appl. Phys. 105 (2009) 1–7. https://doi.org/10.1063/1.3086624.

[28] J.F.S. Bitencourt, A. Ventieri, K.A. Gonçalves, E.L. Pires, J.C. Mittani, S.H. Tatumi, A comparison between neodymium doped alumina samples obtained by Pechini and sol-gel methods using thermo-stimulated luminescence and SEM, J. Non. Cryst. Solids. 356 (2010) 2956–2959. https://doi.org/10.1016/j.jnoncrysol.2010.03.047.

[29] M.K. Sahu, M. Jayasimhadri, K. Jha, B. Sivaiah, A.S. Rao, D. Haranath, Synthesis and enhancement of photoluminescent properties in spherical shaped Sm^{3+}/Eu^{3+} co-doped $NaCaPO_4$ phosphor particles for w-LEDs, J. Lumin. 202 (2018) 475–483. https://doi.org/10.1016/j.jlumin.2018.06.002.

[30] M.M. Kolte, V.B. Pawade, A.B. Bhattacharya, S.J. Dhoble, Tunable emission in Ln^{3+} (Ce^{3+}/Dy^{3+}, Ce^{3+}/Tb^{3+}) doped $KNa_3Al_4Si_4O_{16}$ phosphor synthesized by combustion method, J. Phys. Chem. Solids. 116 (2018) 338–346. https://doi.org/10.1016/j.jpcs.2018.02.004.

[31] Z.M. Chen, S.X. Jiang, R.H. Guo, B.J. Xin, D.G. Miao, Microstructure and photoluminescent properties of Y_2O_3:Eu^{3+} phosphors synthesised by precipitation and combustion methods, Mater. Technol. 29 (2014) 198–203. https://doi.org/10.1179/1753555713Y.0000000123.

[32] A. Prasad, A.S. Rao, G.V. Prakash, Up-conversion luminescence and EPR properties of $KGdF_4$:Yb^{3+}/Tm^{3+} nanophosphors, Optik (Stuttg). 208 (2020) 164538. https://doi.org/10.1016/j.ijleo.2020.164538.

[33] Y. Wang, C. Yu, Y. Zhou, E. Song, H. Ming, Q. Zhang, Mn^{4+} doped narrowband red phosphors with short fluorescence lifetime and high color stability for fast-response backlight display application, J. Alloys Compd. 855 (2021) 157347. https://doi.org/10.1016/j.jallcom.2020.157347.

[34] C. Yang, C. He, X. Huang, G. Chen, G. Leng, R. Mi, X. Min, light-emitting diodes, Ceram. Int. 6 (2021) 2–10. https://doi.org/10.1016/j.ceramint.2021.01.087.

[35] V. V. Popov, A.P. Menushenkov, A.A. Yastrebtsev, A.Y. Molokova, S.G. Rudakov, R.D. Svetogorov, N.A. Tsarenko, K. V. Ponkratov, N. V. Ognevskaya, O.N. Seregina, The effect of the synthesis conditions on the structure and phase transitions in $Ln_2(MoO_4)_3$, Solid State Sci. 112 (2021) 106518. https://doi.org/10.1016/j.solidstatesciences.2020.106518.

[36] S. Behara, K. Ikeda, T. Thomas, Amphoteric behavior of Dy^{3+} in $Na_{0.5}Bi_{0.5}TiO_3$: Neutron diffraction and Raman studies, Ceram. Int. (2021). https://doi.org/10.1016/j.ceramint.2021.01.149.

[37] N. Jain, R. Paroha, R.K. Singh, S.K. Mishra, S.K. Chaurasiya, R.A. Singh, J. Singh, Synthesis and Rational design of Europium and Lithium Doped Sodium Zinc Molybdate with Red Emission for Optical Imaging, Sci. Rep. 9 (2019) 1–14. https://doi.org/10.1038/s41598-019-38787-1.

[38] M. Song, Y. Liu, Y. Liu, L. Wang, N. Zhang, X. Wang, Z. Huang, C. Ji, Sol-gel synthesis and luminescent properties of a novel $KBaY(MoO_4)_3 : Dy^{3+}$ phosphor for white light emission, J. Lumin. 211 (2019) 218–226. https://doi.org/10.1016/j.jlumin.2019.03.052.

[39] B. Verma, R.N. Baghel, D.P. Bisen, N. Brahme, A. Khare, Synthesis and

concentration dependent luminescent characterization of $BaMgSiO_4 : Eu^{3+}$ phosphor, J. Alloys Compd. 838 (2020) 155326. https://doi.org/10.1016/j.jallcom.2020.155326.

[40] R. Mahajan, R. Prakash, S. Kumar, V. Kumar, J. Choudhary, D.M. Phase, Optik Surface and luminescent properties of $Mg_3(PO_4)_2 : Dy^{3+}$ phosphors, Optik (Stuttg). 225 (2021) 165717. https://doi.org/10.1016/j.ijleo.2020.165717.

[41] H.C. Choi, Y.M. Jung, S. Bin Kim, Size effects in the Raman spectra of TiO_2 nanoparticles, Vib. Spectrosc. 37 (2005) 33–38. https://doi.org/10.1016/j.vibspec.2004.05.006.

[42] S. Kaur, M. Jayasimhadri, A.S. Rao, A novel red emitting Eu^{3+}doped calcium aluminozincate phosphor for applications in w-LEDs, J. Alloys Compd. 697 (2017) 367–373. https://doi.org/10.1016/j.jallcom.2016.12.150.

[43] B. V. Ratnam, M.K. Sahu, A.K. Vishwakarma, K. Jha, H.J. Woo, K. Jang, M. Jayasimhadri, Optimization of synthesis technique and luminescent properties in Eu^{3+}-activated NaCaPO4 phosphor for solid state lighting applications, J. Lumin. 185 (2017) 99–105. https://doi.org/10.1016/j.jlumin.2017.01.006.

[44] Y. Liu, G. Li, R. Wang, G. Cai, Dependence of Luminous Performance on Eu^{3+}Site Occupation in $SrIn_2(P_2O_7)_2$: The Effect of the Local Environment, Inorg. Chem. 60 (2021) 17219–17229. https://doi.org/10.1021/acs.inorgchem.1c02550.

[45] M.K. Sahu, M. Jayasimhadri, Conversion of blue emitting thermally stable $Ca_3Bi(PO_4)_3$ host as a color tunable phosphor via energy transfer for luminescent devices, J. Lumin. 227 (2020) 117570. https://doi.org/10.1016/j.jlumin.2020.117570.

[46] X. Gao, F. Song, A. Khan, Z. Chen, D. Ju, X. Sang, Room temperature synthesis , Judd Ofelt analysis and photoluminescence, J. Lumin. 230 (2021) 117707.

https://doi.org/10.1016/j.jlumin.2020.117707.

[47] L. Su, Y. Liu, G. Li, Z. Wu, G. Cai, L. Ma, X. Wang, Multicolor emission leading by energy transfer between Dy^{3+} and Eu^{3+} in wolframite $InNbTiO_6$, J. Lumin. 227 (2020). https://doi.org/10.1016/j.jlumin.2020.117578.

[48] H. Kaur, M. Jayasimhadri, Optimization of structural and luminescent properties with intense red emitting thermally stable Sm^{3+} doped $CaBiVO_5$ phosphors for w-LED applications, Opt. Mater. (Amst). 107 (2020) 110119. https://doi.org/10.1016/j.optmat.2020.110119.

[49] B. Li, X. Huang, J. Lin, phosphors with high-e ffi ciency : Photoluminescence , energy transfer and application in near-UV-pumped white LEDs, J. Lumin. 204 (2018) 410–418. https://doi.org/10.1016/j.jlumin.2018.08.044.

[50] M. Jiao, Q. Xu, Y. Zhao, D. Wang, L. Liu, C. Yang, Photoluminescence properties and energy transfer of high thermal stable $Na_2GdPO_4F_2$: RE(RE=Sm^{3+}, Ce^{3+}, Tb^{3+}) phosphor for solid-state lighting, 226 (2020).

[51] Y. Il Jeon, L.K. Bharat, J. Su, phosphors for solid-state lighting applications, J. Lumin. 166 (2015) 93–100. https://doi.org/10.1016/j.jlumin.2015.05.010.

[52] G.L. Bhagyalekshmi, D.N. Rajendran, Luminescence dynamics of Eu^{3+} activated and co-activated defect spinel zinc titanate nanophosphor for applications in WLEDs, J. Alloys Compd. 850 (2021) 156660. https://doi.org/10.1016/j.jallcom.2020.156660.

[53] X. Fan, J. Si, M. Xu, G. Li, J. Tang, G. Cai, Photoluminescence and energy transfer of efficient and thermally stable white-emitting $Ca_9La(PO_4)_7$:Ce^{3+}, Tb^{3+}, Mn^{2+} phosphors, Ceram. Int. 47 (2021) 12056–12065. https://doi.org/10.1016/j.ceramint.2021.01.049.

[54] V. Uma, M. Vijayakumar, K. Marimuthu, G. Muralidharan, Luminescence and energy

transfer studies on Sm^{3+}/Tb^{3+} codoped telluroborate glasses for WLED applications TBLT2S, J. Mol. Struct. 1151 (2018) 266–276. https://doi.org/10.1016/j.molstruc.2017.09.053.

[55] S. Kaur, A.S. Rao, M. Jayasimhadri, B. Sivaiah, D. Haranath, Synthesis optimization , photoluminescence and thermoluminescence studies of Eu^{3+} doped calcium aluminozincate phosphor, J. Alloys Compd. 802 (2019) 129–138. https://doi.org/10.1016/j.jallcom.2019.06.169.

[56] Y. Chang, Z. Shi, Y. Tsai, S. Wu, H. Chen, The effect of Eu^{3+} -activated $InVO_4$ phosphors prepared by sol – gel method, 33 (2011) 375–380. https://doi.org/10.1016/j.optmat.2010.09.018.

[57] A. Prasad, A.S. Rao, M. Gupta, G.V. Prakash, Morphological and luminescence studies on $KGdF_4:Yb^{3+}/Tb^{3+}$ up-conversion nanophosphors, Mater. Chem. Phys. 219 (2018) 13–21. https://doi.org/10.1016/j.matchemphys.2018.07.056.

[58] G.A. Kumar, M. Pokhrel, D.K. Sardar, Absolute quantum yield measurements in Yb / Ho doped M_2O_2S (M =Y , Gd , La) upconversion phosphor, Mater. Lett. 98 (2013) 63–66. https://doi.org/10.1016/j.matlet.2013.02.001.

[59] D. Zhang, S. Liang, S. Yao, H. Li, J. Liu, Y. Geng, X. Pu, Highly efficient visible/NIR photocatalytic activity and mechanism of Yb^{3+}/Er^{3+} co-doped $Bi_4O_5I_2$ up-conversion photocatalyst, Sep. Purif. Technol. 248 (2020) 117040. https://doi.org/10.1016/j.seppur.2020.117040.

[60] S. Liang, D. Zhang, X. Yao, R. Han, Q. Zhang, C. Jin, X. Pu, Y. Geng, Deposition-precipitation synthesis of Yb^{3+}/Er^{3+} co-doped BiOBr/AgBr heterojunction photocatalysts with enhanced photocatalytic activity under Vis/NIR light irradiation,

Sep. Purif. Technol. 238 (2020) 116450. https://doi.org/10.1016/j.seppur.2019.116450.

[61] A. Roy, A. Dwivedi, H. Mishra, D. Kumar, S.B. Rai, Dual mode (upconversion and downshifting) behavior of $Ho^{3+}/Yb^{3+}/Bi^{3+}$ co-doped $YTaO_4$ phosphor and its application as a security ink, J. Alloys Compd. 821 (2020) 153202. https://doi.org/10.1016/j.jallcom.2019.153202.

[62] A. Shandilya, R.S. Yadav, A.K. Gupta, K. Sreenivas, Effects of Yb^{3+} ion doping on lattice distortion, optical absorption and light upconversion in Er^{3+}/Yb^{3+} co-doped $SrMoO_4$ ceramics, Mater. Chem. Phys. 264 (2021) 124441. https://doi.org/10.1016/j.matchemphys.2021.124441.

[63] D. Chiriu, L. Stagi, C.M. Carbonaro, P.C. Ricci, pss to replace critical raw materials, 997 (2016) 989–997. https://doi.org/10.1002/pssc.201600116.

[64] K. Fabitha, Ho^{3+} -doped ZnO nano phosphor for low-threshold sharp red light emission at elevated temperatures, (2018). https://doi.org/10.1364/JOSAB.34.002485.

[65] Ravita, A.S. Rao, Effective sensitization of Eu^{3+} visible red emission by Sm^{3+} in thermally stable potassium zinc alumino borosilicate glasses for photonic device applications, J. Lumin. 244 (2022) 118689. https://doi.org/10.1016/j.jlumin.2021.118689.

[66] A. Roy, A. Dwivedi, H. Mishra, D. Kumar, S.B. Rai, Dual mode (upconversion and downshifting) behavior of $Ho^{3+}/Yb^{3+}/Bi^{3+}$ co-doped $YTaO_4$ phosphor and its application as a security ink, J. Alloys Compd. 821 (2020) 153202. https://doi.org/10.1016/j.jallcom.2019.153202.

[67] P. Rohilla, A.S. Rao, Synthesis optimisation and efficiency enhancement in Eu^{3+} doped barium molybdenum titanate phosphors for w-LED applications, Mater. Res.

Bull. 150 (2022) 111753. https://doi.org/10.1016/j.materresbull.2022.111753.

[68] A. Roy, A. Dwivedi, H. Mishra, S.B. Rai, Host dependent upconversion , color tunability and laser induced optical heating via NIR excitation in Ho^{3+} , Yb^{3+} doped YXO_4 (X =V ,Nb ,Ta) phosphor materials : Application as a security tool and optical heater, Mater. Res. Bull. 145 (2022) 111568. https://doi.org/10.1016/j.materresbull.2021.111568.

[69] K. Dharendra, A. Roy, A. Dwivedi, A. Kumar, S. Bahadur, D. Kumar, Two steps enhancement of dual mode (UC and DS) behaviour of Ho^{3+}/ Yb^{3+} and Tm^{3+} /Yb^{3+} co-doped $GdVO_4$ phosphors : Improvement in spectral and color purity, Mater. Res. Bull. 139 (2021) 111280. https://doi.org/10.1016/j.materresbull.2021.111280.

[70] P.K. Vishwakarma, S.B. Rai, A. Bahadur, Intense red and green emissions from Ho^{3+}/Yb^{3+} co-doped Sodium Gadolinium Molybdate Nano-phosphor : Effect of calcination temperature and Intrinsic optical bistability, Mater. Res. Bull. 133 (2021) 111041. https://doi.org/10.1016/j.materresbull.2020.111041.

[71] Z. Yan, R. Huang, X. Yang, S. Xiao, Broadband up-conversion in SrLaAlO4 : Yb^{3+}/ Ho^{3+}/Mn^{4+} phosphor, Opt. Mater. (Amst). 109 (2020) 110416. https://doi.org/10.1016/j.optmat.2020.110416.

[72] T. Zhang, W. Yang, H. Li, X. Wang, X. Jiang, Z. Leng, W. Yang, C. Li, H. Lin, H. Liu, K. Huang, C. Li, F. Zeng, Z. Su, Enhanced red emission of Yb, Ho: $NaYGd(WO_4)_2$ phosphors by codoping Ce^{3+}, J. Lumin. 240 (2021). https://doi.org/10.1016/j.jlumin.2021.118432.

[73] H. Bensouyad, H. Sedrati, H. Dehdouh, M. Brahimi, F. Abbas, H. Akkari, R. Bensaha, Structural , thermal and optical characterization of TiO_2 : ZrO_2 thin fi lms prepared by

sol – gel method, 519 (2010) 96–100. https://doi.org/10.1016/j.tsf.2010.07.062.

[74] A. Roy, A. Dwivedi, H. Mishra, S.B. Rai, Host dependent upconversion, color tunability and laser induced optical heating via NIR excitation in Ho^{3+}, Yb^{3+} doped YXO_4 (X = V, Nb, Ta) phosphor materials: Application as a security tool and optical heater, Mater. Res. Bull. 145 (2022) 111568. https://doi.org/10.1016/j.materresbull.2021.111568.

[75] P. Singh, R.S. Yadav, P. Singh, S.B. Rai, Upconversion and downshifting emissions of Ho^{3+}-Yb^{3+} co-doped $ATiO_3$ perovskite phosphors with temperature sensing properties in Ho_{3+}-Yb_{3+} co-doped $BaTiO_3$ phosphor, J. Alloys Compd. 855 (2021) 157452. https://doi.org/10.1016/j.jallcom.2020.157452.

[76] X. Yuhang, Z. Xiangyu, Z. Hongbo, Z. Mengjie, M. Shuo, S. Chunhui, J. Shao, Luminescence properties of Eu^{3+} doped $BaMoO_4$ transparent glass ceramics, J. Non. Cryst. Solids. 500 (2018) 243–248. https://doi.org/10.1016/j.jnoncrysol.2018.08.007.

[77] P.K. Vishwakarma, S.B. Rai, A. Bahadur, Intense red and green emissions from Ho^{3+}/Yb^{3+} co-doped Sodium Gadolinium Molybdate Nano-phosphor: Effect of calcination temperature and Intrinsic optical bistability, Mater. Res. Bull. 133 (2021) 111041. https://doi.org/10.1016/j.materresbull.2020.111041.

[78] P. Du, J.S. Yu, red-emitting phosphors with ultrabroad excitation band for white light-emitting diodes, Sci. Rep. 3 (2017) 1–10. https://doi.org/10.1038/s41598-017-12161-5.

[79] T.T.M. Phan, N.C. Chu, V.B. Luu, H. Nguyen Xuan, D.T. Pham, I. Martin, P. Carrière, Enhancement of polarization property of silane-modified $BaTiO_3$ nanoparticles and its effect in increasing dielectric property of epoxy/$BaTiO_3$ nanocomposites, J. Sci. Adv. Mater. Devices. 1 (2016) 90–97.

https://doi.org/10.1016/j.jsamd.2016.04.005.

[80] S. Mahamuda, K. Swapna, M. Venkateswarlu, A. Srinivasa Rao, S. Shakya, G. Vijaya Prakash, Spectral characterisation of Sm^{3+} ions doped Oxy-fluoroborate glasses for visible orange luminescent applications, J. Lumin. 154 (2014) 410–424. https://doi.org/10.1016/j.jlumin.2014.05.017.

[81] S. Mahamuda, K. Swapna, P. Packiyaraj, A.S. Rao, G.V. Prakash, Lasing potentialities and white light generation capabilities of Dy^{3+} doped oxy- fl uoroborate glasses, J. Lumin. 153 (2014) 382–392. https://doi.org/10.1016/j.jlumin.2014.03.009.

[82] N. Deopa, A.S. Rao, Spectroscopic studies of Sm^{3+} ions activated lithium lead alumino borate glasses for visible luminescent device applications, Opt. Mater. (Amst). 72 (2017) e105–e105. https://doi.org/10.1016/j.optmat.2017.04.067.

[83] K. Dharendra, A. Roy, A. Dwivedi, A.K. Rai, S.B. Rai, D. Kumar, Two steps enhancement of dual mode (UC and DS) behaviour of Ho^{3+}/Yb^{3+} and Tm^{3+}/Yb^{3+} co-doped $GdVO_4$ phosphors: Improvement in spectral and color purity, Mater. Res. Bull. 139 (2021) 111280. https://doi.org/10.1016/j.materresbull.2021.111280.

[84] Monika, R.S. Yadav, A. Rai, S.B. Rai, NIR light guided enhanced photoluminescence and temperature sensing in $Ho^{3+}/Yb^{3+}/Bi^{3+}$ co-doped $ZnGa_2O_4$ phosphor, Sci. Rep. 11 (2021) 1–17. https://doi.org/10.1038/s41598-021-83644-9.

[85] P.K. Vishwakarma, A. Bahadur, A. Maurya, S.B. Rai, Large enhancement in upconverted green emission intensity from Ho_{3+}/Yb_{3+} co-doped $Y_2Ti_2O_7$ phosphor in the presence of Zn^{2+}, Mater. Res. Bull. 115 (2019) 219–226. https://doi.org/10.1016/j.materresbull.2019.03.029.

[86] Abhishek Roya, Abhishek Dwivedib,∗∗, Devendra Kumarc, H. Mishrad, S.B.

Raia.pdf, (n.d.).

[87] A. Roy, A. Dwivedi, S. Kumar, H. Mishra, A.K. Rai, S.B. Rai, Study of near-infrared induced color tunability and optical bistability in Ho^{3+}/Yb^{3+} codoped $YV_{0.75}Ta_{0.25}O_4$ phosphor, Opt. Mater. (Amst). 122 (2021) 111701. https://doi.org/10.1016/j.optmat.2021.111701.

[88] X. Yu, H. Li, X. Li, Y. Jiang, R. Zheng, H. Wu, Z. Song, Z. Jiang, P. Zhao, Up-conversion luminescence and near-infrared quantum cutting of Ho^{3+}/Yb^{3+} co-doped hexagonal $NaGdF_4$ phosphors, J. Mater. Sci. Mater. Electron. 32 (2021) 21032–21043. https://doi.org/10.1007/s10854-021-06588-w.

[89] T. Zhang, W. Yang, H. Li, X. Wang, X. Jiang, Z. Leng, Enhanced red emission of Yb , Ho : NaYGd $(WO_4)_2$ phosphors by codoping Ce^{3+}, 240 (2021). https://doi.org/10.1016/j.jlumin.2021.118432.

[90] J. Tang, C. Cheng, Y. Chen, Y. Huang, Yellow – green upconversion photoluminescence in Yb^{3+} , Ho^{3+} co-doped $NaLa(MoO_4)_2$ phosphor, 609 (2014) 268–273. https://doi.org/10.1016/j.jallcom.2014.04.134.

[91] P. Singh, R. Sagar, P. Singh, S. Bahadur, Upconversion and downshifting emissions of Ho^{3+} -Yb^{3+} co-doped $ATiO_3$ perovskite phosphors with temperature sensing properties in Ho^{3+} -Yb^{3+} co-doped $BaTiO_3$ phosphor, J. Alloys Compd. 855 (2021) 157452. https://doi.org/10.1016/j.jallcom.2020.157452.

[92] J. Zhang, J. Chen, Y. Zhang, S. An, Journal of Alloys and Compounds, 860 (2021). https://doi.org/10.1016/j.jallcom.2020.158473.

[93] X. Zhou, Z. Zhang, Y. Wang, Ce^{3+} and Tb^{3+} singly- and co-doped $MgGd_4Si_3O_{13}$ for ultraviolet light emitting diodes and field emission displays, J. Mater. Chem. C. 3

(2015) 3676–3683. https://doi.org/10.1039/c4tc02807d.

[94] Z. Zhu, Y. Zhang, Y. Qiao, H. Liu, D. Liu, Luminescence properties of $Ce^{3+}/Tb^{3+}/Sm^{3+}$ co-doped $CaO\text{-}SiO_2\text{-}B_2O_3$ glasses for white light emitting diodes, J. Lumin. 134 (2013) 724–728. https://doi.org/10.1016/j.jlumin.2012.07.003.

[95] C.H. Chiang, H.H. Su, Y.C. Fang, S.Y. Chu, Effects of argon sintering atmosphere on luminescence characteristics of $Ca_6BaP_4O_{17}:Sm^{3+}$ phosphors, Ceram. Int. 44 (2018) 6278–6284. https://doi.org/10.1016/j.ceramint.2018.01.016.

[96] Z. Jia, C. Yuan, Y. Liu, Strategies to approach high performance in Cr^{3+} -doped phosphors for high-power NIR-LED light sources, Light Sci. Appl. (2020). https://doi.org/10.1038/s41377-020-0326-8.

[97] W.U. Khan, L. Zhou, Q. Liang, X. Li, J. Yan, N.U. Rahman, L. Dolgov, S.U. Khan, J. Shi, M. Wu, Luminescence enhancement and energy transfers of Ce^{3+} and Sm^{3+} in $CaSrSiO_4$ phosphor, J. Mater. Chem. C. 6 (2018) 7612–7618. https://doi.org/10.1039/c8tc02143k.

[98] M. Janulevicius, P. Marmokas, M. Misevicius, J. Grigorjevaite, L. Mikoliunaite, S. Sakirzanovas, A. Katelnikovas, Luminescence and luminescence quenching of highly efficient $Y_2Mo_4O15:Eu^{3+}$ phosphors and ceramics, Sci. Rep. 6 (2016) 1–12. https://doi.org/10.1038/srep26098.

[99] S.E. Brinkley, N. Pfaff, K.A. Denault, Z. Zhang, H.T. Hintzen, R. Seshadri, S. Nakamura, S.P. Denbaars, Robust thermal performance of $Sr_2Si_5N_8:Eu^{2+}$: An efficient red emitting phosphor for light emitting diode based white lighting, Appl. Phys. Lett. 99 (2011). https://doi.org/10.1063/1.3666785.

[100] G. Annadurai, S.M.M. Kennedy, Synthesis and photoluminescence properties of

$Ba_2CaZn_2Si_6O_{17}:Eu^{3+}$ red phosphors for white LED applications, J. Lumin. 169 (2016) 690–694. https://doi.org/10.1016/j.jlumin.2015.03.007.

[101] A.K. Vishwakarma, M. Jayasimhadri, Pure orange color emitting Sm^{3+} doped $BaNb_2O_6$ phosphor for solid - State lighting applications, J. Lumin. 176 (2016) 112–117. https://doi.org/10.1016/j.jlumin.2016.03.025.

[102] T. Srikanth, D.V.K. Reddy, K.S. Rudramamba, S. Taherunnisa, N.M. Reddy, T.L. Viveka, M.R. Reddy, Red light component tuning by n-UV / blue light excitations in Sm^{3+} / Eu^{3+} co-doped $Y_2O_3 – Al_2O_3 – Bi_2O_3 – B_2O_3 – SiO_2$ glasses for W-LED applications, Opt. Mater. (Amst). 134 (2022) 113148. https://doi.org/10.1016/j.optmat.2022.113148.

[103] S. Kaur, N. Deopa, A. Prasad, R. Bajaj, A.S. Rao, Intense green emission from Tb 3 + ions doped zinc lead alumino borate glasses for laser and w-LEDs applications, Opt. Mater. (Amst). 84 (2018) 318–323. https://doi.org/10.1016/j.optmat.2018.07.020.

[104] N. Deopa, M.K. Sahu, P.R. Rani, R. Punia, A.S. Rao, Realization of warm white light and energy transfer studies of Dy^{3+} /Eu^{3+} co-doped Li_2O-PbO-Al_2O_3 -B_2O_3 glasses for lighting applications, J. Lumin. 222 (2020) 117166. https://doi.org/10.1016/j.jlumin.2020.117166.

[105] N. Deopa, B. Kumar, M.K. Sahu, P.R. Rani, A.S. Rao, Effect of Sm^{3+} ions concentration on borosilicate glasses for reddish orange luminescent device applications, J. Non. Cryst. Solids. 513 (2019) 152–158. https://doi.org/10.1016/j.jnoncrysol.2019.03.025.

[106] K.N. Kumar, L. Vijayalakshmi, J.S. Kim, Enhanced red luminescence quantum yield from Gd^{3+}/Eu^{3+}: $CaLa_2ZnO_5$ phosphor spheres for photonic applications, Mater. Res.

Bull. 103 (2018) 234–241. https://doi.org/10.1016/j.materresbull.2018.03.045.

[107] Y. Tian, Development of phosphors with high thermal stability and efficiency for phosphor-converted LEDs, (2014) 1–15.

[108] D. Chiriu, L. Stagi, C.M. Carbonaro, P.C. Ricci, Strength and weakness of rare earths based phosphors: Strategies to replace critical raw materials, Phys. Status Solidi Curr. Top. Solid State Phys. 13 (2016) 989–997. https://doi.org/10.1002/pssc.201600116.

[109] L. Su, Y. Liu, G. Li, Z. Wu, G. Cai, L. Ma, X. Wang, Multicolor emission leading by energy transfer between Dy^{3+} and Eu^{3+} in wolframite InNbTiO6, J. Lumin. 227 (2020). https://doi.org/10.1016/j.jlumin.2020.117578.

[110] Y. Tang, S. Zhou, X. Yi, D. Hao, X. Shao, J. Chen, The characterization of Ce/Pr-doped YAG phosphor ceramic for the white LEDs, J. Alloys Compd. 745 (2018) 84–89. https://doi.org/10.1016/j.jallcom.2018.02.129.

[111] P. Du, J.S. Yu, Eu^{3+}-activated La_2MoO_6-La_2WO_6 red-emitting phosphors with ultrabroad excitation band for white light-emitting diodes, Sci. Rep. 7 (2017) 1–10. https://doi.org/10.1038/s41598-017-12161-5.

[112] P. Rohilla, A.S. Rao, Linear and non-linear photoluminescence studies of Ho^{3+}/Yb^{3+} co-doped titanate phosphors for photonic applications, J. Alloys Compd. 928 (2022) 167156. https://doi.org/10.1016/j.jallcom.2022.167156.

[113] S. Kaur, A.S. Rao, M. Jayasimhadri, Spectroscopic and photoluminescence characteristics of Sm^{3+} doped calcium aluminozincate phosphor for applications in w-LED, Ceram. Int. 43 (2017) 7401–7407. https://doi.org/10.1016/j.ceramint.2017.02.129.

[114] M. Fu, Q. Wu, C. Gu, S. Hu, S. Lu, B. Wang, Y. Hong, Y. Wang, l P re r f, (2023).

https://doi.org/10.1016/j.vacuum.2023.112147.

[115] F. Xu, L. Zhong, Y. Xu, S. Feng, C. Zhang, F. Zhang, G. Zhang, Highly efficient flame-retardant kraft paper, J. Mater. Sci. 54 (2019) 1884–1897. https://doi.org/10.1007/s10853-018-2911-2.

[116] X. Zhao, J. Zhang, L. Shi, M. Xian, C. Dong, S. Shuang, Folic acid-conjugated carbon dots as green fluorescent probes based on cellular targeting imaging for recognizing cancer cells, RSC Adv. 7 (2017) 42159–42167. https://doi.org/10.1039/c7ra07002k.

[117] C.P. Huang, M.A. Rather, C.T. Wu, R. Loganathan, Y.H. Ju, K.L. Lin, J.I. Chyi, K.Y. Lai, Crystal Transformation of Cubic BN Nanoislands to Rhombohedral BN Sheets on AlN for Deep-UV Light-Emitting Diodes, ACS Appl. Nano Mater. 3 (2020) 5285–5290. https://doi.org/10.1021/acsanm.0c00681.

[118] B. Viswanathan, S. Murugesan, A. Ariharan, K.S. Lakhi, Hetero Atom Substituted Carbon—Potential Hydrogen Storage Materials, Adv. Porous Mater. 1 (2013) 122–128. https://doi.org/10.1166/apm.2013.1008.

[119] L. Zhang, B. Sun, C. Shao, F. Zhen, S. Wei, W. Bu, Q. Yao, Z. Jiang, H. Chen, Preparation, band-structure and luminescence of double perovskite $Ba_2MgMoO_6:Eu^{3+}$ orange-red phosphor for white LEDs, Ceram. Int. 44 (2018) 17305–17312. https://doi.org/10.1016/j.ceramint.2018.06.192.

[120] W. Yuan, R. Pang, S. Wang, T. Tan, C. Li, C. Wang, H. Zhang, Enhanced blue-light excited cyan-emitting Bi^{3+} phosphors for AC-LEDs via defect modulation, (2022). https://doi.org/10.1038/s41377-022-00868-8.

[121] A.S. Asyikin, M.K. Halimah, A.A. Latif, M.F. Faznny, S.N. Nazrin, Physical , structural and optical properties of bio-silica borotellurite glass system doped with

samarium oxide nanoparticles, J. Non. Cryst. Solids. 529 (2020) 119777. https://doi.org/10.1016/j.jnoncrysol.2019.119777.

[122] S.P. Khambule, S. V Motloung, T.E. Motaung, L.F. Koao, R.E. Kroon, M.A. Malimabe, Results in Optics Tuneable blue to orange phosphor from Sm^{3+} doped $ZnAl_2O_4$ nanomaterials, Results Opt. 9 (2022) 100280. https://doi.org/10.1016/j.rio.2022.100280.

[123] C. Ta, H. Wen, Z. Mo, Y. Huo, Z. Mu, E.A. Dawi, L. Luo, D. Abdul, Preparation and luminescence investigations of garnet-based $Y_2Ca_2Ga_3VO_{12}$: RE (RE = Eu^{3+},Sm^{3+} , and Dy^{3+}) phosphors, 164 (2023).

[124] S. Dai, D. Zhao, R. Zhang, L. Jia, Q. Yao, Enhancing luminescence intensity and improving thermostability of red phosphors $Li_3Ba_2La_3(WO_4)_8$_Eu^{3+} by co-doping with Sm^{3+} ions, J. Alloys Compd. 891 (2021) 161973. https://doi.org/10.1016/j.jallcom.2021.161973.

[125] S. Lou, P. Zhang, Y. Chen, Q. Xiong, K. Qiu, phosphors by Sm^{3+} co-doping, 47 (2021) 10174–10184. https://doi.org/10.1016/j.ceramint.2020.12.166.

[126] J. Yang, H. Xiong, J. Dong, C. Yang, S. Gan, L. Zou, Journal of Physics and Chemistry of Solids Facile hydrothermal synthesis and luminescent properties of Sm^{3+}/ Eu^{3+} codoped $GdPO_4$ phosphors, J. Phys. Chem. Solids. 111 (2017) 355–363. https://doi.org/10.1016/j.jpcs.2017.08.031.

[127] M.K. Sahu, M. Jayasimhadri, K. Jha, B. Sivaiah, A.S. Rao, D. Haranath, Synthesis and enhancement of photoluminescent properties in spherical shaped Sm^{3+}/Eu^{3+} co-doped $NaCaPO_4$ phosphor particles for w-LEDs, J. Lumin. 202 (2018) 475–483. https://doi.org/10.1016/j.jlumin.2018.06.002.

[128] J. Gou, D. Zhang, B. Yu, J. Wang, S. Liu, The Photoluminescence Behaviors of a Novel Reddish Orange Emitting Phosphor $CaIn_2O_4 : Sm^{3+}$ Codoped with Zn^{2+} or Al3+ Ions, 2015 (2015).

[129] H. Tang, X. Zhang, L. Cheng, L. Jiang, X. Mi, Q. Liu, Photoluminescence properties and energy transfer mechanisms of, J. Lumin. 214 (2019) 116532. https://doi.org/10.1016/j.jlumin.2019.116532.

[130] X. Gao, W. Zhang, X. Wang, X. Huang, H. Du, J. Lin, Enhancing the photoluminescence performance of $Ca(PO_4)_2SiO_4 : Re^{3+}$(Re = Eu , Sm) phosphors with A^{3+}(A = La , Bi) codoping and white light-emitting diode application, Ceram. Int. 48 (2022) 13080–13089. https://doi.org/10.1016/j.ceramint.2022.01.184.

[131] M.N. Huang, Y.Y. Ma, X.Y. Huang, S. Ye, Q.Y. Zhang, Spectrochimica Acta Part A : Molecular and Biomolecular Spectroscopy The luminescence properties of Bi^{3+} sensitized $Gd_2MoO_6 : RE^{3+}$ (RE = Eu or Sm) phosphors for solar spectral conversion, 115 (2013) 767–771. https://doi.org/10.1016/j.saa.2013.06.111.

[132] M. Yan, G. Liu, J. Wen, Y. Wang, Characterizations and Red Emission Enhancement for WLEDs, (2018). https://doi.org/10.3390/ma11071090.

[133] V.A. Online, L. Wu, Y. Bai, L. Wu, H. Yi, Y. Kong, Y. Zhang, J. Xu, RSC Advances, (2017) 1146–1153. https://doi.org/10.1039/C6RA26752A.

[134] N. Liu, L. Mei, L. Liao, J. Fu, D. Yang, High Thermal Stability Apatite Sm^{3+} for White Light Emission : Synthesis , Structure , Luminescence Properties and Energy Transfer, Sci. Rep. 8 (2019) 1–9. https://doi.org/10.1038/s41598-019-51915-1.

[135] Y. Ding, N. Guo, M. Zhu, W. Lv, R. Ouyang, Y. Miao, Luminescence and temperature sensing abilities of zincate phosphors co-, Mater. Res. Bull. 129 (2020)

110869. https://doi.org/10.1016/j.materresbull.2020.110869.

[136] S. Ling, F.B. Xiong, W.B. Yang, H.F. Lin, W.Z. Zhu, Novel Sm^{3+}/Eu^{3+} co-doped $Sr_7Sb_2O_{12}$ red-emitting phosphor for white LED, Inorg. Chem. Commun. 150 (2023) 110365. https://doi.org/10.1016/j.inoche.2022.110365.

[137] P.K. Pandey, P. Dixit, V. Chauhan, P.C. Pandey, Luminescence properties and energy transfer studies in thermally stable Bi_2O_3_ Sm^{3+}, Eu^{3+} phosphor, J. Alloys Compd. 952 (2023) 169911. https://doi.org/10.1016/j.jallcom.2023.169911.

[138] D. Liu, G. Li, P. Dang, Q. Zhang, Y. Wei, L. Qiu, M.S. Molokeev, H. Lian, M. Shang, J. Lin, Highly ef fi cient Fe^{3+} -doped $A_2BB'O_6$ (A =Sr^{2+} , infrared-emitting phosphors for spectroscopic analysis, (2022). https://doi.org/10.1038/s41377-022-00803-x.

[139] R. Cui, X. Wang, Q. Chen, C. Deng, Optik Photoluminescence properties and energy transfer of $ZnNb_2O_6 : Eu^{3+}$, Sm^{3+} orange-red phosphors for WLEDs, Optik (Stuttg). 261 (2022) 169116. https://doi.org/10.1016/j.ijleo.2022.169116.

[140] X. Zhang, R. Cui, K. Guo, M. Zhang, J. Zhang, C. Deng, Luminescence properties of $Ca_2GdNbO_6 : Sm^{3+}$, Eu^{3+} red phosphors with high quantum yield and excellent thermal stability for WLEDs, Ceram. Int. (2023) 1–11. https://doi.org/10.1016/j.ceramint.2023.01.125.

[141] M. Kumar, A.S. Rao, S. Kaur, Downshifting analysis of Sm^{3+}/Eu^{3+} co-doped LiBiAlBSi glasses for red emission element of white LEDs, Chem. Phys. Lett. 788 (2022) 139303. https://doi.org/10.1016/j.cplett.2021.139303.

[142] P. Ramesh, J. Gangareddy, K.N. Sathish, A.G. Pramod, V. Hegde, U.M. Pasha, S. Khan, K. Annapurna, M.I. Sayyed, A.M.S. Alhuthali, D.A. Agarkov, M.K. Kokila, Effect of heavy metal oxides on photoluminescence and spectroscopic attributes of Eu

$^{3+}$ activated borate glasses, Opt. Mater. (Amst). 114 (2021) 110933. https://doi.org/10.1016/j.optmat.2021.110933.

[143] Z. Wang, J. Chen, Q. Li, Y. Liu, Multi-color luminescence and energy transfer behavior of $Ba_3Lu_4O_9 : Tb^{3+}$, Eu^{3+} phosphor for solid-state lighting, Chem. Phys. Lett. 771 (2021) 138481. https://doi.org/10.1016/j.cplett.2021.138481.

[144] S. Kaur, V. Katyal, V. Plakkot, N. Deopa, A. Prasad, S. Rao, Radiative emission analysis of Sm^{3+} ions doped borosilicate glasses for visible orange photonic devices, 572 (2021).

[145] Y. Hua, Z. Li, Synthesis and photoluminescence properties of novel orange-emitting $Sr_2YSbO_6 : Sm^{3+}$ phosphors for potential solid-state lighting, Inorg. Chem. Commun. 128 (2021) 108576. https://doi.org/10.1016/j.inoche.2021.108576.

[146] J. Bhemarajam, M.M. Babu, P.S. Prasad, M. Prasad, Spectroscopic studies on Er^{3+} ions incorporated bismuth borolead lithium glasses for solid state lasers and fiber amplifiers Spectroscopic studies on Er^{3+} ions incorporated bismuth borolead lithium glasses for solid state lasers and fiber amplifiers, Opt. Mater. (Amst). 113 (2021) 110818. https://doi.org/10.1016/j.optmat.2021.110818.

[147] V. Hegde, G. Devarajulu, A.G. Pramod, S.B. Kolavekar, D.A. Aloraini, A.H. Almuqrin, M.I. Sayyed, G. Jagannath, Analysis of Optical and Near-Infrared Luminescence of Er^{3+} and Er^{3+} / Yb^{3+} Co-Doped Heavy Metal Borate Glasses for Optical Amplifier Applications, (2022).

[148] V.E.C.-O. H.U. Lopez-Herrer, J. Escorcia-Garcia, CA Gutierrez-Chavarria, V. Agarwal, Influence of CaO and Dy_2O_3 on the structural , chemical and optical properties of thermally stable luminescent silicate nanoglass-ceramics, J. Mater. Res.

Technol. 20 (2022) 1544–1557. https://doi.org/10.1016/j.jmrt.2022.07.148.

[149] M. Kumar, A.S. Rao, Influence of Tb^{3+} ions concentration and temperature on lithium bismuth alumino borosilicate glasses for green photonic device applications, Opt. Mater. (Amst). 120 (2021) 111439. https://doi.org/10.1016/j.optmat.2021.111439.

[150] H. George, N. Deopa, S. Kaur, A. Prasad, M. Sreenivasulu, M. Jayasimhadri, A.S. Rao, Judd-Ofelt parametrization and radiative analysis of Dy^{3+} ions doped Sodium Bismuth Strontium Phosphate glasses, J. Lumin. 215 (2019) 116693. https://doi.org/10.1016/j.jlumin.2019.116693.

[151] R. Bajaj, A. Prasad, A.V.S. Yeswanth, P. Rohilla, S. Kaur, Down-shifting photoluminescence studies of thermally stable Dy^{3+} ions doped borosilicate glasses for optoelectronic device applications, J. Mater. Sci. Mater. Electron. 33 (2021) 4782–4793. https://doi.org/10.1007/s10854-021-07667-8.

[152] A. Prasad, A.S. Rao, G.V. Prakash, A study on up-conversion and energy transfer kinetics of $KGdF_4 : Yb^{3+/} Er^{3+}$ nanophosphors, J. Mol. Struct. 1205 (2020) 127647. https://doi.org/10.1016/j.molstruc.2019.127647.

[153] V. Singh, A. Prasad, N. Deopa, A.S. Rao, S. Jung, N. Singh, J.L. Rao, G. Lakshminarayana, Luminescence features of Mn^{2+}-doped Zn<inf>2</inf>SiO<inf>4</inf>: A green color emitting phosphor for solid-state lighting, Optik (Stuttg). 225 (2021). https://doi.org/10.1016/j.ijleo.2020.165715.

[154] K. Siva Rama Krishna Reddy, K. Swapna, S. Mahamuda, M. Venkateswarlu, A.S. Rao, G. Vijaya Prakash, Investigation on structural and luminescence features of Dy^{3+} ions doped alkaline-earth boro tellurite glasses for optoelectronic devices, Opt. Mater. (Amst). 85 (2018) 200–210. https://doi.org/10.1016/j.optmat.2018.08.057.

[155] N. Deopa, M.K. Sahu, P.R. Rani, R. Punia, A.S. Rao, Realization of warm white light and energy transfer studies of Dy^{3+}/Eu^{3+} co-doped Li2O-PbO-Al_2O_3-B_2O_3 glasses for lighting applications, J. Lumin. 222 (2020) 117166. https://doi.org/10.1016/j.jlumin.2020.117166.

[156] C. Sumalatha, R. Doddoji, M. Venkateswarlu, P.R. Rani, K. Swapna, S. Mahamuda, A.S. Rao, White light emission from Dy^{3+}-doped ZnO + Bi_2O_3 + BaF_2 + B_2O_3 + TeO_2 glasses: Structural and spectroscopic properties, Spectrochim. Acta - Part A Mol. Biomol. Spectrosc. 240 (2020) 118568. https://doi.org/10.1016/j.saa.2020.118568.

[157] N. Deopa, S. Saini, S. Kaur, A. Prasad, A.S. Rao, Spectroscopic investigations on Dy^{3+} ions doped zinc lead alumino borate glasses for photonic device applications, J. Rare Earths. 37 (2019) 52–59. https://doi.org/10.1016/j.jre.2018.04.013.

[158] Y. Fu, P. Xiong, X. Liu, X. Wang, S. Wu, Q. Liu, M. Peng, Y. Chen, A promising blue-emitting phosphor $CaYGaO_4$:Bi^{3+} for near-ultraviolet (NUV) pumped white LED application and the emission improvement by Li+ ions, (2020). https://doi.org/10.1039/D0TC03941A.

[159] S. Wu, P. Xiong, X. Liu, Y. Fu, Q. Liu, Y. Chao, Q. Dong, Y. Li, W. Chen, Y. Chen, Z. Ma, M. Peng, $Sr_3Y(BO_3)_3$:Bi^{3+} phosphor with excellent thermal stability and color tunability for near-ultraviolet white-light LEDs, J. Mater. Chem. C. (2021). https://doi.org/10.1039/D0TC05960A.

[160] S.K. Gupta, K. Sudarshan, R.M. Kadam, Materials & Design Tunable white light emitting $Sr_2V_2O_7$: Bi^{3+} phosphors : Role of bismuth ion, Mater. Des. 130 (2017) 208–214. https://doi.org/10.1016/j.matdes.2017.05.056.

[161] X. Huang, J. Liang, S. Rtimi, B. Devakumar, Z. Zhang, Ultra-high color rendering

warm-white light-emitting diodes based on an efficient green-emitting garnet phosphor for solid-state lighting, Chem. Eng. J. 405 (2021) 126950. https://doi.org/10.1016/j.cej.2020.126950.

[162] S. Wang, B. Devakumar, Q. Sun, J. Liang, L. Sun, X. Huang, Highly efficient near-UV-excitable, (2020) 4408–4420. https://doi.org/10.1039/d0tc00130a.

[163] J. Liang, B. Devakumar, L. Sun, S. Wang, Q. Sun, X. Huang, Full-visible-spectrum lighting enabled by an excellent cyan-emitting garnet phosphor, (2020) 4934–4943. https://doi.org/10.1039/d0tc00006j.

[164] M. Wang, Z. Zhong, J. Lin, R. Zhang, Structure and luminescence properties of Bi^{3+} -doped $ZrSiO_4$ phosphors for near-UV excited white LEDs, Mater. Lett. 324 (2022) 132750. https://doi.org/10.1016/j.matlet.2022.132750.

[165] V. Chauhan, P. Dixit, P.C. Pandey, Optik Enhancement in greenish-white photoluminescence of $Zn_3(VO_4)_2$ phosphor by Bi^{3+} doping, Optik (Stuttg). 238 (2021) 166682. https://doi.org/10.1016/j.ijleo.2021.166682.

[166] H.C. Swart, R.E. Kroon, Optical Materials : X (INVITED) Ultraviolet and visible luminescence from bismuth doped materials, Opt. Mater. X. 2 (2019) 100025. https://doi.org/10.1016/j.omx.2019.100025.

[167] S. Wu, P. Xiong, X. Liu, Y. Fu, Q. Liu, M. Peng, Y. Chen, Z. Ma, Bismuth activated high thermal stability blue-emitting phosphor $Na_2Y_2B_2O_7$:Bi used for near-UV white-light LEDs, (2020). https://doi.org/10.1039/d0tc04148c.

[168] Q. Lin, J. Lin, X. Yang, Y. He, L. Wang, J. Dong, The e ff ects of Mg^{2+} and Ba^{2+} dopants on the microstructure and magnetic properties of doubly-doped LaFeO 3 perovskite catalytic nanocrystals, Ceram. Int. 45 (2019) 3333–3340.

https://doi.org/10.1016/j.ceramint.2018.10.246.

[169] S. V Zubkov, Crystal structure and dielectric properties of layered perovskite-like solid, 11 (2021) 1–5. https://doi.org/10.1142/S2010135X2160016X.

[170] A. Chithambararaj, N. Rameshbabu, A.C. Bose, Study of microwave assisted growth of meta-stable 1-D h-MoO3, Sci. Adv. Mater. 6 (2014) 1302–1312. https://doi.org/10.1166/sam.2014.1797.

[171] L.S. Chougala, M.S. Yatnatti, R.K. Linganagoudar, R.R. Kamble, J.S. Kadadevarmath, A simple approach on synthesis of TiO_2 nanoparticles and its application in dye sensitized solar cells, J. Nano- Electron. Phys. 9 (2017). https://doi.org/10.21272/jnep.9(4).04005.

[172] N. Laohavisuti, B. Boonchom, W. Boonmee, K. Chaiseeda, S. Seesanong, Simple recycling of biowaste eggshells to various calcium phosphates for specific industries, Sci. Rep. 11 (2021) 1–12. https://doi.org/10.1038/s41598-021-94643-1.

[173] B.M. Jaffar, H.C. Swart, H.A.A.S. Ahmed, A. Yousif, R.E. Kroon, Comparative study of the luminescence of Bi doped LaOCl and LaOBr phosphor powders, J. Lumin. 250 (2022) 119050. https://doi.org/10.1016/j.jlumin.2022.119050.

[174] M. Peddaiah, C. Salma, B.H. Rudramadevi, Optik Structural and an orange-red emission studies of Sm^{3+} doped $Ba_3La_2(BO_3)_4$ phosphor for solid state lighting application, Optik (Stuttg). 244 (2021) 166695. https://doi.org/10.1016/j.ijleo.2021.166695.

[175] R.S. Yadav, S.B. Rai, Surface analysis and enhanced photoluminescence via Bi^{3+} doping in a Tb^{3+} doped Y_2O_3 nano-phosphor under UV excitation, J. Alloys Compd. 700 (2017) 228–237. https://doi.org/10.1016/j.jallcom.2017.01.074.

[176] S. Wang, M. ru Chen, W. jing Zhang, Y. jie Han, P. mei Shi, Y. nan Guo, Z. fei Mu, X.L. Lu, Z. wei Zhang, A. jun Song, A novel blue-emitting $Sr_2Gd_8(SiO_4)_6O_2:Bi^{3+}$ phosphor with oxyapatite structure, Inorg. Chem. Commun. 124 (2021) 108372. https://doi.org/10.1016/j.inoche.2020.108372.

[177] A. Prasad, A.S. Rao, G.V. Prakash, Up-conversion luminescence and EPR properties of $KGdF_4:Yb^{3+}/Tm^{3+}$ nanophosphors, Opt. - Int. J. Light Electron Opt. 208 (2020) 164538.

[178] N.A.M. Saeed, E. Coetsee, R.E. Kroon, M. Bettinelli, H.C. Swart, Photoluminescence of Bi^{3+} doped in YOF phosphor as an activator, Opt. Mater. (Amst). 119 (2021) 111291. https://doi.org/10.1016/j.optmat.2021.111291.

[179] G. Fan, X. Wang, X. Qiu, D. Fan, R. Hu, Z. Tian, Luminescent properties of orange-red emitting phosphors $NaGd(MoO_4)(WO_4)$: Sm^{3+} for white LED, Opt. Mater. (Amst). 91 (2019) 363–370. https://doi.org/10.1016/j.optmat.2019.02.023.

[180] R. Cao, T. Fu, H. Xu, W. Luo, D. Peng, Z. Chen, J. Fu, Synthesis and luminescence enhancement of $CaTiO_3:Bi^{3+}$ yellow phosphor by codoping Al^{3+}/B^{3+} ions, J. Alloys Compd. 674 (2016) 51–55. https://doi.org/10.1016/j.jallcom.2016.02.252.

[181] L. Wang, M. Xu, H. Zhao, D. Jia, Luminescence, energy transfer and tunable color of Ce^{3+},Dy^{3+}/Tb^{3+} doped $BaZn_2(PO_4)_2$ phosphors, New J. Chem. 40 (2016) 3086–3093. https://doi.org/10.1039/c5nj03148f.

[182] L.K. Bharat, Y. Il Jeon, J.S. Yu, RE^{3+} (RE^{3+} = Tm^{3+}, Tb^{3+} and Sm^{3+}) ions activated Y_6WO_{12} phosphors: Synthesis, photoluminescence, cathodoluminescence and thermal stability, J. Alloys Compd. 685 (2016) 559–565. https://doi.org/10.1016/j.jallcom.2016.05.321.

[183] X. Min, Y. Sun, L. Kong, M. Guan, M. Fang, Y. Liu, X. Wu, Z. Huang, Novel pyrochlore-type La_2Zr_2O7: Eu^{3+} red phosphors: Synthesis, structural, luminescence properties and theoretical calculation, Dye. Pigment. 157 (2018) 47–54. https://doi.org/10.1016/j.dyepig.2018.04.045.

[184] Q. Wu, Q. Zhao, P. Zheng, W. Chen, D. Xiang, Z. He, Q. Huang, J. Ding, J. Zhou, Insight into a concentration-sensitive red-emitting phosphor $Li_2Ca_4Si_4O_{13}$:Eu^{3+} for multifunctional applications: Crystal structure, electronic structure and luminescent properties, Ceram. Int. 46 (2020) 2845–2852. https://doi.org/10.1016/j.ceramint.2019.09.277.